THE UNIVERSITY OF QUEENSLAND

AUSTRALIA

Mechanisms of calcium handling during a malignant hyperthermia event.

Rocky Hyun Suk Choi
M.S., Molecular Biosciences & Bioengineering
B.S., Molecular Biology

A thesis submitted for the degree of Doctor of Philosophy at
The University of Queensland in 2018
Faculty of Medicine

Abstract

Malignant hyperthermia (MH) is a clinical syndrome of the skeletal muscle that presents as a hypermetabolic response to volatile gas anaesthetics such as halothane, isoflurane, and to the depolarizing muscle relaxant succinylcholine. Genetic predisposition mainly arises from mutations in the gene for skeletal muscle ryanodine receptor (RyR1); a calcium channel that is tightly regulated to release Ca^{2+} for muscle contraction. MH susceptible RyR1 are more prone to open by RyR1 agonist, resulting in the uncontrolled release of Ca^{2+} from the sarcoplasmic reticulum (SR). The hypermetabolic state is due to the excessive consumption of adenosine triphosphate (ATP) as the muscle works to clear the high cytosolic Ca^{2+}. Dantrolene has been used to great effect by clinicians in treating MH. However the mechanism of its action remains highly contested.

This thesis examines Ca^{2+} handling in muscle fibers where RyR1 activity is changed due to mutations. RyR1 activity was also acutely changed by altering the cytoplasmic environment and by treating the muscle fiber with varying RyR1 modulators. The release of SR Ca^{2+} was monitored using fluorescent Ca^{2+} indicators in mechanically skinned fibers isolated from rat, toad and human muscle susceptible to MH. The results show that the inhibitory effect of dantrolene is dependent on cytosolic concentrations of Mg^{2+} ($[Mg^{2+}]_{cyto}$), an endogenous negative regulator of the RyR1. Furthermore, it was demonstrated in human muscle susceptible to MH that dantrolene was ineffective at reducing halothane-induced Ca^{2+} release in the presence of resting levels of $[Mg^{2+}]_{cyto}$ (1 mM). These results suggest that raised $[Mg^{2+}]_{cyto}$, a condition which is likely to arise during an MH event, works synergistically with dantrolene to inhibit Ca^{2+} release from the RyR1. It was also demonstrated that halothane induced Ca^{2+} release took the form of a repetitive Ca^{2+} wave in human MH, and toad muscle. A close examination of the release mechanism in human MH muscle revealed that the release of SR Ca^{2+} and the mechanism underlying the propagation of the Ca^{2+} wave was not due to Ca^{2+}-induced-Ca^{2+}-release (CICR). These results were contrasted to the observation made in toad skeletal muscle which showed the involvement of CICR. However, it was found that both luminal SR and cytosolic Ca^{2+} plays an important role in the mechanisms involved in overactive Ca^{2+} release.

The demonstration of the Mg^{2+} dependence on dantrolene inhibition of the RyR1 emphasized the importance of studying the RyR1 under near physiological conditions. Utilizing a novel approach by trapping Ca^{2+} indicator in either the SR or the transverse tubule (t-system) of mechanically skinned rat skeletal muscle fibers, it was determined if

either compartment would be able to report changes in RyR1 activity. The activity of the RyR1 was experimentally manipulated by exposing the preparation to varying concentrations of Mg^{2+}, RyR1 agonists (halothane, caffeine), and RyR1 antagonist (dantrolene, tetracaine). Though it is well known that RyR1 activation will deplete the SR of Ca^{2+}, it is only a relatively recent finding that activation of the RyR1 also will deplete the t-system of Ca^{2+} via a store-operated-Ca^{2+}-entry (SOCE) mechanism. It was found that the free $[Ca^{2+}]_{SR}$ remained comparable over the broad range of $[Mg^{2+}]_{cyto}$ tested. Therefore, it was concluded that the free $[Ca^{2+}]_{SR}$ was not able to report changes in RyR1 activity. In contrast, an increase in RyR1 activity (induced by low-Mg^{2+} or pharmacological agonist) resulted in the depletion of the $[Ca^{2+}]_{t\text{-}system}$. Importantly, the degree of $[Ca^{2+}]_{t\text{-}system}$ depletion was shown to be dependent on the activity of the RyR1. Utilizing this novel approach the Mg^{2+} dependence on RyR1 inhibition by dantrolene was again demonstrated.

Declaration by author

This thesis is composed of my original work, and contains no material previously published or written by another person except where due reference has been made in the text. I have clearly stated the contribution by others to jointly-authored works that I have included in my thesis.

I have clearly stated the contribution of others to my thesis as a whole, including statistical assistance, survey design, data analysis, significant technical procedures, professional editorial advice, financial support and any other original research work used or reported in my thesis. The content of my thesis is the result of work I have carried out since the commencement of my higher degree by research candidature and does not include a substantial part of work that has been submitted to qualify for the award of any other degree or diploma in any university or other tertiary institution. I have clearly stated which parts of my thesis, if any, have been submitted to qualify for another award.

I acknowledge that an electronic copy of my thesis must be lodged with the University Library and, subject to the policy and procedures of The University of Queensland, the thesis be made available for research and study in accordance with the Copyright Act 1968 unless a period of embargo has been approved by the Dean of the Graduate School.

I acknowledge that copyright of all material contained in my thesis resides with the copyright holder(s) of that material. Where appropriate I have obtained copyright permission from the copyright holder to reproduce material in this thesis and have sought permission from co-authors for any jointly authored works included in the thesis.

Publications during candidature

Choi RH, Koenig X & Launikonis BS. (2017). Dantrolene requires Mg^{2+} to arrest malignant hyperthermia. Proceedings of the National Academy of Sciences 114, 4811-4815.

Conference abstracts

R.H. Choi, and B.S. Launikonis (2017). Dantrolene requires Mg^{2+} to arrest malignant hyperthermia. Oral presentation at the Australian Physiological Society annual meeting for 2017 in Melbourne, Victoria, Australia.

R.H. Choi, X. Koenig, and B.S. Launikonis (2017). Dantrolene requires Mg^{2+} to arrest malignant hyperthermia. Poster presentation at the Gordon Research conference (Muscle: Excitation contraction coupling).

R.H. Choi, X. Koenig, T.R. Cully and B.S. Launikonis (2016). Exercise partially reverses the changes in calcium handling in skeletal muscle with age. Oral presentation as a representative of the University Of Queensland School of Biomedical Science at The Otago School of Medical Sciences Postgraduate Symposium for 2016 in Dunedin, New Zealand

R.H. Choi, X. Koenig, T.R. Cully and B.S. Launikonis (2016). Integral role of Mg^{2+} in observing the inhibitory effect of dantrolene. Poster presentation at the Australian Physiological Society annual meeting for 2016 in Adelaide, SA, Australia.

R.H. Choi, X. Koenig, T.R. Cully and B.S. Launikonis (2016). The transverse tubule Ca^{2+} handling properties are a sensitive detector of ryanodine receptor activity. Poster presentation at the Gage Muscle Conference 2016 in Canberra, NSW, Australia.

R.H. Choi, X. Koenig, T.R. Cully and B.S. Launikonis (2015). The effect of intracellular $[Mg^{2+}]$ on Ca^{2+} handling by the sarcoplasmic reticulum. Oral presentation at the Australian Physiological Society annual meeting for 2015 in Hobart, TAS, Australia.

R.H. Choi, T.R. Cully and B.S. Launikonis (2014). Effect of changing the $[Mg^{2+}]$ on ryanodine receptor leak activity in rat skeletal muscle. Poster presentation at the Australian Physiological Society annual meeting for 2014 in Brisbane, QLD, Australia.

R.H. Choi, T.R. Cully and B.S. Launikonis (2014). Effect of changing the $[Mg^{2+}]_{cytoplasm}$ on ryanodine receptor leak activity in rat skeletal muscle. Poster presentation at the Australian Physiological Society annual meeting for 2014 in Brisbane, QLD, Australia.

Publications included in this thesis

Choi RH, Koenig X & Launikonis BS. (2017). Dantrolene requires Mg^{2+} to arrest malignant hyperthermia. Proceedings of the National Academy of Sciences 114, 4811-4815. Publication citation – incorporated as Chapter 3.

Contributor	Statement of contribution
Rocky H Choi (Candidate)	Conception and design (70%) Analysis and interpretation (70%) Drafting and production (20%)
Xaver X Koenig	Conception and design (15%) Analysis and interpretation (15 %) Drafting and production (20%)
Bradley S Launikonis	Conception and design (15%) Analysis and interpretation (15%) Drafting and production (60%)

Contributions by others to the thesis

Dr. Robert Fassett and Dr. Claire Hyam (Stewart) performed the muscle biopsy used in this thesis.

Crystal Seng and Jeremy Briggs helped perform the experiments necessary to determine the relative halothane evaporation rate.

Statement of parts of the thesis submitted to qualify for the award of another degree

None

Research Involving Human or Animal Subjects

Animal ethics was approved by the School of Biomedical Science at The University of Queensland (Chief investigator: Dr. Bradley Launikonis; Title: Calcium regulation in healthy and dystrophic skeletal muscle; AEC approval Number: SCMB/032/14/ARC, approval duration: 17-March-2014 to 17-March-2017).

The use of human muscle biopsy was approved by the Human Ethics Committee at The University of Queensland (Chief investigator: Dr. Bradley Launikonis; Title: Examining Functional and Structural Changes of Skeletal Muscle in Inherited Muscly Myopathies; approval number: 2014000826; approval duration: 31-July-2019).

Acknowledgements

I would like to express my sincere appreciation to my Principal Supervisor, Dr. Bradley Launikonis, for giving me an opportunity to join his research laboratory and for the constant guidance and support throughout my doctoral studies. I would also like to thank Dr. Peter Noakes and Dr. Gregory Monteith for their time, support, mentorship, and encouragement during each major thesis milestone examination. I was also fortunate to work with Dr. Daniel Blackmore who I would also like to thank. Dr. Blackmore provided mice to conduct a study on skeletal muscle Ca^{2+} leak in aged skeletal muscle.

I would also like to thank Dr. Xaver Koenig and Dr. Tanya Cully. Their constant support and guidance helped me become a better researcher. I am also grateful for their friendship which made the time spent in the laboratory together all the more enjoyable.

Finally, I would like to thank my family members, David Choi Sr. Myong Sook Choi, David Choi Jr, and James Choi for their constant support. I would not be where I am now without them.

Financial support

This research was supported by the University of Queensland International Scholarship (UQI) and by the Australian Research Council (Bradley Launikonis, ARC Future Fellow (FT140101309).

Keywords

Skeletal muscle, malignant hyperthermia, calcium, magnesium, dantrolene, halothane, ryanodine receptor

Australian and New Zealand Standard Research Classifications (ANZSRC)

ANZSRC code: 060601, Animal Physiology, - Biophysics 60%

ANZSRC code: 060602, Animal Physiology, - Cell 20%

ANZSRC code: 111504, Pharmaceutical Sciences, 20%

Fields of Research (FoR) Classification

FoR code: 0606, Physiology, 60%

FoR code: 1115, Pharmacology and Pharmaceutical Sciences, 40%

Table of Contents

List of Figures

List of Tables

List of Abbreviations

1,6-diaminohexane-N,N,N‘,N‘-tetraacetic acid	HDTA
4-(2-hydroxyethyl)-1-piperazineethanesulfonic acid	HEPES
4-chloro-M-cresol	4-CMC
Acetyl moiety	AM
Acetylcholine	ACh
Adenosine triphosphate	ATP
Alpha	α
Analysis of variance	ANOVA
And others	*et al*
Anisotrophic	A
Arbitrary units	au
Beta	β
Plasma membrane Ca^{2+} ATPase pump	PMCA
Caffeine halothane contracture test	CHCT
Calcium carbonate	$CaCO_3$
Calcium chloride	$CaCl_2$
Calcium concentration in the cytoplasm	$[Ca^{2+}]_{cyto}$
Calcium ion	Ca^{2+}
Calcium ion concentration	$[Ca^{2+}]$
Calcium-induced-calcium-release	CICR
Calmodulin	CaM
Calsequestrin	CSQ
Carbon dioxide	CO_2
Carbonilcyanide p-triflouromethoxyphenylhydrazone	FCCP
Centimeter	cm
Centimeters cubed	cm^3
Creatine phosphate	CP
Dantrolene	dan
Degrees Celsius	°C
Dihydropyridine receptor	DHPR
Dimethyl sulfoxide	DMSO
Disassociation constant Calcium	$Kd,_{Ca}$

Disassociation constant Magnesium	$Kd,_{Mg}$
Endoplasmic reticulum	ER
Excitation contraction coupling	ECC
Extensor digitorum longus	EDL
Flexor digitorum brevis	FDB
Fluorescent minimum	f-minimum
Fluorescent maximum	f-maximum
Fluorescein-5N	fluo-5N
Fluorescence	F
Fluorescence subscript 0	F_0
Free calcium concentration in the sarcoplasmic reticulum	free $[Ca^{2+}]_{SR}$
Full duration at half maximum	FDHM
Gallium arsenide phosphide	GaAsP
Greater than	>
Half inhibitory concentration	IC_{50}
Helle zone	H-zone
Hertz	Hz
Hour	h
id est "that is"	*i.e*
In its original place.	*in situ*
Inhibitory constant	K_i
Isotropic	I
Junctional Space	JS
Kilogram	kg
Less than	<
Magnesium concentration in the cytoplasm	$[Mg^{2+}]_{cyto}$
Magnesium oxide	MgO
Magnesium chloride	$MgCl_2$
Magnesium ion concentration	$[Mg^{2+}]$
Malignant hyperthermia	MH
Malignant hyperthermia equivocal	MHE
Malignant hyperthermia non-susceptible	MHN
Malignant hyperthermia susceptible	MHS
Microliter	µL

Micrometer	µm
Micromolar	µM
Millimolar	mM
Milli-osmolality	mOsmol
Milligram	mg
Milliliter	mL
Millimeter	mm
Milliseconds	ms
N', N' tetra acetic acid	EGTA
Na^+/Ca^{2+} exchanger	NCX
Nano meter	nm
Nano molar	nM
N-benzyl-p-toluene Sulphonamide	BTS
Number	No.
Open probability	P_0
Percent	%
Plus-minus	±
Position	p
Potassium chloride	KCl
Potassium ion	K^+
Potential of hydrogen	pH
Potassium hydroxide	KOH
Probability value	*p*
Rhodamine 2	rhod-2
Rhodamine 5N	rhod-5N
Ryanodine receptor subtype 1	RyR1
Ryanodine receptor subtype 2	RyR2
Ryanodine receptors	RyR
Sample size	n
Sarco-endoplasmic reticulum Calcium ATPase	SERCA
Sarcoplasmic reticulum	SR
Seconds	s
Sodium chloride	NaCl
Sodium hydroxide	NaOH

Sodium ion	Na^+
Solution used for human fiber experiments	(H)
Solution used for rat fiber experiments	(R)
Solution used for toad fiber experiments	(T)
Standard error of the mean	SEM
Store operated Ca^{2+} entry	SOCE
Store-overload- induced calcium release	SOICR
stromal interaction molecule 1	STIM1
Tau time constant	(τ)
Tetracaine	tet
The *in vitro* contracture test	IVCT
Total calcium concentration in the sarcoplasmic reticulum	total $[Ca^{2+}]_{SR}$
Transverse tubule of skeletal muscle	t-system
Two	di-
Underneath/lower	sub
Wild type	WT
xy coordinate	xy
xy coordinate over time	xyt
Years old	y/o
Zwitter	Z

Chapter 1: General Introduction

1.1 Introduction

Skeletal muscle composes the largest organ system in the human body and is the effector organ of the locomotor system. The ability of skeletal muscles to contract and relax plays an integral part in movement and maintenance of posture which is necessary for independent living in society. For this reason, understanding the underlying mechanisms involved in the maintaining the skeletal muscle is of importance.

Skeletal muscle contraction is mediated by the release of Ca^{2+} from an intracellular Ca^{2+} store in a process known as excitation contraction coupling (ECC). Ca^{2+} is a common secondary messenger and is involved in a wide array of cellular processes in biological systems. The effectiveness of Ca^{2+} signalling is maintained by creating a Ca^{2+} gradient between the cytoplasm, extracellular space, and the intracellular Ca^{2+} stores. In skeletal muscle, several highly specialized Ca^{2+} handling proteins localized to specific junctions coordinate to rapidly release and re-sequester Ca^{2+}. During a single Ca^{2+} release event the intracellular Ca^{2+} concentration ($[Ca^{2+}]_{cyto}$) can oscillate 100-1000 fold in a little as a few milliseconds (Melzer *et al.*, 1995). Disruption of Ca^{2+} homeostasis can lead to irregularly high $[Ca^{2+}]_{cyto}$ which can ultimately lead to skeletal muscle degradation through the activation of Ca^{2+}-dependent proteases.

The release of Ca^{2+} from the intracellular Ca^{2+} store is mediated by the ryanodine receptor (RyR) (Meissner *et al.*, 1988). Importantly, multiple diseases of the skeletal muscle such as Duchenne muscular dystrophy and central cores disease are thought to have irregular RyR function (Turner *et al.*, 1991; Spencer & Mellgren, 2002; Jungbluth, 2007). Furthermore, mutations on the RyR has also been implicated in a pharmacogenetics disorder known as malignant hyperthermia (MH). An MH susceptible individual develops a life threatening hypermetabolic response to inhaled anaesthetics such as halothane and sevoflurane which were later found to be an RyR agonist (Nelson, 1992; Duke *et al.*, 2003; Hopkins, 2011). The development of drugs that target and inhibit the RyR is an active field of research (Andersson & Marks, 2010; Dulhunty *et al.*, 2011; Rebbeck *et al.*, 2017). Dantrolene is a drug that is administered to alleviate the symptoms of MH and is an example of a successful drug candidate that targets the RyR. Interestingly, the mechanism by which dantrolene can inhibit the RyR is unresolved. This thesis aims to characterize in detail the underlying mechanisms involved in Ca^{2+} handling

during an MH event. Furthermore, the mechanism by which dantrolene can arrest MH will be investigated.

1.2 Skeletal muscle structure and organization

Before discussing Ca^{2+} handling in skeletal muscle, it is important to understand how the structural organization of the muscle lends to the overall function. Individual muscle fibers are composed of multiple myofibrils which are cylindrical structures largely composed of two filaments: thick myosin filaments and actin thin filaments (Figure 1.1; *top*). The actin thin filaments are 'coiled' around by tropomyosin and the troponin-complex which regulates the interactions between actin and myosin (Huxley, 1973; Parry & Squire, 1973). The thick and thin filaments intercalate and forming repeating functional units called the sarcomeres, which are defined by the distance between two Z-disc. Titin and nebulin as shown in Figure 1.1 (*top*) are thought to play an important role in the assembly of the sarcomere.

The muscle fiber is enclosed by a plasma membrane. This surface membrane is often referred to as the sarcolemma. The sarcolemma has become highly specialized to support the function of the muscle. The sarcolemma forms deep invaginations which create an extensive network known as the transverse-tubule (t-system or t-tubule used interchangeably) which encloses each myofibril. The t-system network is estimated to account for more than 80% of the total surface area of the plasma membrane (Franzini-Armstrong & Peachey, 1981). The main purpose of converting the majority of the sarcolemma into t-system is to allow propagation of the action potential deep into the muscle fiber (Franzini-Armstrong & Peachey, 1981).

Each t-system forms a junction with the sarcoplasmic reticulum (SR). The SR is a specialization of the endoplasmic reticulum (ER) in muscles, and functions as the main intracellular Ca^{2+} store. The SR membrane forms two distinct functional regions including the terminal cisterna of the SR which faces the t-system membrane and the longitudinal SR which spans the A-band of each sarcomere (Figure 1.1; *Bottom*). The terminal cisterna has a high density of Ca^{2+} release channels known as the ryanodine receptors and is the site of Ca^{2+} release from the SR (Endo, 1977; Melzer *et al.*, 1995). The longitudinal SR is found to have a high density of sarco/endoplasmic reticulum Ca^{2+}ATPase (SERCA) pumps (estimated density of 30,000/μm^2) which are responsible for

sequestering Ca^{2+} back into the SR after a Ca^{2+} release event (Marie & Silva, 1998; Martonosi & Pikula, 2003; Murphy *et al.*, 2009; Lamboley *et al.*, 2014).

In mammalian skeletal muscle, the point at which the membrane of one t-system and two terminal cisternae of the SR meet at each A-I band junction is known as the triad region. The gap between these two membranes meets around 12 nm which can be spanned by transmembrane proteins (Endo, 1977; Melzer *et al.*, 1995). This region forms a critical signalling micro-domain where the membrane bound proteins located either on the t-system or terminal cisterna of the SR can physically couple (Melzer *et al.*, 1995). Furthermore, this micro-domain (referred to as the junctional space) is diffusional restricted from the bulk cytoplasm, giving it a different ionic composition relative to the bulk cytoplasm (Despa *et al.*, 2014).

1.3 Skeletal muscle fiber types

It is well known that the skeletal muscle forms a heterogeneous mixture of fiber types that differ in their metabolic and contractile properties. Muscle fibers can be identified as being either a slow type I or a fast type II fiber. Two muscles commonly studied due to its fairly pure fiber type population include the extensor digitorum longus (EDL) and the soleus (SOL), which are predominantly composed of type II and type I fiber, respectively (Augusto *et al.*, 2004). Type I fibers contract and relax at a slow rate and utilize an oxidative phosphorylation pathway to produce adenosine triphosphate (ATP). In contrast, type II fibers contract and relax rapidly and utilize a glycolytic pathway for energy production. Type II fiber classification can be further divided into three fiber types as follows, IIA (high oxidative), IIX (intermediate) and IIB (high glycolytic) fibers (Augusto *et al.*, 2004). The functional property of the muscle predominantly dictates the proportions of these four fiber types. It is important to note that changes in the activity of the skeletal muscle and different disease conditions can alter these proportions (Schiaffino & Reggiani, 2011).

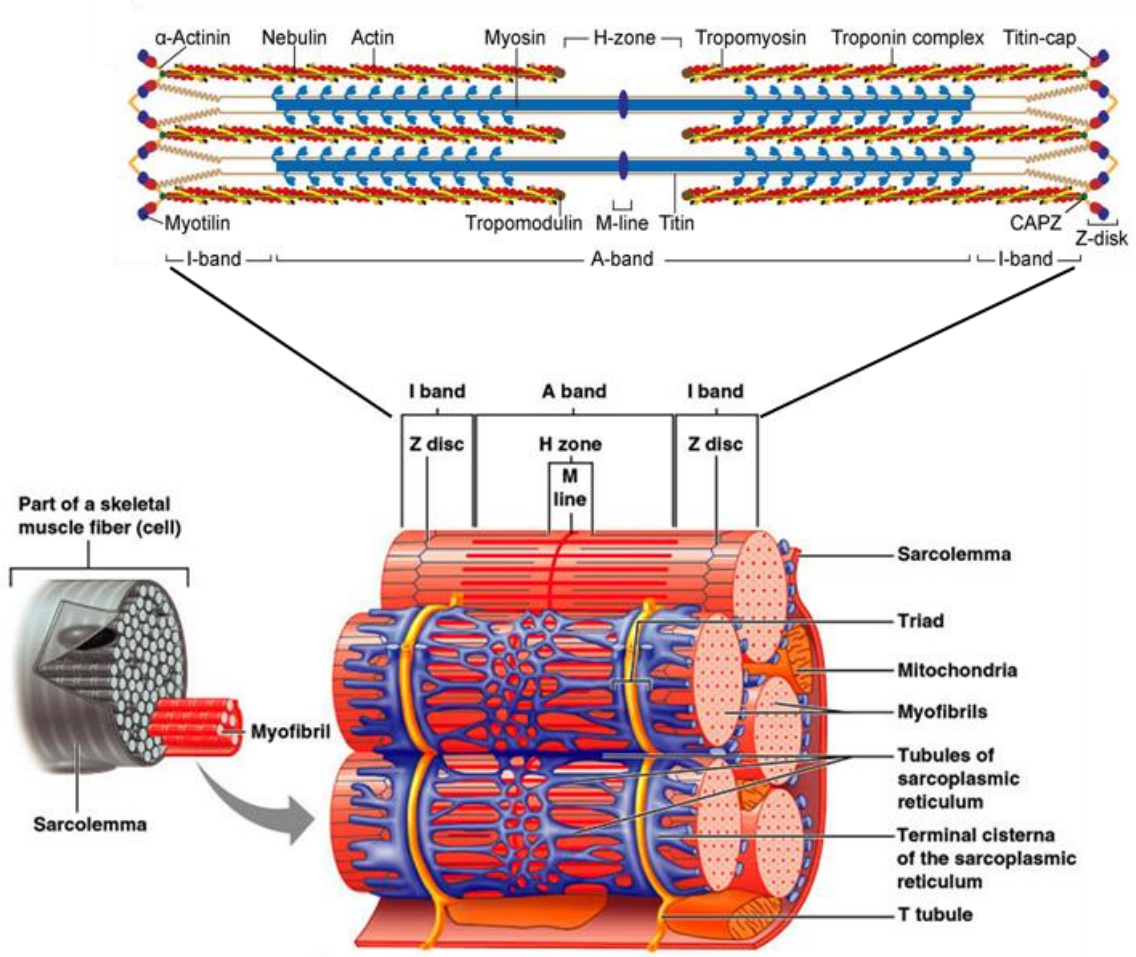

Figure 1.1 Whole skeletal muscle organization and schematic representation of the sarcomere structure.

The muscle fibre is made up of multiple myofibrils and is surrounded by a plasma membrane, also known as the sarcolemma. The sarcomere structure is shown above. The A-band (anisotrophic band) is the sarcomere region which contains myosin filaments, and the I-band (isotropic) contains the actin filaments. The region which contains no myosin-actin overlap is the H-Zone (Helle zone). The zone that bisects the I-band is the Z-disc (zwitter). Each myofibril is enclosed by the transverse tubule and sarcoplasmic reticulum, two membranes essential for Ca^{2+} release (modified from Marieb *et al.*, (2001) (bottom) and Rahimov *et al.*, (2013) (top).

1.4 Overview of excitation contraction coupling

The steps in excitation contraction coupling (ECC) can be explained at the level of the sarcomere. These steps effectively occur simultaneously across the fiber, synchronized by the action potential that propagates into the t-system from the sarcolemma (Figure 1.2*A*). ECC can be broken down and summarized as follows; (*i*) the neuronal action potential propagates down the axons to the site of the neural muscular junction, which causes the release of the neural transmitter, acetylcholine (ACh) from the synaptic terminal. ACh diffuses into the synaptic cleft and onto the motor endplate where it then binds to ACh receptors, resulting in localized membrane depolarization. The action potential then propagates from the surface of the sarcolemma and then deep into the muscle through the t-system network (*ii*). The membrane depolarization is sensed by the dihydropyridine receptor (DHPR) which then activates the skeletal muscle isoform of the RyR (RyR1; *iii*) (Melzer *et al.*, 1995). SR Ca^{2+} is then released into the cytosol as Ca^{2+} moves down its concentration gradient. Released Ca^{2+} then binds to the Ca^{2+} binding sites on troponin (troponin-C) which causes a conformational change of the tropomyosin protein complex (Figure 1.2*B*) (Lehman *et al.*, 1994). The conformational change then reveals myosin binding sites on the actin thin filaments which initiates the cross bridge cycle of the contractile apparatus (*iv*). Relaxation of the contractile apparatus begins as the Ca^{2+} is actively transported back into the SR by the SERCA pump (*v*), thus returning the cytoplasmic Ca^{2+} concentration to its resting levels.

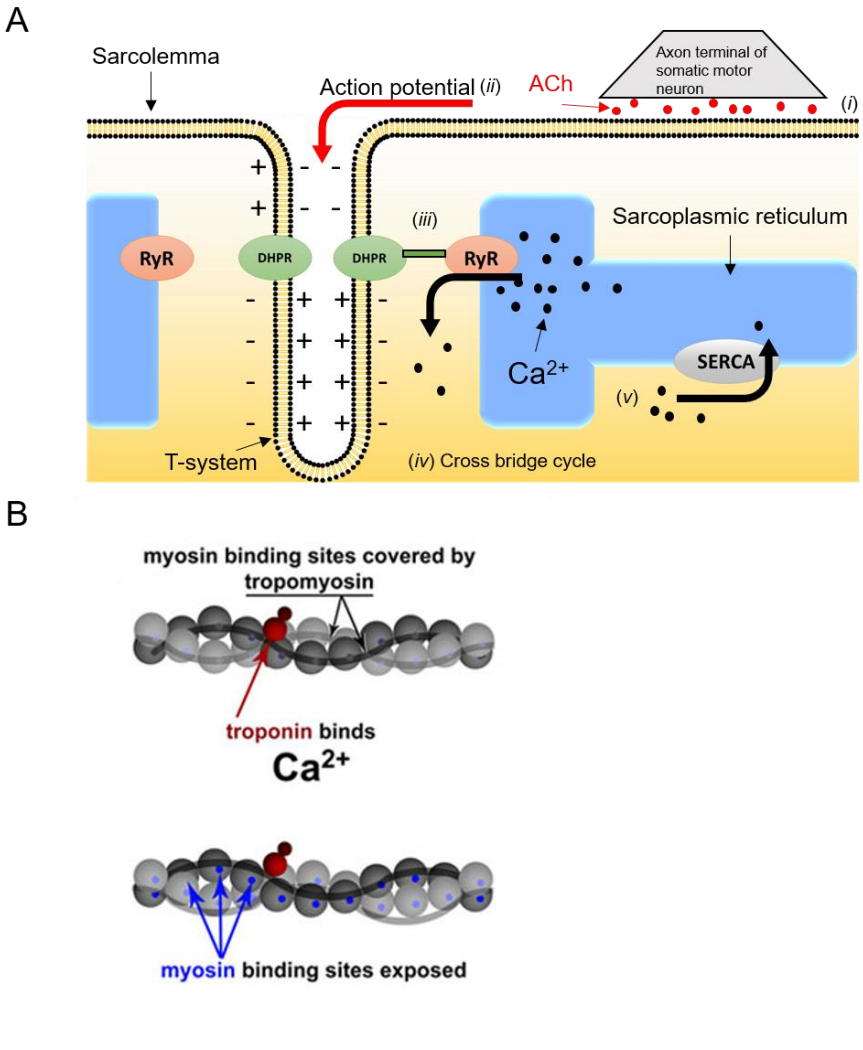

Figure 1.2 Overview of the steps involved in ECC.

*(*A) Schematic diagram of the skeletal muscle triad. The action potential is initiated upon binding of acetylcholine (ACh) to nicotinic receptors on the motor endplate (*i*). The action potential then propagates into the t-system (*ii*) which initiates Ca^{2+} release from the SR through the interactions between the dihydropyridine receptor (1,4-dihydropyridine receptor; DHPR) and the ryanodine receptor subtype-1 (RyR1; *iii*). The cross bridge cycle (*iv*) is then initiated as the released Ca^{2+} binds to troponin-C revealing myosin binding sites on the actin thin filaments (*B;* image modified from (Lehman *et al.*, 1994)). The released Ca^{2+} is then actively transported back into the SR by the sarco/endoplasmic reticulum Ca^{2+}ATPase (SERCA) pump (*v*).

1.5 Comparative overview of excitation contraction coupling in mammalian skeletal and cardiac muscle

The physiological activation of the RyR1 to produce a coordinated muscle contraction described above is in contrast to the uncontrolled release of Ca^{2+} during an MH event (see Chapter 3, 4 for full description). Importantly, the mechanism of RyR1 activation during an MH event remains unresolved. It has been proposed that the RyR1 is activated by a mechanism similar to that of the cardiac muscle (Endo, 2009); therefore in further examining this hypothesis, it will be important to distinguish the mechanism of RyR activation in the two muscle types. Furthermore, it is also interesting to consider the mechanism of Ca^{2+} release in amphibian skeletal muscle which have been shown to have similar release properties associated with both mammalian skeletal and cardiac muscle (Shirokova *et al.*, 1996; Sutko & Airey, 1996; Kashiyama *et al.*, 2010; Figueroa *et al.*, 2012).

The mechanism of activating Ca^{2+} release from the SR in vertebrate skeletal and cardiac muscle involves homologous proteins. However, the mode of activation differs (Melzer *et al.*, 1995; Bers, 2002). In skeletal muscle, the membrane depolarization is sensed by the DHPR, and upon activation, the DHPR undergoes a conformational change which causes the DHPR to physically couple to the RyR1 (Schneider & Chandler, 1973; Melzer *et al.*, 1995; Nakai *et al.*, 1996). Upon membrane depolarization a small amount of extracellular Ca^{2+} enters the cell through the DHPR (Hidalgo *et al.*, 1979; Lamb & Walsh, 1987); however it is important to note that skeletal muscle contractions can persist for long periods in the absence of extracellular Ca^{2+} with little to no decline in the force produced (Armstrong *et al.*, 1972). This suggests that extracellular Ca^{2+} entry is not necessary for Ca^{2+} release in vertebrate skeletal muscle. The physical interactions between the DHPR and the RyR1 are thought to alleviate Mg^{2+} inhibition on the RyR1 (discussed in Chapter 1.5). The physical coupling between the DHPR and RyR does not occur during cardiac ECC but rather relies on Ca^{2+} binding to an activation site on the RyR (Bers, 2002).

In cardiac muscle, Ca^{2+} is released through a mechanism known as calcium induced calcium release (CICR). The membrane depolarization is sensed by a homologous DHPR protein that is a different isoform to that of the skeletal muscle (Bers, 2002). The activation of the DHPR allows for extracellular Ca^{2+} to enter the cytoplasm (Fabiato, 1985). Extracellular Ca^{2+} that has entered the cell then binds to a high affinity activation sites on the cardiac RyR homologue (RyR2) (Rich *et al.*, 1988; Melzer *et al.*,

1995; Bers, 2002). Binding of Ca^{2+} to the activation site on the RyR2 triggers Ca^{2+} release from the SR, and the resulting increase in the Ca^{2+} concentration in the junctional space ($[Ca^{2+}]_{JS}$), leads to the further activation of adjacent RyR2 molecules (Melzer *et al.*, 1995; Bers, 2002). Thus, the initial Ca^{2+} release signal is amplified by the additional release of SR Ca^{2+}. In contrast to skeletal muscle, the removal of extracellular Ca^{2+} abolishes contractions in cardiac muscle (Rich *et al.*, 1988).

Spontaneous Ca^{2+} release events from the SR known as Ca^{2+} sparks are also observed in cardiac cells (Cheng *et al.*, 1993; Cheng *et al.*, 1996). Ca^{2+} sparks originating from a cluster of RyRs are brief, isolated and localized release events spanning only several microns (Cheng *et al.*, 1993; Cannell *et al.*, 1995). Under certain conditions, Ca^{2+} sparks have been shown to evolve into a Ca^{2+} wave which can propagate across the entire cardiac cell (Cheng *et al.*, 1996; Chen *et al.*, 2014). Spontaneous Ca^{2+} waves are thought to play a role in triggering arrhythmias (Cheng *et al.*, 1996; Chen *et al.*, 2014; Song *et al.*, 2017). CICR wave propagation is best described by the 'fire-diffuse-fire' model (Keizer *et al.*, 1998; Dawson *et al.*, 1999). This model describes the spatiotemporal evolution of the Ca^{2+} wave where the initial Ca^{2+} spark from the RyR ('fire') diffuses through the cytosol ('diffuse') and activates adjacent RyR clusters ('fire'). It is important to note that Ca^{2+} sparks are not observed in adult mammalian skeletal muscle (Shirokova *et al.*, 1998).

Interestingly, the positions and the relative density of DHPR and RyRs are likely related to their functional role in ECC (Franzini-Armstrong, 2004). As depicted in Figure 1.3*A* (skeletal muscle, left), 4 groups of DHPR (shown as closed circles) form a diamond shaped tetramer; similarly, 4 monomers of RyRs (open circles) are also grouped as a tetramer (Franzini-Armstrong, 2004). In cardiac cells, the DHPR do not form into tetramers (Figure 1.3*A*, cardiac muscle). In mammalian skeletal muscle, the ratio of DHPR to RYR1 is close to 2:1 (Bers & Stiffel, 1993); however in cardiac muscle, the DHPR to RYR2 ratio is approximately 1:10 (note that these ratios are species dependent) (Block *et al.*, 1988; Bers & Stiffel, 1993). It is assumed that the increased density of DHPR found in mammalian skeletal muscle is to increase the proportion of RyR1 that are directly coupled to the DHPR (Franzini-Armstrong, 2004). In cardiac muscle ECC, the initial Ca^{2+} release signal is amplified by the additional release of SR Ca^{2+}, and therefore it is not necessary for each Ca^{2+} release channel to be in close proximity to a DHPR molecule

(Franzini-Armstrong, 2004). This may explain the relatively low density of DHPR found in cardiac muscle.

Amphibian skeletal muscle express two isoforms of the RyR: α-RyR and β-RyR, which are homologous to mammalian RyR1 and the RyR isoform 3 (RyR3), respectively (Sutko & Airey, 1996; Murayama & Kurebayashi, 2011). These two isoforms are expressed in relatively equal proportions however they are localized in different regions of the SR (Sutko & Airey, 1996; Murayama & Kurebayashi, 2011). As depicted in Figure 1.3*B*, α-RyR are located in the junctional space directly opposed to the DHPR and β-RyR are positioned parajunctional on the SR membrane (Felder & Franzini-Armstrong, 2002). It has been proposed that the α-RyR due to its position on the SR junctional face is under the direct influence of the voltage sensor whereas the β-RyR are activated by Ca^{2+} (similar to CICR mechanism in cardiac muscle) (O'Brien *et al.*, 1995; Shirokova & Rios, 1997; Kashiyama *et al.*, 2010). This is supported by studies in myotubes expressing either α or β-RyR which show that membrane depolarization induced Ca^{2+} transients are only observed in myotubes expressing α-RyR (Kashiyama *et al.*, 2010). Furthermore, it has been demonstrated that CICR likely contributes to the physiological release of SR Ca^{2+} in amphibian skeletal muscle due to the relatively low cytoplasmic [Ca^{2+}] (~280 nM) needed to induce CICR (Figueroa *et al.*, 2012). This is in contrast to the mammalian skeletal muscle where CICR plays little to no role in the physiological release of SR Ca^{2+} (Shirokova *et al.*, 1998; Endo, 2009; Figueroa *et al.*, 2012; Bakker *et al.*, 2017).

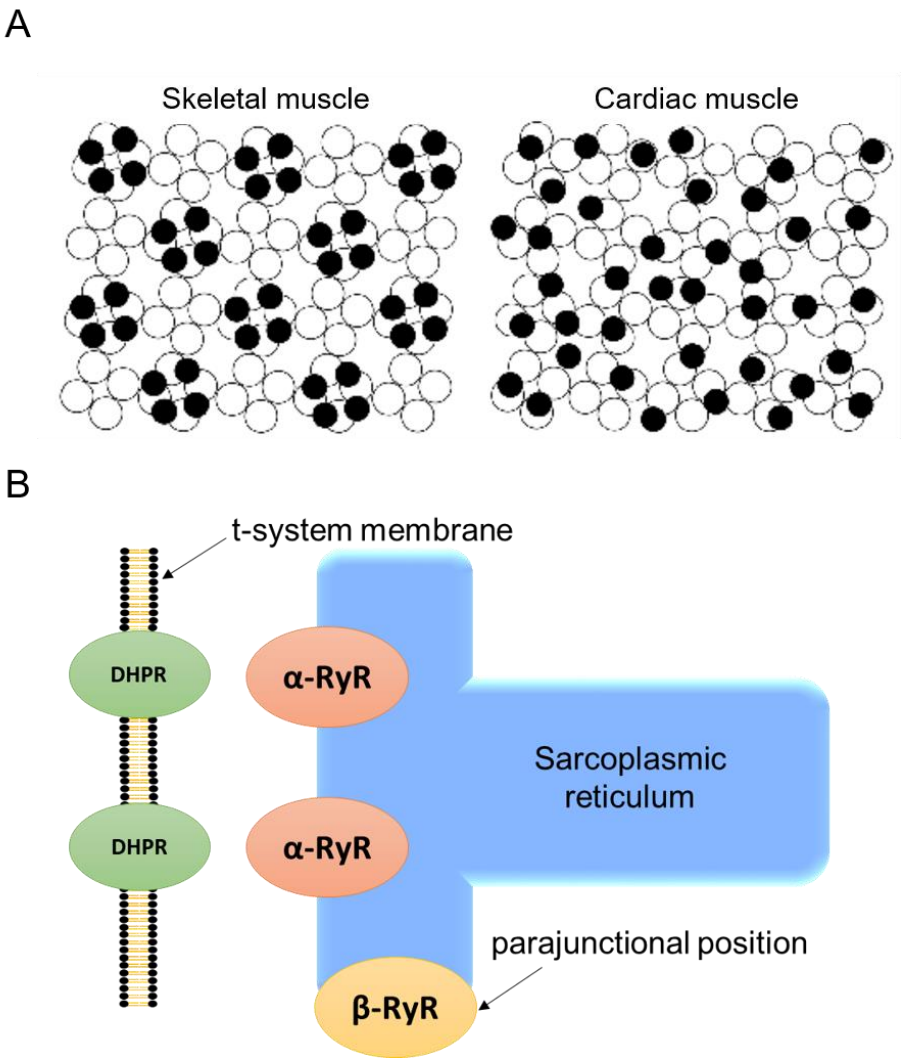

Figure 1.3 Organization of the RyR on the SR membrane.

(*A*) Schematic diagram of the relative position of RyR (open circles) and DHPR (closed circles) in skeletal and cardiac muscle (the image was modified from Franzini-Armstrong, (2004). (B) Diagram depicting the relative position of α and β RyRs on the SR membrane of amphibian skeletal muscle.

1.6 Mg^{2+} and Ca^{2+} regulation of the ryanodine receptor

The differing modes of activation observed between RyR1 and RyR2 are mainly attributed to the strong inhibitory effect of Mg^{2+} on the RyR1 (Lamb & Stephenson, 1991, 1994). In resting skeletal muscle, the 'free' $[Mg^{2+}]_{cyto}$ and $[Ca^{2+}]_{cyto}$ is estimated to be 1 mM and 0.0001 mM, respectively (Melzer *et al.*, 1995). Intracellular Mg^{2+} is thought to modulate RyR1 activity at two sites, the inhibitory site and activation site (Figure 1.4*A*) (Laver *et al.*, 1997a; Lamb, 2000; Laver *et al.*, 2004). At the inhibition site, Ca^{2+} and Mg^{2+} compete for binding at similar binding affinities ($K_{i,\ Ca/Mg}$= 0.1 mM) (Melzer *et al.*, 1995; Laver *et al.*, 1997a; Lamb, 2000; Laver *et al.*, 2004). The binding of either Ca^{2+} or Mg^{2+} to this site inhibits the RyR1 to approximately the same extent (Laver *et al.*, 1997a). However, it is important to note that the concentration of Mg^{2+} in the cytoplasm is considerably greater than that of Ca^{2+}; therefore, it is expected that the majority of the inhibition sites will be occupied by Mg^{2+} (Melzer *et al.*, 1995; Laver *et al.*, 1997a; Lamb, 2000). At the activation site of RyR1, Mg^{2+} also competes for binding with Ca^{2+} (Laver *et al.*, 1997a). The binding affinity for Ca^{2+} and Mg^{2+} is approximately 1 µM, and 20-100 µM, respectively (Laver *et al.*, 1997a; Laver *et al.*, 2004). The activation site is selectively activated by Ca^{2+}, and the binding of Mg^{2+} does not activate the channel (Laver *et al.*, 2004). Therefore, an increase $[Mg^{2+}]_{cyto}$ will also increase the $[Ca^{2+}]_{cyto}$ necessary to activate the channel, due to increased Mg^{2+} competition (Lamb, 2000). In addition to the two regulatory sites described here, there is also evidence to suggest that the activity of RyR1 is also modulated by a luminal Ca^{2+} regulatory site (Laver *et al.*, 2004; Jiang *et al.*, 2008). This mechanism suggests that raised luminal SR $[Ca^{2+}]$ reduces the affinity of Mg^{2+} at the activation site (Laver *et al.*, 2004).

The current understanding of RyR1 activation during ECC suggest that the release of SR Ca^{2+} is mediated by the physical interactions between the DHPR and the RyR1, which is thought to alleviate the Mg^{2+} inhibition of the channel (Lamb & Stephenson, 1994; Melzer *et al.*, 1995; Lamb, 2000). As mentioned, the organization of the triad region facilitates direct coupling between these two proteins (Melzer *et al.*, 1995). Depolarization of the t-system membrane is sensed by the α_1 (185kDa) subunit of DHPR, which then elicits a conformational change to occur between the cytoplasmic loop (II-III loop) located between the second and third repeat of the $\alpha_1$subunit (depicted in Figure 1.4*B*) (Tanabe *et al.*, 1990; Nakai *et al.*, 1998; Grabner *et al.*, 1999). The II-III loop of DHPR is thought to physically couple to the foot region of RyR1, which initiates the release of Ca^{2+} from the

SR (Nakai *et al.*, 1998; Grabner *et al.*, 1999). Chimeric studies have further revealed critical amino acids within the II-III loop (671-790) which are necessary for ECC (Tanabe *et al.*, 1990; Nakai *et al.*, 1998; Grabner *et al.*, 1999).

In cardiac cells, the binding affinity of Ca^{2+} at the activation site of RyR2 is similar to that of RyR1 (1 µM) (Rousseau & Meissner, 1989; Xu *et al.*, 1996). In contrast to skeletal muscle, cytosolic Mg^{2+} has a relatively modest inhibitory effect with a binding affinity of $K_{i,\ Ca/Mg}$ ~1 mM at the inhibitory site (Rousseau & Meissner, 1989; Xu *et al.*, 1996). Therefore, the modest rise in $[Ca^{2+}]$ in the junctional space which is facilitated by Ca^{2+} entry through the DHPR is sufficient to moderately activate the RyR2 (Bers, 2002). This release will then be reinforced by the additional release of Ca^{2+} on nearby RyR2 molecules.

As mentioned the physiological resting levels of $[Mg^{2+}]_{cyto}$ is approximately 1 mM (Melzer *et al.*, 1995). However, the $[Mg^{2+}]_{cyto}$ can alter drastically during muscle fatigue. The majority of Mg^{2+} found in the cytosol is bound to ATP. With declining [ATP] observed during skeletal muscle fatigue, it is expected that the free $[Mg^{2+}]_{cyto}$ will increase due to Mg^{2+} having a much lower binding affinity to adenosine diphosphate and adenosine monophosphate (Westerblad & Allen, 1992). The measured physiological range of free $[Mg^{2+}]_{cyto}$ was found to be approximately 1-3 mM (Westerblad & Allen, 1992). In regards to the inhibitory effect on the RyR1, raising $[Mg^{2+}]_{cyto}$ from 1 to 3 mM was found to reduce action potential induced Ca^{2+} release by 40% (Dutka & Lamb, 2004). Also, further increasing $[Mg^{2+}]_{cyto}$ to 10 mM abolishes ECC (Lamb & Stephenson, 1994). In contrast, the RyR1 can be nearly maximally activated by reducing the $[Mg^{2+}]_{cyto}$ to 50 µM (Lamb & Stephenson, 1991).

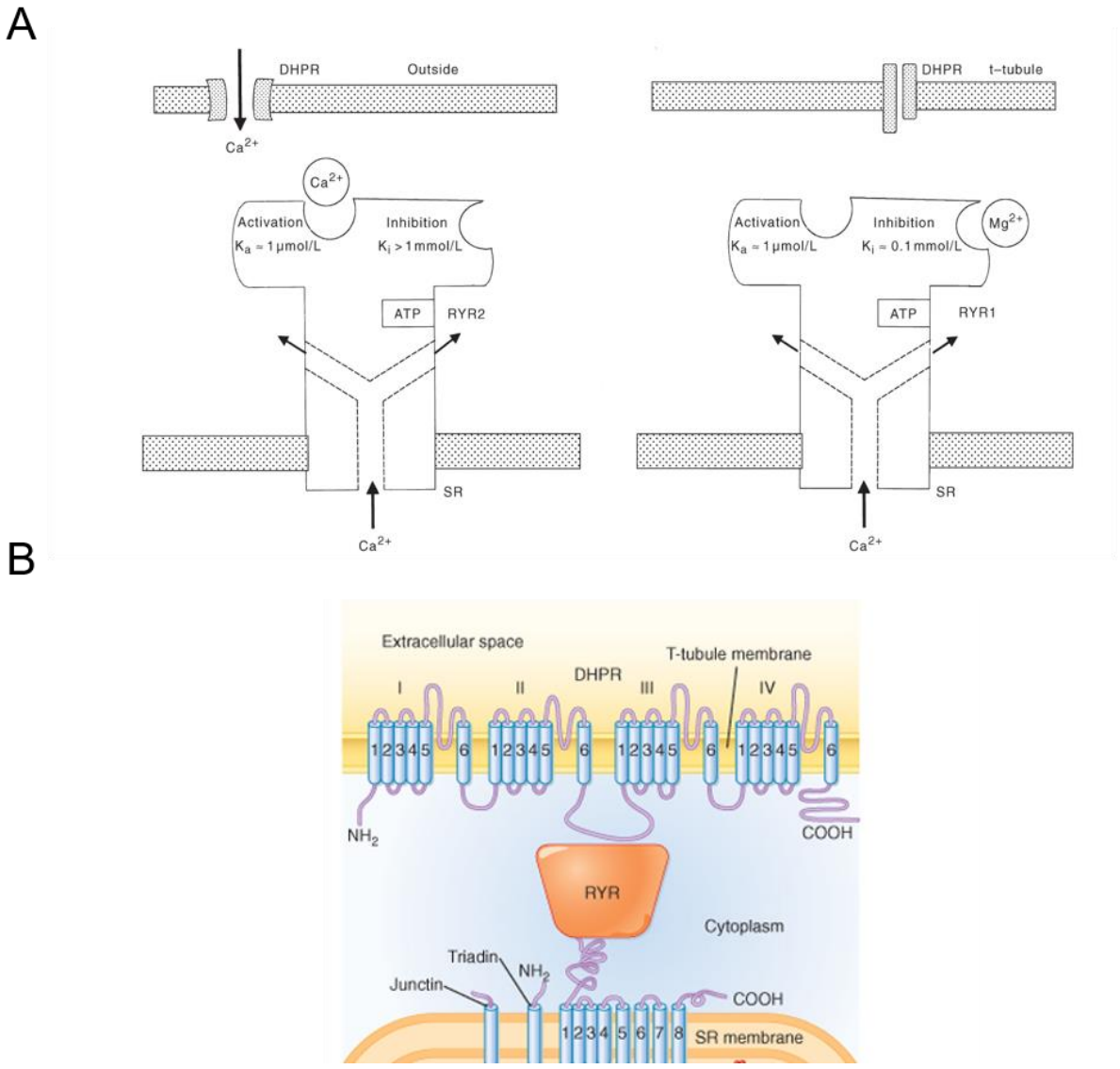

Figure 1.4 Schematic representation of DHPR and RYR.

(*A*) Schematic diagram describing the binding affinity for Ca^{2+} and Mg^{2+} at two regulatory sites on skeletal muscle isoform RyR1 (right) and cardiac isoform RyR2 (left) (the image was modified from (Lamb, 2000). (*B*) Schematic diagram of the DHPR (modified from (Hopkins, 2006). DHPR contains 5 subunits (α_1, α_2, β, γ, and δ) and is organized as a homotetramer on the t-system surface membrane (Murayama *et al.*, 1987; Franzini-Armstrong & Jorgensen, 1994; Melzer *et al.*, 1995).

1.7 Sarcoplasmic reticulum

The SR forms an extensive continuous network that surrounds every myofibril and is the main site for Ca^{2+} storage in the muscle fiber (Franzini-Armstrong & Peachey, 1981; Pinali *et al.*, 2013; Manno *et al.*, 2017). Structurally, the SR is organized into two functional regions which include the terminal cisternae and longitudinal SR (Franzini-Armstrong & Peachey, 1981). The portion of the SR that comes into close contact with the t-system at is known as the terminal cisternae of the SR and functions as the main site of Ca^{2+} release. The majority of Ca^{2+} in the SR is bound to calsequestrin (CSQ), a high capacity Ca^{2+} binding protein (Park *et al.*, 2004; Murphy *et al.*, 2009; Royer & Ríos, 2009; Manno *et al.*, 2017). In the resting skeletal muscle, CSQ polymerizes into a multimeric structure and can be found in high concentrations near the terminal cisternae which is facilitated by CSQ binding to the SR membrane bound proteins triadin and junctin (Györke *et al.*, 2004; Park *et al.*, 2004; Dulhunty *et al.*, 2009; Manno *et al.*, 2017).

A unique property of CSQ polymers (depicted in Figure 1.5) is that the number of binding sites for Ca^{2+} increases in response to increasing free calcium concentration in the SR (free $[Ca^{2+}]_{SR}$); in addition, the number of binding sites is dependent on the degree of CSQ aggregation (Ikemoto *et al.*, 1991; Park *et al.*, 2004; Launikonis *et al.*, 2006; Pape *et al.*, 2007; Royer & Ríos, 2009). Skeletal muscle expresses two isoforms of CSQ which includes CSQ1 and CSQ2 (Murphy *et al.*, 2009). CSQ1 is predominantly expressed in mammalian skeletal muscle fast twitch fibers whereas the SR in slow twitch fibers contains both the CSQ1 and CSQ2 molecules (Sacchetto *et al.*, 1993; Murphy *et al.*, 2009). The maximal binding of Ca^{2+} to CSQ1 and CSQ2 was found to approximately ~ 80 and 60 mol_{Ca}/mol_{CSQ}, respectively (Park *et al.*, 2004). The endogenous total Ca^{2+} content in the SR (total $[Ca^{2+}]_{SR}$) was estimated to be approximately 11 mM (relative to SR volume) in both slow and fast twitch fibers (Fryer & Stephenson, 1996; Murphy *et al.*, 2009). Interestingly, the endogenous SR Ca^{2+} load in both fast and slow twitch fibers were found to be sub-maximal (22% and 68% of maximal load in EDL and SOL fibers, respectively) (Fryer & Stephenson, 1996; Owen *et al.*, 1997a; Murphy *et al.*, 2009).

It is proposed that the stability of the CSQ polymer is dependent on the SR Ca^{2+} content (Manno *et al.*, 2013a; Manno *et al.*, 2017). That is, decreased occupancy of Ca^{2+} on CSQ causes the polymeric structure of CSQ to destabilize; thus, resulting in CSQ depolymerization and a subsequent reduction in its buffering capacity (Park *et al.*, 2004;

Manno *et al.*, 2013b; Manno *et al.*, 2017). The total $[Ca^{2+}]_{SR}$ decreases moderately during normal muscle function. However, it is important to note that the degree of depletion is not sufficient enough to significantly alter the polymerized state of CSQ (Owen *et al.*, 1997a; Canato *et al.*, 2010). CSQ has been found to partially depolymerize in mouse flexor digitorum brevis (FDB) muscle when challenged with a long-lasting field pulse depolarizations and when the fiber was treated with low concentrations of the RyR1 agonist, 4-chloro-M-cresol (4-CMC) (Manno *et al.*, 2017). Also, it has been demonstrated that CSQ fully depolymerizes when the SR was maximally depleted of Ca^{2+} (Fryer & Stephenson, 1996; Owen *et al.*, 1997a; Murphy *et al.*, 2009; Manno *et al.*, 2017). The endogenous SR Ca^{2+} load can be recovered by restoring the resting conditions in the cytosol, which indicates that the polymeric structure of CSQ can also be recovered from a depolymerized state (Lamb, 1993; Lamb *et al.*, 1995; Murphy *et al.*, 2009; Cully *et al.*, 2016).

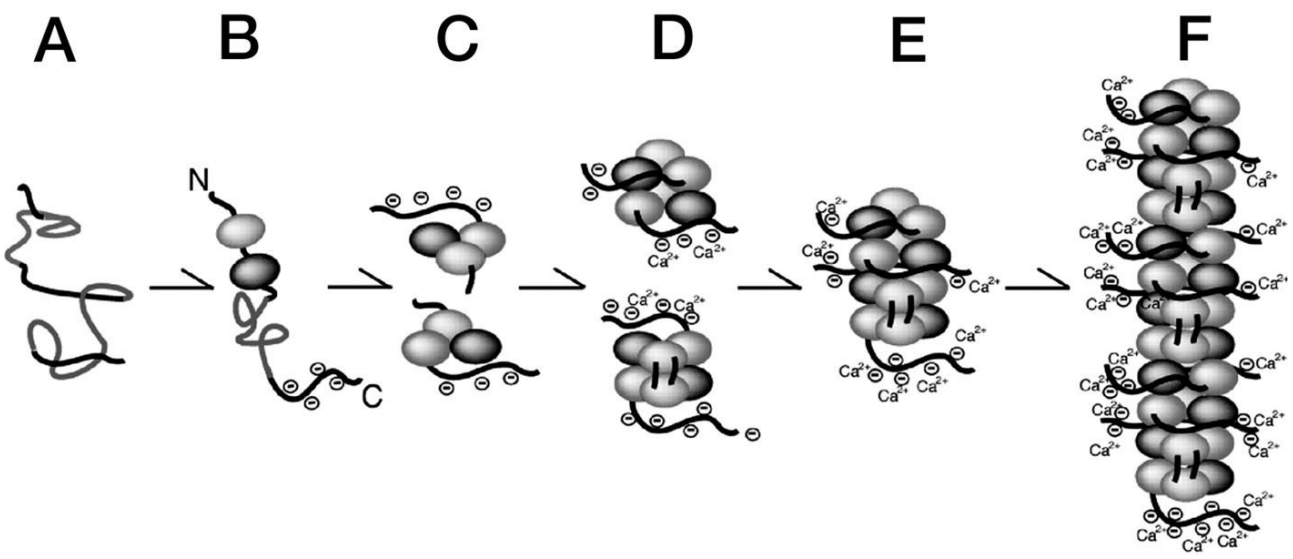

Figure 1.5 Proposed model for CSQ folding and polymerization.

(*A*) CSQ monomers are thought to be in an 'unfolded' state in the absence of Ca^{2+}. (*B, C*) As [Ca^{2+}] increases, CSQ begins to fold (represented as the circles seen the Figure), which reveals additional Ca^{2+} binding sites on CSQ. CSQ monomers begin to form dimers (*D, E*) and eventually forms into a linear polymeric structure (*F*; Figure was modified from (Park *et al.*, 2003).

In the relaxation phase of ECC, $[Ca^{2+}]_{cyto}$ begins to fall as Ca^{2+} is transported into the SR by the SERCA pump which is located on the longitudinal SR (Franzini-Armstrong & Peachey, 1981). The SERCA pump is a high affinity Ca^{2+} pump, driven by the hydrolysis of MgATP and transports 2 Ca^{2+} ions into the SR lumen (Yu *et al.*, 1993; Martonosi & Pikula, 2003). Skeletal muscle expresses two isoforms of SERCA. Fast twitch fibers express almost exclusively the SERCA1 isoform whereas slow twitch fibers express the SERCA2a isoform (Murphy *et al.*, 2009).

Skeletal muscle fast twitch fibers are highly specialized to contract and relax at a rapid rate. To facilitate the rapid release of large amounts of Ca^{2+}, the density of DHPR and RyR1 is increased nearly 2-5 fold in fast twitch fibers (relative to slow twitch fibers) (Baylor & Hollingworth, 2003). This results in a 2-3 fold increase in released Ca^{2+} during a single twitch stimulation (350 µM and 120 µM per fibre volume in fast twitch and slow twitch fibres, respectively) (Baylor & Hollingworth, 2003). To facilitate rapid relaxation, the fast twitch fibre has a relatively large SR volume and increased Ca^{2+} buffering (due to an increase in the amount of CSQ1; which results in a partially filled SR with the free $[Ca^{2+}]_{SR}$ maintained at approximately 0.3-0.6 mM) (Fryer & Stephenson, 1996; Murphy *et al.*, 2009; Eisenberg, 2010). This has important implications in maintaining an environment in which the rapid uptake of Ca^{2+} through SERCA is optimal (Fryer & Stephenson, 1996; Baylor & Hollingworth, 2003). Furthermore, the rate of Ca^{2+} uptake is much more rapid in type II fibres, due to an increased density of the high capacity SERCA1 isoform (Wu, 1993; Murphy *et al.*, 2009).

1.8 Ca^{2+} handling within the junctional space of skeletal muscle

In skeletal muscle, Ca^{2+} handling in the junctional space is thought to be important for normal muscle function (Despa *et al.*, 2014). In resting skeletal muscle, Ca^{2+} leaks from the RyR1 to the cytoplasm, where it is re-sequestered by the SERCA pump, back into the SR (Dumonteil *et al.*, 1993; Marie & Silva, 1998). This basal activity of the RyR1 (also commonly referred to as basal Ca^{2+} leak) in the resting skeletal muscle sets a higher $[Ca^{2+}]$ within the junctional space, relative to the bulk cytoplasm (Despa *et al.*, 2014). The net leak of Ca^{2+} from the RyR1 contributes minimally to the overall $[Ca^{2+}]_{cyto}$ but increases metabolic rate and ATP turnover as 'leaked' Ca^{2+} is actively transported back into the SR by the SERCA pump (Dumonteil *et al.*, 1993; Marie & Silva, 1998). Importantly, the hydrolysis of MgATP by the SERCA pump generates heat; and therefore, Ca^{2+} leak is considered to contribute to thermoregulation in mammals (Barclay, 1996; Bakker *et al.*, 2017). A 'leaky' RyR has important implication in regards to Ca^{2+} homeostasis, as any dysregulation in this cycle can result in an increased resting $[Ca^{2+}]_{cyto}$, which can potentially lead to skeletal muscle degradation (Bellinger *et al.*, 2009; Andersson & Marks, 2010).

The junctional t-system and SR membrane house multiple proteins important for Ca^{2+} extrusion and Ca^{2+} entry (depicted in Figure 1.6). In skeletal muscle, little is known about the physiological significance of multiple Ca^{2+} handling proteins within the junctional space. Ca^{2+} regulatory molecules within the junctional space on the t-system membrane includes the plasma membrane Ca^{2+} ATPase pump (PMCA), and Na^{+}/Ca^{2+} exchanger (NCX) which both works to extrude Ca^{2+} (Rosemblatt *et al.*, 1981; Hidalgo *et al.*, 1983; Hidalgo *et al.*, 1986; Donoso & Hidalgo, 1989; Kurebayashi & Ogawa, 2001). Proteins involved in Ca^{2+} entry includes the luminal SR Ca^{2+} sensor stromal interaction molecule 1 (STIM1) located on the SR membrane and the selective Ca^{2+} channel Orai1 located on the junctional t-system membrane.

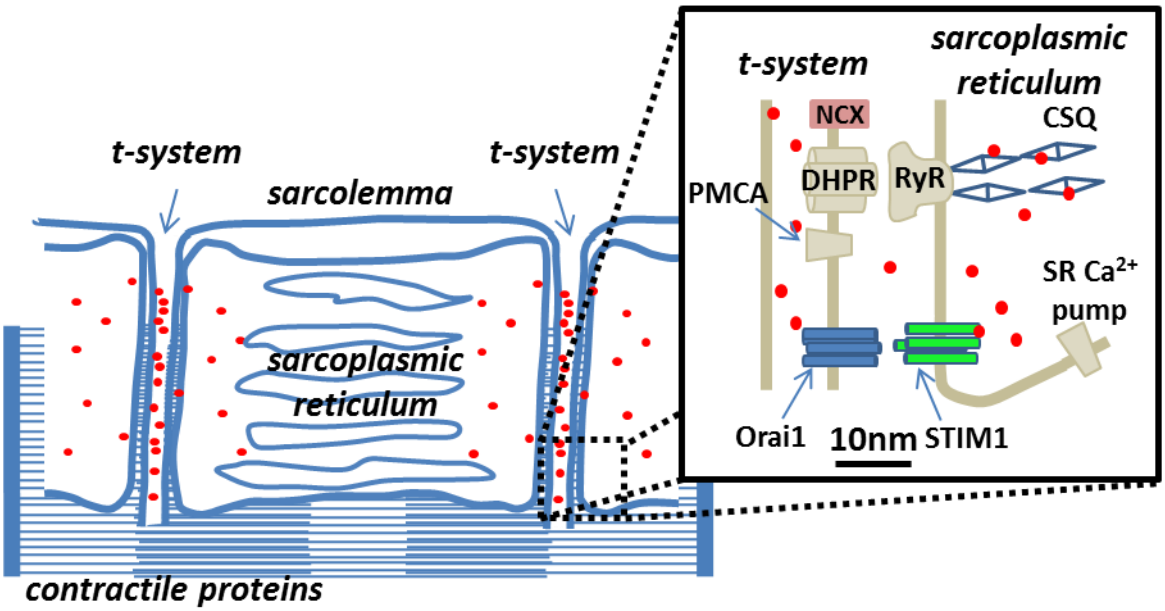

Figure 1.6 Ca^{2+} regulatory proteins of the triad region of skeletal muscle.

This schematic diagram depicts the major Ca^{2+} regulatory molecules of skeletal muscle. The major Ca^{2+} extruders located on the t-system membrane include plasma membrane Ca^{2+} ATPase pump (PMCA), and Na^{+}/Ca^{2+} exchanger (NCX). The Ca^{2+} channel Orai1 and luminal SR Ca^{2+} sensor STIM1 are located on the t-tubule and SR membrane, respectively (Edwards *et al.*, 2010). STIM1 and Orai1 play a key role in a Ca^{2+} entry mechanism known as store operated Ca^{2+} entry.

1.8.1. Plasma membrane Ca^{2+}-ATPase

PMCA is a ubiquitous Ca^{2+} pump located on the t-system and sarcolemma membrane involved in Ca^{2+} extrusion (Niggli et al., 1982; Hidalgo et al., 1983). PMCA is a MgATP driven pump which transports one Ca^{2+} ion to the extracellular space in exchange for an H^+ ion (Niggli et al., 1982; Hidalgo et al., 1983). PMCA is described as a high affinity, low capacity Ca^{2+} pump with the reported Michaelis constant of 0.3-1 µM (Niggli et al., 1982; Hidalgo et al., 1986; Enyedi et al., 1989). In mammals, there are four isoforms of PMCA (Keeton et al., 1993). The expression of PMCA1 and PMCA4 are ubiquitous and are thought to function as housekeeping Ca^{2+} pump (Keeton et al., 1993; Stauffer et al., 1995). The expression of PMCA2 is tissue specific and are predominantly expressed in neuronal tissues (Keeton et al., 1993; Stauffer et al., 1995). The structure of PMCA consists of 10 transmembrane domains, two cytosolic loops and a cytosolic carboxyl terminal tail (Verma et al., 1988; Strehler & Zacharias, 2001). The carboxyl terminal contains a calmodulin (CaM) binding domain, which in the absence of CaM, interacts and auto inhibits the catalytic site of PMCA (Enyedi et al., 1989; Verma et al., 1994). Binding of Ca^{2+}- CaM to the CaM binding domain reveals the catalytic site, thus activating the pump (Verma et al., 1994). In skeletal muscle, PMCA is embedded throughout the sarcolemma and t-system membrane (Hidalgo et al., 1983; Hidalgo et al., 1986). The main isoforms of PMCA found in skeletal muscles include PMCA1 and PMCA3f (Keeton et al., 1993; Filoteo et al., 2000). The PMCA3f isoform lacks the majority of the CaM binding domain and can be activated without the presence of Ca^{2+}- CaM (Keeton et al., 1993; Filoteo et al., 2000).

1.8.2. Sodium calcium exchanger

NCX is a ubiquitous transmembrane antiporter that utilizes an electrochemical gradient to move one Ca^{2+} ion in exchange for three Na^+ ions (Donoso & Hidalgo, 1989). The directionality in which these ions move (either forward or reverse mode) is thought to be dependent on the membrane potential and the ionic concentration of Ca^{2+} and Na^+ (Donoso & Hidalgo, 1989). In contrast to PMCA, NCX is considered to be a low affinity high capacity Ca^{2+} transporter with a Michaelis constant of 3 µM (Hidalgo et al., 1986; Donoso & Hidalgo, 1989; Hidalgo et al., 1991). In striated muscle, NCX is found to be expressed throughout the sarcolemma and t-system membrane (Donoso & Hidalgo, 1989; Fraysse et al., 2001). The role of NCX as a Ca^{2+} extruder is well characterized and widely

accepted to be involved in cardiac ECC (Bers, 2002). However, little is known about the role NCX plays in ECC in skeletal muscle.

1.8.3 Store operated Ca^{2+} entry

Store operated Ca^{2+} entry (SOCE) is an extracellular Ca^{2+} entry pathway which was first described in non-excitable cells (Putney, 1977; Parod & Putney, 1978; Parekh & Putney, 2005). SOCE is triggered upon the depletion of Ca^{2+} from the ER, and the primary function of Ca^{2+} entry is to refill the Ca^{2+} stores (Parekh & Putney, 2005). Therefore, the process of SOCE is terminated upon refilling the internal Ca^{2+} stores (Parekh & Putney, 2005; Hogan & Rao, 2015). The depletion of ER Ca^{2+} is detected by the Stromal interaction molecule 1 (STIM1) (Roos *et al.*, 2005; Zhang *et al.*, 2005; Luik *et al.*, 2006; Luik *et al.*, 2008). STIM1 is a transmembrane protein located on the ER membrane with the Ca^{2+} sensing domain (EF hand motif) located in the ER lumen (Zhang *et al.*, 2005). At rest, Ca^{2+} is bound to the EF hand domain, and the depletion of ER-Ca^{2+} causes Ca^{2+} to disassociate from this domain, which then activates STIM1 (Zhang *et al.*, 2005). Upon store depletion it was found that multiple STIM1 proteins form oligomers close to the ER-plasma membrane junction where the STIM1 molecule can interact with the calcium channel Orai1 (also known as the Ca^{2+}-release activated channel, CRAC) on the plasma membrane to allow for Ca^{2+} to occur (Roos *et al.*, 2005; Luik *et al.*, 2008; Zhou *et al.*, 2009). The activation of SOCE in most cell types was observed to occur within 10-30 seconds of ER-Ca^{2+} depletion (Putney, 1977; Parod & Putney, 1978; Parekh & Putney, 2005)

SOCE in skeletal muscle was first described by Kurebayashi and Ogawa (2001). In this study, they demonstrated that the depletion of SR Ca^{2+} with a membrane depolarizing potassium solution in the presence of cyclopiazonic acid (a SERCA pump inhibitor) could invoke a Ca^{2+} entry response similar to that described in non-excitable cells (Kurebayashi and Ogawa, 2001; Putney, 1977). It was later found that the SR membrane of skeletal muscle contain multiple isoforms of STIM1, which includes STIM1L which is thought to form a 'pre-formed' complex with Orai1 to rapidly activate SOCE (Edwards *et al.*, 2010; Launikonis *et al.*, 2010; Darbellay *et al.*, 2011; Edwards *et al.*, 2011). This is supported by the relatively fast activation of SOCE in skeletal muscle, which was observed to occur within milliseconds of SR Ca^{2+} depletion (Launikonis *et al.*, 2003; Launikonis & Ríos, 2007; Edwards *et al.*, 2010; Edwards *et al.*, 2011; Cully *et al.*, 2016).

1.9 Thesis overview

This thesis focus on the mechanisms of Ca^{2+} handling during an MH event. Chapter 3 aims to determine the mechanism of dantrolene inhibition of the RyR1. Chapter 4 will investigate the mechanism of Ca^{2+} release by the MH triggering agent (halothane). In Chapter 5 a novel methodology for determining the activity of the RyR1 will be presented.

Chapter 2: General Materials and Methods

2.1. Experimental Animals

Male Wistar rats (*Rattus norvegicus*) were obtained from The University of Queensland Biological Resources, (Brisbane, Qld Australia) and were housed at The Animal House in The School of Molecular and Microbial Sciences (The University of Queensland). Wistar rats were housed together in a temperature controlled (21-23 ºC) well ventilated environment with a 12:12 h light: dark cycle and fed standard chow and water *ad libitum.* Male Wistar rats, between 2-6 months of age, were culled by CO_2 asphyxiation followed by cervical dislocation. The hind limb extensor digitorum longus (EDL) muscle were quickly dissected from both hind limbs, and each muscle was then blotted on filter paper (Whatman 1) to remove any extracellular fluid or blood.

Cane toads (*Bufo marinus*) were obtained from Peter Krauss (Mareebra, Qld, Australia) or collected locally. Toads were housed in a large cage with a moist environment with a sawdust base. Cane toads were euthanized following cooling in a 4 ºC environment for 1 h by double pithing. The iliofibularis muscle was removed and blotted as previously described. All procedures were approved by the Animal Ethics Committee at The University of Queensland (Appendix).

2.2. Human Biopsy sample preparation

The use of human muscle biopsy was approved by the Human Ethics Committee at The University of Queensland (Appendix). Subjects signed informed consent forms before their involvement in this study (Chapter 3-4). Muscle biopsies were collected under local anaesthesia (Xylocaine, 10 $mg \cdot mL^{-1}$) from the mid-portion of the vastus lateralis muscle, using a 6 mm Bergstrom biopsy needle modified for manual suction. The length of the incision (<1 cm) required for this procedure is shown in Figure 2.1.

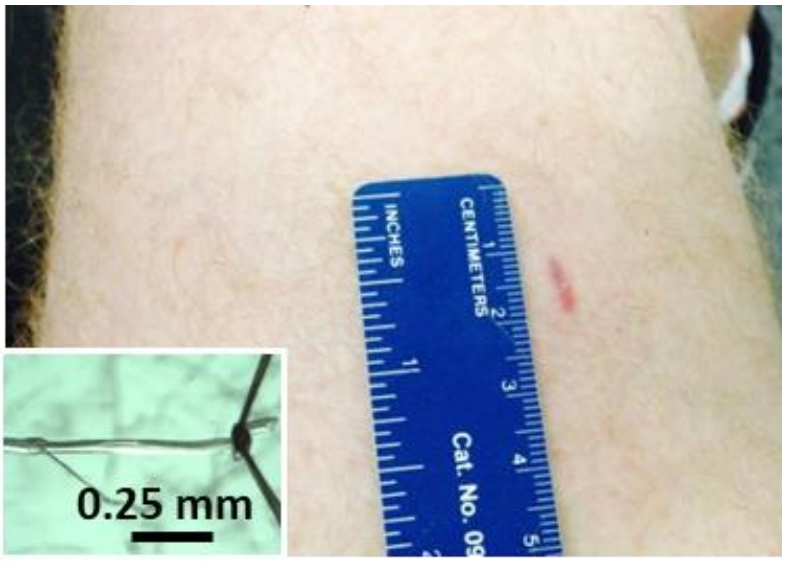

Figure 2.1 Obtaining muscle biopsies for testing the physiological function of muscle.

Wound in the leg of a 42 year old male ~4 weeks post-biopsy. The biopsy was taken under a local anaesthetic using a Bergstrom needle. The inlet shows a muscle bundle obtained from the biopsy.

2.3. Muscle preparation

Excised muscle from rat, toad, and human to be used for the mechanically skinned fiber preparation was pinned down at resting length on to the surface of a petri dish lined with SYLGARD under a layer of paraffin oil and kept at 21-23°C.

2.4. Mechanically skinned fiber preparation

The main preparation used in this thesis was the mechanically skinned fiber (Natori, 1954). The process of mechanically skinning a skeletal muscle fiber and the relevant terminology used in this section is depicted in Figure 2.2.

Using fine tip scissors and jewellers forceps (Inox No. 5, Dumont Switzerland), individual muscle bundles were cut transversely near one end of the tendon. The muscle bundle was then separated longitudinally down the length of the muscle, with one end of the bundle still attached. Great care was taken not to damage the middle portion of the muscle bundle. To mechanically skin a skeletal muscle fiber, fine jewellers forceps are used to split apart myofibrils (>70% of the fiber) of a single muscle fiber. It is possible to leave most of the myofibrils in one section of the skinned fiber, as shown by the maintenance of the vast majority of the sub-sarcolemmal t-system network in the skinned fiber (Edwards & Launikonis, 2008; Jayasinghe *et al.*, 2013; Cully *et al.*, 2017). Splitting the myofibrils causes the sarcolemma to roll back on itself forming a “cuff,” which can be used as a visual confirmation of a successfully skinned fiber.

The mechanically skinned fiber was then tied with an over-hand knot on two points of the fiber with a 0.02 mm surgical silk suture as depicted in Figure 2.2. The surgical suture was used to handle the muscle fiber without damage. Furthermore, the knot provides points at which the experimental preparation can be stabilized on the experimental apparatus (Chapter 2, Figures 2.4-2.5). Note that preparation remained submerged in paraffin oil for the entire procedure.

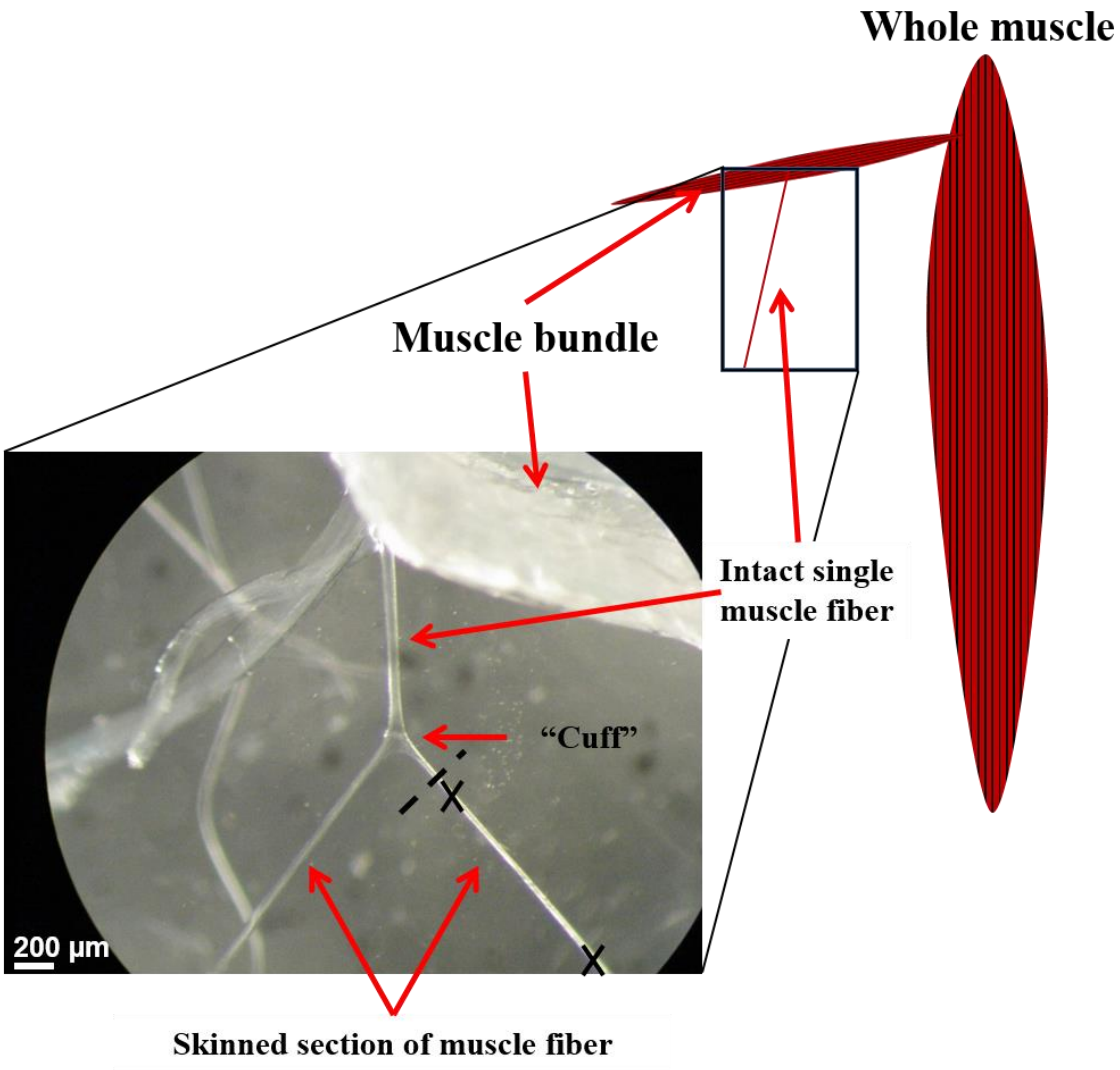

Figure 2.2 Schematic diagram of dissected muscle with micrograph inset of mechanically skinned fiber.

The whole muscle as depicted is separated into smaller individual muscle bundles and further separated into single muscle fibers. Under a stereoscopic microscope, the intact single muscle fiber can be mechanically skinned. This causes the sarcolemma to roll back on itself forming a "cuff." Note the three sections of the dissected fiber (intact, skinned and cuff) are indicated on the micrograph. The black 'x' shown on the micrograph indicates the location where a 0.02 mm silk surgical suture was tied to the fiber using an over-hand knot. The dashed line indicates the location at which the skinned muscle fiber was cut from the muscle bundle.

2.5. Skinned fiber solutions

The mechanically skinned fiber allows for experimental access to the internal environment. The 'internal solutions' used in this thesis was developed to closely mimic the normal myoplasmic environment. To maintain a normal resting membrane potential K^+ and Na^+ were added close to physiological range.

The solutions were prepared in accordance with the procedure described in Stephenson and Williams (1981). Calcium was heavily buffered by N', N' tetra acetic acid (EGTA). The free [Ca^{2+}] and [Mg^{2+}] was calculated assuming an apparent EGTA binding affinity of Kd, $_{Ca}$ 204 nM and Kd, $_{Mg}$ 9 mM, respectively. Magnesium and calcium were added in the form of MgO and $CaCO_3$, respectively. The carbonyl was removed from the solution by heating the solution to 60°C for 30 minutes in the presence of HEPES and EGTA. After the solution cooled to room temperature (~21°C) creatine phosphate and ATP was added in the form of a di-sodium salt. Solutions contained (mM): K^+, 136; Na^+, 36; ATP, 8; and creatine phosphate, 10. The amount of Mg^{2+}, Ca^{2+}, EGTA, HEPES, and 1,6-diaminohexane-N,N,N',N'-tetraacetic acid (HDTA) were adjusted depending on differing experimental parameters. In weakly buffered Ca^{2+} solutions HDTA was added to keep the ionic strength consistent. The pH was adjusted to 7.1 with KOH in all internal solutions (measured with Hanna Instruments pH meter). All chemicals were obtained from Sigma-Aldrich unless stated otherwise.

The osmolality of the internal solution matched that occurring in the myoplasm in mammalian and toad muscle. Osmolality was measured using a freezing point osmometer (Advanced Instruments micro-osmometer), and the final osmolality of the solutions was 290 ± 10 and 250 ± 10 mOsmol kg^{-1} for mammalian and toad, respectively. The solution composition used in each Chapter is presented as a Table in the respective method sections.

Some experiments required the use of the general aesthetic halothane (Chapter 3-5). Since the physiological solution containing halothane is exposed to air, the evaporation rate of halothane needed to be considered. Figure 2.3 shows the normalized evaporation rate by mass of halothane over time. The evaporation rate of the physiological solution and the physiological solution supplemented with 10% halothane by mass was compared. It was found that the evaporation rate of halothane was constant. These experiments were repeated in three trials and an evaporation rate of 9.6% · min^{-1} was derived.

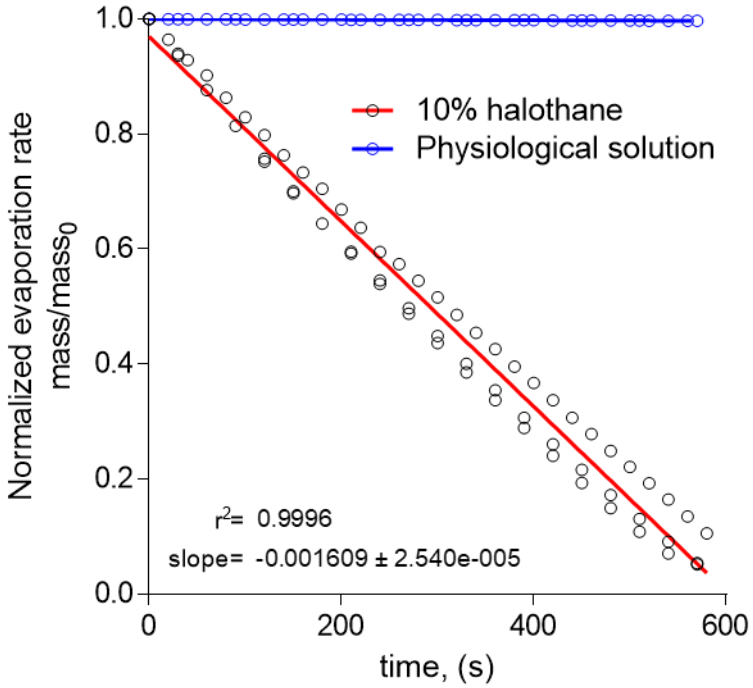

Figure 2.3 Evaporation rate of halothane

The change in mass/mass$_0$ of halothane over time in room temperature (~21˚C) is shown as the open black circles (n=3). 10% halothane by mass was mixed with an physiological solution ((mM): K^+, 3; Na^+, 140; Cl^-, 140; Ca^{2+}, 2; Mg^{2+}, 1; Hepes, 10; and glucose, 5; pH, 7.4 at ~21˚C). The evaporation rate of the physiological solution alone is shown as the open blue circles. As shown, the evaporation rate of the physiological solution over the time course of the experiment is negligible. The data was fitted with a liner regression, and an evaporation rate of halothane of 9.6%·min^{-1} was derived.

2.6. Design of experimental chambers used for confocal imaging of individual mechanically skinned fibers

The experimental chamber used to image an individual muscle fiber is shown in Figure 2.4. The chamber consisted of a coverslip (76mm x 26mm x 1.2mm) (*A*), epoxy resin (*E*), and two entomological pins (*C*). The epoxy resin was used to stabilize the entomological pins to the coverslip. Furthermore, the resin also provides a solution well with a capacity of ~100 µL (*B*).

The preparation as described in Chapter 2.4 was initially removed from the paraffin oil and blotted on filter paper to remove the excess oil. The fiber was then placed in the chamber (in solution) and oriented so that the long axis of the fiber was perpendicular to the entomological pins. The two knots were then placed underneath each entomological pin. The fiber was then stretched with slight tension (~5% stretched from of slack length). Importantly, the experimental chamber allows for rapid manual solution exchange during image acquisition. To perform manual solution exchange, the bathing solution was aspirated by a vacuum pump, and the following solution of interest was added with a manual pipetter. The residual volume remaining in the solution well was ~5-10 µL. To minimize carry over from one solution to another, manual solution exchange was commonly performed twice.

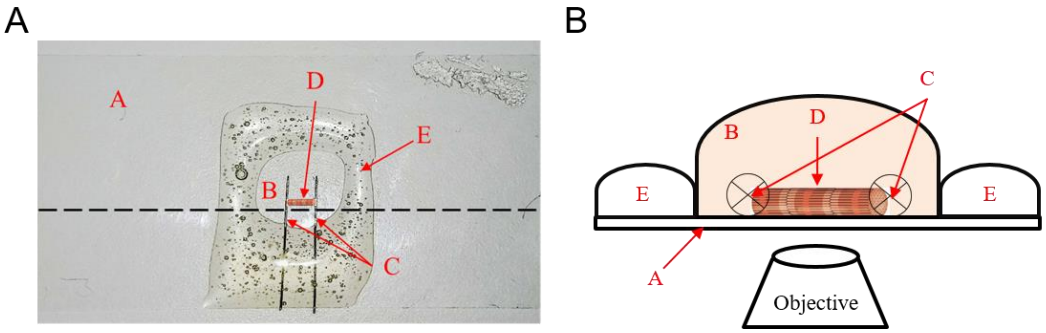

Figure 2.4 Experimental chamber used to image mechanically skinned muscle fibers.

(A) The main components of the experimental chamber include a 76mm x 26mm x 1.2mm glass coverslip (*A*), epoxy resin (*E*) which forms the solution well (*B*) and two entomological pins (*C*). The mechanically skinned fiber (*D*) is placed underneath each pin, as shown. The cross section perspective (dashed line) is shown in (B).

2.7. Design of experimental chambers used to image electrically evoke a Ca^{2+} transients

The apparatus used to evoke electrically-stimulated Ca^{2+} transients is shown in Figure 2.5. Skinned fibers were mounted underneath the entomological pins as previously shown in Figure 2.4. Importantly, the skinned fibers were positioned so that the long axis of the fiber was perpendicular to the electric field. The preparation was stimulated with a 5-ms square field pulse at 100 volts using a Grass S44 Stimulator (Grass Instruments Co., Quincy, Massachusetts, USA).

A limitation of the apparatus shown in Figure 2.5 (*Top*) is the inability to perform manual solution exchange during image acquisition. This is due to the narrow access to the solution well. To improve on this design, the platinum electrodes and the apparatus used to mount the fiber was separated into individual components as shown in Figure 2.5 (*Bottom*). Another advantage of this approach is that the platinum electrodes can now be placed closer to the preparation which increases the electric field strength.

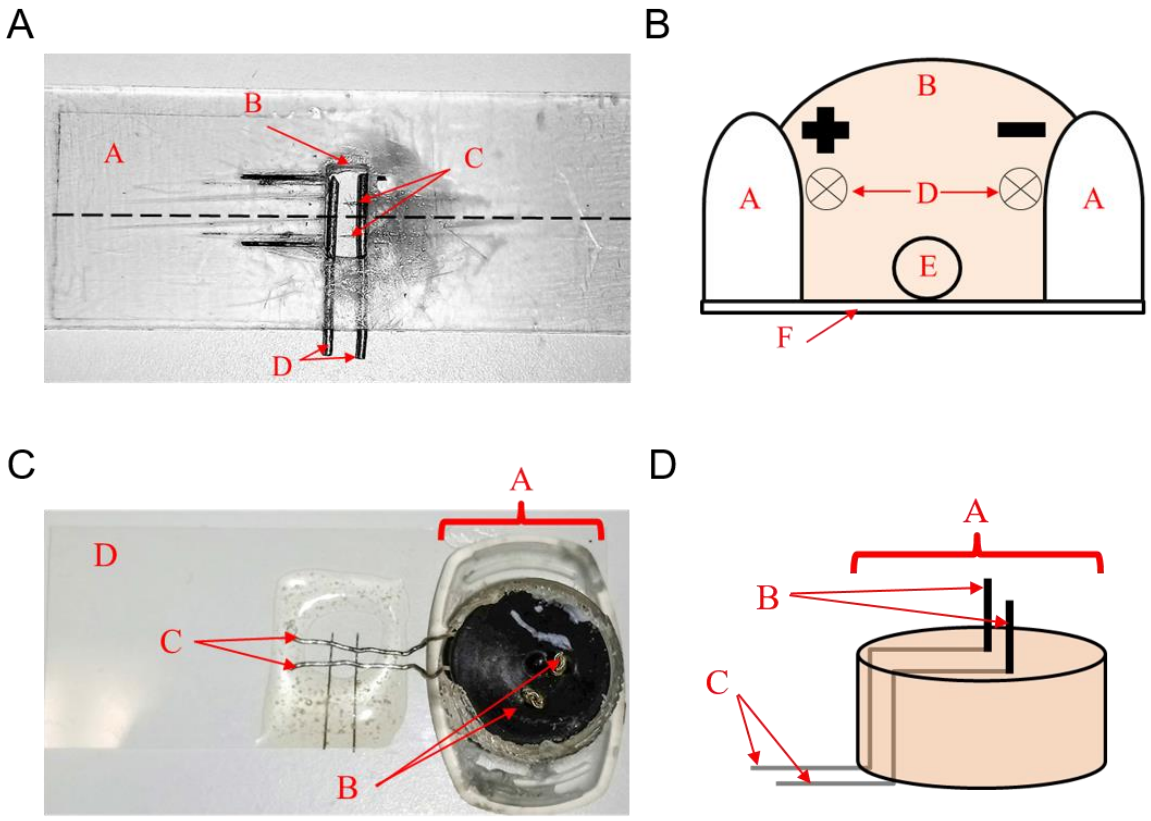

Figure 2.5 Experimental chambers used to electrically evoke a Ca^{2+} transient.

Top: (A, B) The main features of this experimental chamber includes a plastic housing (*A*) for the platinum electrode (diameter ~ 1 mm) (*D*) and a central well with a total volume of ~0.2 cm^3 (*B*). A glass coverslip (*F*) and entomological pins (*C*) was attached with epoxy resin to the bottom of the plastic housing to seal the central well and hold the sample preparation (*E*). **Bottom: (C, D)** This experimental setup uses the chamber described in Figure 2.4 (*D*) and a custom designed housing (*A*) for the platinum wires (diameter ~ 0.1 mm) (*C*). (*B*) The site where the thin platinum wires can be connected to the stimulator (Grass S44 Stimulator; Grass Instruments Co., Quincy, Massachusetts, USA).

2.8. Confocal imaging

Confocal imaging is a common tool used in the life sciences to visualize fluorescent dyes within a cell. Unlike the conventional wide field microscopy (which produces an image from both in-focus and out of focus light), a pinhole aperture is used in confocal microscopy to reject out of focus light. This produces an image from the emissions collected from a single optical plane. In Figure 2.6 the arrangement of light paths through filters and mirrors that allows the collection of a single plane of light from a pool of fluorescent signal is displayed. The light from the laser is first focused through a pinhole before contact with the dichroic mirror. The dichroic mirror functions to reflect the excitation wavelength while being transparent to the emission wavelength. The excitation light is then passed through a series of mirrors and lenses and out the objective lens. The emitted light follows the same path back and through the dichroic mirror. Light from which originated from the focal plane passes through the second set of pinholes and on to the light detector.

The mechanically skinned fiber was mounted onto the experimental apparatus (Figure 2.4 - 2.5), before placing it above a 40 x (Numerical aperture 0.9) water immersion objective of the laser scanning confocal system (Olympus FV1000). Rhod-2 (Chapters 3-5) and rhod-5N (Chapter 5) was excited at 543 nm (Helium Neon laser) with the emitted light collected in the 562-666 nm range. Fluo-5N (Chapters 4-5) was excited at 488 nm (Argon ion laser), and the emitted light was collected in the 500-540 nm range. The emitted light was collected using a high sensitive gallium arsenide phosphide (GaAsP) detectors. The high sensitivity of the GaAsP detector made it possible to conduct experiments with relatively low laser power (>1.5±1%). This mitigates photo-bleaching during long imaging sessions. Imaging was conducted at ~21±1°C.

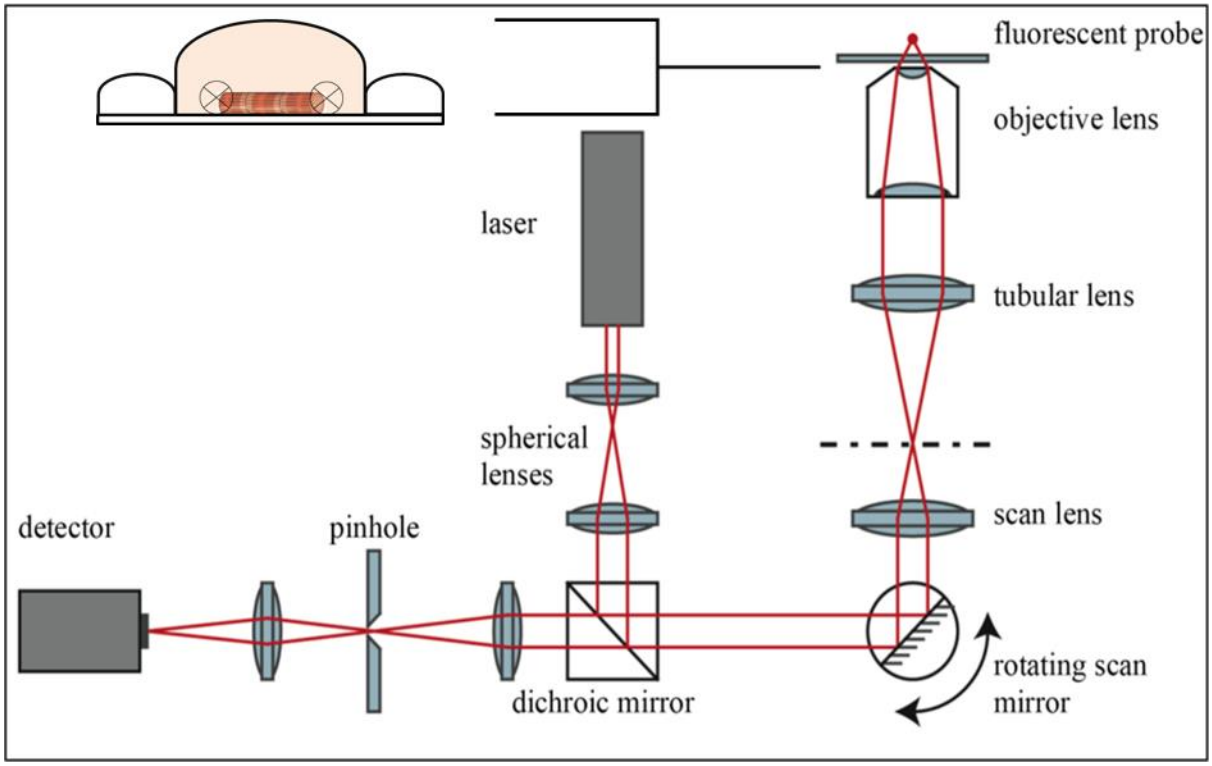

Figure 2.6 Schematic diagram of the principles of confocal imaging and the experimental apparatus.

(Top left) Image depicting the custom glass slide (76mm x 26mm x 1.2mm) used as the experimental chamber (Figure 2.4).

2.9. T-system dye loading

Confocal imaging of a Ca^{2+} indicator (fluo-5N and rhod-5N) trapped in the t-system of a mechanically skinned fiber was first reported by Lamb et al. (1995). Mechanically skinning a skeletal muscle fibre causes the t-system to seal at the point where it was previously joined to the sarcolemma. The t-system becomes a sealed compartment, which provides a number of advantages (Launikonis & Stephenson, 2002a). The removal of the sarcolemma allows for direct access to the cytoplasmic environment while maintaining the structural integrity of the t-system, and SR membrane in its native triad organization (Jayasinghe & Launikonis, 2013).

Under paraffin oil an isolated muscle bundle was exposed to a Ringer solution containing rhod-5N ((mM): NaCl, 140; KCl, 4; $CaCl_2$, 2; $MgCl_2$, 1; rhod-5N salt, 2; and Hepes, 10 (pH adjusted to 7.4 with NaOH)) and allowed to equilibrate for 10 minutes. A 1 µL microcap (Drummond) was used to apply the dye to the muscle bundle. The allotted incubation time has been previously shown to be sufficient to allow the dye to diffuse into the t-system compartment (Lamb *et al.*, 1995; Launikonis & Stephenson, 2002b; Cully *et al.*, 2016). A single fiber was then isolated and mechanically skinned, as previously described (Chapter 2.4). Successful dye loading can be confirmed by confocal microscopy, as shown in Figure 2.7. Note that all Ca^{2+} indicators used in this thesis were obtained from Thermo Fisher Scientific.

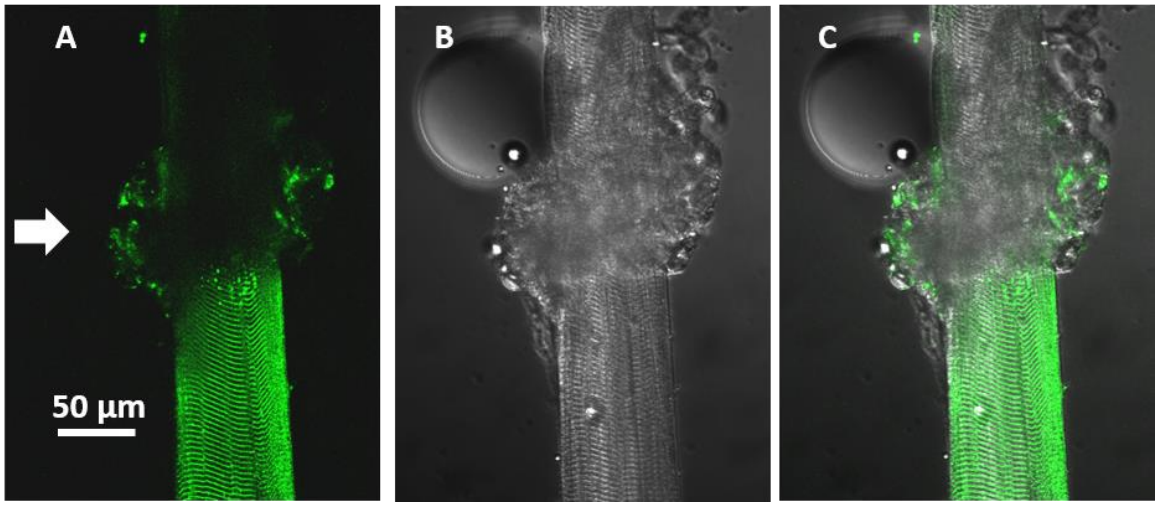

Figure 2.7 Mechanically-skinned fiber preparation with dye trapped in the t-system.

Confocal image of a partially skinned fiber. The cuff (white arrow) splits the intact portion of the fiber (above cuff) from the skinned portion (below cuff). (*A*) Fluo-5N fluorescence (*B*) and transmitted light in the t-system. (*C*) Overlay of both images. It is important to mention that the fluorescent dye is lost to the bathing solution in the intact portion of the fiber, due to the absence of a sealed compartment (Figure was modified from Edwards *et al*., (2008)).

2.10. SR dye loading

The method used to load the sarcoplasmic reticulum (SR) of single muscle fibers was modified from that originally described in intact fibers similar to that of Kabbara & Allen (2001). Single mechanically skinned fibres were mounted in an experimental chamber and bathed in 100 nM $[Ca^{2+}]_{cyto}$ internal solution with 10 µM fluo-5N AM, 10 µM carbonilcyanide p-triflouromethoxyphenylhydrazone (FCCP) and 0.05% Pluronic detergent. FCCP is a protonophore which has previously been shown to inhibit Ca^{2+} transport into the mitochondria (Boitier *et al.*, 1999). This step was found to be essential as Ca^{2+} released from the SR showed a persistent increase in fluorescence that did not originate from the SR (Figure 2.8). After 1-hour incubation at 30°C, the dye solution was removed and replaced with a 100 nM $[Ca^{2+}]_{cyto}$ internal solution. An additional 1 hour incubation at room temperature was conducted to allow for complete hydrolysis of the acetyl moiety.

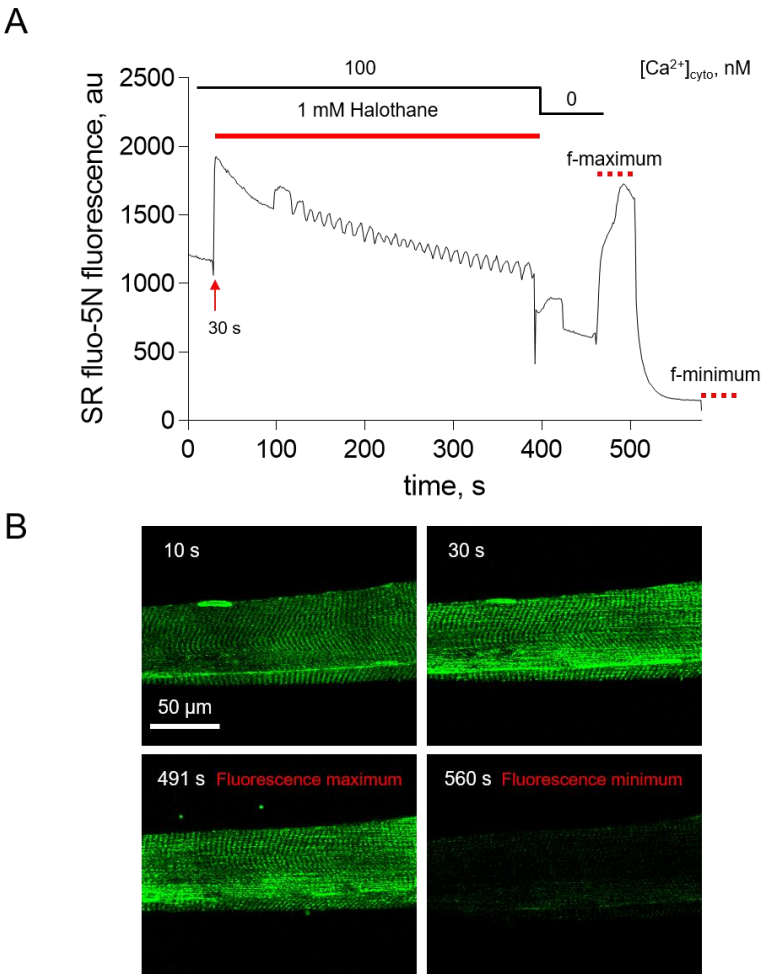

Figure 2.8 Persistently raised Ca^{2+} dependent fluorescence observed in fibers not treated with FCCP.

(*A*) Spatially averaged profile of fluo-5N fluorescence in the SR of a mechanically skinned fiber obtained from a human subject. The fiber was initially bathed in physiological internal solution containing 0.1 mM EGTA, 1 mM $[Mg^{2+}]_{cyto}$ and 100 nM $[Ca^{2+}]_{cyto}$ (*B*, *top left*) then by manual solution exchange the internal solution was replaced with a solution containing 0.1 mM EGTA, 0.4 $[Mg^{2+}]_{cyto}$, 1 mM halothane, and 100 nM $[Ca^{2+}]_{cyto}$. A persistently raised Ca^{2+} dependent fluorescence was observed when the fiber was exposed to halothane (*B, top right*). The maximum (*B, bottom left*) and minimum (B, *bottom right*) fluorescence were obtained by exposing the fiber to a Ca^{2+} ionophore (see below, Chapter 2.11). As shown, fibers not treated with FCCP caused Ca^{2+} entry into other dye loaded compartments. This was not observed in fibers treated with FCCP (Figure 2.9).

2.11. SR fluo-5N *in situ* dye calibration

An *in situ* calibration of fluo-5N in the SR was performed to provide a quantitative evaluation of the free $[Ca^{2+}]_{SR}$. This procedure is necessary as the ionic conditions and the presence of proteins in the SR will alter the apparent affinity of fluo-5N for Ca^{2+} compared to solutions only. Solutions used for calibration are listed in Table 2.1. All solutions with Ca^{2+} < 1.5 µM contained 50 mM EGTA to heavily buffer the $[Ca^{2+}]$.

As shown in Figure 2.9*A,* fluo-5N fluorescence was continuously tracked during exposure to various internal physiological solutions. Exposure to a 'maximum SR release solution' (black arrows) containing nominal Mg^{2+} and 30 mM caffeine reduced the fluorescent signal of fluo-5N. Replacing the maximum SR release solution with a 200 nM Ca^{2+} internal solution restored the SR fluorescent signal. These responses which were found to be highly reproducible are consistent with the physiological depletion and restoration of Ca^{2+} within the SR.

To perform the *in situ* calibration, the skinned fiber was exposed to a Ca^{2+} ionophore (50 µM ionomycin) in the presence of varying $[Ca^{2+}]_{cyto}$ ((µM); 0, 0.2, 83, 316, 1590 and, 5000). The minimum and maximum fluo-5N fluorescence were expected to be achieved in 0 and 5 mM Ca^{2+}, respectively given previous calibrations of this dye in the SR of cardiomyocytes by others (Shannon *et al.*, 2003). Note that after permeabilizing the SR, the exposure to 200 nM $[Ca^{2+}]_{cyto}$ solution no longer altered the fluo-5N fluorescence (1000 s). This demonstrates the permeablized SR is no longer able to maintain a Ca^{2+} gradient after exposer to the Ca^{2+} ionophore. The procedure was repeated in 6 fibers isolated from 3 rats. A Hill curve was fitted to the results and the reported apparent $K_{D,Ca}$ was found to be 403 ± 37.75 µM (Figure 2.9*B*).

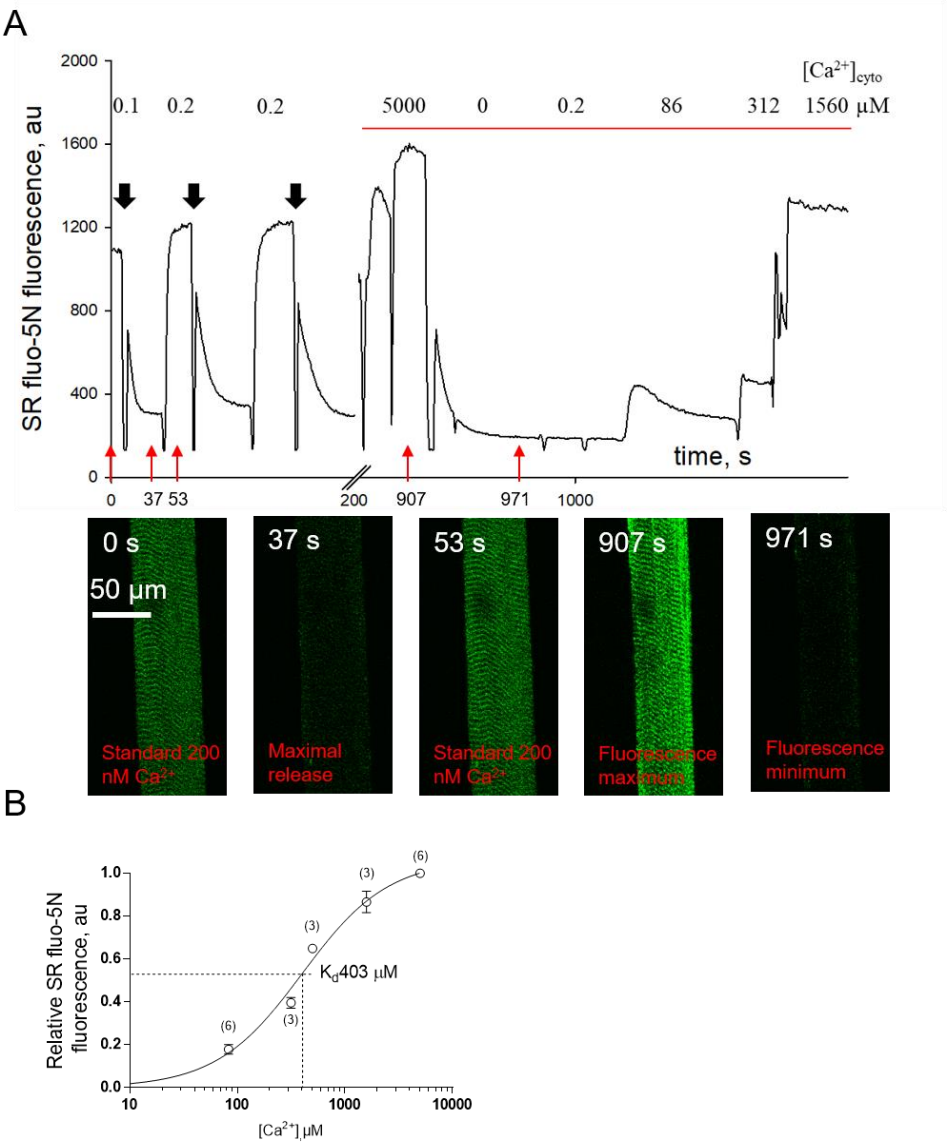

Figure 2.9. *In situ* calibration of fluo-5N trapped in the SR.

(*A*) A representative trace of tracking the Ca^{2+} dependent fluorescence of fluo-5N in the SR. Skinned rat EDL fibers were continuously imaged and exposed to a cycle of an internal (200 nM $[Ca^{2+}]_{cyto}$) and a maximal SR Ca^{2+} release solution (black arrow) buffered with 50 mM EGTA. The skinned fiber was then exposed to ionomycin (50µM) and 5 mM Ca^{2+} before exposing the cell to a range of $[Ca^{2+}]$ ((µM); 0, 0.2, 83, 316, and 1590). The red underscore represents the continuous exposure to ionomycin. (*B*) The normalized data were then fitted with a Hill curves, with a reported K_d value of 403 ± 37.75 µM (n=3-6 (brackets)). Continuous xy imaging of fluo-5N fluorescence was done at 0.841 s·frame^{-1} (at 21˚C).

Table 1.1. Solutions used to calibrate fluo-5N fluorescence.

Solution	EGTA	ATP	CP	NTA	Ca^{2+}	HDTA	Mg^{2+}	Ionomycin	K^{+}	Na^{+}
	Concentration in mM									
200 nM Ca^{2+} Internal solution	50	8	10	0	24.25	0	8.5	0 – 0.05	126	36
0 Ca^{2+} Maximal SR release solution (30 mM caffeine)	50	8	10	0	>0.01	0	0	0 - 0.05	126	36
83 µM Ca^{2+}	0	0	0	10	0.083	40	1	0.05	126	36
316 µM Ca^{2+}	0	0	0	10	0.316	40	1	0.05	126	36
500 µM Ca^{2+}	0	0	0	0	0.5	0	1	0.05	3	145
1590 µM Ca^{2+}	0	0	0	0	1.59	0	1	0.05	3	145
5000 µM Ca^{2+}	0	0	0	0	5.0	0	1	0.05	3	145

All solutions contained 50 µM BTS. Osmolality was 290±10 mOsmol kg^{-1}, and the pH was adjusted to 7.1 with KOH or NaOH (1590-5000 µM Ca^{2+} solutions), as necessary.

Chapter 3: Dantrolene requires Mg^{2+} to arrest malignant hyperthermia

3.1 Introduction

Malignant hyperthermia (MH) is a clinical syndrome of the skeletal muscle that presents as a hypermetabolic response to volatile gas anaesthetics such as halothane, isoflurane, and to the depolarizing muscle relaxant succinylcholine. The early sign of an MH event includes hyperthermia, tachycardia, tachypnea, and muscle rigidity. If left untreated, the occurrence of rhabdomyolysis leads to raised serum levels of creatine kinase, myoglobin, and K^+, which can ultimately lead to renal failure, and cardiac arrest. The prevalence of an MH episode during anaesthesia is estimated to be around 1:10,000 to 1:250,000 aesthetic. The vast majority of the causative mutations for MH have been linked to proteins involved in excitation contraction coupling in the skeletal muscle, of which over 30 RyR1 and 2 DHPR causative mutations have been linked to MH susceptibility (Sambuughin *et al.*, 2001; Monnier *et al.*, 2002; Weiss *et al.*, 2004).

Studies of MH susceptible muscle have shown that the RyR1 is highly sensitized to multiple RyR1 agonists including halothane, isoflurane, caffeine, and 4-chlorom-cresol (López *et al.*, 2000; Duke *et al.*, 2002, 2003). The *in vitro* contracture test (IVCT), and the caffeine halothane contracture test (CHCT) are both common assays used by clinicians to diagnose MH susceptibility (The European Malignant Hyperpyrexia Group 1984, Larach 1989). Though this process requires surgery to excise the required amount of fresh muscle tissue (1 gram) needed for the assay, it remains to be the 'gold standard' for diagnosis. These diagnostic tests involve assessing the threshold of which a muscle contraction is elicited at varying concentrations of halothane and caffeine, under the premise that MH susceptible muscle will generate a threshold force at much lower concentrations of both RyR1 agonists. The IVCT categories individuals into 3 groups: MHS (susceptible), MHE (equivocal) or MHN (non-susceptible) depending if the muscle produces significant force in response to both the agonist, one of agonist, or neither, respectively (Hopkins *et al.*, 2015).

It is proposed the affinity of the RyR1 channel for Mg^{2+} is lowered in MHS individuals which leads to its increased propensity to open (Laver *et al.*, 1997b; Steele & Duke, 2007). In skeletal muscle, cytosolic Mg^{2+} ($[Mg^{2+}]_{cyto} \approx 1$ mM) plays a duel role not only as an important cofactor for ATP but also a key negative regulator of the RyR1. Early studies on single RyR1 isolated from MHS pigs have reported an increase in the half

maximal inhibition of Mg^{2+} from 100 µM in MHN to 300 µM in MHS (Laver *et al.*, 1997b). This is supported in skinned fiber experiments from MHS pigs and humans which have been found to have a much lower threshold of activation by reduced [Mg^{2+}] (Lamb, 1993; Duke *et al.*, 2002; Duke *et al.*, 2004). The reduced Mg^{2+} inhibition in MHS is also consistent with the increased sensitivity of the RyR1 to be activated by a low concentration of caffeine and halothane at physiologically relevant levels of $[Mg^{2+}]_{cyto}$ (Duke *et al.*, 2002, 2003; Duke *et al.*, 2004). Though it is not very well understood how Mg^{2+} binding to the inhibitory site of the RyR1 regulates the catalytic sites of multiple RyR1 agonists, it is important to mention that in order for any RyR1 agonist to significantly open the RyR1, the mechanism of the agent must overcome the inhibitory effect of Mg^{2+} (Lamb, 2000). This explains why high concentration of caffeine or halothane fail to significantly activate the RyR1 in MHN muscle at physiologically relevant levels of Mg^{2+} (Lamb *et al.*, 2001; Duke *et al.*, 2003).

Currently, the muscle relaxant dantrolene is the only effective drug used to halt an MH episode (Hainaut & Desmedt, 1974). Since its approval by the Food and Drug Administration, the mortality rate due to a complication during an of MH episode in the North American population has been reduced from 80% to less than 1.4% (Larach *et al.*, 2008). During an MH event, an initial intravenous bolus injection of 2.5 mg/kg (of body weight) of dantrolene is administered, with up to 4 injections spaced 5 minutes apart up to 10 mg/kg. This can be repeated every 6 hours up to 48 hours to prevent reoccurrence of an MH episode. Typically this regimen results in a serum dantrolene concentration of 10-60 µM (Podranski *et al.*, 2005).

Although dantrolene has robustly been used to treat MH, its mechanism of action is poorly understood. Intravenous bolus injection of 5 mg/kg of dantrolene in WT rats has been shown to reduce force production by 25% and 30% in the extensor digitorum longus and soleus, respectively (Leslie & Part, 1981). A similar reduction in voltage induced Ca^{2+} release was observed in the flexor digitorum brevis of MHN mice (Szentesi *et al.*, 2001). Furthermore, 20 µM dantrolene has been shown to increase the Mg^{2+} sensitivity or the RyR1 in muscle fibers isolated from MHS pigs (Owen *et al.*, 1997b). This evidence suggests that dantrolene binds directly to the RyR1 to inhibit Ca^{2+} release (Fruen *et al.*, 1997), and indeed studies have found the corresponding RyR1 binding sites for dantrolene (Paul-Pletzer *et al.*, 2001; Paul-Pletzer *et al.*, 2002; Kobayashi *et al.*, 2005). However, the

inhibitory effect of dantrolene is all but absent in isolated RyR1 reconstituted in lipid bilayers (Szentesi *et al.*, 2001; Diaz-Sylvester *et al.*, 2008; Wagner Ii *et al.*, 2014).

A recent study conducted by Oo et al., (2015) demonstrated that CaM is an important co-factor in observing the inhibitory effect of dantrolene in the isolated RyR1 preparation. CaM has been previously shown to regulate the activity of the RyR1 and may play an important role in stabilizing the closed state of the RyR1 (Tripathy et al., 1995). In the study conducted by Oo et al., (2015) the observed inhibition on the RyRs by dantrolene was lost at raised $[Ca^{2+}]_{cyto}$ (1 µM), a condition which is likely to arise during an MH event. Furthermore, it is also unknown if dantrolene would be able to inhibit the RyR1 in the presence of halothane. Therefore, it still remains unclear if dantrolene would be able to inhibit the RyR1 during and MH event.

Single channel recordings have been used to great extent to characterize the function of the RyR1. However single channel recordings occur as an isolated system and may not necessarily translate directly to the physiological intact system (Laver, 2001). This is because the RyR1 is bathed in solutions (on both luminal and cytoplasmic sides) that are not physiological. Typically they are prepared to favour channel activation such as a high luminal $[Ca^{2+}]$, and most commonly lack Mg^{2+} in the cytoplasm (Laver *et al.*, 1997b; Laver, 2001). As previously mentioned Mg^{2+} is a key regulator of RyR1 channel activity and interestingly studies which reported no inhibition of the RyR1 by dantrolene also lack physiological levels Mg^{2+} in the cytoplasm (Szentesi *et al.*, 2001; Diaz-Sylvester *et al.*, 2008; Wagner Ii *et al.*, 2014).

During an MH event, the $[Mg^{2+}]_{cyto}$ is likely to increase above its basal level of 1 mM. The $[Mg^{2+}]_{cyto}$ is expected to rise due to depletion of ATP and CP stores which normally buffers Mg^{2+} in the cytoplasm (Westerblad & Allen, 1992). This is best described in metabolic fatigue where the rise in $[Mg^{2+}]_{cyto}$ can increase to 1.5-2 mM. However, it is unknown to what extent free Mg^{2+} can increase in an MH event (Westerblad & Allen, 1992). Elevated levels of $[Mg^{2+}]_{cyto}$ are not considered in studies of MHS. Assessments of MH events and the action of dantrolene needs to be performed in the presence of Mg^{2+} in the physiological range. The lack of qualitative assays that are sensitive to small changes in RyR1 activity makes it difficult to make such an assessment. As mentioned, the single channel assays are not an appropriate measure of RyR1 activity in MH since the $[Mg^{2+}]_{cyto}$ must be dropped to sub physiological levels.

3.1.1 Aims

This chapter will aim to determine the mechanism by which dantrolene can depress over-active Ca^{2+} release during an MH episode. It was necessary first to identify if dantrolene inhibited the RyR1. It was hypothesized that the lack of dantrolene action on single RyR1s activity in bilayers was due to the fact that the experiments were carried out either in the absence of or in low $[Mg^{2+}]_{cyto}$ (Szentesi *et al.*, 2001; Diaz-Sylvester *et al.*, 2008; Wagner Ii *et al.*, 2014). In contrast, the intact fiber experiments, where dantrolene inhibited the RyR1, maintained the endogenous level of $[Mg^{2+}]_{cyto}$ (Szentesi *et al.*, 2001). Using mechanically skinned fibers, where the cytoplasmic environment can be rapidly manipulated (Lamb & Stephenson, 1991; Lamb *et al.*, 2001), the effectiveness of dantrolene across a range of $[Mg^{2+}]_{cyto}$ was tested. Thus, skinned fibers were used to mimic the ionic conditions of both bilayer experiments and intact fiber experiments in the same preparation. Additionally, because the skinned fiber is bathed in, effectively, an infinite volume of internal solution, any metabolites generated during experiments diffuse from the preparation in less than a second so that the ionic conditions set in the bath are maintained inside the fiber.

3.2 Methods

3.2.1 Experimental animals, human muscle biopsy, and muscle preparation

Wistar rats (6-8 months old) and human muscle biopsies were collected as described elsewhere (Chapter 2.1 and Chapter 2.2, respectively). Biopsy was taken from a 30 y/o female with a RyR1 variant (exon 36, pArg1976Cys) and a 45 y/o MHS male. The excised muscle was blotted on filter paper (Whatman no.1) to remove excess blood and extracellular fluid. Under paraffin oil individual fibers were then isolated and mechanically skinned (Chapter 2.4). The skinned fiber was then mounted to the experimental apparatus as described in Chapter 2.3-2.4.

3.2.2 Internal physiological solution

Table 3.1 shows in detail the solution composition used in this study. The methods in preparing the internal physiological solution are described in detail in Chapter 2.5. All chemicals were obtained from Sigma-Aldrich (USA) unless otherwise stated. Halothane (density ~1.87 $g \cdot mL^{-1}$), dantrolene, and the contractile apparatus inhibitor *n*-benzyl-*p*-toluene sulphonamide (BTS) were added from a stock solution prepared in dimethyl sulfoxide (DMSO). The final concentration of DMSO did not exceed 0.7%. The total DMSO concentration was kept constant between the reference and all test conditions. All solutions contained 10 µM of the Ca^{2+} indicator, rhod-2. CaM derived from bovine testes was used in experiments. To prevent significant vaporization of halothane, solutions were made up immediately before application and were stored in an air tight syringe. The rate of halothane evaporation was found to be > 9.6% $\cdot$ $minute^{-1}$ by mass (Chapter 2.5; Figure 2.3) in our experimental apparatus, but no detectible reduction in potency was detected with short exposure (20-60 seconds) to the open environment.

Table 3.1: Internal solution composition

Solutions	[EGTA]	Total [Ca]	Free [Ca^{2+}]	Total[Mg]	Free[Mg^{2+}]
	Concentration in mM				
Loading solution: 1 mM Mg^{2+}, 300 nM Ca^{2+} (R)	1	0.485	0.0003	8.5	1
Release solution: 0 Mg^{2+}, 271 nM Ca^{2+} (R)	1	0.485	0.000271	0	0
0.4 mM Mg^{2+}, 100 nM Ca^{2+} (R)	1	0.247	0.0001	7	0.4
1 mM Mg^{2+}, 100 nM Ca^{2+} (R)	1	0.247	0.0001	8.5	1
3 mM Mg^{2+}, 100 nM Ca^{2+} (R)	1	0.247	0.0001	11.9	3
10 mM Mg^{2+}, 100 nM Ca^{2+} (R)	1	0.247	0.00016	22	10.8
Loading solution: 1 mM Mg^{2+}, 100 nM Ca^{2+} (H)	0.1	0.024	0.0001	8.5	0.92
Release solution: 0 Mg^{2+}, 100 nM Ca^{2+} (H)	0.1	0.024	0.0001	0	0
1.5 mM Mg^{2+}, 100 nM Ca^{2+} (H)	0.1	0.024	0.0001	9.6	1.5
2 mM Mg^{2+}, 100 nM Ca^{2+} (H)	0.1	0.024	0.0001	10.3	1.96
3 mM Mg^{2+}, 100 nM Ca^{2+} (H)	0.1	0.024	0.0001	11.8	2.98

Each solution contained (mM): K^+, 136; Na^+, 36; ATP, 8; creatine phosphate, 10; Hepes, 90; BTS, 0.05; and HDTA, 49 (R) or 49.9 (H). Final pH was 7.1. The solution name in the left column represents the rounded value of free [Mg^{2+}], and free [Ca^{2+}] in solutions and the value in the associated row represent the calculated values. The letters in parentheses (R) and (H) refer to solutions used for rat and human fiber experiments. Dantrolene, caffeine, and halothane were added to these solutions as indicated in the text.

3.2.3 Confocal imaging

These methods are described in Chapter 2.8. Rhod-2 was excited at 543 nm, and the emitted light was collected in the 562-666 nm range. Imaging was performed at 22 ± 1 °C.

3.2.4 Rhod-2 imaging of cytoplasmic Ca^{2+} transients induced by low $[Mg^{2+}]_{cyto}$, caffeine, and halothane

Continuous xyt imaging was performed with an aspect ratio of 256:512 (87.3:174.59 µm) at an acquisition rate of 0.841 seconds·frame^{-1}, 0.17 milliseconds·line^{-1} and a pixel distance of 0.21 µm as shown in Figure 3.1*A*. The fiber was oriented so that the scanning line was transversal to the fiber axis. The temporal and spatial information can also be interpreted along the y axis. The time delay of the line acquisition from the first to last scanning line of one frame is 0.841 seconds. The regions of interest in all experiments were averaged within the boundary of the muscle fiber, and the averaged fluorescence was normalised to baseline (F/F_0 as shown in Figure 3.1*B*). The peak amplitude and full duration at half maximum (FDHM) were analysed as shown in Figure 3.1*B*.

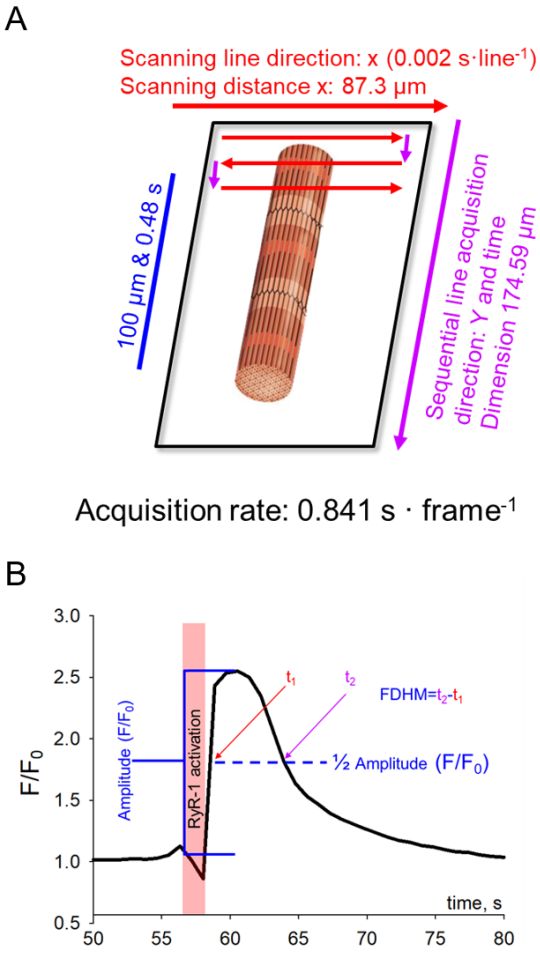

Figure 3.1 Image acquisition and analysis.

(*A*) Diagram depicting the sequential image acquisition throughout a series of x:y coordinates on a point scanning confocal system. (*B*) The spatially average profile of rhod-2-Ca^{2+} dependent fluorescence within the border of the fiber was normalized to the baseline fluorescence (F/F_0). Activation of the RyR1 caused a Ca^{2+} dependent rise in the fluorescent signal of the bathing solution eventually reaching a peak and subsequent decay of the signal. From each Ca^{2+} transient, the amplitude and full duration at half maximum (FDHM) can be interpreted.

3.2.5 Rhod-2 imaging of electrically evoked action potentials and image analysis

The mechanically skinned fiber was mounted on an experimental apparatus with the platinum electrodes positioned parallel to the long axis of the fiber (Figure 3.2*A*, and Chapter 2.7). Field pulses stimulations at 0.5 to 1 Hz were applied across the platinum electrodes. Image acquisition for these experiments was performed in xt line scan mode at a temporal resolution of ~2 ms· $line^{-1}$. As shown in Figure 3.2*A* the scanning line ran parallel to the fiber axis. The corresponding rhod-2 fluorescence was normalized to the baseline fluorescence (F/F_0) (Figure 3.2*B*).

3.2.6 Statistics

All data are presented as mean ± SEM. Statistical analysis and nonlinear curve fitting were performed with GraphPad Prism. IC_{50} values were derived from fits to Hill equations. Curves were compared with an extra sum of square *F*- test. The significance of the reference and test values were tested with either a paired Student's *t*-test or one-way analysis of variance with Tukey multiple comparison tests, as appropriate. Significance of the reference and test values were determined, where $p<0.05$.

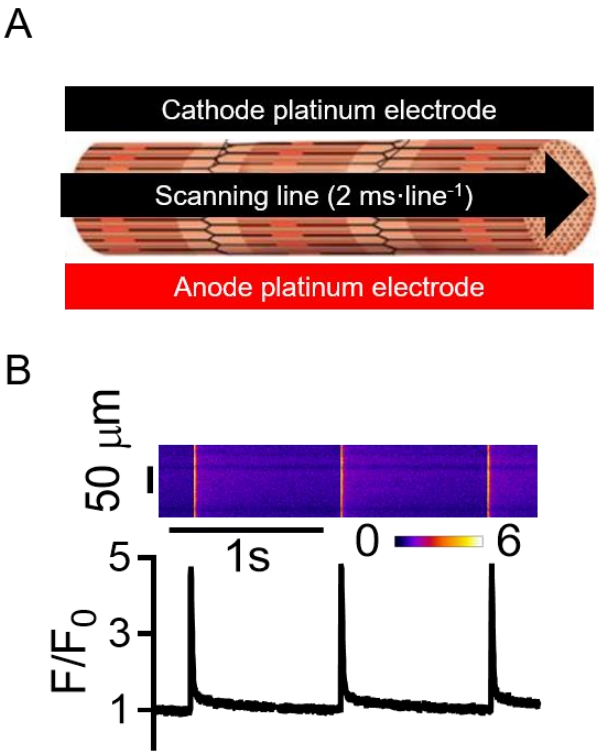

Figure 3.2 Confocal line scan image acquisition and analysis of electrically evoked Ca^{2+} transients in skinned fibers.

(*A*) Diagram depicting the position of the skinned fiber relative to the scanning line (scanning line distance ~174 µm at 2 ms·line^{-1}) and platinum electrodes. (*B*) An example of an original continuous line scan recording of rhod-2 fluorescence (top) with the corresponding normalized line average (F/F_0) shown on the bottom. The preparation was stimulated with a 5-ms square field pulse at 100 volts using a Grass S44 Stimulator at either 0.5 or 1 Hz (Grass Instruments Co., Quincy, Massachusetts, USA).

3.3 Results

3.3.1 Ca^{2+} transients elicited by low $[Mg^{2+}]_{cyto}$ are not inhibited by dantrolene

Ca^{2+} release from the RyR1 was reported by the Ca^{2+} indicator rhod-2 (10 µM). The release of SR Ca^{2+} through the RyR1 can be elicited by removing Mg^{2+} from the physiological solution by manual solution exchange (Lamb & Stephenson, 1991; Lamb *et al.*, 2001; Duke *et al.*, 2002). Lowering the $[Mg^{2+}]_{cyto}$ from endogenous levels (~1 mM) to nominal $[Mg^{2+}]_{cyto}$ (< 0.01 mM) removes the endogenous inhibition of Mg^{2+} on the RyR1. Figure 3.3*A* shows the selected images of a continuous xyt recording (0.841 $s \cdot frame^{-1}$) of an SR Ca^{2+} transient elicited by bathing the fiber in a nominal Mg^{2+} solution (release solution) with the corresponding normalized spatially average values over time shown in Figure 3.3*B*. The baseline normalized fluorescent ratio (F/F_0) corresponds to a $[Ca^{2+}]_{cyto}$ of 300 nM.

After SR Ca^{2+} depletion, the SR can be reloaded with Ca^{2+} by restoring the resting inhibition of the RyR1. During prolonged opening of the RyR1, CSQ remains in a depolymerized state which lowers the capacity of the SR to store Ca^{2+}, therefore the total $[Ca^{2+}]_{SR}$ remains at low levels (Fryer & Stephenson, 1996; Murphy *et al.*, 2009; Lamboley *et al.*, 2013; Manno *et al.*, 2017). Restoring the resting inhibition of the RyR1 allows Ca^{2+} to accumulate in the SR to levels which favour CSQ polymerization, thus restoring the total $[Ca^{2+}]_{SR}$ back to endogenous levels (Fryer & Stephenson, 1996; Murphy *et al.*, 2009; Lamboley *et al.*, 2013; Manno *et al.*, 2017). In the following experiments after each Ca^{2+} transient, the fiber was bathed in a loading solution (Chapter 3.2.2) for two minutes before the next Ca^{2+} transient was elicited. As shown in Figure 3.3*C* a two minute loading period produced a reproducible Ca^{2+} transient which did not differ in amplitude or shape.

At the decay of the Ca^{2+} transient, F/F_0 fell below the baseline when the loading solution was reintroduced as shown Figure 3.3*C* (blue arrows, F/F_0 lower inside the fiber then the surrounding solution). The fluorescent levels recovered after 2-3 minutes. As shown in Figure 3.3*B* this drop in baseline fluorescence did not occur when the fiber was continuously bathed in the release solution. The fluorescent drop below baseline is consistent with the SR being depleted of Ca^{2+} and the SERCA pump working toward replenishing the SR Ca^{2+} store as observed previously by Duke & Steele (2001). In this experiment the bathing solution was static. Therefore the fiber is limited by the inward diffusion of the applied solution. It is then reasonable to suggest that the rate of Ca^{2+}

uptake into the SR must have been greater than the inward diffusion of Ca^{2+} from the bathing solution. Furthermore, as demonstrated by Duke & Steele (2001) in mechanically skinned fibers, this drop in the baseline is not observed when the preparation was perfused.

It is important to mention that the nominal $[Mg^{2+}]_{cyto}$ of the release solution in this study is analogous to the cytosolic condition imposed in planar lipid bilayer studies where the inhibitory effect of dantrolene is not readily observed (in the absence of CaM) (Szentesi *et al.*, 2001; Diaz-Sylvester *et al.*, 2008; Wagner Ii *et al.*, 2014). Figure 3.4*A* shows an example trace of the Ca^{2+} transient in the presence of dantrolene. The $[Ca^{2+}]_{cyto}$ was held constant at ~300 nM throughout the experiment. To ensure dantrolene (50 µM) was present at the RyR1s of the fiber upon lowering $[Mg^{2+}]_{cyto}$, it was introduced in the loading solution prior to exposure to the release solution containing dantrolene. Analysis of the spatially averaged profile of rhod-2 fluorescence showed that dantrolene did not reduce the amplitude (Figure 3.4*B*) nor the shape (Figure 3.4*C*) of the Ca^{2+} transient. The addition of exogenous CaM in the presence of dantrolene did not affect this result (Figure 3.4*D*, *E*).

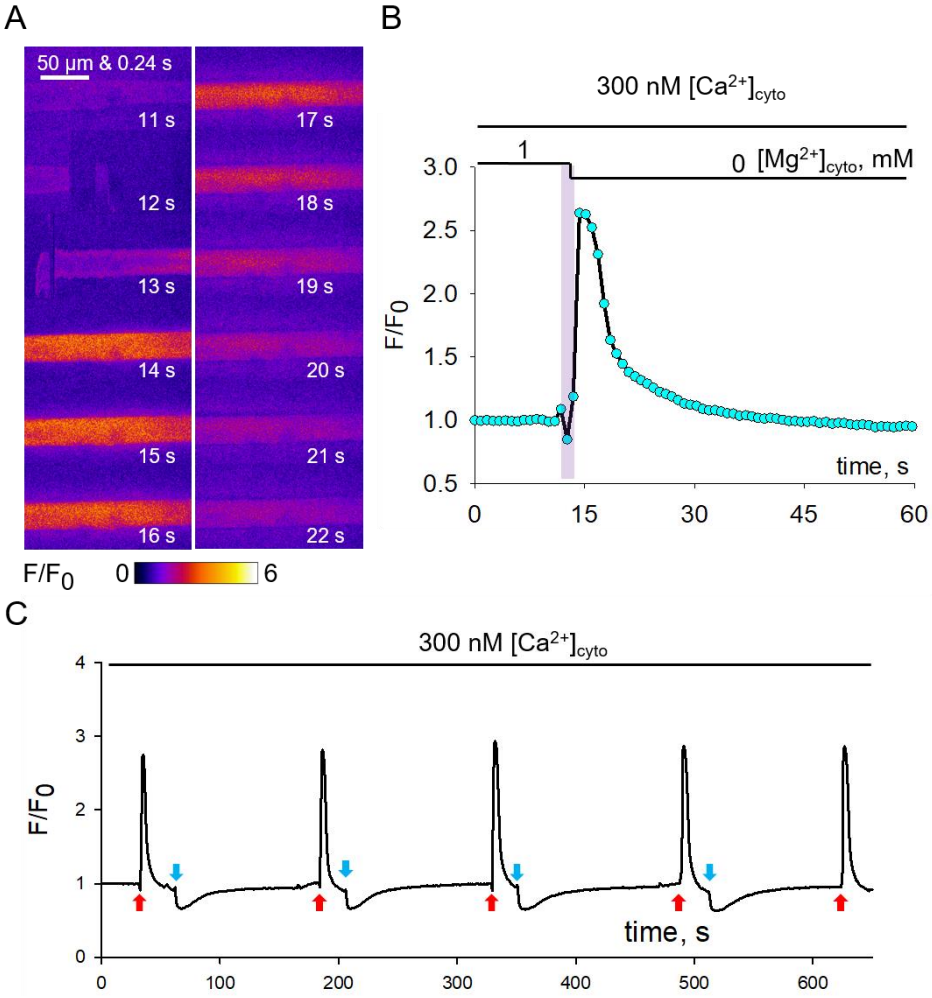

Figure 3.3 Ca^{2+} transients evoked by the removal of Mg^{2+}.

(*A*) Selected consecutive images of cytoplasmic rhod-2 fluorescence during continuous xyt recording (at a temporal resolution of ~0.841 s·frame^{-1}) in rat mechanically skinned fibers. The time indicated in the Figure was rounded to the nearest whole number. (*B*) Spatially averaged values of normalized fluorescence intensity (F/F_0) versus elapsed time from the experiment shown in *A*. Fibers were continuously bathed in 1 mM EGTA, 1 mM $[Mg^{2+}]_{cyto}$ and 300 nM $[Ca^{2+}]_{cyto}$ then by manual solution exchange (the purple vertical bar indicating the movement artefact during solution exchange at ~12 s) the bathing solution was replaced with a nominal low $[Mg^{2+}]_{cyto}$ solution to elicit the release of SR Ca^{2+}. (*C*) The SR can be loaded with Ca^{2+} by reintroducing 1mM Mg^{2+} back into the bathing solution (blue arrows) which produced reproducible Ca^{2+} transients (red arrows) with similar amplitude and shape.

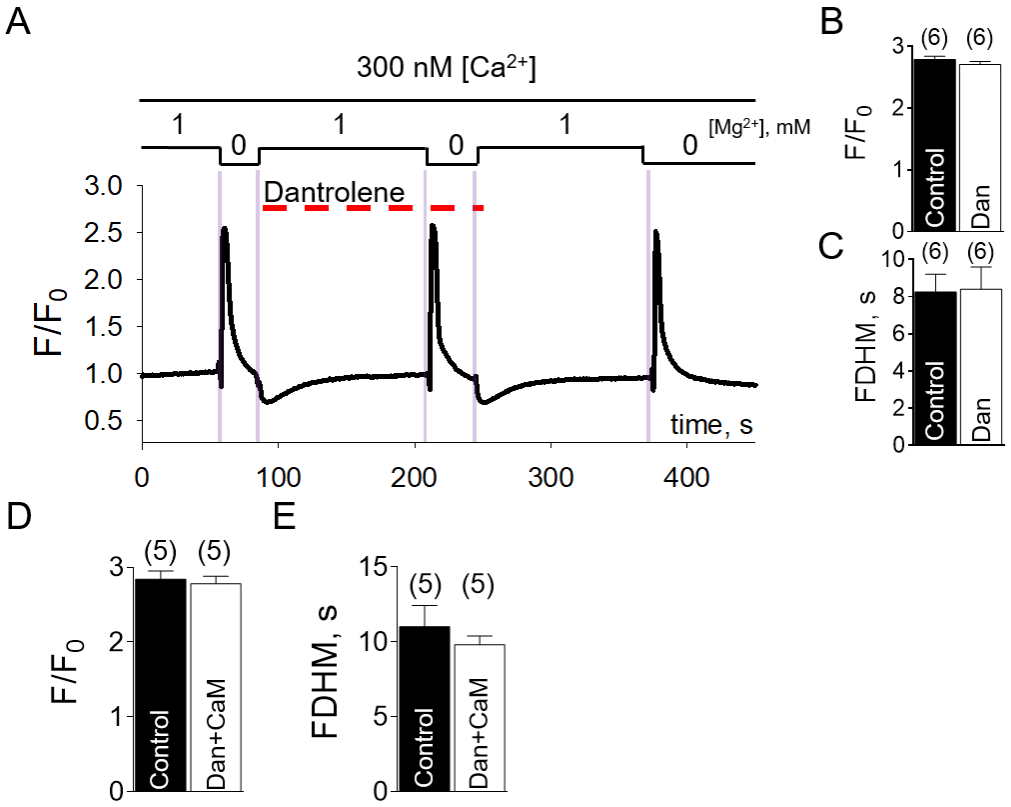

Figure 3.4 Ca^{2+} transients evoked by the removal of Mg^{2+} are not inhibited by dantrolene in the presence of exogenous CaM.

(*A*) Spatially averaged profile of xyt recordings of Ca^{2+} transients in rat skinned fibers evoked by the nominal removal of Mg^{2+} either in the absence (first Ca^{2+} release) or presence of dantrolene (second Ca^{2+} release). $[Mg^{2+}]_{cyto}$ is given at the top and exchange of solutions is indicated by pale purple vertical bars. A two minute time interval was allowed for after each low Mg^{2+} transient to recover SR Ca^{2+} levels in a solution with 1 mM Mg^{2+} and 300 nM Ca^{2+}. The presence of 50 µM dantrolene is indicated by the dashed horizontal red bar. Mean normalized peak amplitude values (F/F_0) (*B*) and FDHM (*C*) in the absence and presence of dantrolene (n = 6 fibers). This experiment was repeated in the presence of exogenous CaM~100 nM. The resulting mean normalized peak amplitude values (*D*) and FDHM (*E*) in the presence and absence of CaM are shown (n = 5 fibers). A paired Student's t-test revealed no significant difference ($p > 0.05$) in *B*, *C*, *D,* and *E*. All data presented as mean ± SEM.

3.3.2 Dantrolene requires physiological Mg^{2+} to inhibit electrically evoked Ca^{2+} transients

Next, it was determined if physiologically relevant $[Mg^{2+}]_{cyto}$ is necessary to observe the inhibitory effect of dantrolene. Electrical field pulse stimulations at 1 Hz was used to release Ca^{2+} from the SR at various $[Mg^{2+}]_{cyto}$. In the resting muscle, 1 mM $[Mg^{2+}]_{cyto}$ exerts a strong inhibitory action on the RyR1 by binding to an inhibitory site (Lamb & Stephenson, 1991; Laver *et al.*, 1997a; Laver *et al.*, 1997b; Lamb, 2000). Applying an electrical field pulse stimulus activates the DHPR and causes the temporary removal of this inhibition, thus resulting in the release of SR Ca^{2+} (Lamb & Stephenson, 1991). Confocal line scans parallel to the long axis of the fiber were taken with a temporal resolution of 2 $ms \cdot line^{-1}$ as shown in Figure 3.2 and Figure 3.5 (*top*). The corresponding normalized line average of rhod-2 fluorescence is shown on the bottom. Note that the images shown in Figure 3.5 were from the same muscle fiber. The baseline fluorescence corresponds to a $[Ca^{2+}]_{cyto}$ of 100 nM.

The left side of Figure 3.5 shows example traces at varying $[Mg^{2+}]_{cyto}$ ($[Mg^{2+}]_{cyto}$ (mM); 0.4, 1, and 3). The physiological range of $[Mg^{2+}]_{cyto}$ is estimated to be about 0.8-1 mM at rest and up to 3 mM during metabolic fatigue. Sub physiological $[Mg^{2+}]_{cyto}$ of 0.4 mM does not occur in the muscle but was used to determine if the inhibitory effect of dantrolene required physiological relevant $[Mg^{2+}]_{cyto}$. It is also important to note that 0.4 mM $[Mg^{2+}]_{cyto}$ is above the half-inhibiting concentration of Mg^{2+} of 0.1 mM (Laver *et al.*, 2004). The normalized peak amplitude was not different between 0.4 and 1 mM $[Mg^{2+}]_{cyto}$. Increasing the $[Mg^{2+}]_{cyto}$ to 3 mM halved the normalized peak amplitude and further increasing the $[Mg^{2+}]_{cyto}$ to 10 mM failed to elicit a measureable Ca^{2+} transient.

In the presence of 50 µM dantrolene (right side of Figure 3.5) the normalized amplitude was not affected when the $[Mg^{2+}]_{cyto}$ was set at 0.4 mM. However, when the $[Mg^{2+}]_{cyto}$ was increased to 1 and 3 mM, the normalized peak Ca^{2+} transient was reduced in the presence of 50 µM dantrolene.

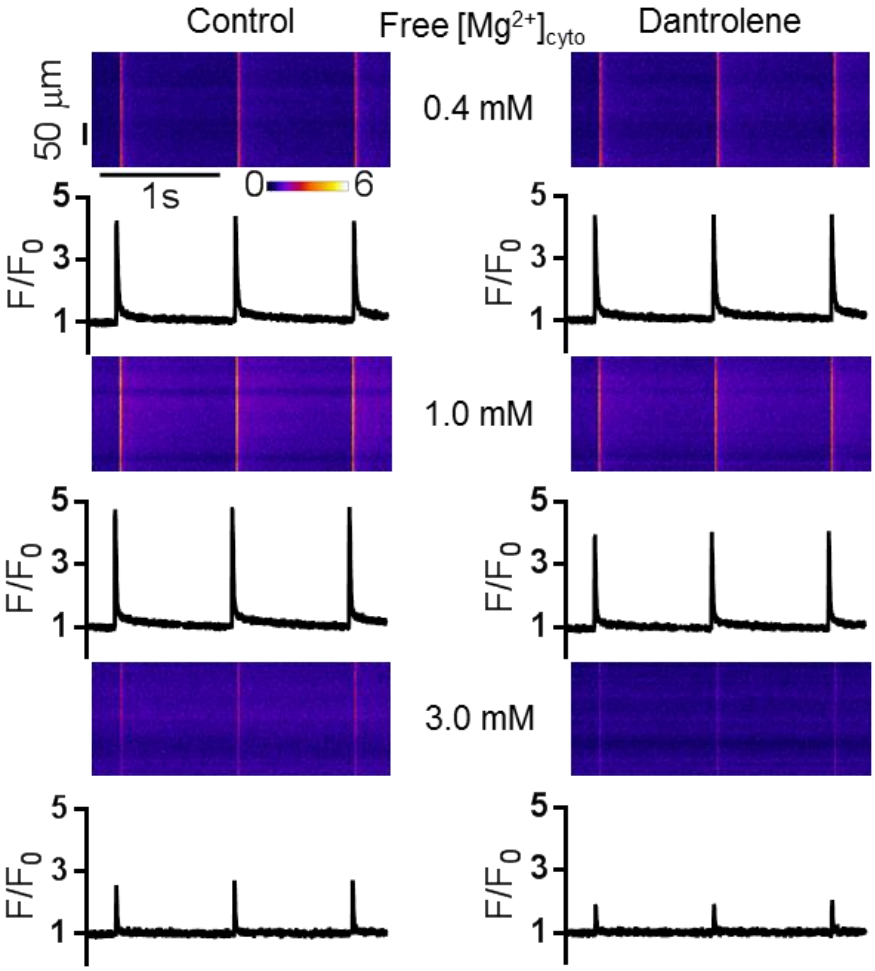

Figure 3.5 Inhibition of electrically evoked Ca^{2+} transients by dantrolene requires physiologically relevant $[Mg^{2+}]_{cyto}$.

Original line scan recording of rhod-2 fluorescence taken parallel along the long axis of the mechanically skinned rat fiber at a temporal resolution of 2 ms·line^{-1} (top). The corresponding normalized line average (F/F_0) shown on the bottom. The Ca^{2+} transients were elicited by field pulse stimulation (2-5 ms pulse duration) at 1 Hz in the absence (left) and presence (right) of 50 µM dantrolene at varying $[Mg^{2+}]_{cyto}$ (0.4, 1 and 3 mM). All solutions contained 1 mM EGTA, 100 nM $[Ca^{2+}]$, and 10 µM rhod-2. Note that the representative trace shown in this Figure was obtained from a single fiber.

The summary of the effects of dantrolene on electrically evoked Ca^{2+} transients at various $[Mg^{2+}]_{cyto}$ is shown in Figure 3.6*A*. The data were fitted with a Hill equation, and the reported IC_{50} values in the absence and the presence of 50 µM dantrolene was 2.95 ± 1.42 mM and 1.74 ± 1.63 mM, respectively. An extra-sum of square F-test revealed that the two curves were significantly different ($p<0.05$) and importantly shows that Mg^{2+} inhibition of the RyR1 in the presence of dantrolene is left shifted. Figure 3.6*B* shows that the % inhibition induced by dantrolene increased with increasing $[Mg^{2+}]_{cyto}$. These results indicate that physiologically relevant $[Mg^{2+}]_{cyto}$ is necessary to observe the inhibitory effect of dantrolene. The concentration response of dantrolene is shown in Figure 3.6*C*. The $[Mg^{2+}]_{cyto}$ during these experiments were set at 3 mM where the inhibition of dantrolene was at the greatest. A Hill slope was fitted to the data, and the reported IC_{50} value was 0.41 ± 2.66 µM.

Oo et al. (2015) have previously demonstrated that CaM is an important factor in observing the reduced open probability of the RyR1 by dantrolene in planar lipid bilayer studies. It was also considered that the lack of dantrolene inhibition at 0.4 mM $[Mg^{2+}]_{cyto}$ may be due to some loss of CaM from the skinned fiber or was simply lost to the bathing solution, which presents a virtually infinite volume relative to the fiber. The loss of endogenous CaM may have occurred during the preparation of the mechanically skinned fiber. To address this possibility, we repeated the above experiments in the presence of 100 nM exogenous CaM and 50 µM dantrolene throughout the range of $[Mg^{2+}]_{cyto}$. These results are summarized in Figure 3.6*A* (red data points) and demonstrate that exogenous CaM did not further inhibit the RyR1 in the presence of dantrolene. This is also consistent with the fact that CaM remains in the skinned fiber preparation long after the surface sarcolemma is removed (Rodney & Schneider, 2003).

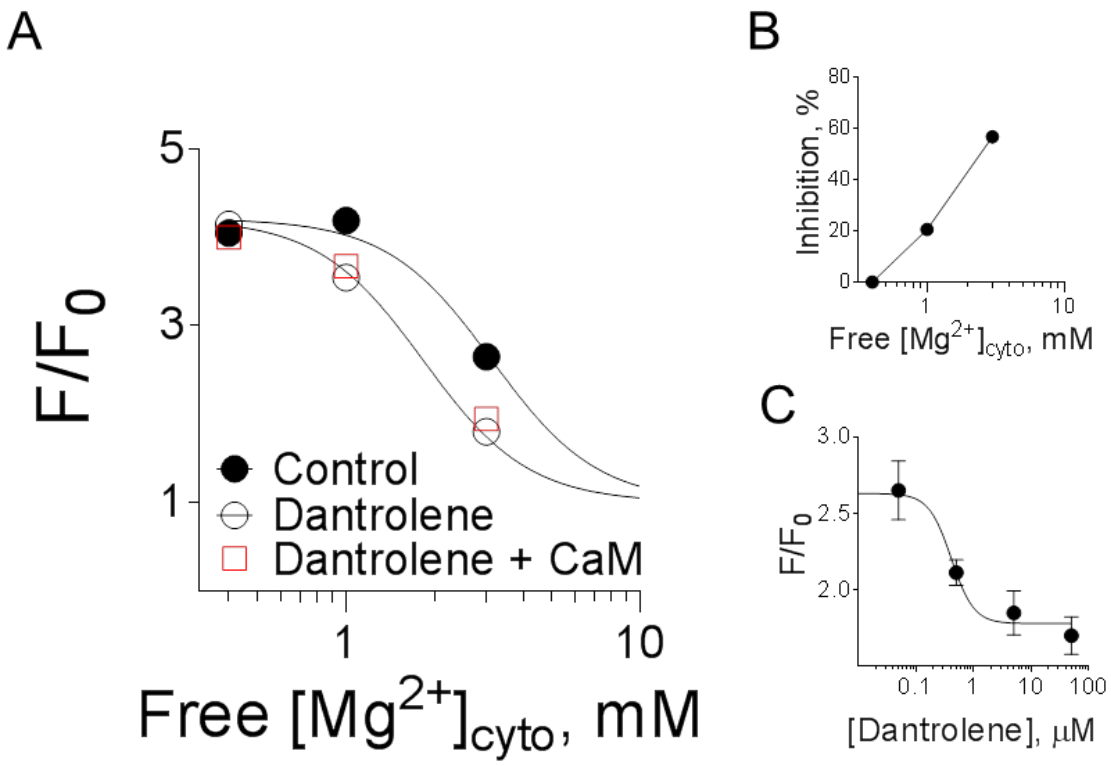

Figure 3.6 The inhibitory effect of dantrolene increases with raised $[Mg^{2+}]_{cyto}$.

(*A*) The summarized data showing the effect of dantrolene at various $[Mg^{2+}]_{cyto}$ on electrically evoked Ca^{2+} transients as shown in Figure 3.5. The data were fitted with a Hill equation and yielded an IC_{50} value of 2.95 ± 1.42 mM and 1.74 ± 1.63mM in the absence and presence of dantrolene, respectively. Curves are significantly different from each other (Extra-sum of square F test). The red data points represent the normalized Ca^{2+} transient in the presence of 100 nM exogenous CaM, and 50 µM dantrolene (*B*) % inhibition of Ca^{2+} transient by dantrolene at the indicated $[Mg^{2+}]_{cyto}$. (*C*) Concentration dependent inhibition of electrically evoked Ca^{2+} transient by dantrolene at 3 mM $[Mg^{2+}]_{cyto}$ yielding an IC_{50} value of 0.41 ± 2.66 µM dantrolene. All data were derived from 5-18 fibers isolated from a minimum of 3 rats. All data is presented at mean ± SEM.

3.3.3 Inhibition by dantrolene at low $[Mg^{2+}]_{cyto}$ observed in the presence of an additional stabilizer

The previous experiments of this section showed that lowering the $[Mg^{2+}]_{cyto}$ to 0.4 mM is not sufficient to open the RyR1 as observed in Figure 3.3, however it is thought to increase the sensitivity of the RyR1 to be activated by RyR1 agonists (i.e., lower [agonist] is needed to activate the channel at 0.4 mM $[Mg^{2+}]_{cyto}$ compared to 1 mM $[Mg^{2+}]_{cyto}$) (Laver *et al.*, 1997b; Duke *et al.*, 2002, 2003; Laver *et al.*, 2004). Therefore it is reasonable to suggest that raised [dantrolene] is also required to inhibit the RyR1 at lower $[Mg^{2+}]_{cyto}$. In the next series of experiments, it was determined if the inhibitory effect of dantrolene can be observed at low $[Mg^{2+}]_{cyto}$ when an additional RyR1 inhibitor (tetracaine) was used synergistically with dantrolene. This approach was necessary as the [dantrolene] (50 µM) used in previous sections was near the solubility limit.

Figure 3.7*A* shows a continuous line scan recording (taken at 2 ms·line^{-1}) of rhod-2 fluorescence from a single rat mechanically skinned fiber. The fiber was initially bathed in an internal solution containing 0.4 mM $[Mg^{2+}]_{cyto}$, 100 nM $[Ca^{2+}]_{cyto}$, and 1 mM EGTA. The Ca^{2+} transient was evoked by field pulse stimulation at 0.5 Hz. The introduction and removal of various drugs were done during the data acquisition period which lasted 40 s per recording. Similar to previous results 50 µM dantrolene (top left) did not reduce the peak amplitude of electrically evoked Ca^{2+} transient. Introducing 10 µM tetracaine, however, reduced the normalized peak amplitude by ~24% (top right), with a complete ablation of the Ca^{2+} transient observed at 15 µM tetracaine (Figure 3.7*C*). Initially, the recording with 10 µM tetracaine (bottom left) the addition of 50 µM dantrolene further reduced the peak Ca^{2+} transient. The initial levels were recovered after removing both dantrolene and tetracaine from the bathing solution (Note that the time scale was reduced in the bottom right section and that generally it required multiple solution exchanges to remove dantrolene from the preparation). These results are summarized in Figure 3.7*B* which shows the inhibitory effect of dantrolene can be observed at 0.4 mM $[Mg^{2+}]_{cyto}$ when an additional RyR1 stabilizer is present.

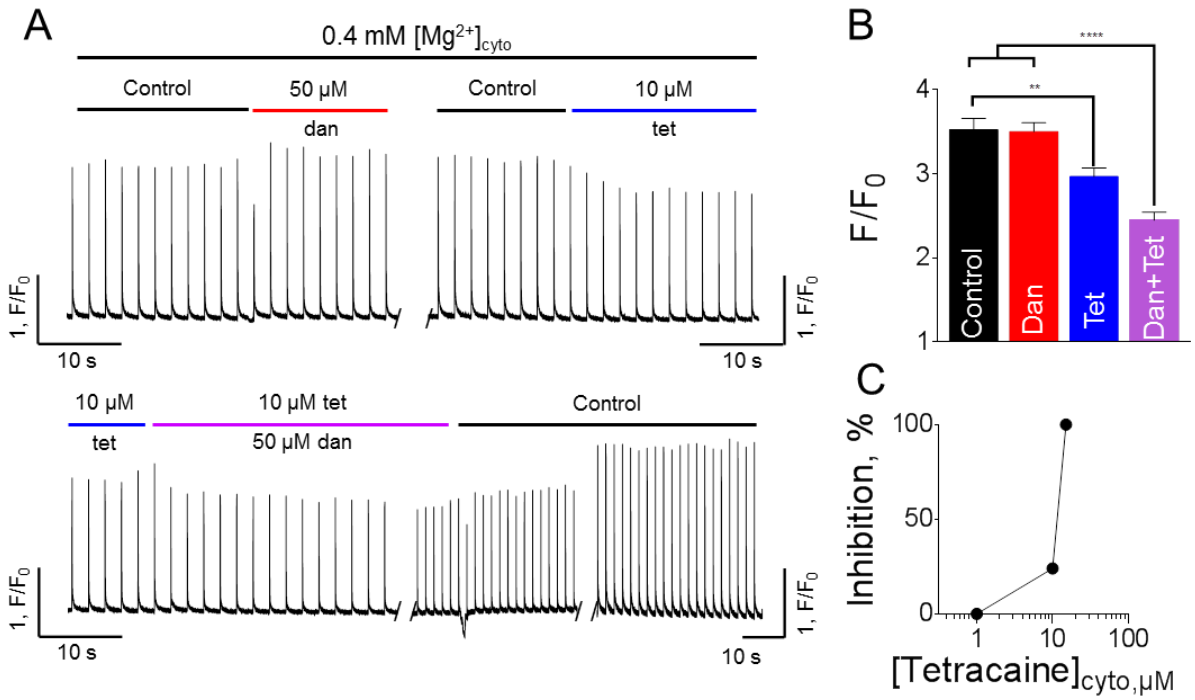

Figure 3.7 Inhibition by dantrolene at low $[Mg^{2+}]_{cyto}$ observed in the presence of an additional stabilizer.

(*A*) Normalized line average (F/F_0) of rhod-2 fluorescence of rat mechanically skinned fiber with the scanning line parallel along the long axis of the fiber. Acquisition rate was 2 ms · $line^{-1}$. Ca^{2+} transients were elicited by field pulse stimulation (2-5 ms pulse duration) at 0.5 Hz in the presence of 100 nM $[Ca^{2+}]_{cyto}$, and 0.4 mM $[Mg^{2+}]_{cyto}$. The bathing solution was then supplemented with 50 µM dantrolene (dan: red bar), 10 µM tetracaine (tet: blue bar), or a combination of both drugs (purple bar). The diagonal line indicates a stopping of the recording to prepare for the next manual solution exchange which took on average 1-2 minutes. Note that manual solution exchanges were performed during imaging. (*B*) Mean normalized amplitude (F/F_0) from experiments as shown in (*A*) (n=5-6 fibers). For statistical analysis, we used a one-way ANOVA test with Tukey's multiple-comparison test ($P<0.0001$). (*C*) % inhibition by varying concentrations of tetracaine in the presence of 100 nM $[Ca^{2+}]_{cyto}$, and 0.4 mM $[Mg^{2+}]_{cyto}$ (n = 9-10 fibers). All data are shown as mean ± SEM.

3.3.4 Dantrolene require raise $[Mg^{2+}]_{cyto}$ to lower frequency of halothane induced Ca^{2+} waves in human MHS skeletal muscle fibers

Next, the mechanism in which dantrolene is able to inhibit halothane induced Ca^{2+} release in MHS skeletal muscle fibers was investigated. This section utilizes mechanically skinned fibers isolated from needle biopsy taken from the vastus lateralis muscle from two unrelated subjects. Subject (A) carried a RyR1 variant in exon 36 pArg1976Cys. The subject (B) was previously diagnosed with MHS following a positive IVCT test performed at The Royal Melbourne Hospital, Melbourne, Australia (with responses of 0.07 g at 2 mM caffeine; 0.26 g at 2% halothane) (Gillies *et al.*, 2015).

As shown previously by Duke & Steele (2004), the sensitivity of the RyR1 to various MH triggers can be determined in single skinned fibers by tracking the Ca^{2+} dependent fluorescence of the cytosol using a similar protocol used in this study (Figure 3.3). In the study conducted by Duke & Steele, 1 mM halothane failed to trigger a Ca^{2+} transient in single fibers isolated from 71 individuals (71/71 fibers) whom previously has been diagnosed MHN following an IVCT test. MHS positive fibers, in contrast, produced a Ca^{2+} transient in the presence of relatively low concentrations of halothane (1 mM) and caffeine (2 mM). This study by Duke & Steele (2004) allows the probable determination of MH status of the fibers examined in a similar fashion.

Figure 3.8 shows a control response of a human MHN skinned fiber (isolated from a 28y/o Male) to 1 mM halothane in the presence of either 1 or 0.4 mM $[Mg^{2+}]_{cyto}$. Unexpectedly, the addition of 1 mM halothane in 1 mM $[Mg^{2+}]_{cyto}$ induced a Ca^{2+} transient. This Ca^{2+} transient, however, was starkly contrasted with the halothane response at 0.4 mM $[Mg^{2+}]_{cyto}$. At reduced $[Mg^{2+}]_{cyto}$ the amplitude of the Ca^{2+} transient was increased. Importantly, the Ca^{2+} transients at reduced $[Mg^{2+}]_{cyto}$ took the form of a repetitive propagating Ca^{2+} wave. These experiments were repeated in an additional 5 fibers and resulted in only 1 of 6 fibers producing a Ca^{2+} wave at 1 mM $[Mg^{2+}]_{cyto}$ and 6 of 6 fibers at 0.4 mM $[Mg^{2+}]_{cyto}$. The halothane induced Ca^{2+} transient observed at 1 mM $[Mg^{2+}]_{cyto}$, therefore, may not be indicative of an MHS like response but may rather be due to an acute release of Ca^{2+} by halothane. Note that 1 mM halothane is much higher than the concentrations used in the IVCT and CHCT testing (2-3% halothane is equivalent to 0.44-0.66 mM respectively) (The European Malignant Hyperpyrexia Group 1984, Larach 1989; (Hopkins *et al.*, 2015)).

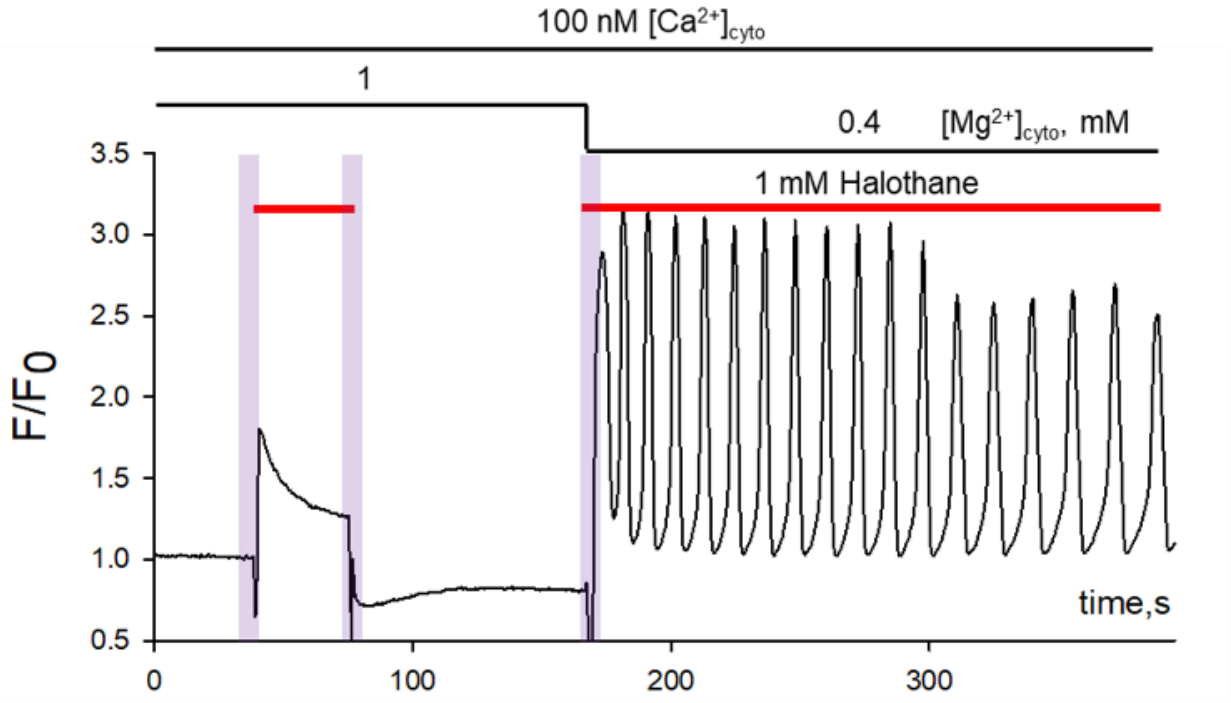

Figure 3.8 Representative trace of the effect of halothane on human MHN muscle fiber.

The muscle fiber was initially bathed in a solution containing 100 nM Ca^{2+} weakly buffered by 100 µM EGTA and 1 mM Mg^{2+}. The fiber was then exposed to 1 mM halothane at varying concentrations of Mg^{2+}. The purple vertical bar indicates the movement artefact during solution exchange. This experiment was repeated in 6 fibers with only 1 of 6 fibers producing a Ca^{2+} wave at 1 mM Mg^{2+}. All fibers produced a Ca^{2+} wave at 0.4 mM Mg^{2+}.

Figure 3.9 shows the recorded normalized rhod-2 fluorescence of mechanically skinned fiber isolated from subject (A). A single mechanically skinned fiber from subject (A) was initially exposed to a release solution. Following the Ca^{2+} transient, the fiber was bathed again in the physiological solution. The fiber was then loaded for 2 minutes before exposing the fiber to either 3 mM caffeine (Figure 3.9 *A*) or 1 mM halothane (Figure 3.9 *B*) at 1 mM Mg^{2+}. In fibers from subject A, the exposure to low concentrations of caffeine and halothane induced a Ca^{2+} wave. (The biophysical properties of this Ca^{2+} wave will be investigated in Chapter 4). Every fiber tested in subject (A) responded positively to RyR1 agonist which is consistent with an MHS status.

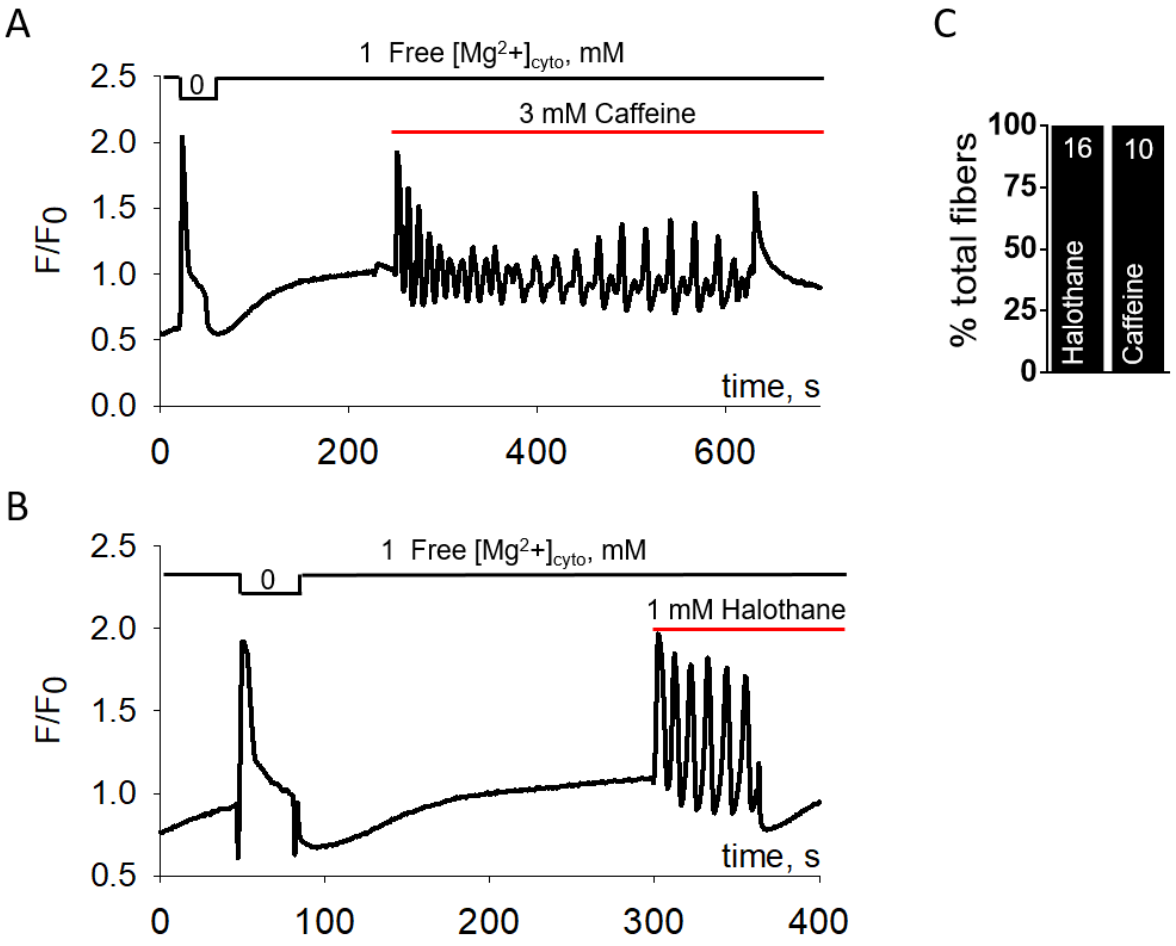

Figure 3.9. The effect of low [caffeine] and [halothane] on human muscle fiber from biopsied subject A.

Spatially-averaged profile of cytoplasmic rhod-2 fluorescence of human skinned fiber during the reduction of $[Mg^{2+}]_{cyto}$ from 1 to nominal 0 mM; and the exposure to (*A*) 3 mM caffeine or (*B*) 1 mM halothane. The fiber was in the constant presence of 0.1 mM EGTA and 100 nM $[Ca^{2+}]_{cyto}$. (*C*) Summary of the number of fibers from the biopsy used responding with regenerative Ca^{2+} waves. The response to low concentration of both caffeine and halothane are consistent with the subject being MH susceptible (Duke *et al.*, 2004).

Figure 3.10*A* (subject A), 3.10*C* (subject B) shows the halothane induced repetitive Ca^{2+} waves in isolated skinned fibers in the presence (blue trace) and absence (red trace) of dantrolene at varying $[Mg^{2+}]_{cyto}$. Note that the frequency of the Ca^{2+} wave varied between the two subjects tested. This variance is expected as different causative mutations are expected to have varying degrees of sensitivity to halothane. In both subjects, the incremental increase in $[Mg^{2+}]_{cyto}$ greatly reduced the frequency of the Ca^{2+} waves. In subject A and B, the addition of 50 µM dantrolene did not affect the frequency of the Ca^{2+} waves at 1 mM $[Mg^{2+}]_{cyto}$. However, when the $[Mg^{2+}]_{cyto}$ was raised to 2 mM, and 3 mM, 50 µM dantrolene greatly slowed the period between the Ca^{2+} transients in Subject A. These experiments were repeated using a clinically relevant [dantrolene] of 5 µM. Similar to subject A, dantrolene greatly reduced the frequency of the Ca^{2+} transient. Halothane failed to trigger a Ca^{2+} transient in 5 out of 6 fibers tested from Subject B when the $[Mg^{2+}]_{cyto}$ was raised to 3 mM in the presence of 5 µM dantrolene. These results are summarized in Figure 3.10*B* (subject A) and 3.10*D* (subject B) which shows that the inhibition of halothane induced Ca^{2+} wave is left shifted in the presence of dantrolene.

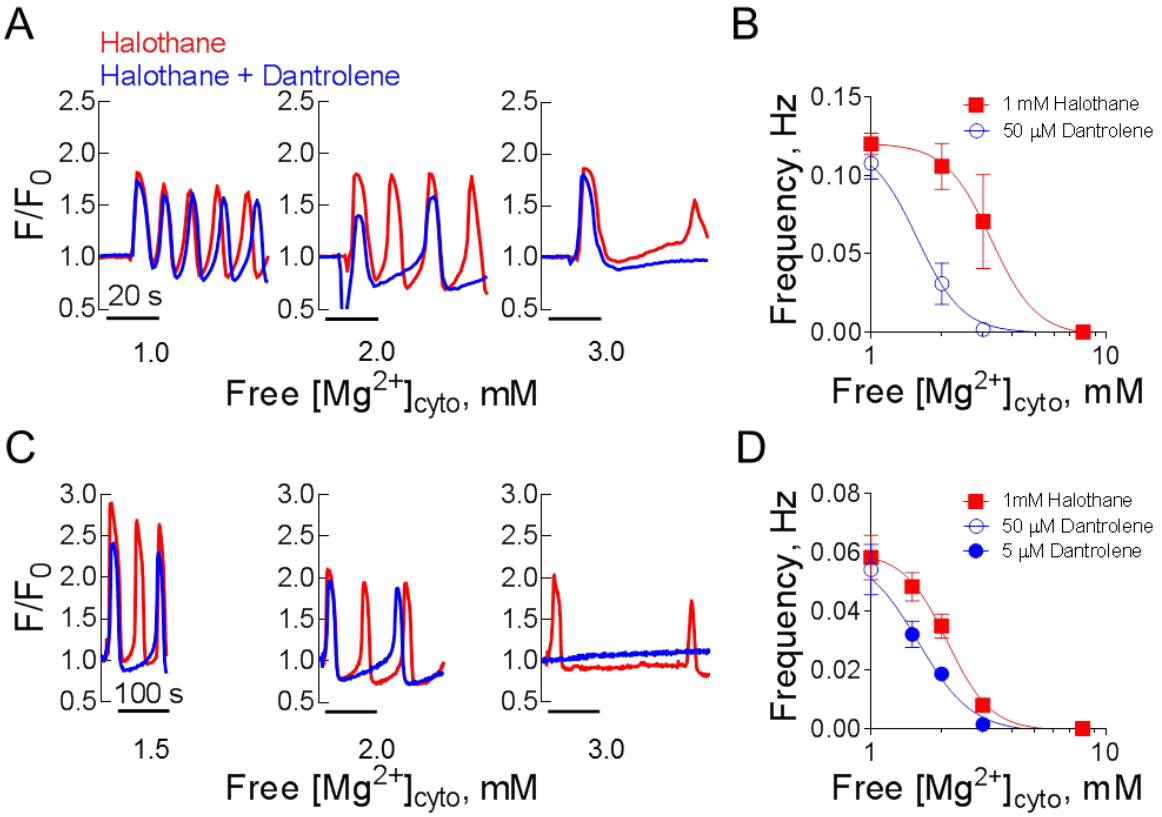

Figure 3.10 Dantrolene require raise $[Mg^{2+}]_{cyto}$ to slow frequency of halothane induced Ca^{2+} waves in human MHS skeletal muscle fibers.

(*A*) Examples of MHS fibers from subject A exposed to 1 mM halothane and 1, 2, and 3 mM $[Mg^{2+}]_{cyto}$ and the presence and absence of 50 µM dantrolene. (*B*) Examples of MHS fibers from subject B in the presence and absence of 5 µM dantrolene and 1 mM halothane. Data is summarized in (*C*) and (*D*) from a biopsy taken from subject A and subject B, respectively. The data were fitted with a Hill equation. The IC_{50} values are 3.2 ± 1.05 and 1.6 ± 1.06 mM (*C*) and 2.1 ± 1.05 and 1.6 ± 1.06 (*D*) in the presence of halothane and halothane plus dantrolene, respectively. Curves were significantly different from each other (extra sum of square *F* test). All data points are derived from 4-5 fibers and presented as mean ± SEM.

3.4 Discussion

In this section, I have examined the mechanism in which dantrolene is able to inhibit Ca^{2+} release from the RyR1. These results indicate that dantrolene and Mg^{2+} stabilize the closed state of the RyR1 to suppress Ca^{2+} release (Figure 3.6 and 3.10) (Laver *et al.*, 1997b; Duke *et al.*, 2002; Duke *et al.*, 2004). In this study on human MHS muscle fibers, low concentrations of halothane (~1 mM) induced a Ca^{2+} release event that took the form of a regenerative Ca^{2+} wave. Interestingly, dantrolene was ineffective at slowing down the periods between the waves at endogenous levels of Mg^{2+} and required raised levels of $[Mg^{2+}]_{cyto}$ (> 1.5 mM $[Mg^{2+}]_{cyto}$) to antagonise RyR1 activity, a condition inside the muscle fiber that is likely to arise during an MH episode.

3.4.1 Comparative look at the intact fibers and lipid bilayer studies

This study reconciles the apparent contradictory results obtained from intact muscle fibers (Leslie & Part, 1981; Szentesi *et al.*, 2001) and isolated RyR1s incorporated into lipid bilayers (Szentesi *et al.*, 2001; Diaz-Sylvester *et al.*, 2008; Wagner Ii *et al.*, 2014). The finding that dantrolene inhibition requiring physiologically relevant $[Mg^{2+}]_{cyto}$ (>1 mM) provides an answer to why dantrolene fails to inhibit Ca^{2+} currents in isolated RyR1s, where the measurements are commonly performed in the absence of or in low $[Mg^{2+}]_{cyto}$ (< 0.4mM $[Mg^{2+}]_{cyto}$). Note that the ionic conditions imposed in bilayer studies are not standardized between groups and commonly are done under conditions which favour channel activation (i.e., low $[Mg^{2+}]_{cyto}$, and high $[Ca^{2+}]_{SR\ \&\ cyto}$) (Lamb, 2000). This is a common practice in bilayer studies to induce measureable Ca^{2+} currents, which cannot be resolved in the presence of physiologically relevant $[Mg^{2+}]_{cyto}$ (Laver *et al.*, 2004). Here the function of dantrolene across this broad range of $[Mg^{2+}]_{cyto}$ was assessed by using skinned fibers, where the ionic environment could be rapidly and accurately manipulated. In conjunction with this technique, the RyR1 activity can also be assessed by directly imaging the Ca^{2+} dependent fluorescence that arises from RyR1 mediated Ca^{2+} release (Lamb & Stephenson, 1991; Lamb, 1993; Cully *et al.*, 2014).

The results from this chapter also demonstrate that dantrolene weakly stabilizes the closed state of the RyR and requires the presence of physiologically relevant Mg^{2+} to antagonize the channel (Figure 3.6, 3.7, and 3.10). Although this is certainly the case *in vivo* (Leslie & Part, 1981; Szentesi *et al.*, 2001), however, as demonstrated Figure 3.7 other channel stabilizers can be used in place of Mg^{2+}. The effect of dantrolene on RyR1 in

bilayers in the presence of CaM was only to lower open probability (P_o) to levels that would be equivalent to that with excessively leaky RyR1 in a muscle fiber. That is, if channel P_o is 1.0 during normal Ca^{2+} release in a muscle fiber, a Ca^{2+} flux close to 200 $mM \cdot s^{-1}$, and the normal resting RyR1 Ca^{2+} leak is about 5 $nM \cdot s^{-1}$ (Laver *et al.*, 2004; Baylor & Hollingworth, 2012; Bakker *et al.*, 2017) (which hence equates to a Po of $\sim 2.5 \times 10^{-8}$), then the P_o of 0.009 reported by Oo et al. under conditions of dantrolene and CaM still corresponds to a very large leak flux through the RyR1s of about 0.18 $mM \cdot s^{-1}$. Adding exogenous CaM in this study did not further inhibit the RyR1 even when the RyR1 was inhibited by 3 mM $[Mg^{2+}]_{cyto}$ (Figure 3.4 and 3.6). Therefore this suggests that either endogenous CaM remained bound in the preparation as shown previously (Rodney & Schneider, 2003), or more likely that Mg^{2+} is the main mechanism that stabilizes the closed state of the RyR1s *in vivo*. The observations made in this chapter and that made by Oo et.al (2015) suggests that the key factor in observing the inhibitory effect of dantrolene *ex vivo* is not the presence Mg^{2+}, nor CaM *per se* but it is the net inhibition of the RyR1 which needs to be met above a certain level in order for dantrolene to further inhibit the RyR1. Thus suggesting that dantrolene, $Mg^{2+,}$ and CaM work synergistically to stabilize the closed state of the RyR1.

3.4.2 Mechanism in which dantrolene arrest an MH episode

Dantrolene, even at a high concentration (50 µM), did not affect halothane-induced Ca^{2+} release in the presence of resting levels of $[Mg^{2+}]_{cyto}$ (Figure 3.10). Ca^{2+} waves induced by the action of halothane could only be supressed by dantrolene when the $[Mg^{2+}]_{cyto}$ was increased above its normal resting levels (Figure 3.10). Pre-administration of dantrolene prior to halothane did not affect this requirement for raised $[Mg^{2+}]_{cyto}$ (Figure 3.10). These results suggest that in a clinical setting, even if dantrolene were pre-administered to an MHS person undergoing general anaesthesia using halothane, $[Mg^{2+}]_{cyto}$ would still need to rise above its normal resting level of 1 mM for dantrolene to be effective. This requirement for raised $[Mg^{2+}]_{cyto}$ may not be necessary for the less volatile anaesthetics such as sevoflurane (Duke *et al.*, 2006), however, raised $[Mg^{2+}]_{cyto}$ indeed aids in dantrolene ability to arrest MH (Figure 3.10). A rise in muscle metabolites must precede any clinical symptoms of MH such as increasing body temperature, as they are a result of MgATP hydrolysis, which includes the defining heat production of the condition. Evidence for the rise of $[Mg^{2+}]_{cyto}$ during extensive muscle use is best documented during metabolic fatigue, which can be used as a model of metabolic changes inside the muscle

during over-active Ca^{2+} release under an MH trigger. It has been shown in human type II fibers that ATP is depleted in the order of seconds during maximal activity (Karatzaferi *et al.*, 2001). Similarly, we can expect that muscle contractures in an MH episode lead to major [ATP] decline. This decline of [ATP] significantly retards its capacity as the major cytoplasmic buffer of Mg^{2+}, causing a parallel rise in $[Mg^{2+}]_{cyto}$ (Westerblad & Allen, 1992). Indeed, increases in $[Mg^{2+}]_{cyto}$ to levels in the order of 1.5 to 3 mM are reached during metabolic fatigue (Westerblad & Allen, 1992; Allen *et al.*, 2008).

3.5 Concluding remarks

In summary, this chapter have shown that: (i) dantrolene acts by increasing the affinity of the RyR1 for Mg^{2+}; (ii) repetitive Ca^{2+} waves generated by halothane can occur even with $[Mg^{2+}]_{cyto}$ increased above resting levels; and that (iii) dantrolene requires the metabolite Mg^{2+} to adequately close the RyR1 and inhibit over-active Ca^{2+} release. Overall these results suggest that dantrolene is a poor antagonist of RyR1 activity, but one that is good enough to arrest MH, where the susceptibility to this condition arises from only a relatively minor decrease in RyR1 affinity for the endogenous inhibitory stabilizer Mg^{2+}. This study importantly points out limitations associated with studying the skeletal muscle RyR1 in an isolated system where the ionic conditions imposed are not physiological. Thus this highlights the necessity for a more sensitive measure of RyR1 activity. Chapter 5 of this thesis will investigate and characterize a system in which the RyR1 can be measured under near physiological conditions.

Chapter 4: Mechanism of Ca^{2+} wave propagation during an malignant hyperthermia event

4.1 Introduction

During an MH event, the RyR1 is activated by a volatile aesthetic causing a subsequent rise in cytosolic Ca^{2+} levels in the skeletal muscle. As the muscle works towards clearing the persistently high Ca^{2+}, heat is generated as a product of ATP hydrolysis. The physiological mechanisms involved in overactive Ca^{2+} release during an MH event are not well understood. As demonstrated in Chapter 3 and previously reported by Duke & Steele (2003, 2004) halothane induced Ca^{2+} transients takes the form of oscillating Ca^{2+} waves. Interestingly, oscillating Ca^{2+} wave patterns have been shown to have important roles in various signalling pathways in many cell types (reviewed by (Parkash & Asotra, 2012)). Notably, in cardiac muscle Ca^{2+} waves underlie an arrhythmogenic process in the heart (reviewed by Stuyvers 2000). This chapter will investigate the mode of Ca^{2+} wave propagation in human MHS muscle, which must also be considered a pathophysiological event.

The mechanisms involved in driving the propagation of a Ca^{2+} wave during an MH event in human skeletal muscle remains contested. Some argue for a CICR mechanism similar that observed in cardiac muscle (Endo, 1977; Duke *et al.*, 2003; Duke *et al.*, 2004; Steele & Duke, 2007; Endo, 2009). There is also evidence to suggest that Ca^{2+} wave propagation is modulated by a luminal SR Ca^{2+} activation site located on the RyR1, which either acts to directly activate the RyR1 or 'sensitizes' the RyR1 to be activated by cytosolic Ca^{2+} (Keller *et al.*, 2007; Maxwell & Blatter, 2012; Chen *et al.*, 2014). A similarity between these two proposed mechanisms is the involvement of Ca^{2+} as the trigger. If Ca^{2+} is indeed the trigger, the activation of propagating Ca^{2+} must be supported by sites in the cytosol or the SR network (Kort *et al.*, 1985; Dawson *et al.*, 1999; Figueroa *et al.*, 2012; Maxwell & Blatter, 2012; Cully *et al.*, 2014). It remains possible that both cytoplasmic and luminal sites support regenerative Ca^{2+} waves.

In this study, a CICR wave was defined by its 'classical' definition in which the released Ca^{2+} originating from one RyR1 couplon located on a junctional SR diffuses through the cytosol and then activates RyR1 Ca^{2+} release on adjacent junctional SR with little to no involvement of the SERCA pump. This mode of cytosolic wave propagation is best described by the 'fire-diffuse-fire' model (Keizer *et al.*, 1998; Dawson *et al.*, 1999).

This model describes the spatiotemporal evolution of the Ca^{2+} wave where the initial Ca^{2+} spark (fire) diffuses through the cytosol (diffuse) and activates adjacent RyR clusters. To differentiate a cytosolic propagating mechanism to one that involves the SR, luminal activation of the RyR1 incorporates both paradigms of SR luminal RyR1 ‘sensitization’ and direct luminal RyR1 activation by Ca^{2+} as both of these are luminal factors.

4.1.1 Aims

This chapter aims to clarify the mode of Ca^{2+} wave propagation during an MH event and determine if the Ca^{2+} release signal propagates through the cytosol or the SR. To accomplish this aim I first characterized Ca^{2+} wave properties in toad skeletal muscle, which is prone to CICR (reviewed in Chapter 1). These properties were then directly compared to the wave properties of human MHS skeletal muscle.

4.2 Methods

4.2.1 Experimental animals, human muscle biopsy, and muscle preparation

Muscle samples used in this Chapter includes the iliofibularis obtained from Cane toads (*Bufo marinus*) and human muscle biopsies collected from mid-portion of the vastus lateralis muscle. The procedure used for preparing the mechanically skinned fiber are described in detail in Chapter 2.1-2.4. Subjects diagnosed previously as MH susceptible via IVCT at The Royal Melbourne Hospital. Samples were obtained from a total of 4 MHS subjects. In some experiments, the SR was loaded with the cell permeant Ca^{2+} indicator fluo-5N-AM. The details of this procedure are described in Chapter 2.10.

4.2.2 Internal physiological solution

Table 4.1 shows in detail the ionic composition of the various internal solutions used in this study. The methods in preparing the internal physiological solution is described in detail in Chapter 2.5 and Chapter 3.2.2. In some experiments, the skinned fiber was exposed to an internal solution containing 0.5-1 mM halothane over a prolonged period (10-15 minutes) where the evaporation of halothane becomes appreciable. An evaporation rate of 9.6% min^{-1} was used to determine the approximate [halothane]. Details on measuring the evaporation rate of halothane in solution are described in Chapter 2.5 (Figure 2.3).

Table 4.1: Internal solution composition

Solutions	[EGTA]	Total [Ca]	Free [Ca^{2+}]	Total[Mg]	Free[Mg^{2+}]
	Concentration in mM				
Release solution: 0 Mg^{2+}, 271 nM Ca^{2+} (T)	0.1	0.048	0.000271	0	0
1 mM Mg^{2+}, 271 nM Ca^{2+} (T)	0.1	0.048	0.000271	8.5	1
3 mM Mg^{2+}, 271 nM Ca^{2+} (T)	0.1	0.048	0.000271	11.9	3
SR loading solution: 1 mM Mg^{2+}, 100 nM Ca^{2+}, 10 µM fluo-5N-AM, 10 µM FCCP, 0.05% pluronic detergent (H)	0.1	0.024	0.0001	8.5	0.92
1 mM Mg^{2+}, 100 nM Ca^{2+} (H)	0.1	0.024	0.0001	8.5	0.92
1.5 mM Mg^{2+}, 100 nM Ca^{2+} (H)	0.1	0.024	0.0001	9.6	1.5
2 mM Mg^{2+}, 100 nM Ca^{2+} (H)	0.1	0.024	0.0001	10.3	1.96
3 mM Mg^{2+}, 100 nM Ca^{2+} (H)	0.1	0.024	0.0001	11.8	2.98
1 mM Mg^{2+}, 100 nM Ca^{2+} , 10 mM EGTA (H)	10	2.425	0.0001	9.50	1
Release solution: 0 mM Mg^{2+}, 100 nM Ca^{2+} (H)	0.1	0.024	0.0001	0	0

Each solution contained (mM): K^+, 136; Na^+, 36; ATP, 8; creatine phosphate, 10; Hepes, 90 (H) or 60 (T); rhod-2, 0.01; BTS, 0.05; and HDTA 49.9 (H). Final pH was 7.1. The solution name in the left column represents the rounded value of free $[Mg^{2+}]_{cyto,}$ and free $[Ca^{2+}]_{cyto}$ in solutions and the value in the associated row represent the calculated values. The letters in parentheses (T) and (H) refer to solutions used for toad and human fiber experiments. Caffeine and halothane were added to these solutions as indicated in the text.

4.2.3 Confocal Imaging

These methods are described in Chapter 2.8. In addition to tracking the $[Ca^{2+}]_{cyto}$ as described in Chapter 3.2.4, in some experiments the free $[Ca^{2+}]_{SR}$ was recorded sequentially, line-by-line to produce two simultaneously acquired images. The fluorescent spectrum of rhod-2 and fluo-5N is shown in Figure 4.1*A,* and the process of acquiring sequential images on the point scanning confocal system is depicted in Figure 4.1*B*. Sequential excitation and emission collection of an individual fluorophore were done to minimize 'bleed-through' where the emission from the fluo-5N excited rhod-2. Imaging was performed at 22 ± 1 ^{o}C.

4.2.4 Calculation of free $[Ca^{2+}]_{SR}$

SR calcium dependent fluorescence was monitored with fluo-5N (Chapter 2.10). In each preparation, the $F_{maximum}$ and $F_{minnimum}$ were determined as described in Chapter 2.11. This was done to account for variation in fluo-5N dye loading between fibers. The free $[Ca^{2+}]_{SR}$ can be quantified from the fluorescent values using the determined $K_{D,Ca}$ ($K_{D,Ca}$ ~ 0.4 mM; Chapter 2.11) and the following relationship:

$$\text{Free SR } [Ca]_{(t)} = K_{d,Ca} \frac{F_{(t)} - F_{min}}{F_{max} - F_{(t)}} \quad (1)$$

where *F(t)* is the fluorescent value of fluo-5N at time (t).

A

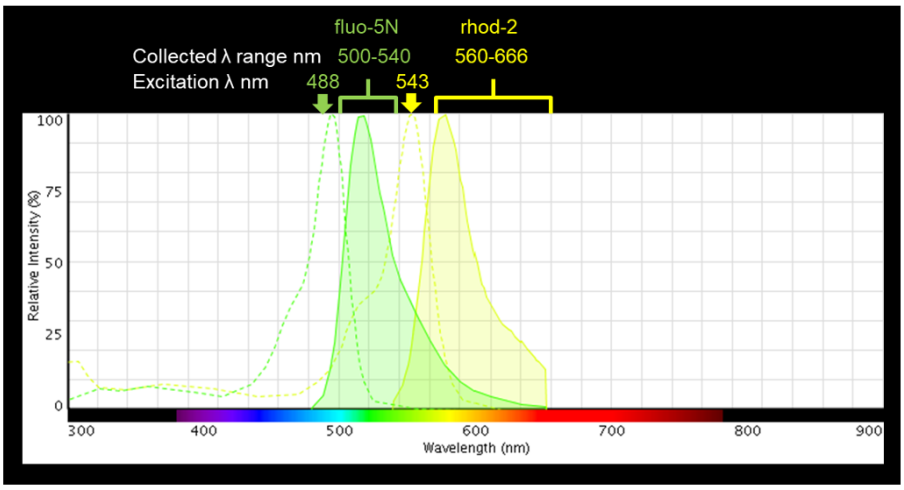

B

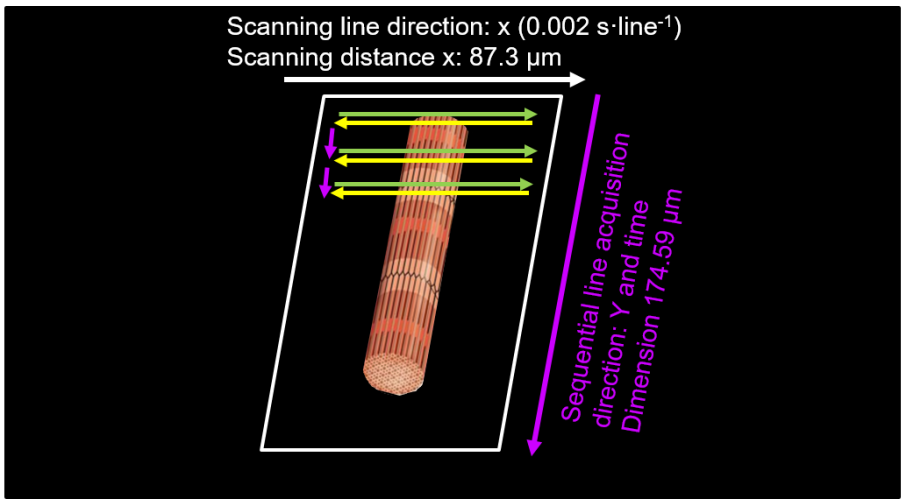

Figure 4.1 Sequential image acquisition of two fluorophores.

(*A*) Fluorescence spectral analysis of fluo-5N and rhod-2. The excitation and emission spectrum are shown as a dashed and solid line, respectively. Fluo-5N and rhod-2 were excited at 488, and 543 nm and the emission was collected in the 500-540 and 560-666 nm range, respectively. (*B*) Diagram depicting the sequential image acquisition of two laser lines throughout a series of x:y coordinates on a point scanning confocal system. In most experiments, continuous xyt imaging was performed with an aspect ratio (x:y) of 320:512 (87.3:174.59 µm) at an acquisition rate of 1.033 seconds·frame^{-1} and a pixel distance of 0.21 µm. Any deviation from these acquisition parameters is described in the text.

4.2.5 Confocal image analysis

Confocal image analysis employed in this chapter is described in Chapter 3.2.4. This analysis needed to take into account how the confocal image was built by the sequential scanning of lines (512 lines at 0.17 ms·line^{-1}). This scanning meant the long axis of the frame was space (y) and time. Figure 4.2 depicts the original confocal images of a mouse mechanically skinned fiber obtained during xyt recording with the respective fluorescent line averages shown below (this figure was modified from Cully et al. (2014). The propagation velocity (velocity=d/(t_1-t_2) and FDHM (horizontal double red arrows) of Ca^{2+} waves can be determined from this analysis. The period between waves was defined as the time between the peak amplitude of two successive waves.

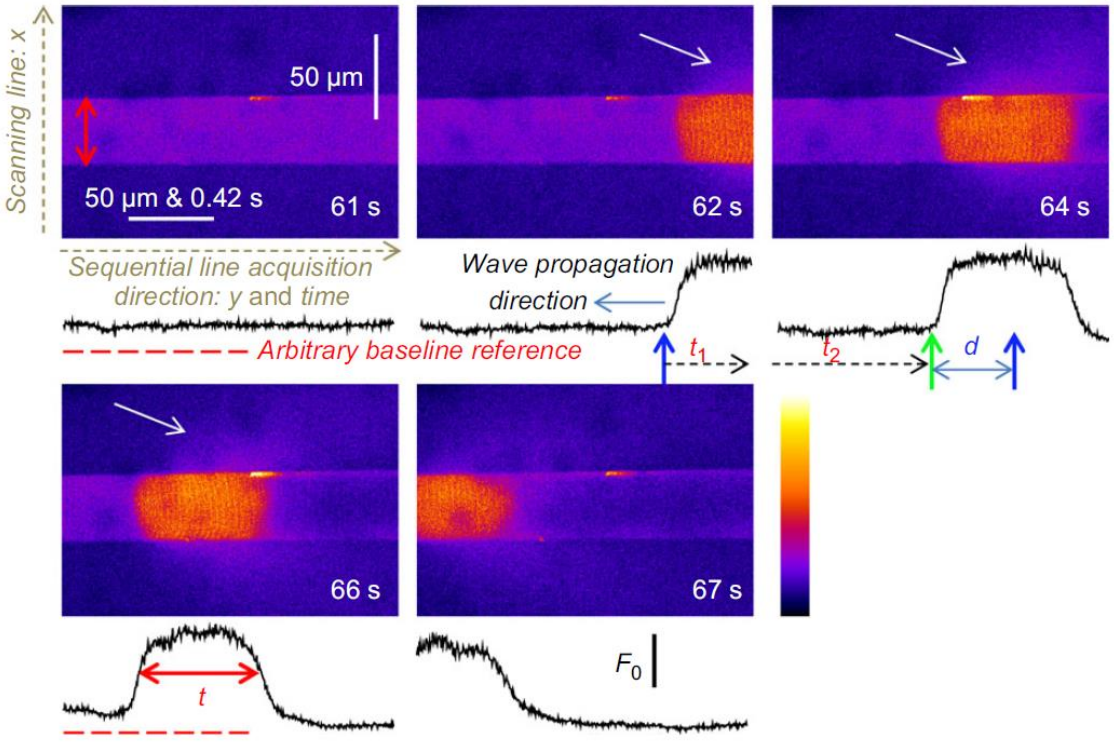

Figure 4.2 Image acquisition and analysis.

This figure showing the xyt imaging of Ca^{2+} dependent-rhod-2 fluorescence was modified from Cully et al. (2014). The spatially averaged profiles are indicated by the vertical double red arrow in the first image. The averaged line fluorescence is shown in black below the image. From the plotted profile the wave propagation velocity (Velocity=d/(t_1-t_2)) and FDHM (t, as indicated by the red horizontal double arrow) was determined. The white arrow indicates diffusion of Ca^{2+} from the preparation into the bathing solution.

4.3 Results

In order to understand the Ca^{2+} wave propagation mechanism in human MHS muscle, it was first necessary to investigate the much better understood toad muscle. Toad muscle possesses different RyR isoforms that support classic CICR. Thus, toad muscle defines how CICR-carried Ca^{2+} waves behave in skeletal muscle fibres. By applying RyR agonists (caffeine and halothane), the pattern of Ca^{2+} waves and the fronts of the waves will carry specific signatures of Ca^{2+} release activation characteristic for either a CICR or SR-mediated mechanism within the different muscle types. In this section, I will present images of Ca^{2+} waves in toad and human muscle challenged with caffeine or halothane and describe the properties of the events that drive Ca^{2+} release for wave propagation and regeneration.

4.3.1 The properties of Ca^{2+} waves in toad skeletal muscle

Figure 4.3*B* shows the normalized spatially average values of cytoplasmic rhod-2 fluorescence from a toad skinned fiber where a Ca^{2+} wave was induced by exposing the fiber to halothane (time of manual solution exchange indicated by the blue arrow). Similar to the repetitive Ca^{2+} waves observed in human MHS muscle fibers (Chapter 3.3.4); halothane induced an initial cell-wide Ca^{2+} release followed by a repetitive propagating Ca^{2+} wave (Figure 4.3*B*). Toad skeletal muscle has previously been demonstrated to be sensitive to low concentrations of RyR agonists even at physiological $[Mg^{2+}]_{cyto}$, which is not observed in mammalian skeletal muscle (Lamb *et al.*, 2001).

A selected image of a Ca^{2+} wave induced by halothane from Figure 4.3*B* traveling from left to right, as indicated by the horizontal white arrow is shown in Figure 4.3*A* (bottom, with the corresponding transmitted light image shown above). The dashed horizontal line indicates the edge of the skinned fiber. As shown, the Ca^{2+} wave-front in the direction of propagation spans across multiple sarcomeres with the wave-front at the top portion of the fiber (*a*) trailing behind the bottom (*b*). Note that the scanning line (2 $ms \cdot line^{-1}$) was parallel to the transvers axis of the fiber which ensure the propagating front of the Ca^{2+} wave is spatiotemporally resolved. That is, the propagating front of the wave at each y (fiber short axis) is scanned faster than the wave-front.

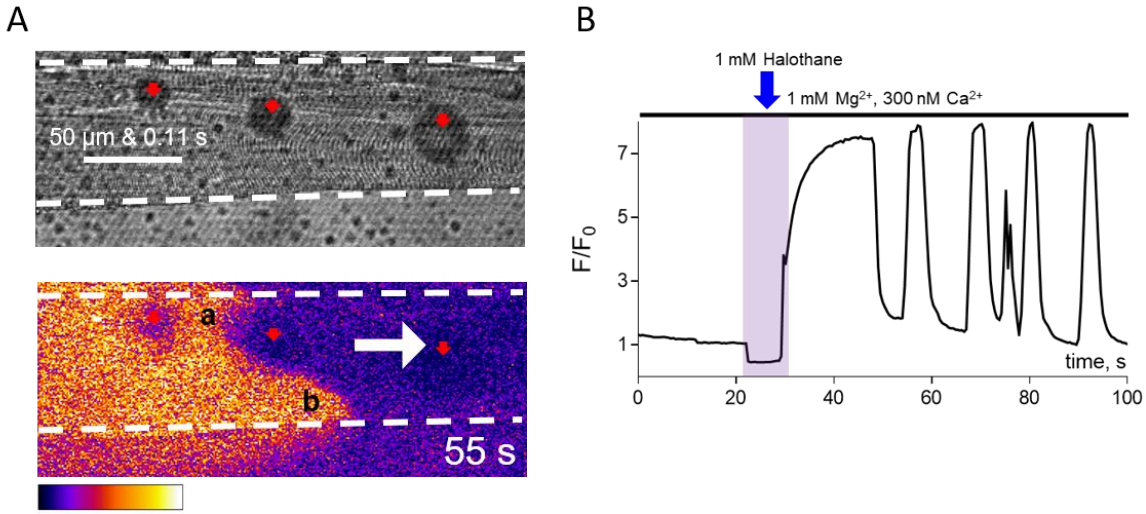

Figure 4.3 Halothane induced Ca^{2+} waves in toad skeletal muscle

(*A*) Selected image of cytoplasmic rhod-2 fluorescence (bottom) during continuous xyt recording (at a temporal resolution of ~0.841 s·frame^{-1}) in toad mechanically skinned fiber with the corresponding transmitted light image shown above. The dashed white lines indicate the borders of the skinned fiber. The white horizontal arrows indicate the direction of propagation of the Ca^{2+} wave and the red downward facing arrows indicates the location of oil droplets from the preparation. The time indicated in the figure was rounded to the nearest second. (*B*) The corresponding spatially averaged values (from within the borders of the preparations) of normalized fluorescence intensity (F/F_0) versus elapsed time from the experiment shown in *A*. Fibers were continuously bathed in 0.1 mM EGTA, 1 mM $[Mg^{2+}]_{cyto}$ and 300 nM $[Ca^{2+}]_{cyto}$. Manual solution exchange (the purple vertical bar indicating the movement artefact during solution exchange at ~22 s) replaced the bathing solution with a solution containing 1 mM halothane.

Two consecutive Ca^{2+} waves in a toad skinned fiber are shown in Figure 4.4. In this preparation, the initial Ca^{2+} wave (Wave 1) propagated along the fiber (left to right as indicated by the white arrow). Thereafter, a second wave (Wave 2) was observed moving in the opposite directions (right to left). Wave 2 showed similar properties in regards to the wave-front as Wave 1. The steep rise in rhod-2 fluorescence at the wave-front reflected the opening of RyRs and the concomitant release of Ca^{2+}. As the angle of the wave-front was significantly different to that of the line of RyRs at the SR terminal cisternae (assumed to be largely transverse across the fiber), we concluded that a sequential opening of RyRs occurred, continuously (in an unbroken fashion) across the line of RyRs. Importantly these series of images demonstrates that the Ca^{2+} wave-front propagates along the fiber on a distinctive angle.

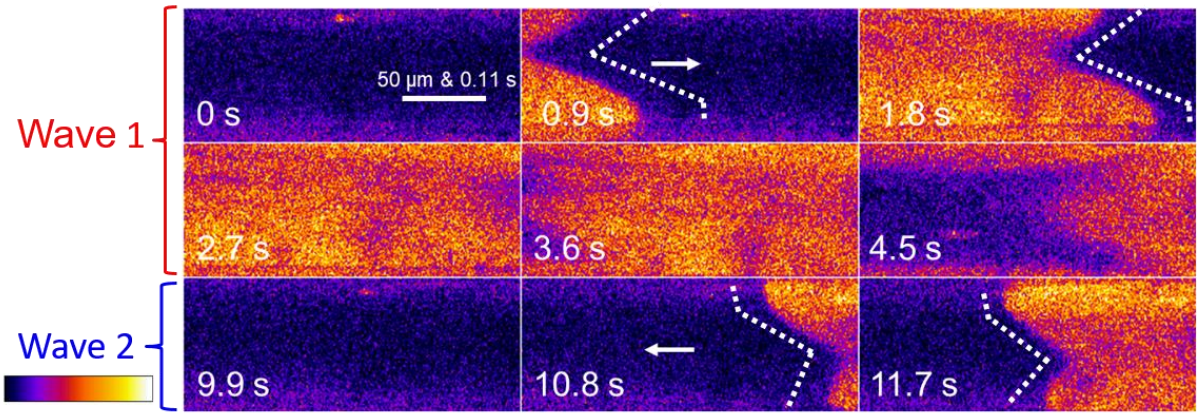

Figure 4.4 Angled Ca^{2+} wave-front observed in toad skinned fibers.

Selected images were taken of two Ca^{2+} waves (induced by 1 mM halothane) observed in a toad mechanically skinned fiber. Note that the two waves occurred consecutively. The white arrows shown at ~0.9 s and ~10.8 s indicate the direction of propagation. The dashed white lines illustrate the morphology of the Ca^{2+} wave-front. Images of cytoplasmic rhod-2 fluorescence were taken at a temporal resolution of ~0.841 s·frame^{-1} with the scanning line parallel to the transverse axis of the fiber. Fibers were continuously bathed in 0.1 mM EGTA, 1 mM $[Mg^{2+}]_{cyto}$ and 300 nM $[Ca^{2+}]_{cyto}$.

4.3.2 Origin of Ca^{2+} waves and angled wave-front in toad skinned fibers

As previously observed in cardiomyocytes, Ca^{2+} waves typically propagate along the long axis of the myocyte on an angle (Lukyanenko *et al.*, 1999; Kaneko *et al.*, 2000; Izu *et al.*, 2001; Okada *et al.*, 2005; Kashiyama *et al.*, 2010). This angled Ca^{2+} wave-front can be explained assuming a time delay of the Ca^{2+} release signal from the originating local source of release to the peripheral boundary of the fiber, as described by the 'fire-diffuse-fire' model (Keizer *et al.*, 1998; Dawson *et al.*, 1999). How this delay effects the morphology of the wave-front is important in understanding the mechanisms which drive the propagation of a Ca^{2+} wave. Description of the spatiotemporal changes in Ca^{2+} at the origin of the Ca^{2+} wave is of interest, as the delay of the release signal can be observed along both the transverse and longitudinal axis of the fiber. The origins of RyR activation can be concluded to be cytoplasmic or luminal.

Figure 4.5*A* shows a series of images where halothane triggered Ca^{2+} wave originated along the periphery of the toad skinned fiber (red arrows shown at 0.96 s) and then proceeded to propagate along both axes (note that the images shown here are from the same preparation as Figure 4.3). For this preparation, the scanning line was parallel to the longitudinal axis of the fiber. Interestingly, the Ca^{2+} wave appeared to be more compact along the transverse axis of the fiber. From the acquired images the propagation velocity along both axes can be determined as shown in Figure 4.5*B*. Thus, the delay of the Ca^{2+} release signal along the transverse axis of the fiber, in addition to the faster propagation velocity along the longitudinal axis produces a 'trailing' wave-front.

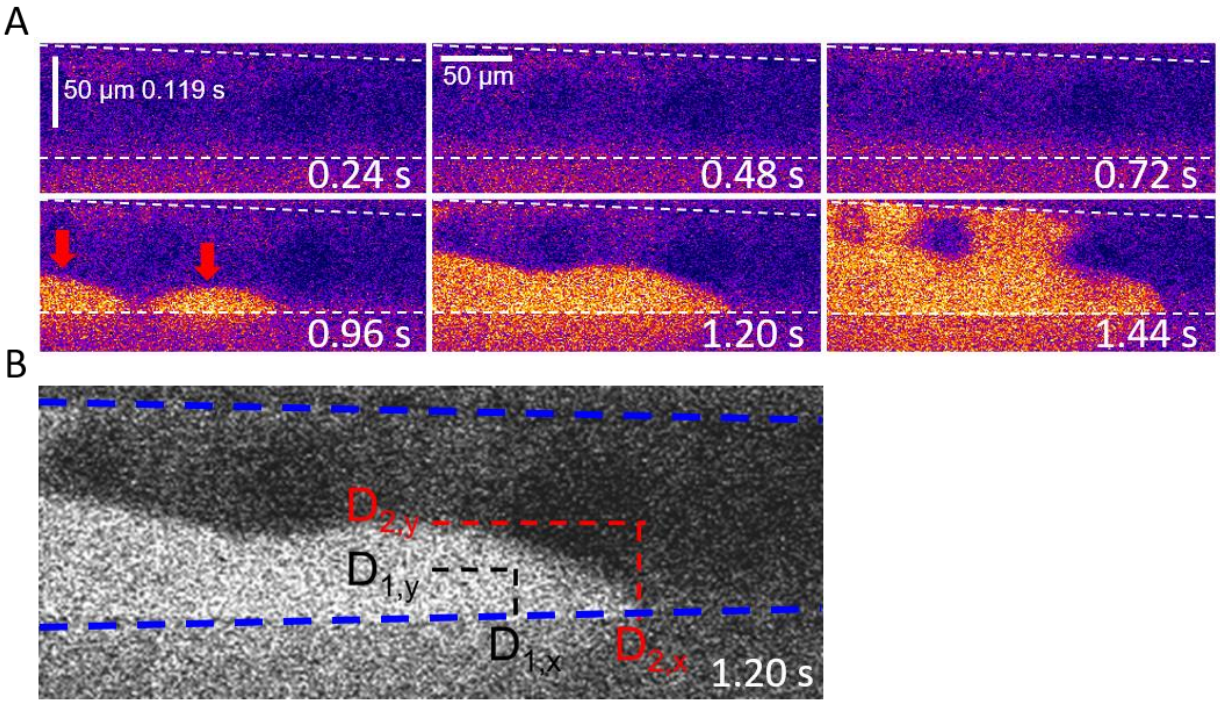

Figure 4.5 Origin of Ca^{2+} waves and angled wave-front in toad skinned fibers.

(*A*) Consecutive images depicting the origin of a Ca^{2+} wave (as indicated by the red arrow) in toad skinned fiber with the Ca^{2+} waves induced by 1 mM halothane. The white dashed lines indicate the borders of the skinned fiber. (*B*) The position of the Ca^{2+} wave at ~0.96 s as indicated by the dashed black lines were transposed over the position of the Ca^{2+} wave in the following image taken ~0.24 s (~1.20 s) later in time as indicated by the red dashed arrows. The velocity at the longitudinal and transverse axis of the fiber was calculated to be $((D_{2,x}-D_{1,x})/0.24)$ ~133 µm·s^{-1} and $((D_{2,y}-D_{1,y})/0.21)$ ~ 70 µm·s^{1}, respectively. The blue dashed lines indicate the borders of the skinned fiber. Fibers were continuously bathed in 0.1 mM EGTA, 1 mM $[Mg^{2+}]_{cyto}$ and 300 nM $[Ca^{2+}]_{cyto}$.

4.3.3 Propagation velocity of Ca^{2+} waves in toad skinned fibers is SR load dependent

Next, it was examined if the SR Ca^{2+} load would affect Ca^{2+} wave velocity, as previously described (Miura *et al.*, 1993; Miura *et al.*, 1999; Kaneko *et al.*, 2000; Okada *et al.*, 2005; Figueroa *et al.*, 2012; Petrovič *et al.*, 2015). Since the propagation of a Ca^{2+} wave through the cytosol is thought to surpass an activation threshold on adjacent RyR, it is reasonable to suggest that greater SR Ca^{2+} load will directly translate to a greater SR Ca^{2+} flux in addition to a greater RyR open probability and therefore will reach the threshold at a faster rate (Figueroa *et al.*, 2012). On a larger scale spanning multiple SR junctions, this will lead to a faster propagation velocity. Importantly, this correlation has been observed in cells that are prone to CICR and has not been observed in mammalian skeletal muscle (Miura *et al.*, 1993; Kaneko *et al.*, 2000; Figueroa *et al.*, 2012).

The steady reduction in [halothane], due to its volatile nature gives a unique opportunity to assess wave properties at differing agonist concentrations. Figure 4.6*A* shows the spatially averaged values of cytoplasmic rhod-2 fluorescence from a toad skinned fiber with the corresponding ionic conditions of the bathing solution shown above the trace. At time ~ 5 s, the bathing solution was exchanged for a solution containing 1 mM halothane. The halothane evaporation rate of 9.6% min^{-1} was used to calculate the approximate [halothane] over the course of the measurement (Figure 4.6*A*).

Multiple changes in the wave behaviour were observed with declining [halothane]: the first being an increase in the period between waves (comparing *a* and *b* as shown in Figure 4.6*A*). Importantly, an increase in wave period will increase the time for the SR to load Ca^{2+}. It is expected that during the 'refractory' period between two Ca^{2+} waves the RyR would remain in a closed state; since an open RyR during this period would not allow for Ca^{2+} to accumulate inside the SR. Note that this was not observed when the fibers were bathed in caffeine which represents a nearly constant [agonist] during the duration of the experiment, as shown later (Figure 4.11). From a series of experiments the following relationship between wave velocity and wave period (which can be used as an indicator of SR load) was derived as shown in Figure 4.6*B*. These results suggest that in toad skeletal muscle, the velocity of the Ca^{2+} wave is indeed SR load dependent, which is consistent with the involvement of a release mechanism that propagates through the cytosol via CICR.

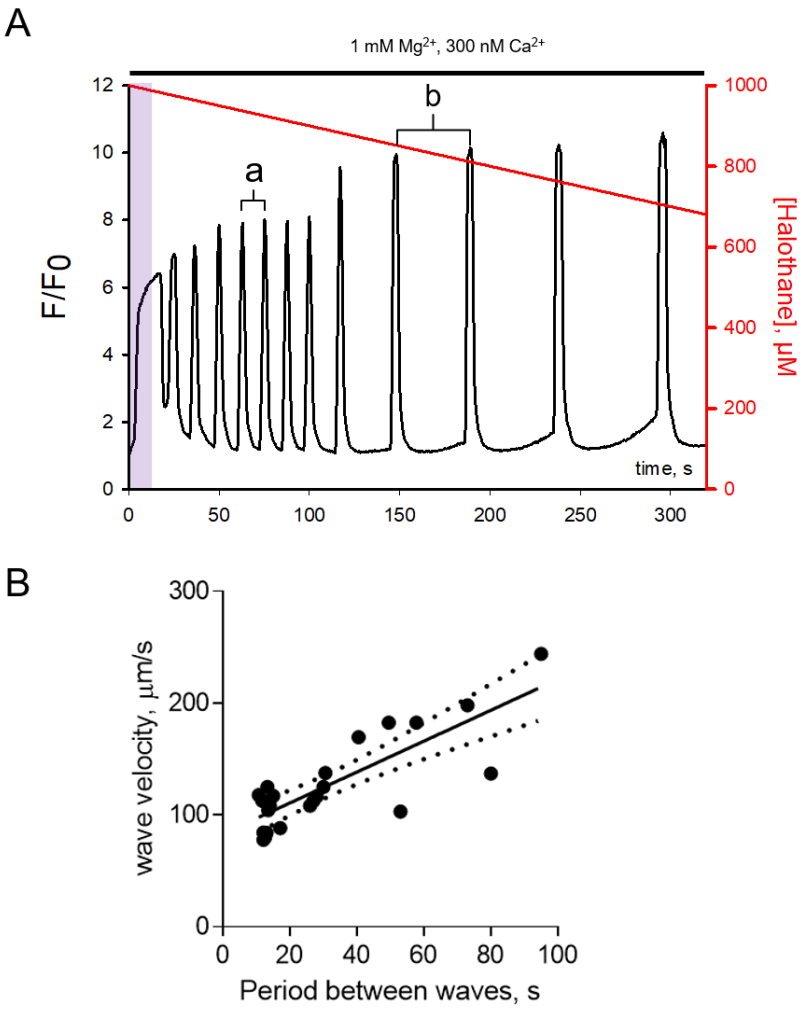

Figure 4.6 Velocity of the Ca^{2+} wave is SR load dependent in toad skeletal muscle.

(*A*) Spatially-averaged profile (F/F_0) of cytoplasmic rhod-2 fluorescence of toad skinned fiber where the fiber was exposed to 1 mM halothane as indicated by the vertical purple bar. The approximate [halothane] overtime is shown in red (right y axis). The change in wave-period over time which indicates a longer SR load time is highlighted in the figure (*a, b*). The fiber was in the constant presence of 0.1 mM EGTA, 1 mM $[Mg^{2+}]_{cyto}$ and 300 nM $[Ca^{2+}]_{cyto}$. (*B*) The data summarizing the relationship between Ca^{2+} wave velocity over varying SR loading periods. The data was fitted with a line (r^2=0.67) with the dotted line showing the 95% confidence interval. Data was collected from 5 skinned fibers obtained from 4 toads.

4.3.4 Cytosolic propagation of a CICR wave is abolished in raised Mg^{2+}

From previous works, it is understood that $[Mg^{2+}]_{cyto}$ is a competitive antagonist of the RyRs (Lamb & Stephenson, 1991; Laver *et al.*, 1997a). Therefore, raised $[Mg^{2+}]_{cyto}$ is expected to limit or slow the rate of CICR. Figure 4.7 shows three images of Ca^{2+} waves (induced by 1 mM halothane) propagating left to right (white arrow) at either 1 or 3 mM $[Mg^{2+}]_{cyto}$. Note that these images were taken from the same preparation. The two images shown at 1 mM $[Mg^{2+}]_{cyto}$ are waves produced at varying SR Ca^{2+} loads as demonstrated above. Consistent with the previous results shown above, the Ca^{2+} wave-front at 1 mM Mg^{2+} propagates at a distinct angle along the longitudinal axis of the fiber. An increase in wave velocity did not change this result. This result is contrasted to the uniform transverse wave-front that is observed at 3 mM $[Mg^{2+}]_{cyto}$. These uniformly transverse wave-fronts are similar to that observed in rat and mouse skeletal muscle where CICR is thought to not contribute an active mechanism of Ca^{2+} release (Figueroa *et al.*, 2012; Cully *et al.*, 2014).

It could be argued that although raised $[Mg^{2+}]_{cyto}$ is present in the bathing solution, halothane may still sensitize the RyR and increase the propensity to open through a CICR mechanism. Under the assumption that the origin of the Ca^{2+} wave was along the periphery of the fiber (as demonstrated in Figure 4.5), a uniform wave-front can be produced if the CICR signal propagated across the short axis of the fiber (~ 80μm) at a rate that is faster than the scanning line (~ 2 ms). This will equate to a CICR propagation rate of greater than (0.08 mm/ 0.002 s) 40 mm/s. This rate was not observed experimentally as shown previously in Figure 4.6 (even at conditions that favors an accelerated rate CICR). Furthermore as shown, an angled wave was still observed at accelerated rates of CICR (1 mM Mg^{2+}, bottom image).

In toad skeletal muscle two isoforms of the RyRs (α, β) are expressed in equal proportions and are thought to be activated by different mechanisms (Lai *et al.*, 1992; Sutko & Airey, 1996; Kashiyama *et al.*, 2010). The α-RyR is thought to be activated directly from the DHPR, whereas activation of the β-RyR is thought to be supported by CICR (Murayama & Ogawa; Shirokova & Rios, 1997; Murayama & Ogawa, 2001; Figueroa *et al.*, 2012). From previous studies where either toad α or β-RyR was expressed in myotubes, and a Ca^{2+} wave was induced by caffeine, it was found that angled waves were only observed in myotubes expressing the more CICR prone β-RyR (Kashiyama *et al.*, 2010). Interestingly, the α-RyR expressing myotubes produced a

uniform wave front similar to that observed in 3 mM $[Mg^{2+}]_{cyto}$. This suggests that in toad skeletal muscle where both α and β-RyR are expressed, the resulting Ca^{2+} wave was due to a combined mode of propagation. Therefore, the angled wave-front observed at 1 mM $[Mg^{2+}]_{cyto}$ is likely due to CICR and the straight wave-front is likely a property of a Ca^{2+} wave which is CICR independent.

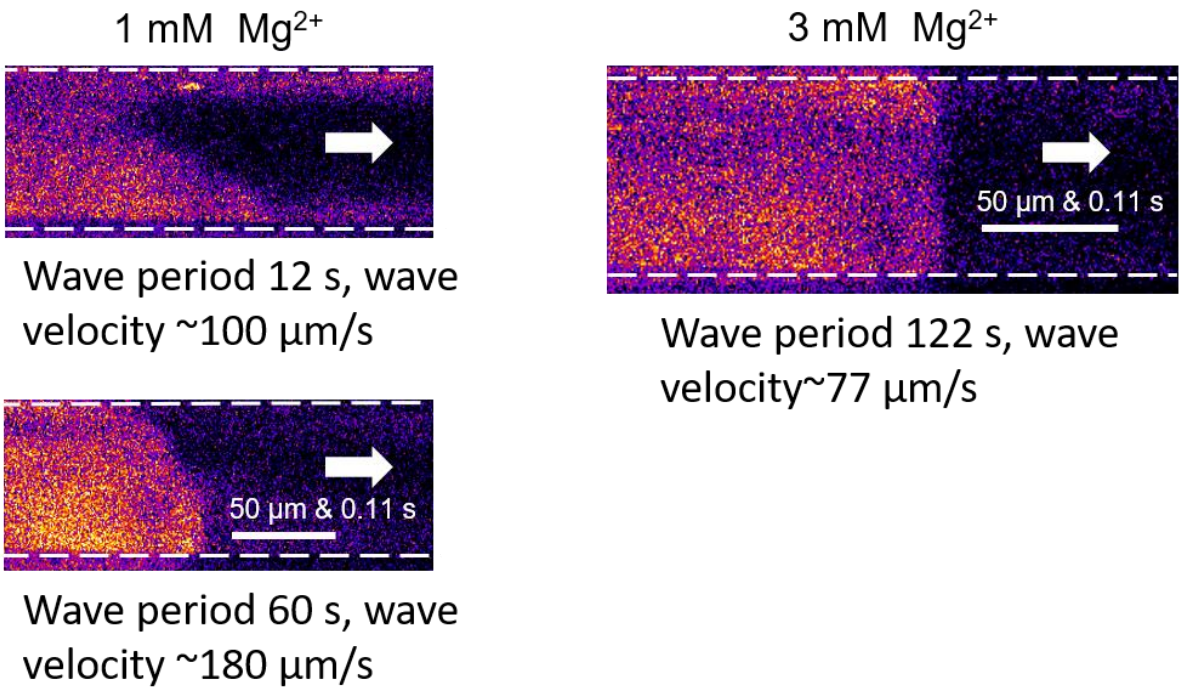

Figure 4.7 Inhibition of CICR by raised $[Mg^{2+}]_{cyto}$ produced a uniform wave-front.

Selected images taken from the same preparation showing the wave-front produced in toad skinned fibers by varying SR Ca^{2+} loads (indicated by the wave period) and varying $[Mg^{2+}]_{cyto}$ (1-3 mM; left and right, respectively). The Ca^{2+} wave was generated by exposing the fiber to 1 mM halothane. The white dashed lines indicate the borders of the skinned fiber and the white arrow indicates the direction of propagation. The toad skinned fiber was bathed in 300 nM $[Ca^{2+}]_{cyto}$.

4.3.5 'Classic' CICR wave properties not observed in halothane induced Ca^{2+} waves in human MHS muscle

The previous experiments demonstrated a likely involvement of CICR in the propagation of Ca^{2+} waves in toad skeletal muscle. In addition, the flat wave-front observed at raised $[Mg^{2+}]_{cyto}$ suggest that another mechanism is involved in driving the propagation of a Ca^{2+} wave in the absence of CICR. Next, by comparing the Ca^{2+} wave properties in human MHS muscle to that of toad, it was determined if halothane induced Ca^{2+} waves in human MHS fibers also propagate through a CICR mechanism or not. Similar to the experiments on toads, Ca^{2+} waves in human MHS muscles was induced by exposing the fiber to either halothane or caffeine (as indicated in the text).

Figure 4.8*A* shows the spatially averaged profile of rhod-2 fluorescence within the borders of a skinned fiber isolated from a human MHS subject. The fiber was initially bathed in a 100 nM $[Ca^{2+}]_{cyto}$, 1 mM $[Mg^{2+}]_{cyto}$ physiological solution before exposing the fiber to 0.5 mM halothane (~10 s). The continuous series of images taken from this experiment (from 16-26 seconds at an acquisition rate of ~1 $s \cdot frame^{-1}$) is shown in Figure 4.8*B*. In this series of images, the Ca^{2+} transient began as a local diffuse rise in Ca^{2+} before the rapid onset of a Ca^{2+} transient (22.7 s). This can be more clearly observed by plotting the fluorescent line averages over the distance of the imaged section of the skinned fiber (Figure 4.8*C*). As shown, the diffuse rise in Ca^{2+} is in the region of the fiber where the Ca^{2+} wave will originate. In the multiple fibers tested the origin of the Ca^{2+} release event was either centrally located in the fiber or synchronous across the short axis of the fiber.

Similar diffuse release behavior was observed when the preparation was challenged with raised $[Mg^{2+}]_{cyto}$ (3 mM; Figure 4.9*A* indicated by the green arrow). Note that raised $[Mg^{2+}]_{cyto}$ would shift the expected activating concentration of Ca^{2+} of the RyR1 to levels far above that observed during these diffuse Ca^{2+} release events. These diffuse release events were also observed in a previous study in mouse skeletal muscle where the release of Ca^{2+} was induced by lowering the $[Mg^{2+}]_{cyto}$ to 0.01 mM, a condition that would increase the likeliness of a CICR event due to reduced Mg^{2+} competition (Cully *et al.*, 2014). These observations indicate that CICR did not occur; even under favorable conditions for cytosolic Ca^{2+} activation (Cully *et al.*, 2014). Therefore, collectively these

results suggest that the initiation of a Ca^{2+} wave induced by halothane in MHS muscle is probably not due to CICR.

Another observation shown at ~ 20.6 s (Figure 4.8*C*) was that the average fluorescence was greater along the borders of the fiber in comparison to the central region (as indicated by the green arrow). Similar to previous results (Chapter 3, Figure 3.3), the 'undershoot' of the Ca^{2+} dependent fluorescence is likely due to the slow diffusion of Ca^{2+} from the bathing solution to the central portion of the fiber due to a standing Ca^{2+} gradient created by the activity of the SERCA pump. Therefore under these experimental conditions, the outer portions of the fiber are exposed to a higher [Ca^{2+}] for longer periods relative to the central portion of the fiber. If CICR were the driving mechanism to initiate a Ca^{2+} wave in mammalian muscle, it would be expected that the outer portion of the fiber would initiate a Ca^{2+} wave (similar to the observed results in toad muscle, Figure 4.5).

The morphology of a typical halothane-induced Ca^{2+} wave-front as observed in human MHS fiber is shown in Figure 4.9*B*. The wave-front was nearly perpendicular to the long axis of the fiber. A close inspection of the front of the Ca^{2+} wave corresponding to the top and bottom of the fiber revealed that the wave-front at the bottom portion (b) of the fiber is 10 µm ahead of the top (a). This may indicate that the Ca^{2+} wave-front is propagating at an angle, similar to that observed in toad skeletal muscle (Figure 4.3-4.4). However, since the scanning line was parallel to the longitudinal axis of the fiber in this experiment, it was important to consider how this may skew the position of the Ca^{2+} wave-front. Taking into account the effects of the line by line confocal image acquisition, the Ca^{2+} wave front was found to be virtually perpendicular to the longitudinal axis to the fiber (demonstrated in the figure legend; Figure 4.9*B*). This result was in contrast to the angled wave-front observed in toad fibers (Figure 4.3–4.4).

A flat wave-front was observed across multiple fibers and at varied $[Mg^{2+}]_{cyto}$ (1-3 mM) in human MHS fibers. The flat wave-front was also observed in previous studies in rat skeletal muscle at low cytosolic [Mg^{2+}] (~0.01 mM) (Cully *et al.*, 2014). The morphology of the wave-front suggests that the Ca^{2+} release was synchronous across the line of RyR1s at the SR terminal cisternae. The relatively slow propagation velocity observed here (43 $\mu m \cdot s^{-1}$) is incompatible with the release mechanism occurring through CICR. As demonstrated in toad fibers, the propagation velocity can change the morphology of the Ca^{2+} wave-front (Figures 4.7), with slower propagating waves producing an increasing angled wave-front. This observation is consistent with a propagating

mechanism occurring through the cytosol via CICR (Dawson *et al.*, 1999; Coombes *et al.*, 2004; Figueroa *et al.*, 2012). Therefore, if CICR is an active mechanism in human MHS fibers the relatively slow propagation velocity would also be expected to produce an angled wave-front.

These results collectively suggest that cytosolic propagation defined by the 'classic' release mechanism of CICR plays little to no role in the propagation mechanism of a Ca^{2+} wave during an MH event.

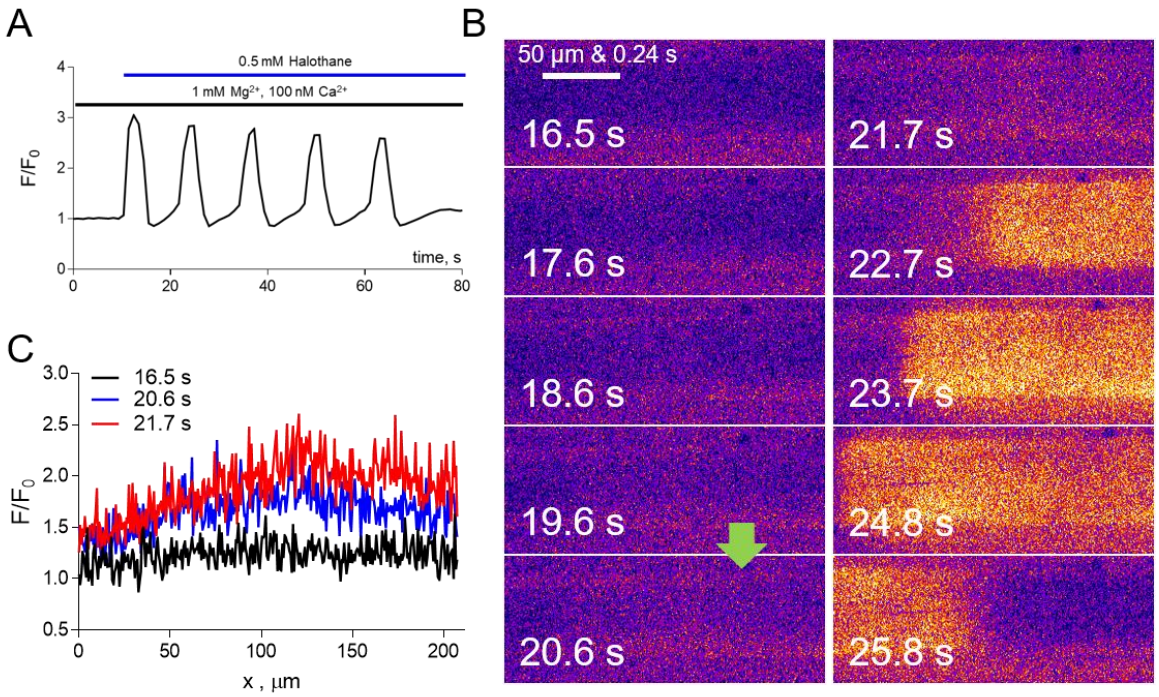

Figure 4.8 Diffuse Ca^{2+} release events observed proceeding the generation of a Ca^{2+} wave in human MHS muscle.

(*A*) Spatially-averaged profile (F/F_0) of cytoplasmic rhod-2 fluorescence of human MHS skinned fiber where the fiber was exposed to 0.5 mM halothane at ~10 s. The fiber was bathed in the constant presence of 0.1 mM EGTA, 1 mM $[Mg^{2+}]_{cyto}$ and 100 nM $[Ca^{2+}]_{cyto}$. (*B*) The corresponding consecutive images are demonstrating a diffuse rise in Ca^{2+} before the onset of a Ca^{2+} wave. The increased Ca^{2+} dependent fluorescence along the borders of the fiber is highlighted by the green arrow. (*C*) Fluorescent line averages over the distance of the fiber taken at 3 time points from the series of images shown in *B*.

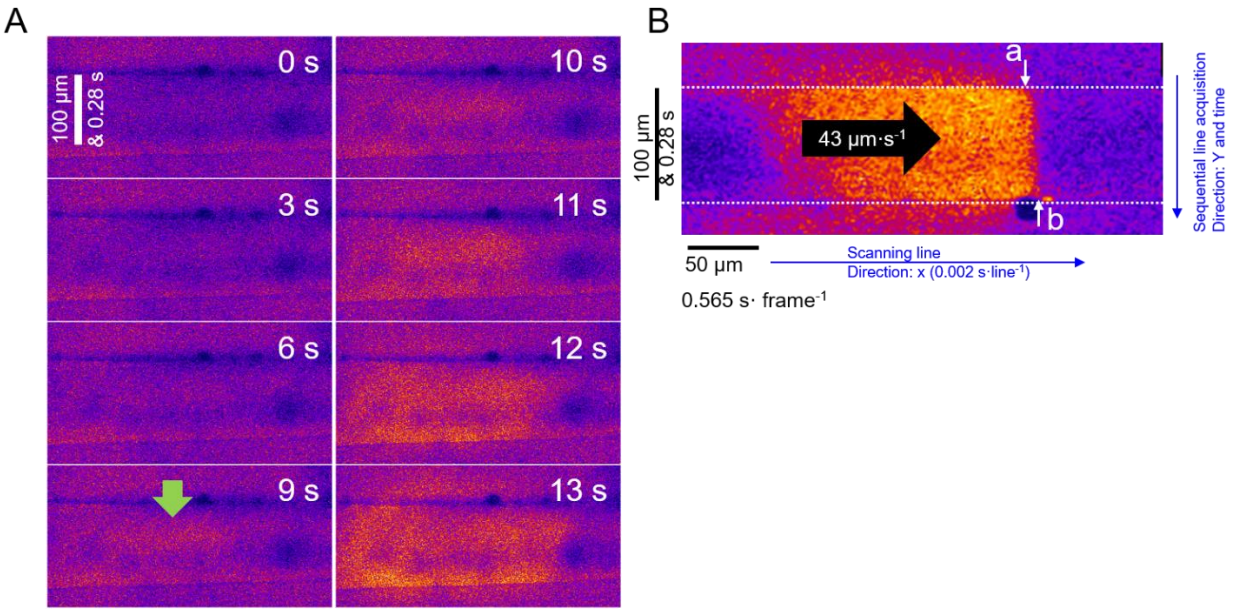

Figure 4.9 Diffuse Ca^{2+} release events observed proceeding the generation of a Ca^{2+} wave in human MHS muscle cont.

(*A*) Series of selected images of a Ca^{2+} wave in human MHS muscle in the presence of 3 mM $[Mg^{2+}]_{cyto,}$ 100 nM $[Ca^{2+}]_{cyto}$, and 1 mM halothane. The green arrow highlights the location of the diffuse Ca^{2+} release event. (*B*) Selected image of rhod-2 Ca^{2+} dependent fluorescence depicting the uniform wave-front observed in human MHS muscle. The fiber was bathed continuously in 100 nM $[Ca^{2+}]_{cyto}$, 0.1 mM EGTA, and 1 mM $[Mg^{2+}]_{cyto}$. The Ca^{2+} wave was induced by exposing the fiber to 1 mM halothane. The dashed white lines indicate the borders of the fiber and the white arrows indicate the position of the Ca^{2+} wave at two distinct time points (a,b) separated by ~0.28 s. The distance separating these two points along the x axis is approximately 10 µm. Taking into account the 0.23 s delay between the confocal image acquisition of the top and bottom portions of the fiber and the average propagation rate of the Ca^{2+} wave-front, the 'actual' position of the Ca^{2+} wave-front along the bottom is (0.23 s·43 µm·s^{-1}) 10.58 µm behind its current position as shown in the figure. Correcting for the time delay in acquiring images in this manner revealed that the wave-front is nearly perpendicular to the longitudinal axis of the fiber.

4.3.6 Ca^{2+} wave velocity is not SR load dependent in human MHS muscle

Next, it was examined whether increased SR Ca^{2+} loads would affect wave velocity in human MHS muscle fibers. Figure 4.10*A* and Figure 4.11*A* show the normalized rhod-2 fluorescence (F/F_0) of an isolated human MHS fiber, where a Ca^{2+} wave was induced by either halothane or caffeine, respectively. Prolonged exposure to the preparation to halothane caused a gradual increase in the period of the waves (Figure 4.10*A*). The corresponding selected images from Figure 4.10*A* are shown in Figure 4.10*B*. These selected images show that the duration of the Ca^{2+} wave (indicated by the horizontal white arrow) gradually increased from points *a* to *b* which suggest a greater SR load in the latter. Interestingly, the increased time to load the SR (6 s and 39 s for the wave observed at *a* and *b,* respectively) did not result in accelerated wave velocity. Note that change in wave period was not observed when the [agonist] was kept constant, which would be the case for a solution containing caffeine Figure 4.11*A*. The range of the acquired values for wave periods for the two agonists are summarized in Figure 4.11*B*.

The change in wave velocity over increasing SR Ca^{2+} loads is summarized in Figure 4.11*C*. These results suggest that the velocity of the Ca^{2+} wave was not dependent on the SR Ca^{2+} load, nor was it dependent on the RyR1 release flux (which is expected to increase with increasing SR loads due to the increased driving force of Ca^{2+} (Figueroa *et al.*, 2012)). The propagation of a CICR wave is expected to accelerate with increasing Ca^{2+} flux due to reduced time to reach a Ca^{2+} activation threshold on adjacent or RyRs. Therefore, these results are also at odds with the propagation mechanism being driven by CICR.

The propagation velocity remained comparable between varying SR loads. The 'speed-limit' of the wave velocity may be due to the diffusional properties of Ca^{2+}. That is, Ca^{2+} release from RyR1s along a single junctional SR cannot be initiated until the arrival of the 'release-trigger' from adjacent RyR1s. The following sections investigated the possible mode of propagation of the Ca^{2+} release trigger, and determine the contributions of both luminal and cytosolic Ca^{2+}.

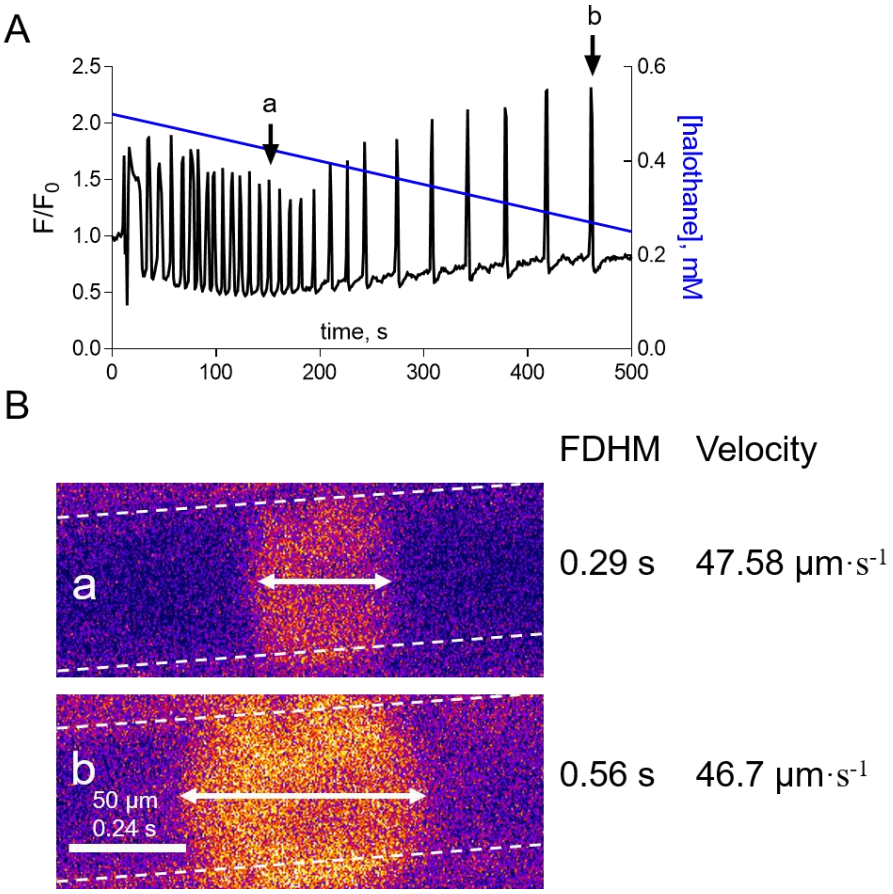

Figure 4.10 Velocity of the Ca^{2+} wave is human MHS muscle is not SR load dependent.

(*A*) Spatially-averaged profile (F/F_0) of cytoplasmic rhod-2 fluorescence of human MHS skinned fiber where the fiber was exposed to either 0.5 mM halothane as indicated by the vertical purple bar. The approximate [halothane] over time is shown in blue (right y axis). The fiber was bathed continuously in 100 nM $[Ca^{2+}]_{cyto}$, 0.1 mM EGTA, and 1 mM $[Mg^{2+}]_{cyto}$. (*B*) Selected images of Ca^{2+} waves observed in *A* at time points *a* and *b*. The horizontal dashed lines show the borders of the skinned fiber and the white double-sided arrows shows the duration of the Ca^{2+} wave.

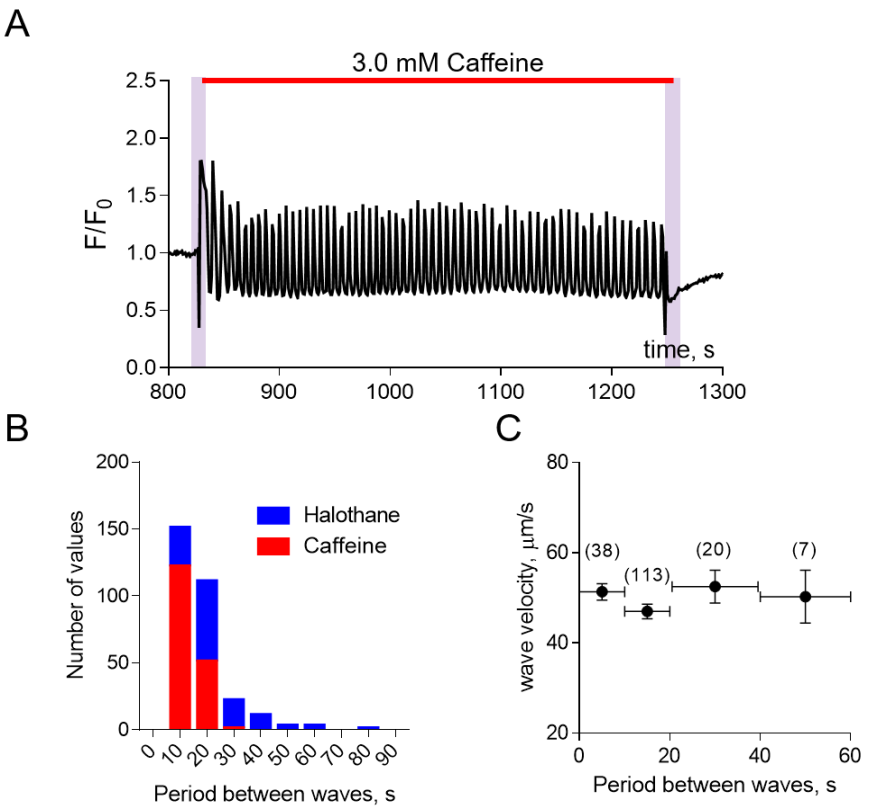

Figure 4.11 Velocity of the Ca^{2+} wave is human MHS muscle is not SR load dependent cont.

(*A*) Spatially-averaged profile (F/F_0) of cytoplasmic rhod-2 fluorescence of human MHS skinned fiber exposed to 3 mM caffeine as indicated by the vertical purple bar. The fiber was bathed continuously in 100 nM $[Ca^{2+}]_{cyto}$, 0.1 mM EGTA, and 1 mM $[Mg^{2+}]_{cyto}$. As shown, the duration of the Ca^{2+} wave remains constant in the presence of 3 mM caffeine throughout the recording. These experiments were repeated on additional 5 fibers. The duration of time the fiber was exposed to either halothane or caffeine remained constant (~10 mins). (*B)* Histogram depicting the range of wave periods observed with either halothane (blue) or caffeine (red). (*C*) Data summarizing the relationship between Ca^{2+} wave velocity over varying SR load (induced by caffeine and halothane). The wave period was binned along the x-axis, and the number of measurements are shown above. All data presented as mean ± SEM. The mean velocity observed at 1 mM $[Mg^{2+}]_{cyto}$ was approximately 54.3±2 $\mu m \cdot s^{-1}$ (n=38). However, a slower propagation velocity was observed at 3 mM $[Mg^{2+}]_{cyto}$ (19.7 ± 4.3 $\mu m \cdot s^{-1}$ (n=8)).

4.3.7 Propagation of Ca^{2+} waves is dependent on the luminal SR Ca^{2+}

Next, the contribution of luminal SR Ca^{2+} in the propagation mechanism of a Ca^{2+} wave was investigated. It was previously found that the activation of MHS causative RyR variant by halothane was dependent on the luminal SR Ca^{2+} reaching above an 'store-overload induced Ca^{2+} release (SOICR) threshold' (Jiang *et al.*, 2008; Chen *et al.*, 2017).

To directly assess the contribution of luminal SR Ca^{2+} in activating a Ca^{2+} wave, the SR in human MHS muscle was monitored with the Ca^{2+} indicator fluo-5N (Figure 4.12*A* *right*). The cytosolic rhod-2 fluorescence was acquired sequentially (Figure 4.12*A* *left*). Figure 4.12*B* shows the normalized fluorescent ratio of rhod-2 (red trace) and the free $[Ca^{2+}]_{SR}$ measured by fluo-5N in a human MHS muscle preparation treated with 1 mM halothane (the spatially averaged profile was taken within the borders of the white box as indicated in Figure 4.12*A*). As shown, each Ca^{2+} release event observed in the cytosol corresponded to a drop in the free $[Ca^{2+}]_{SR}$. The free $[Ca^{2+}]_{SR}$ levels at early time points of the recording (20-100 s) nearly recovered back to its original levels before the onset of another Ca^{2+} wave. Interestingly, as the apparent [halothane] in the solution reduced over time (blue trace) the free $[Ca^{2+}]_{SR}$ immediately before the depletion gradually increased in a time dependent manner (white dashed lines indicates the increase in free $[Ca^{2+}]_{SR}$ over time). Note that the cytosolic levels before the onset of the Ca^{2+} transient remained comparable throughout the recording. The gradual rise in free $[Ca^{2+}]_{SR}$ over time was not observed when the fiber was treated with caffeine; suggesting that the conditions required to produce a propagating wave did not change over time (Figure 4.13*A* and comparisons of the two agonists are shown in Figure 4.13*B*). These results demonstrate that raised free $[Ca^{2+}]_{SR}$ is required to initiate a Ca^{2+} wave at reduced [halothane]. Thus, suggesting that the SOICR threshold increased with declining [halothane].

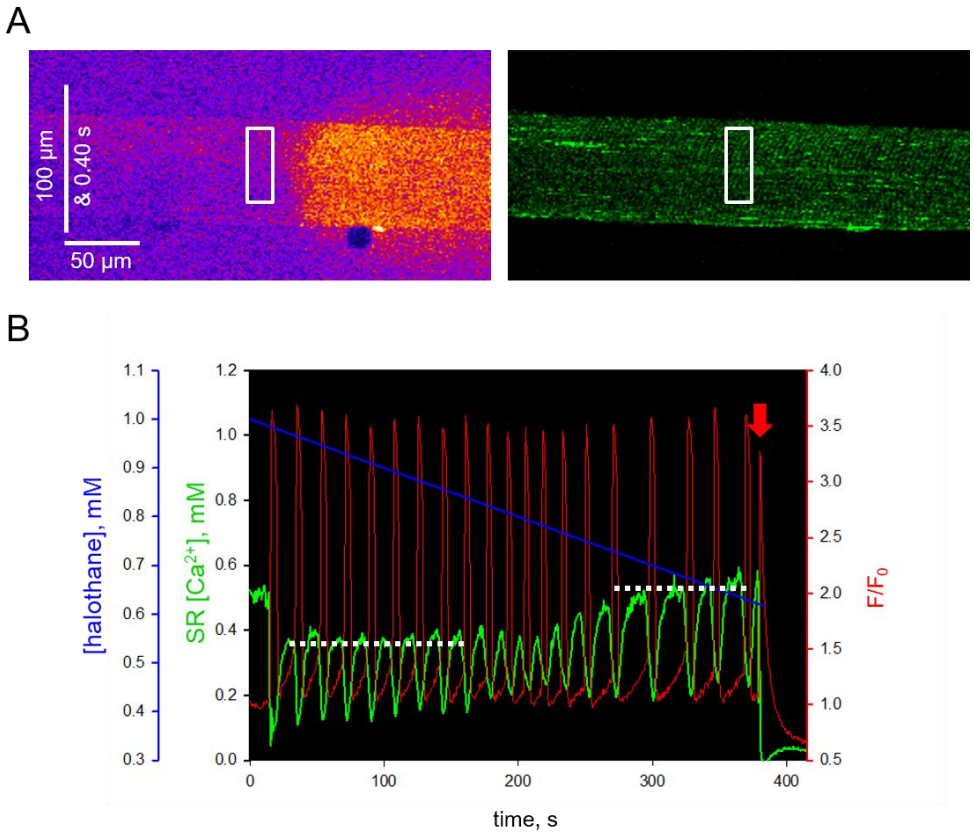

Figure 4.12 Decrease in [Halothane] increased the 'SOICR' threshold necessary to initiate a Ca^{2+} wave.

(*A*) Selected image of cytoplasmic rhod-2 and SR- fluo-5N fluorescence (left and right, respectively) during continuous xyt recording in human MHS mechanically skinned fiber (temporal resolution of ~0.625 s·frame^{-1}). (*B*) The corresponding spatially averaged values (within the borders of the white box shown in *A*) of normalized fluorescence intensity (F/F_0) and converted free $[Ca^{2+}]_{SR}$. Fibers were continuously bathed in 0.1 mM EGTA, 1 mM $[Mg^{2+}]_{cyto}$ and 100 nM $[Ca^{2+}]_{cyto}$ then by manual solution exchange the bathing solution was replaced with a solution containing 1 mM halothane (~ 10 s). The blue trace shows the approximate [halothane] over time. At the end of the recording, the fiber was exposed to a physiological solution containing 0 mM Mg^{2+} and 30 mM caffeine (as indicated by the red arrow) to maximally empty the SR of Ca^{2+}. The thorough depletion of the SR is a value lower than the value that the SR depletion terminated at during any of the Ca^{2+} waves. Thus, the SR is depleted to submaximal levels during each Ca^{2+} transient.

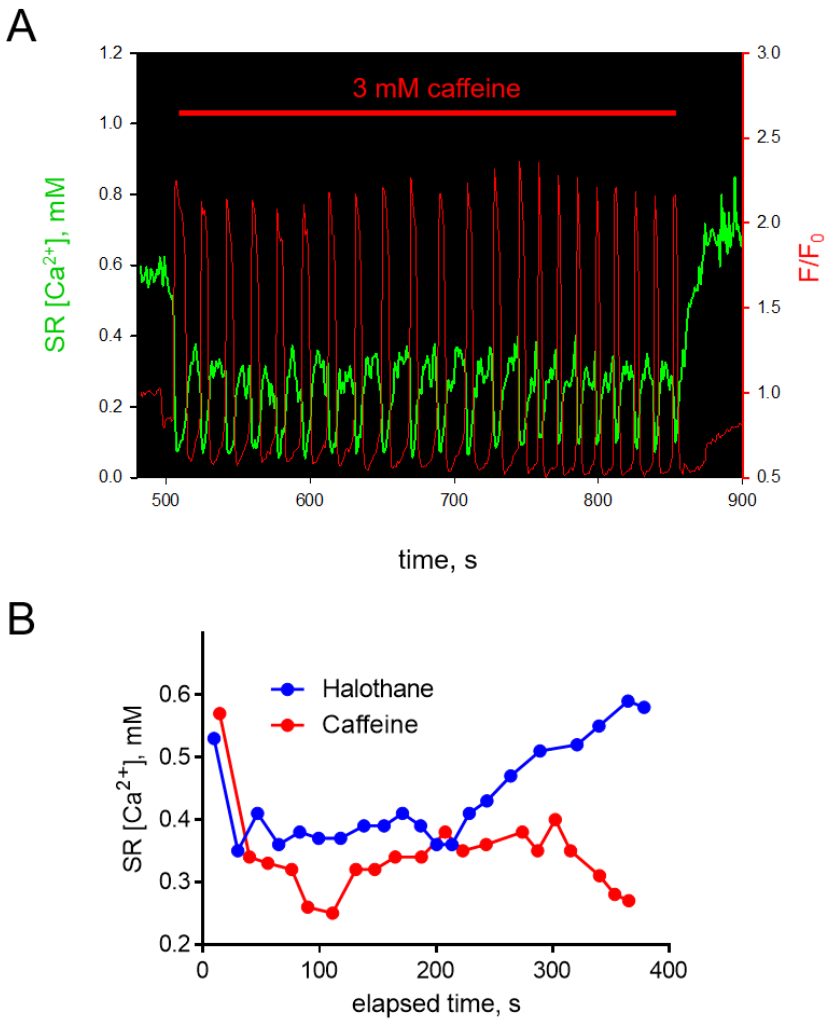

Figure 4.13 'SOICR' threshold remains constant in the presence of caffeine

(*A*) Spatially averaged values of normalized fluorescence intensity (F/F_0) and converted free $[Ca^{2+}]_{SR}$ from a human MHS skinned fiber (temporal resolution of ~0.625 s·frame^{-1}). Fibers were continuously bathed in 0.1 mM EGTA, 1 mM $[Mg^{2+}]_{cyto}$ and 100 nM $[Ca^{2+}]_{cyto}$ then by manual solution exchange the fiber was exposed to 3 mM caffeine (~ 500 s). (*B*) The free $[Ca^{2+}]_{SR}$ measured before the onset of a Ca^{2+} wave is plotted over the elapsed time the fiber was exposed to either caffeine (Figure 4.13*A*) or halothane (Figure 4.12*A*). These traces are representative of what is generally observed in the 8 fibers tested obtained from 2 MHS subjects.

4.3.8 Cytosolic contribution of Ca^{2+} wave propagation in human MHS muscle fibers

Next, the possible role of cytosolic Ca^{2+} in the mechanism of Ca^{2+} wave propagation was investigated. If Ca^{2+} wave propagation relies solely on the diffusion of the release trigger through the SR lumen, it would be expected that Ca^{2+} wave propagation will not be impeded at raised cytosolic buffering. Raised cytosolic buffering will limit the diffusion of Ca^{2+} from one junctional SR to another, and will significantly hinder the re-uptake of released Ca^{2+} from the RyR1 into the SR.

Figure 4.14 shows the sequential image acquisition of Ca^{2+} dependent fluorescence of rhod-2 (cytosol) and fluo-5N (SR) as previously described (Figure 4.12). The skinned fiber was initially bathed in a physiological solution (100 nM Ca^{2+}, 1 mM Mg^{2+}) at low cytosolic buffering (100 µM EGTA) before replacing the solution with one containing 0.5 mM halothane (left, downward facing arrow). The fiber was then reloaded with Ca^{2+} (upward facing arrow indicating the removal of halothane) before inducing another Ca^{2+} transient with 0.5 mM halothane (right, downward facing arrow), but at raised cytosolic buffering (10 mM EGTA). Note that rhod-2 was not present in the raised buffering solutions. The fiber was then treated with a maximal release solution to deplete the SR of Ca^{2+} to nadir.

At raised cytosolic Ca^{2+} buffering, the depletion of SR Ca^{2+} occurred uniformly across the cell which indicates that the release of SR Ca^{2+} was not due to a propagating Ca^{2+} wave. As shown, the readily observed oscillating Ca^{2+} wave pattern at low cytosolic buffering was abolished at raised buffering. Furthermore, upon exposure to halothane at raised buffering, the rate of free $[Ca^{2+}]_{SR}$ depletion was slowed. Fitting an exponential function to the depletion step upon the initial exposure to halothane in low and high buffering resulted in a time constant (τ) of 1 and 58 s, respectively. The slow decline in the free $[Ca^{2+}]_{SR}$ implies that the RyR1 was not open to the same extent in highly buffered conditions. These results suggest that repetitive Ca^{2+} waves are inhibited in the absence of cytosolic propagation of Ca^{2+}.

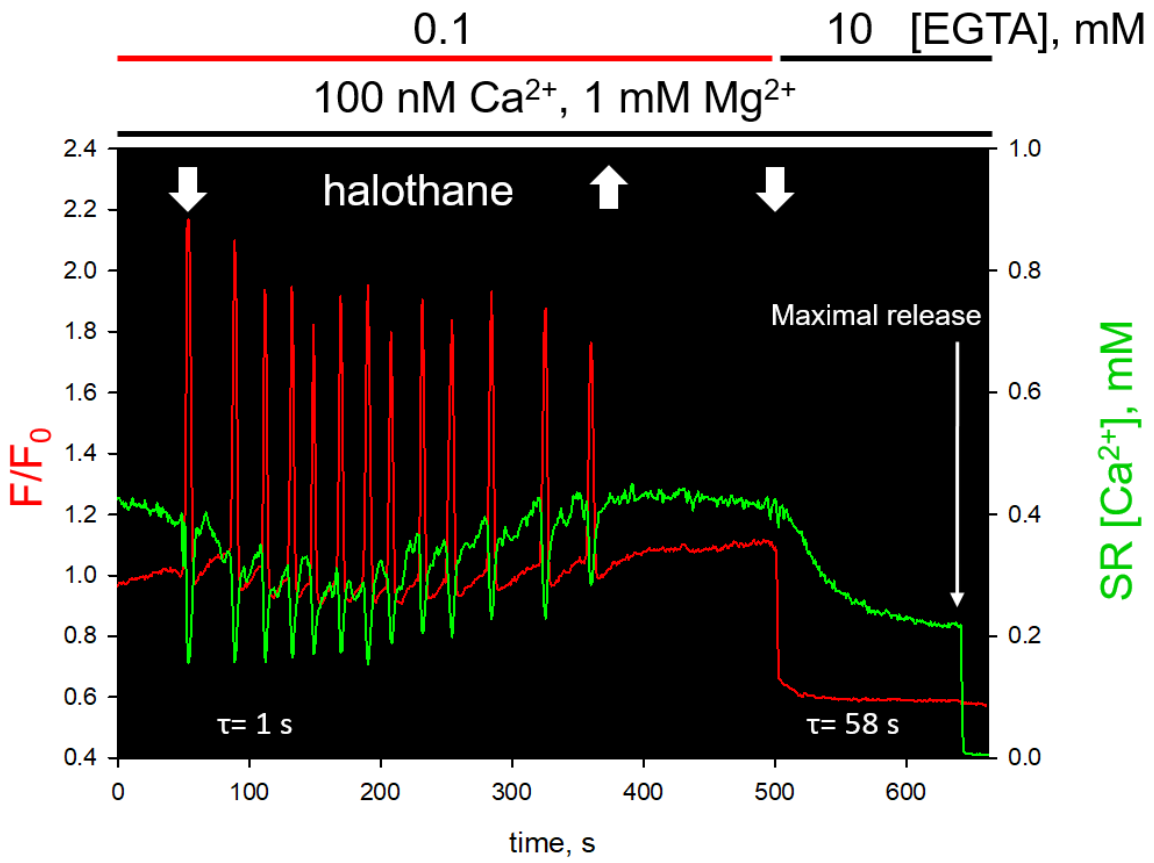

Figure 4.14 Change in Ca^{2+} wave behaviour at raised cytosolic buffering.

Spatially averaged values of normalized fluorescence intensity (F/F_0) and converted free $[Ca^{2+}]_{SR}$ from a human MHS skinned fiber (temporal resolution of ~1.03 s·frame^{-1}). The fiber was initially bathed in a physiological solution containing 0.1 mM EGTA, 1 mM $[Mg^{2+}]_{cyto}$ and 100 nM $[Ca^{2+}]_{cyto}$. The downward facing arrows indicate the addition of 0.5 mM halothane where the upward facing arrows indicate the removal of halothane. The [EGTA] during the experiments are indicated above the trace. Note that rhod-2 was not present in the raised buffering solutions. At the end of the experiment, the fiber was exposed to a maximal release solution to deplete the SR Ca^{2+} to nadir.

4.4 Discussion

This chapter aimed to clarify the mechanism of Ca^{2+} wave propagation in human MHS muscle. This is important in developing a further understanding of overactive Ca^{2+} release during an MH event. Specifically, both the cytosolic and SR Ca^{2+} contribution to the mechanism of Ca^{2+} wave propagation was investigated. To provide better clarity, the 'classic' cytosolic propagation mechanism of CICR was defined in this study as one entirely driven by the cytosolic diffusion of Ca^{2+} from one junctional SR to another. Thus, the released Ca^{2+} will diffuse to activate RyRs at the cytoplasmic activation site with little to no involvement of the SR or the SERCA pump. Therefore, any additional mechanism that involves the SR was considered a luminal SR dependent propagation mechanism. These distinctions were not made clear in previous studies (Endo *et al.*, 1970; Duke *et al.*, 2003; Duke *et al.*, 2004; Endo, 2009).

Skinned fibers allowed the controlled mimicking of an MH event, having well-defined ionic conditions while Ca^{2+} release was spatiotemporally tracked. Additionally, fibers were isolated from biopsies of persons who were MHS. The defined ionic conditions were also applied to toad skinned fibers, which are known to display 'classic' CICR. In this study, it was found that halothane induced activation of RyRs in human MHS and toad skeletal muscle induced repetitive Ca^{2+} waves (Figure 4.3 – 4.8). No evidence was found in this study in regards to the participation of 'classic' CICR in the mechanism of Ca^{2+} wave propagation in human MHS muscle (Figure 4.8 - 4.14). This was contrasted to the results obtained in toad skeletal muscle, which displayed characteristics that are in line with the involvement of CICR (Figure 4.3 – 4.7). Importantly, the apparent inhibition of Ca^{2+} waves in human MHS susceptible muscle at raised cytosolic buffering suggests that luminal SR and cytosolic Ca^{2+} are both integral to the mechanism that drives the propagation of Ca^{2+} waves.

4.4.1 'Classic' CICR does not contribute to RyR1 activation during an MH event

To describe the behaviour of overactive Ca^{2+} release during an MH event Endo (2009) defines CICR as a response that is elicited solely by Ca^{2+}. However, since the triggering general aesthetic is present throughout an MH event this definition does not accurately reflect the mechanisms involved; as the action of the pharmacological agonist cannot be isolated from the action of Ca^{2+} alone.

Defaulting to the 'classic' definition of CICR, this study provides evidence that cytosolic activation of the RyR1 in which the triggering Ca^{2+} propagated from an adjacent RyR1 through the cytosol does not occur during an MH event. The diffuse release events observed here at 1-3 mM $[Mg^{2+}]_{cyto}$ (Figure 4.8) and also observed at low Mg^{2+} (0.01mM) (Cully *et al.*, 2014) are at odds with the involvement of a CICR mechanism (Shirokova *et al.*, 1998).

Additionally, in this study, a positive correlation between SR load (as indicated by increasing periods between waves) and wave velocity was observed in toad skeletal muscle (Figure 4.6). This correlation can be explained by greater SR Ca^{2+} loads leading to greater release flux as described previously (Figueroa *et al.*, 2012). A greater release flux will reach the activating $[Ca^{2+}]$ 'threshold' at a faster rate and thereby accelerating the rate of wave propagation. This relationship was not observed in human MHS muscle, which also suggest no involvement of CICR (Figure 4.10-4.11).

The propagation velocity of the Ca^{2+} wave found at 1 mM $[Mg^{2+}]_{cyto}$ is in close agreement with that found in previous studies where the Ca^{2+} wave was induced by low $[Mg^{2+}]_{cyto}$ (0.01 – 0.3 mM) (Figueroa *et al.*, 2012; Cully *et al.*, 2014). Thus the propagation velocity is not accelerated at reduced $[Mg^{2+}]_{cyto}$ which is likely due to limits sets by Ca^{2+} diffusional properties. This suggests that even in conditions which favours CICR (by reducing competition by Mg^{2+}) the threshold required for Ca^{2+} to activate the RyR1 cannot be met solely by a cytoplasmic propagating mechanism. It is also important to note that MHS RyR1 variants do not have an increased sensitivity to cytosolic Ca^{2+} activation (Murayama *et al.*, 2007; Chen *et al.*, 2014; Chen *et al.*, 2017).

To understand the underlying mechanisms of overactive Ca^{2+} release during an MH event, it is important to consider the inhibitory actions of Mg^{2+}. As mentioned earlier it is likely that $[Mg^{2+}]_{cyto}$ is increased during an MH episode (Chapter 3.4). The inhibition of CICR by cytosolic Mg^{2+} is well known as Mg^{2+} competes with Ca^{2+} for the activation site and also directly inhibit the RyR1 by binding to an inhibitory site (Laver *et al.*, 1997a). In this study, Ca^{2+} wave propagation occurred at varying $[Mg^{2+}]_{cyto}$ (1-3 mM) (Figure 4.8 – 4.9) which at raised $[Mg^{2+}]_{cyto}$ would shift the activating concentration for Ca^{2+} to levels that do not occur *in vivo* even in these extreme circumstances of uncontrolled Ca^{2+} release.

4.4.2 Involvement of luminal SR Ca^{2+} during a Ca^{2+} wave

For every wave, regardless of the mechanism of RyR opening, a load of Ca^{2+} is required inside the SR. This is clear in every example of Ca^{2+} waves here, where the recovery of Ca^{2+} by the SERCA pump was required as the precursor to the next wave at the same site on the fiber. However, within this criteria, the activation of the wave can still be determined to be initiated at luminal or cytoplasmic sites on the RyR. Luminal SR Ca^{2+} levels have been demonstrated to affect the propensity for the RyR to open in bilayer studies (Laver *et al.*, 2004; Chen *et al.*, 2014; Chen *et al.*, 2017). Additional studies in MHS causative RyR variants have also demonstrated an increased sensitivity to luminal Ca^{2+} activation, or alternatively described as having a reduced SOICR threshold (Jiang *et al.*, 2008; Chen *et al.*, 2017). Here a positive correlation between the activating luminal SR Ca^{2+} levels and approximate declining [halothane] was observed (Figure 4.12 – 4.13). In experiments where the [agonist] (caffeine) did not decline significantly during prolonged exposure to the fiber in the bathing solution, the activating SR Ca^{2+} levels remained relatively constant (Figure 4.13). This is consistent with an inverse relationship between the SOICR threshold and [agonist]. The absence of any indication of cytoplasmic recruitment of RyR1 opening by Ca^{2+} excludes CICR involvement, and that luminal SR Ca^{2+} is the likely candidate responsible for triggering RyR1 opening.

In support of this hypothesis, the Ca^{2+} wave propagation at raised $[Mg^{2+}]_{cyto}$ in toad skeletal muscle revealed that an additional wave propagation mechanism exists that is independent of CICR (Figure 4.7). As mentioned previously a uniform wave front along the transverse axis of the fiber is incompatible with a CICR mechanism (Figure 4.5). This observation is consistent with the involvement of multiple RyR isoforms (α & β) with differing release behaviours, with the β-RyR being more prone to CICR (Lai *et al.*, 1992; Sutko & Airey, 1996; Kashiyama *et al.*, 2010). It is likely that to some degree both of these mechanisms occur simultaneously, as these isoforms are generally expressed in equal proportions (Kashiyama *et al.*, 2010; Figueroa *et al.*, 2012). Mammalian skeletal muscle predominantly expresses the RyR1 isoform (analogues to α-RyR) with only a small amount (< 3%) of RyR3 (analogues β-RyR) expressed in the diaphragm and slow-twitch muscles (Rossi *et al.*, 2007). Since the predominantly expressed RyR1 isoform have previously been demonstrated to be incapable of CICR (under physiological Mg^{2+}) (Figueroa *et al.*, 2012) it is likely that during an MH event only a singular mechanism of

wave propagation occurs that is independent of CICR, but surely involves exogenous agonists and luminal SR Ca^{2+} levels.

It is important to note that this does not rule out the possibility that the site of Ca^{2+} activation is on the cytoplasmic side of the RyR1. It remains possible that an increase in luminal SR Ca^{2+} and RyR1 Ca^{2+} leak sensitizes the RyR1 to Ca^{2+} activation (Duke *et al.*, 2002; Shannon *et al.*, 2002; Laver *et al.*, 2004; Keller *et al.*, 2007; Maxwell & Blatter, 2012). In a study by Maxwell et al. (2012) on rabbit ventricular myocytes, Ca^{2+} wave dynamics in two intracellular compartments (cytosol and SR) was monitored using Ca^{2+} indicators in conjuncture with fluorescent confocal imaging. They demonstrated that at the location of the Ca^{2+} wave-front, a transient increase in free $[Ca^{2+}]_{SR}$ preceded the increase in cytosolic Ca^{2+}. This is consistent with the possibility that luminal SR Ca^{2+} sensitizes or alternatively 'prime' the RyR to be activated on the cytosolic facing side of the RyR. Note that this is distinct from 'classic' CICR, where Ca^{2+} from one cluster of RyRs diffuses through the cytosol to activate adjacent RyRs.

It is interesting to consider the role of cytoplasmic Ca^{2+} during an MH event. As demonstrated, the behaviour of the Ca^{2+} wave changed with increased cytosolic buffering (Figure 4.14). At raised cytosolic buffering these changes includes a reduced depletion of SR Ca^{2+} for the same [agonist] and a complete ablation of the oscillating Ca^{2+} wave pattern readily observed throughout this study. These results revealed that the mechanism of Ca^{2+} wave propagation indeed includes the participation of both cytosolic and luminal SR Ca^{2+}.

It is likely that cytosolic diffusion of Ca^{2+} from one junctional SR to another is limited by the high affinity, high capacity SERCA pump (Murphy *et al.*, 2009). Therefore it may be possible that the Ca^{2+} wave during an MH event is driven by the activity of the SERCA pump. This may not come to a surprise, as the SERCA pump is one of the major players in ATP hydrolysis and heat production that the condition is known for. Indeed, there is evidence supporting this hypothesis; studies in cardiomyocytes have shown the velocity of a Ca^{2+} wave is reduced in the presence of a SERCA inhibitor (O'Neill *et al.*, 2004; Keller *et al.*, 2007; Maxwell & Blatter, 2012). Interestingly as demonstrated by Maxwell et al. (2012) in the presence of a SERCA inhibitor, both the transient increase in luminal SR Ca^{2+} (proceeding the Ca^{2+} wave) and release amplitude in the cytosol was reduced. In a sense, this threshold level of activation described by the SOICR mechanism may just reflect a critical level in the RyR channel stability (regulated at both the cytosolic

and luminal facing sides of the RyR) in which the closed state is no longer favourable. Therefore, the reduced SR Ca^{2+} depletion observed at high cytosolic buffering (a condition that will significantly reduce the $[Ca^{2+}]$ near the SERCA pump, Figure 4.14) may be explained by insufficient luminal priming of the RyR to release Ca^{2+}.

Chapter 5: The development of a novel assay to detect RyR1 activity

5.1 Introduction

Single channel recordings of the RyRs incorporated into lipid bilayers have greatly advanced our knowledge in understanding factors that influence RyR gating. However, it is important to evaluate the limitations of this assay. The opening of the RyR can be observed from the stochastic jumps in membrane current from a stationary to a maximal level as ions move accordingly to their electrochemical gradient (Laver, 2001). The open probability of the RyR (P_0) reflects the fraction of time that the RyR remained in an open or conductive state. The RyR1 P_0 under ionic conditions which mimic the resting skeletal muscle is low (RyR1 $P_0 \sim 2.5 \times 10^{-8}$), which is likely due to the potent resting inhibition of the RyR1 by cytosolic Mg^{2+} (Laver *et al.*, 1997b; Owen *et al.*, 1997b; Baylor & Hollingworth, 2003; Laver *et al.*, 2004). Thus, this poses a limitation in evaluating factors that inhibit the RyR1 beyond its resting state (Lamb, 2000; Cannon, 2017). Therefore, to get around this limitation to produce a measurable current, RyR1 bilayer experiments commonly omit Mg^{2+} in the cytosolic bathing solution (Laver, 2001; Cannon, 2017). Such experimental approaches thus assess RyR1 function under nonphysiological conditions; which have likely led to erroneous conclusions about the receptor target of dantrolene as demonstrated in Chapter 3 of this thesis (Szentesi *et al.*, 2001; Wagner Ii *et al.*, 2014). This highlights the need for a more sensitive assay to detect changes in RyR1 activity under near physiological conditions.

In this Chapter, I will compare approaches in assaying the RyR1 activity using fluorescent Ca^{2+} indicators trapped either in the SR or the t-system of a mechanically skinned rat fibers. The Ca^{2+} indicator fluo-5N or rhod-5N was trapped in the SR or the t-system, respectively. The Ca^{2+} environment of both of these compartments is influenced by the activity of the RyR1 (Chapter 1). That is activation of the RyR1 causes the depletion of Ca^{2+} in these two compartments. Thus, a change in the Ca^{2+} dependent fluorescence in either compartment is indicative of RyR1 opening.

It was hypothesized that the degree of Ca^{2+} depletion in either compartment might be graded depending on the degree of RyR1 activity and the $[Ca^{2+}]_{cyto}$. The recent advancements in quantitating $[Ca^{2+}]_{t\text{-}system}$ as described in Cully et al., (2016), and the free $[Ca^{2+}]_{SR}$ described in Chapters 2 and 4 allows for the determination of Ca^{2+} levels in this

two compartment at varying ionic conditions. Therefore, the degree of RyR1 activity can be determined by assessing the graded depletion of Ca^{2+} in these two compartments.

5.1.2 Aims

This Chapter aims to develop a novel assay in which the RyR1 activity can be measured while maintaining physiological relevant levels of $[Mg^{2+}]_{cyto}$. The sensitivity of the SR or the t-system in reporting changes in RyR1 activity was compared. The Ca^{2+} indicators fluo-5N and rhod-5N were trapped either in the SR or t-system, respectively.

5.2 Methods

5.2.1 Experimental animals, and muscle preparation

The EDL muscle from Wistar rats (2-6 months old) was used in this chapter due to the nearly homogenous population of type II (>97% type IIa/type IIb) fibres (Augusto et al. 2004). The procedure of isolating a skinned muscle fiber are described in detail in Chapter 2. The methods used for trapping a Ca^{2+} fluorescent indicator in either the t-system (rhod-5N) or the SR (fluo-5N) of a mechanically skinned fiber are described elsewhere (Chapter 2.9 and 2.10, respectively).

5.2.2 Internal physiological solution

Table 5.1 shows in detail the ionic composition of the various internal solutions used in this Chapter. The methods in preparing the internal physiological solution are described in detail in Chapter 2.5.

5.2.3 Confocal Imaging

These methods are described in Chapter 2.8. Unless indicated confocal images were acquired at a temporal resolution of ~0.841s·frame^{-1} and the fiber positioned perpendicular to the scanning line. Imaging was performed at 22 ± 1 ^{o}C.

5.2.4 Tracking net changes in SR Ca^{2+} dependent fluo-5N fluorescence

The method of tracking SR Ca^{2+} dependent fluorescence of fluo-5N are described in Chapter 2.11. After determining the maximum and minimum fluorescence of each preparation, the fluo-5N fluorescence was converted to free $[Ca^{2+}]_{SR}$ as described in Chapter 4.2.4.

Table 5.1: Internal solution composition

Solutions description	[EGTA]	Total[Ca]	Free[Ca^{2+}]	Total[Mg]	Free[Mg^{2+}]
	Concentration in mM				
SR loading solution: 1 mM Mg^{2+}, 67 nM Ca^{2+}, 10 µM fluo-5N-AM, 10 µM FCCP, 0.05% pluronic detergent	50	12.12	0.000067	9.755	1
T-system rhod-5N dye loading solution: 140 mM Na^{+}, 4 mM K^{+},159 mM Cl^{-}, 2 mM rhod-5N	0	2	2	1	1
Fluorescent maximum solution: 140 mM Na^{+}, 4 mM K^{+},159 mM Cl^{-}, 0.05 mM ionomycin	0	5	5	1	1
Fluorescent minimum solution: 0.05 mM ionomycin	50	0	0	10.02	1
Maximum release solution: 30 mM caffeine	50	0	0	10.02	1
Standard 1 mM Mg^{2+}, 28 nM Ca^{2+}	50	6.062	0.00028	10.02	1
Standard 1 mM Mg^{2+}, 67 nM Ca^{2+}	50	12.12	0.00067	9.755	1
Standard 1 mM Mg^{2+}, 200 nM Ca^{2+}	50	24.25	0.0002	9.21	1
Standard 1 mM Mg^{2+}, 1342 nM Ca^{2+}	50	42.43	0.0001342	8.39	1
3 mM Mg^{2+}, 28 nM Ca^{2+}	50	6.062	0.00028	17.79	3
3 mM Mg^{2+}, 67 nM Ca^{2+}	50	12.12	0.00067	16.98	3
3 mM Mg^{2+}, 200 nM Ca^{2+}	50	24.25	0.0002	15.37	3
3 mM Mg^{2}, 1342 nM Ca^{2+}	50	42.43	0.0001342	12.93	3

10 mM Mg^{2+}, 28 nM Ca^{2+}	50	6.062	0.00028	35.85	10
10 mM Mg^{2+}, 67 nM Ca^{2+}	50	12.12	0.00067	33.8	10
10 mM Mg^{2+}, 200 nM Ca^{2+}	50	24.25	0.0002	29.7	10
10 mM Mg^{2}, 1342 nM Ca^{2+}	50	42.43	0.0001342	23.55	10
0.03 mM Mg^{2+}, 28 nM Ca^{2+}	50	6.062	0.00028	2.06	0.03
0.03 mM Mg^{2+}, 67 nM Ca^{2+}	50	12.12	0.00067	1.951	0.03
0.03 mM Mg^{2+}, 200 nM Ca^{2+}	50	24.25	0.0002	1.842	0.03
0.03 mM Mg^{2}, 1342 nM Ca^{2+}	50	42.43	0.0001342	1.68	0.03
0.13 mM Mg^{2+}, 28 nM Ca^{2+}	50	6.062	0.00028	5.01	0.13
0.13 mM Mg^{2+}, 67 nM Ca^{2+}	50	12.12	0.00067	4.87	0.13
0.13 mM Mg^{2+}, 200 nM Ca^{2+}	50	24.25	0.0002	4.61	0.13
0.13 mM Mg^{2}, 1342 nM Ca^{2+}	50	42.43	0.0001342	4.195	0.13

Unless indicated in the ‘solution description’ each solution contained (mM): K^{+}, 136; Na^{+}, 36; ATP, 8; creatine phosphate, 10; Hepes, 90; and BTS, 0.05. Final pH was 7.1. Caffeine, halothane, tetracaine, BTS, and dantrolene were added to these solutions as indicated in the text.

5.2.5 Tracking net changes in t-system rhod-5N fluorescence

An exemplary trace of tracking the Ca^{2+} dependent rhod-5N fluorescence in the t-system is shown in Figure 5.1. A typical experiment begins with exchanging a standard physiological solution (67 nM $[Ca^{2+}]_{cyto}$, 1 mM $[Mg^{2+}]_{cyto}$, 50 mM EGTA) with a maximal SR release solution containing low Mg^{2+} (<0.01 mM) and 30 mM caffeine (black arrows); which has been previously shown to deplete the SR of Ca^{2+} (Lamb & Stephenson, 1994; Launikonis *et al.*, 2003), leading to a cell wide activation of SOCE. The activation of SOCE depletes Ca^{2+} within the t-system, thus reducing the Ca^{2+} dependent fluorescence. The fiber was then placed in an internal solution containing varying concentrations of Ca^{2+} and Mg^{2+} (Table 5.1). Under these conditions, trans-membrane Ca^{2+} transporters (PMCA and NCX) mediate the re-uptake of Ca^{2+} back into the t-system (Chapter 1), thus restoring the fluorescence signal.

Rhod-5N is a non-ratiometric dye. To calibrate the fluorescence signal, *i.e.,* to derive absolute $[Ca^{2+}]_{t\text{-}system}$, it was necessary to determine the maximum (F_{max}) and minimum (F_{min}) fluorescence for each preparation. To this end, every fiber was exposed to a solution containing 5 mM (F_{max}) or 0 mM (F_{min}) Ca^{2+} in the presence of 10 µM of the Ca^{2+} ionophore ionomycin at the end of the experiment. The $[Ca^{2+}]_{t\text{-}system}$ could then be calculated from the following relationship:

$$\text{t-system } [Ca]_{(t)} = K_{d,Ca} \frac{F_{(t)} - F_{min}}{F_{max} - F_{(t)}} \quad (1)$$

where *F(t)* is the fluorescent value of rhod-5N at time t, and $K_{D,Ca}$ the pre-determined dissociation constant for rhod-5N ($K_{D,Ca}$ ~ 0.8 mM (Cully *et al.*, 2016)).

In some preparations, exposing the fiber to high concentrations of Ca^{2+} caused the t-system to form vacuoles along the longitudinal axis of the fiber as highlighted by the green arrow in Figure 5.1. Since these structures are able to retain a significant amount of Ca^{2+} (Cully *et al.*, 2017) and therefore will cause an underestimate of the $[Ca^{2+}]_{t\text{-}system}$, the spatially averaged profile was taken in areas where vacuoles did not form (ROI1).

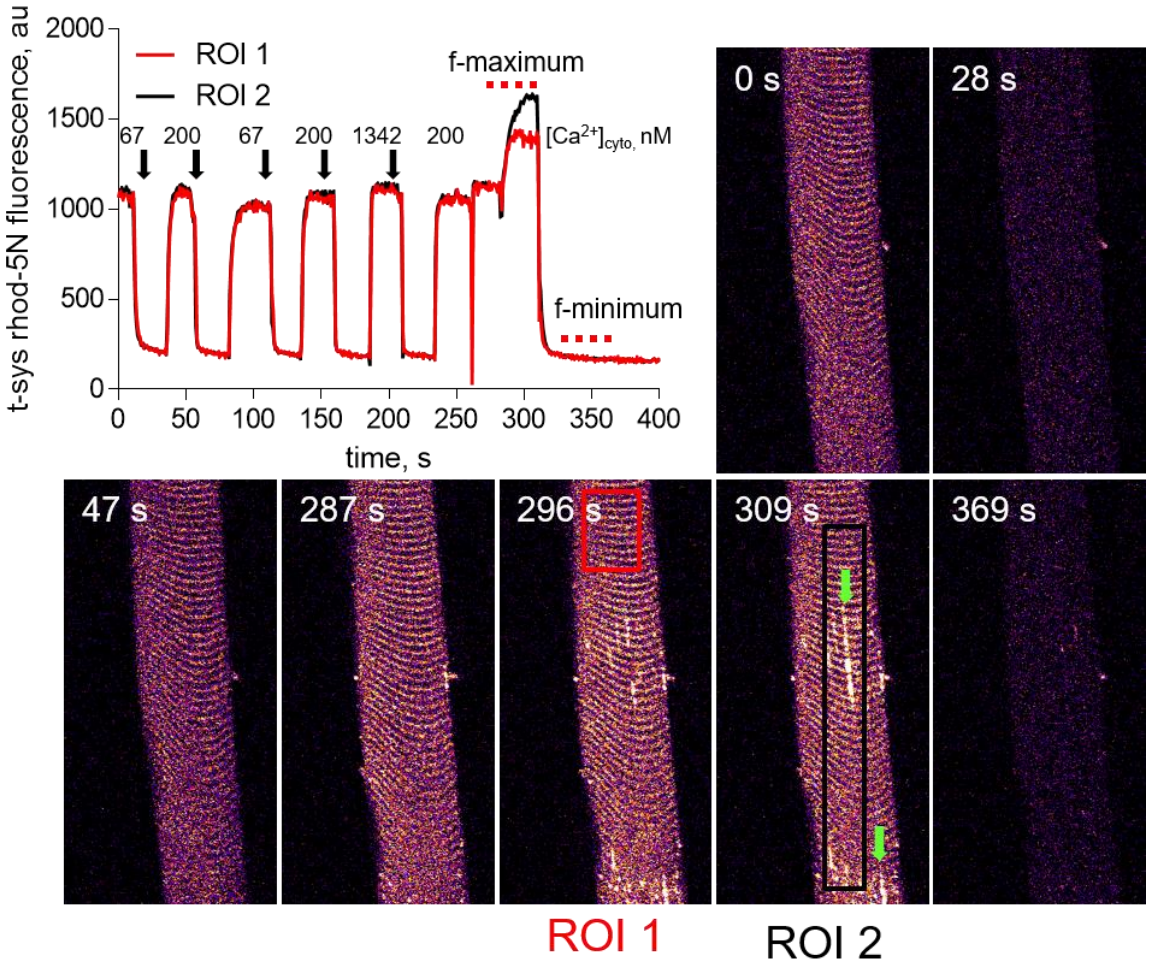

Figure 5.1. Tracking the fluorescence of the Ca^{2+}-dependent dye rhod-5N trapped in the t-system of mechanically skinned rat fast-twitch fibers.

Representative trace (top left) showing the change of t-system rhod-5N fluorescence during repeat cycles of applying a maximal release solution (black arrows; 0 mM $[Mg^{2+}]_{cyto}$, and 30 mM caffeine) and then $[Ca^{2+}]_{cyto}$ between 67 to 1342 nM. To calibrate each fiber, the preparation was exposed to solutions containing ionomycin and either 5 mM or 0 mM $[Ca^{2+}]$ (F_{max} and F_{min} respectively). The corresponding selected images during the experiment are also shown. At 296 s the fiber began to form longitudinal vacuoles (green arrows) which are capable of storing a large amount of Ca^{2+} as previously demonstrated (Cully *et al.*, 2017). These structures may cause an underestimation of the $[Ca^{2+}]_{t\text{-}system}$, therefore, care was taken to avoid including the spatial averaged information from these areas. The spatially averaged profile of both regions of interest (black and red box) is shown in the representative trace.

5.3 Results

In this Chapter, I will present measurements of the free $[Ca^{2+}]_{SR}$ and $[Ca^{2+}]_{t\text{-}system}$ under near physiological conditions and will investigate how their values change under conditions of increased or decreased activity of the RyR1. To this end, I used pharmacological tools to block SR Ca^{2+} efflux through the RyR1. Furthermore, I challenged the fibers with various conditions of low $[Mg^{2+}]_{cyto}$ to remove the endogenous inhibition that Mg^{2+} imparts on the RyR1.

5.3.1 Free $[Ca^{2+}]_{SR}$ steady-state dependence on $[Ca^{2+}]_{cyto}$

Figure 5.2*A* shows an exemplary trace of tracking the Ca^{2+} dependent fluorescence of fluo-5N in the SR, with the converted absolute values of free $[Ca^{2+}]_{SR}$ shown in Figure 5.2*B*. Note that the cytosolic-Ca^{2+} was heavily buffered with 50 mM EGTA to maintain a defined cytosolic Ca^{2+} environment throughout the experiment (Moisescu & Thieleczek, 1978; Cully *et al.*, 2016). Deviations from this are indicated in the text. Typically, the SR was depleted of Ca^{2+} by bathing the fiber in a maximal release solution composed of 0 mM $[Mg^{2+}]_{cyto}$, and 30 mM caffeine (red underscore). After reaching a nadir, the fiber was then bathed in a broad range of $[Ca^{2+}]_{cyto}$ (28, 67, 200, 1342 nM) at physiological $[Mg^{2+}]_{cyto}$ (1 mM). As shown in Figure 5.2*B*, an increase in $[Ca^{2+}]_{cyto}$ resulted in a corresponding increase in the steady-state free $[Ca^{2+}]_{SR}$. The summary of the steady-state free $[Ca^{2+}]_{SR}$ reached over a broad range of $[Ca^{2+}]_{cyto}$ of at least 5 preparations is shown in Figure 5.2*C*.

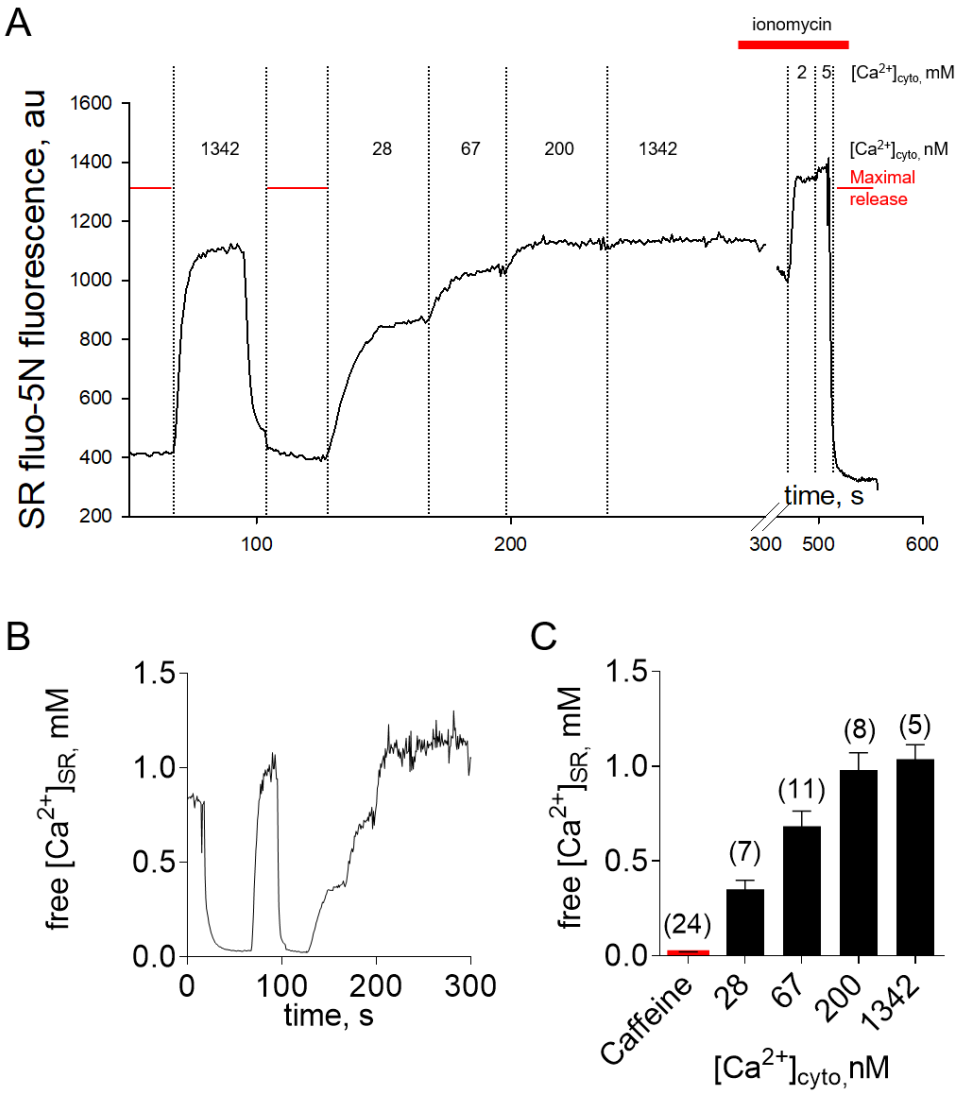

Figure 5.2. Free $[Ca^{2+}]_{SR}$ steady-state dependence on $[Ca^{2+}]_{cyto}$ in rat skinned fast-twitch fiber.

(*A*) A representative trace of tracking the Ca^{2+} dependent fluo-5N fluorescence in the SR. The SR was depleted of Ca^{2+} by bathing the skinned fibre in a low Mg^{2+} release solution containing 30 mM caffeine (thin redline). The preparation was then bathed in a broad range of $[Ca^{2+}]_{cyto}$ at 1 mM $[Mg^{2+}]_{cyto}$. All solutions contained 50 mM EGTA to maintain a defined cytosolic condition. The fiber was then calibrated as previously described (Chapter 2.11; start of the calibration as shown by the thick red line) and the resulting converted values of free $[Ca^{2+}]_{SR}$ is shown in *B*. Steady-state values derived from at least 5 preparations (*n*=5-11; as shown in brackets) are shown in *C*. All data presented as mean ± SEM.

The steady-state values reached a plateau at ~1 mM free $[Ca^{2+}]_{SR}$ when the fiber was bathed at 200 nM $[Ca^{2+}]_{cyto}$. Raising the $[Ca^{2+}]_{cyto}$ to 1342 nM did not affect this result. Note, that the plateau is not due to dye saturation, as free $[Ca^{2+}]_{SR}$ greater than 1.5-2 mM could be resolved during the *in-situ* calibration (Chapter 2.11). The time required to reach the steady-state from a depleted SR was slower in 200 nM $[Ca^{2+}]_{cyto}$ compared to 1342 nM (as shown in Figure 5.3*A*; 15.3 ± 1.16 s and 10.2 ± 1.15 s (n=5-11; p=0.015), respectively). Furthermore, the maximal rate of Ca^{2+} uptake into the SR increased when the $[Ca^{2+}]_{cyto}$ was increased from 200 nM to 1342 nM $[Ca^{2+}]_{cyto}$ (Figure 5.3*B*). Here, it was observed that free $[Ca^{2+}]_{SR}$ saturated at a much faster rate (~15.3 s at 200 nM $[Ca^{2+}]_{cyto}$) than the total $[Ca^{2+}]_{SR}$, which took ~180 s to plateau at 200 nM $[Ca^{2+}]_{cyto}$ as measured previously in rat EDL fibers (Fryer & Stephenson, 1996; Murphy *et al.*, 2009). The ability of the SR to accumulate Ca^{2+} is consistent with the involvement of a dynamic high capacity Ca^{2+} buffer (CSQ). These results are suggestive that free $[Ca^{2+}]_{SR}$ reaches a maximal value, while the total $[Ca^{2+}]_{SR}$ can continue to increase, depending upon the cytoplasmic conditions and the polymerized state of CSQ.

In response to the maximal release solution, a rapid decline in the free $[Ca^{2+}]_{SR}$ was observed. Figure 5.3*C* shows the maximal rate of free $[Ca^{2+}]_{SR}$ depletion plotted against the respective SR steady-state levels that preceded the depletion. As shown, a linear relationship was derived. This suggests that the rate of SR Ca^{2+} depletion is proportional to the Ca^{2+} gradient between the SR lumen and cytosol. Note that the change is the change in free $[Ca^{2+}]_{SR}$ and that the total $[Ca^{2+}]_{SR}$ will be much greater. This value is largely dependent on the SR Ca^{2+} buffering capacity.

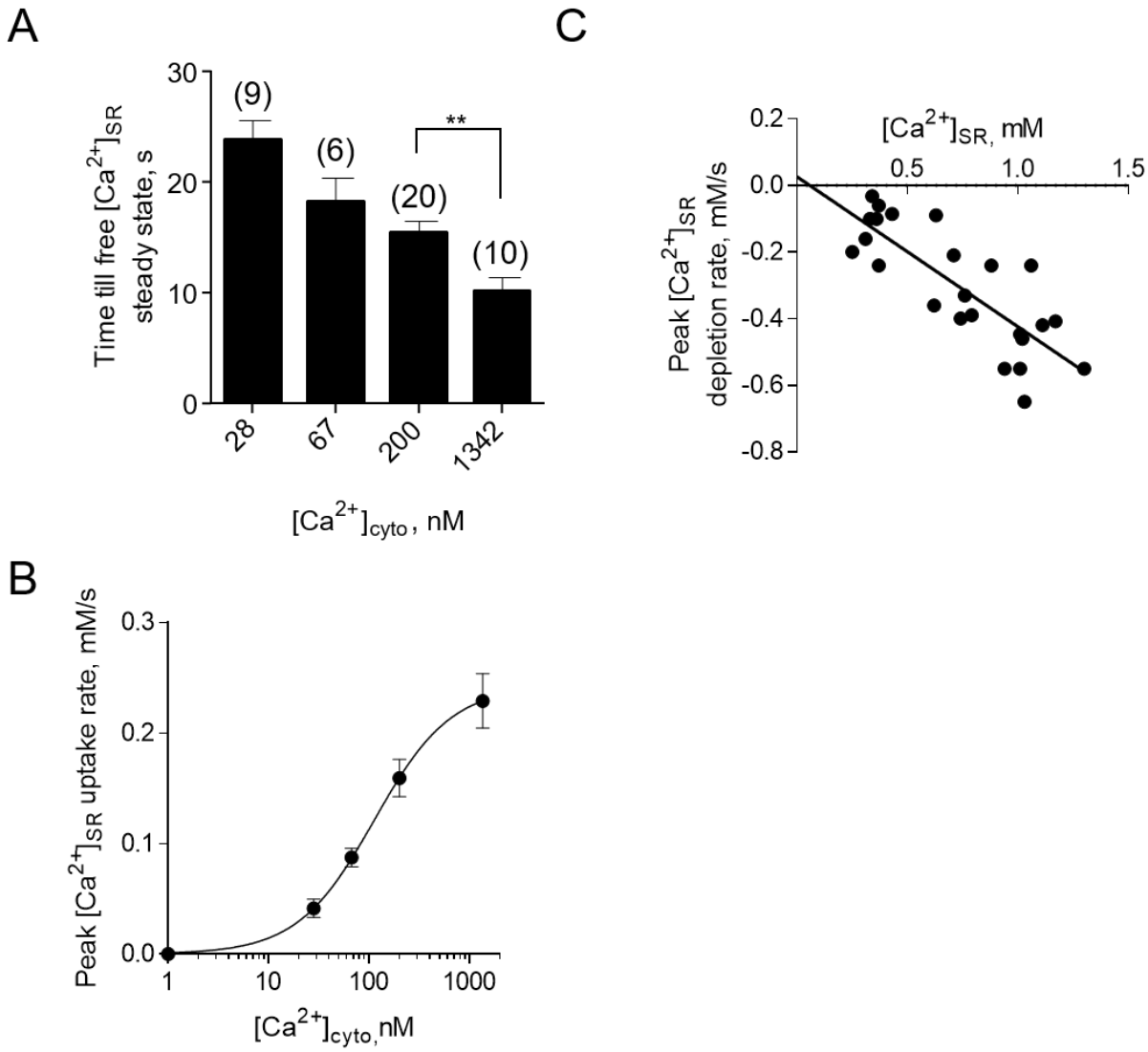

Figure 5.3. Uptake and depletion rate of free $[Ca^{2+}]_{SR}$ in rat muscle fibers.

(*A*) Elapsed time to reach a steady-state value from a depleted SR for a given $[Ca^{2+}]_{cyto}$. The number of Ca^{2+} uptake transients analyzed is shown in brackets. These were derived from at least 5 preparations (*n*=5-11); Welch's t-test analysis was used where statistically significant was considered to be $p<0.05$. (*B*) Peak uptake rate of free $[Ca^{2+}]_{SR}$ from a depleted state with the values representing uptake of Ca^{2+} into the SR in mM/s (analysis of 9-18 uptake profiles derived from at least 5 preparations (*n*=5-11)). The data were fitted with a Hill equation with values for Bmax, Hill coefficient, and Kd_{Ca} of 0.24±0.02; 1.137±0.25; 112±27.23 µM, respectively. (*C*) Scatter plot of peak SR depletion rate for a given free $[Ca^{2+}]_{SR}$. SR Ca^{2+} depletion was induced by bathing the fiber in a maximal release solution. The data were fitted by linear regression (r^2= 0.648). All data presented as mean ± SEM.

5.3.2 Effect of raised and lowered $[Mg^{2+}]_{cyto}$ on free $[Ca^{2+}]_{SR}$

To determine whether the free $[Ca^{2+}]_{SR}$ is altered by increased RyR1 inhibition, the mechanically skinned fibers was challenged with raised $[Mg^{2+}]_{cyto}$ while maintaining similar levels of $[Ca^{2+}]_{cyto}$. Figure 5.4*A* shows the SR Ca^{2+} uptake profile of a mechanically skinned fiber challenged with 28 or 200 nM $[Ca^{2+}]_{cyto}$ and 1 or 10 mM $[Mg^{2+}]_{cyto}$. At raised $[Mg^{2+}]_{cyto}$, the free $[Ca^{2+}]_{SR}$ increased at a noticeably slower rate when the fiber was bathed in 28 nM $[Ca^{2+}]_{cyto}$ (Figure 5.4*B*), but the same steady-state free $[Ca^{2+}]_{SR}$ was reached at 1 and 10 mM $[Mg^{2+}]_{cyto}$ (Figure 5.4*C*). The slow rate of Ca^{2+} accumulation into the SR is likely due to increased competition of Ca^{2+} and Mg^{2+} at the SERCA pump ((Lamboley *et al.*, 2014)). At raised $[Ca^{2+}]_{cyto}$, no noticeable changes in the rate of SR Ca^{2+} uptake or steady-state were observed at 10 mM $[Mg^{2+}]_{cyto}$ (summarized in Figure 5.4*C*). This shows that $[Ca^{2+}]_{cyto}$ has to be in the low nM range for mM levels of $[Mg^{2+}]_{cyto}$ to compete for binding at SERCA.

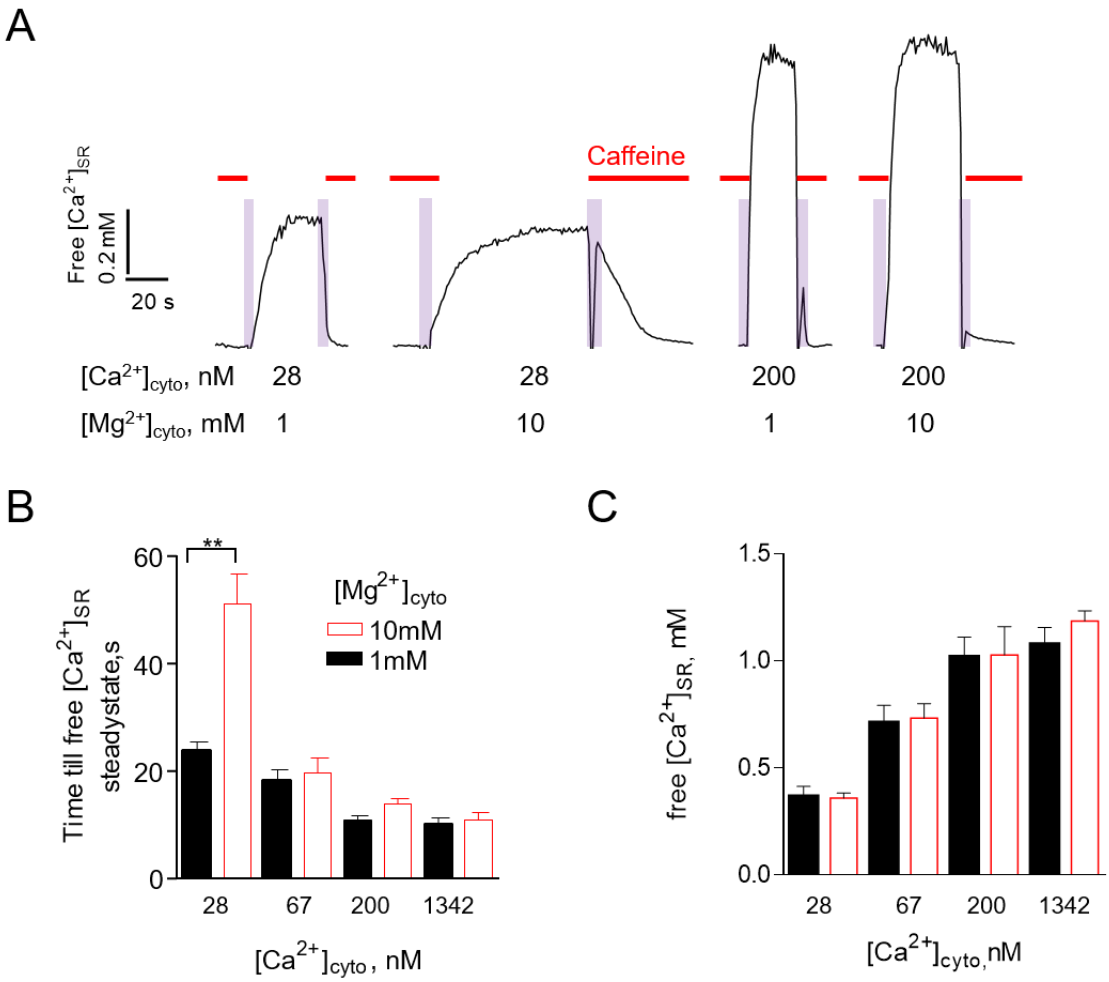

Figure 5.4. Effect of 10 mM $[Mg^{2+}]_{cyto}$ on the uptake profile of free $[Ca^{2+}]_{SR}$.

(*A*) Free $[Ca^{2+}]_{SR}$ uptake and depletion (red underscore) at 28 and 200 nM $[Ca^{2+}]_{cyto}$ in the presence of either 1 or 10 mM $[Mg^{2+}]_{cyto}$. The purple vertical bar is indicating the movement artefact during solution exchange. Note that the uptake profile at 28 nM $[Ca^{2+}]_{cyto}$ in 1 and 10 mM $[Mg^{2+}]_{cyto}$ was from two preparation; however, the uptake profile at 200 nM $[Ca^{2+}]_{cyto}$ was from the same preparation. The dye calibration performed for each fiber allows for the direct comparison between individual fibers of a muscle bundle and fibers obtained from different animals. (*B*) Elapsed time to reach a steady-state value from a depleted SR for a given $[Ca^{2+}]_{cyto}$ and $[Mg^{2+}]_{cyto}$. Data were analyzed with Welch's t-test where $p<0.05$ was considered to be significant ($n=6$;** $p<0.0035$). (*C*) Summary of steady-state values derived from 5-11 preparations ($n=5$-11). All data presented as mean ± SEM.

Next, the effect of increased RyR1 activity on the free $[Ca^{2+}]_{SR}$ steady-state was investigated. This was done by lowering the Mg^{2+} inhibition of the RyR1. The effect of 0.03 mM $[Mg^{2+}]_{cyto}$ on free $[Ca^{2+}]_{SR}$ is shown in Figure 5.5*A*. The SR was initially depleted of Ca^{2+} by bathing the fiber in a maximal release solution (black arrows). The fiber was then bathed in a 200 nM $[Ca^{2+}]_{cyto}$ at 1 mM $[Mg^{2+}]_{cyto}$; this was done to provide a reference of the steady state reached at physiological $[Mg^{2+}]_{cyto}$. After another cycle of SR Ca^{2+} depletion, the skinned fiber was then bathed in a low-Mg^{2+} solution (0.03 mM) at various $[Ca^{2+}]_{cyto}$. The $[Ca^{2+}]_{cyto}$ was increased in a stepwise manner while maintaining the $[Mg^{2+}]_{cyto}$ at 0.03 mM. Interestingly, the free $[Ca^{2+}]_{SR}$ steady-state reached at 28, 67 and 1342 nM $[Ca^{2+}]_{cyto}$ did not differ between 0.03 and 1 mM $[Mg^{2+}]_{cyto}$. In contrast, the steady-state reached at 200 nM $[Ca^{2+}]_{cyto}$ was found to be significantly lowered at 0.03 mM $[Mg^{2+}]_{cyto}$ (two-way ANOVA followed by a Sidak multi-comparison test, $p<0.05$). An additional experiment is showing the direct comparison of the steady-state reached at 28 nM $[Ca^{2+}]_{cyto}$ between 1 and 0.03 mM $[Mg^{2+}]_{cyto}$ is shown in Figure 5.5*B*. These results are summarized in Figure 5.5*C*.

As mentioned previously, a limitation of tracking the free $[Ca^{2+}]_{SR}$ with fluo-5N is that the total $[Ca^{2+}]_{SR}$ is not known. Since both SR Ca^{2+} release and Ca^{2+} uptake occur in parallel (at low $[Mg^{2+}]_{cyto}$), the saturating free $[Ca^{2+}]_{SR}$ observed at 1342 nM $[Ca^{2+}]_{cyto}$ (at 0.03 mM $[Mg^{2+}]_{cyto}$) may only reflect the ability of the SERCA pump to maintain a high free $[Ca^{2+}]_{SR}$. Based on strong evidence provided by single channel studies (Laver *et al.*, 2004), the RyR1 is expected to have a high P_0 under these conditions. An increased in RyR1 P_0 is expected to impede Ca^{2+} accumulation into the SR, thus resulting in a reduction in the total $[Ca^{2+}]_{SR}$ upon reaching equilibrium. A change in total $[Ca^{2+}]_{SR}$ can be directly observed in another experiment by monitoring Ca^{2+} release from the SR into the cytosol using the Ca^{2+} indicator rhod-2 (as shown in Chapter 3 and 4) as a relative measure of total SR Ca^{2+}.

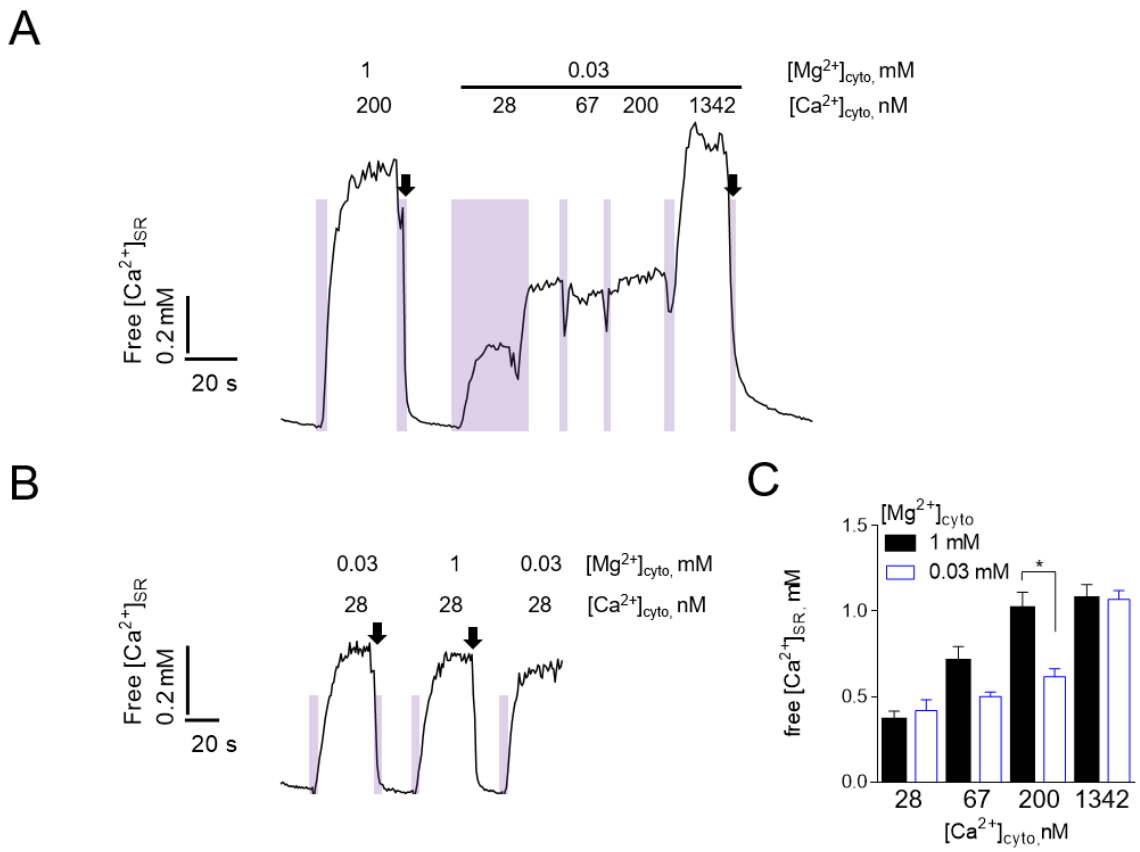

Figure 5.5. Effect of low-cytosolic Mg^{2+} on the uptake profile of free $[Ca^{2+}]_{SR}$.

(*A, B*) Free SR Ca^{2+} uptake and depletion (maximal release solution applied to fiber as indicated by the black arrows) at various $[Ca^{2+}]_{cyto}$ (28, 67, 200, 1342 $[Ca^{2+}]_{cyto,}$ nM) in the presence of either 1 or 0.03 mM $[Mg^{2+}]_{cyto}$. The purple vertical bar is indicating the movement artefact during solution exchange. (*C*) Summary of the steady-state values derived from 5-11 preparations (*n*=5-11). Data were analyzed with a two-way ANOVA ($[Ca^{2+}]_{cyto}$, $[Mg^{2+}]_{cyto}$) with Sidak multi-comparison test, where $p<0.05$ was considered significant. Data are presented as mean ± SEM.

To gain a relative measure of total $[Ca^{2+}]_{SR}$ in the same preparation, the fiber was exposed to 'standard' loading conditions (1 mM $[Mg^{2+}]_{cyto}$, 200 nM $[Ca^{2+}]_{cyto}$, 1 mM EGTA for 3 min) before maximally releasing the SR of Ca^{2+} by lowering $[Mg^{2+}]_{cyto}$ (as demonstrated in Chapter 3.3.1, lowering the $[Mg^{2+}]_{cyto}$ removes the resting inhibition of Mg^{2+} on the RyR1). The time integral of the Ca^{2+} transient reflects the total relative amount of Ca^{2+} released from the SR (Launikonis & Stephenson, 1997).

Figure 5.6 shows the spatially averaged and normalized rhod-2 fluorescence (F/F_0) of a mechanically skinned fiber from rat. The baseline normalized fluorescent ratio (F/F_0) corresponds to a free $[Ca^{2+}]_{cyto}$ of 200 nM, which was maintained throughout the experiment. Also, between each Ca^{2+} transient, the SR was depleted of Ca^{2+} by bathing the fiber in a nominal low $[Mg^{2+}]_{cyto}$ solution (1 mM EGTA, 0 mM $[Mg^{2+}]_{cyto}$, and 200 nM $[Ca^{2+}]_{cyto}$). To evaluate the ability of the SR to accumulate Ca^{2+} at low and endogenous $[Mg^{2+}]_{cyto}$, the fiber was allowed to load Ca^{2+} for a fixed period (~180 s) from a depleted SR with the $[Mg^{2+}]_{cyto}$ set at 0.03 or 1 mM, respectively. Importantly, the allotted 180 s loading time at 200 nM $[Ca^{2+}]_{cyto}$ was previously demonstrated to maximally load the SR of Ca^{2+} under physiological $[Mg^{2+}]_{cyto}$ (Fryer & Stephenson, 1996; Murphy *et al.*, 2009). After the loading period, the fiber was then challenged with a nominal low $[Mg^{2+}]_{cyto}$ solution (as indicated by the black arrows). As shown, a reproducible Ca^{2+} transient was observed when the fiber was bathed in 1 mM $[Mg^{2+}]_{cyto}$ during the loading period (Figure 5.6 (left and right Ca^{2+} transient), and also demonstrated in Chapter 3). This is in stark contrast to the Ca^{2+} transient observed after loading the SR in the presence of reduced $[Mg^{2+}]_{cyto}$ (center). The Ca^{2+} transient was comparatively reduced in amplitude and duration relative to the transient observed a 1 mM $[Mg^{2+}]_{cyto}$. These results are consistent with the reduced capability of the SR to accumulate Ca^{2+} under conditions where the RyR1 is sufficiently open (Pape *et al.*, 2007; Manno *et al.*, 2017).

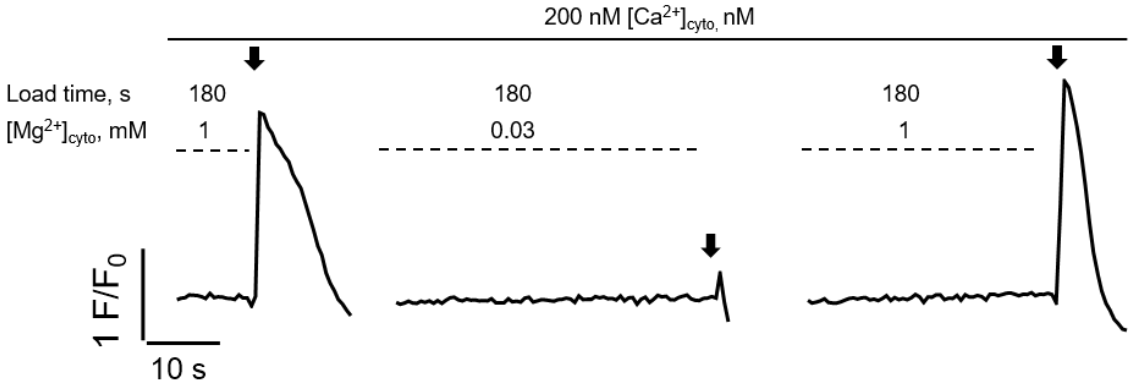

Figure 5.6. Effect of low-cytosolic Mg^{2+} on total SR Ca^{2+} loading.

Spatially averaged values of normalized fluorescence intensity (F/F_0) of 10 μM rhod-2 versus elapsed time. Fibers were continuously bathed in 1 mM EGTA and 200 nM $[Ca^{2+}]_{cyto}$. Note that the [EGTA] was lowered to 1 mM to observe the cytosolic Ca^{2+} transient. The bathing solution was then replaced with a nominal low $[Mg^{2+}]_{cyto}$ solution to elicit the release of SR Ca^{2+} (manual solution exchange is indicated by the black arrows). Note that the nominal low $[Mg^{2+}]_{cyto}$ solution did not contain caffeine. Caffeine has previously been found to accelerate the release of Ca^{2+} from the RyR1 (Klein et al., 1990; Lamb et al., 2001) and therefore may cause difficulty in accurately tracking the Ca^{2+} transient during manual solution exchange. The fiber was either loaded in the presence of 0.03 (center) or 1 mM (left, right) $[Mg^{2+}]_{cyto}$ for 180 s. Note that the elapsed time during the loading periods is not shown for brevity. Similar observations were made in additional two preparations.

A summary of the free $[Ca^{2+}]_{SR}$ obtained through the range of $[Ca^{2+}]$ and $[Mg^{2+}]_{cyto}$ is shown in Figure 5.7. The steady-state free $[Ca^{2+}]_{SR}$ was greater with increasing $[Ca^{2+}]_{cyto}$, which is likely attributed to increased activity of the SERCA pump (Rios & Brum, 2002; Bakker *et al.*, 2017). In interpreting these findings, it is important to note that the RyR1 activity will increase with reduced RyR1 inhibition by Mg^{2+} (Laver *et al.*, 2004). In addition, since the accumulation of SR Ca^{2+} is not favoured when the RyR1 is sufficiently open an inverse relationship can be assumed between the total $[Ca^{2+}]_{SR}$ and the activity of the RyR1 (under similar $[Ca^{2+}]_{cyto}$).

These results collectively suggest that the free $[Ca^{2+}]_{SR}$ is not a reliable means of interpreting the activity of the RyR1. As demonstrated by the similar steady-state values obtained at 28 and 1342 nM $[Ca^{2+}]_{cyto}$ over the range of $[Mg^{2+}]_{cyto}$, the activity of the SERCA pump can greatly influence the free $[Ca^{2+}]_{SR}$ and can set the steady-state value irrespective of the activity of the RyR1.

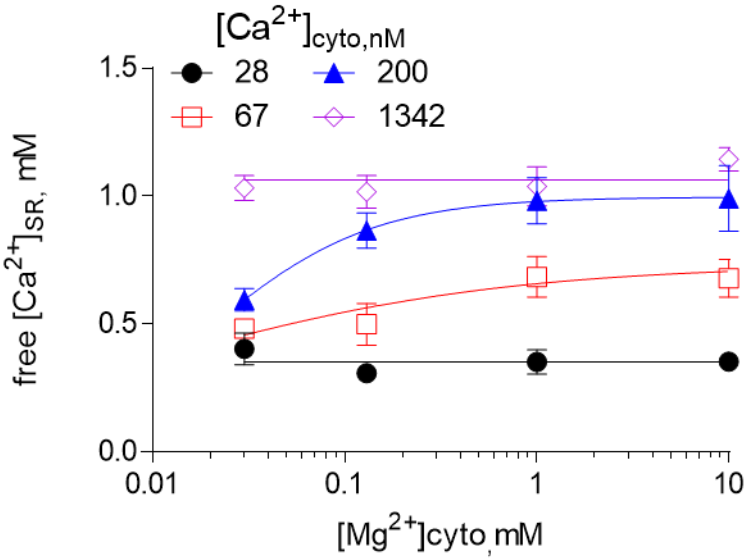

Figure 5.7. Summary of the $[Ca^{2+}]_{cyto}$ and $[Mg^{2+}]_{cyto}$ dependence on free$[Ca^{2+}]_{SR}$ steady-state.

The free $[Ca^{2+}]_{SR}$ is plotted against the range of $[Mg^{2+}]_{cyto}$ tested. The data was fitted with either a Hill equation (for $[Ca^{2+}]_{cyto}$ of 67, and 200 nM; Bmax (0.73±.19, 0.99±0.07), Hill coefficient (0.47±0.7, 1.03±.78), and Kd_{Mg} (0.01±0.017, 0.02±.0.01 mM), respectively) or a horizontal line (28, and 1342 nM $[Ca^{2+}]_{cyto}$, robust sum of squares values of 0.46 and 0.62, respectively). Data points were derived from 4-11 preparations (*n*=4-11). All data presented as mean ± SEM.

5.3.3 The $[Ca^{2+}]_{t\text{-}system}$ steady-state dependence on $[Ca^{2+}]_{cyto}$

Next, the $[Ca^{2+}]_{t\text{-}system}$ steady-state at varying $[Mg^{2+}]_{cyto}$ and $[Ca^{2+}]_{cyto}$ was determined. The 'base-line' recording demonstrating the $[Ca^{2+}]_{t\text{-}system}$ steady-state reached at physiological $[Mg^{2+}]_{cyto}$ (1 mM) have already been published (Cully *et al.*, 2016). However, to control for potential differences in data collection between individuals conducting the experiments, these experiments were performed again.

Similar to the procedure described above, the mechanically skinned fiber was subject to repeated measurements of SR Ca^{2+} depletions and SR Ca^{2+} store refilling. Depletion of the SR Ca^{2+} caused a cell wide activation of SOCE and thus reduced the Ca^{2+} dependent fluorescence of the dye rhod-5N trapped in the t-system (Launikonis *et al.*, 2003; Cully *et al.*, 2016). An example experiment demonstrating the depletion of t-system Ca^{2+} is shown in Figure 5.8*A*. Upon exposure to the maximal release solution (0 mM $[Mg^{2+}]_{cyto}$, 30 mM caffeine) the $[Ca^{2+}]_{t\text{-}system}$ fell to nadir ($[Ca^{2+}]_{t\text{-}system}$, 0.098 ± 0.001 mM). From a depleted state, the fiber was then bathed in a broad range of $[Ca^{2+}]_{cyto}$ (28-1342 nM $[Ca^{2+}]_{cyto}$) at 1 mM $[Mg^{2+}]_{cyto}$. Restoring the Mg^{2+} inhibition of the RyR1 in the presence of cytosolic Ca^{2+} allowed the SR Ca^{2+} stores to refill, rapidly deactivating SOCE (Cully *et al.*, 2016). As described in detail elsewhere (Chapter 5, Methods), the t-system Ca^{2+} levels are restored by Ca^{2+} transporters on the t-system membrane. Therefore, steady-state values are likely dependent on the $[Ca^{2+}]$ in the triadic junction space where increased concentrations would increase the capacity to extrude Ca^{2+}. The steady-state $[Ca^{2+}]_{t\text{-}system}$ reached across the tested range of $[Ca^{2+}]_{cyto}$ at 1 mM $[Mg^{2+}]_{cyto}$ are summarized in Figure 5.8*B*.

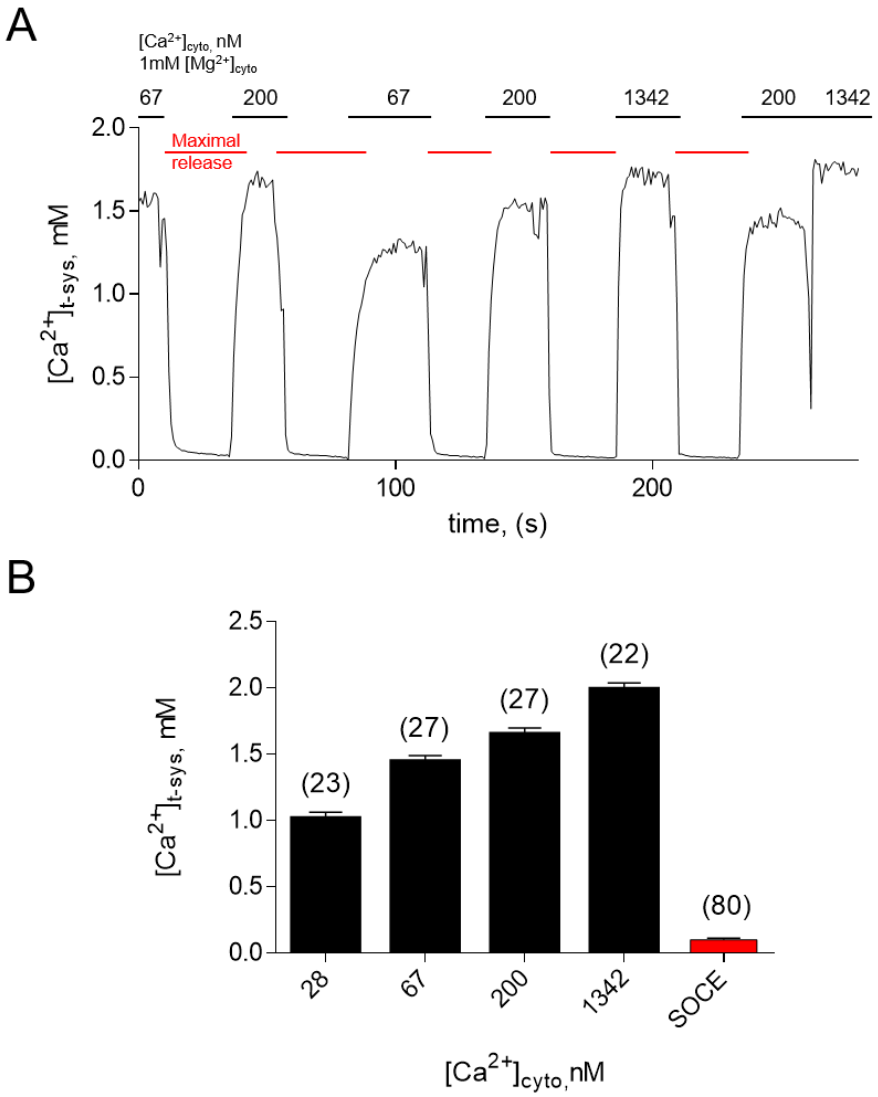

Figure 5.8. The steady-state values of $[Ca^{2+}]_{t\text{-}system}$ reached at 1 mM $[Mg^{2+}]_{cyto}$ at various $[Ca^{2+}]_{cyto}$ in rat skinned fibers.

(*A*) Selected traces of the tracking the $[Ca^{2+}]_{t\text{-}system}$. The red horizontal lines indicate that the skinned fiber was bathed in a maximal release solution containing 0 mM $[Mg^{2+}]_{cyto}$ and 30 mM caffeine. This maximal release leads to an activation of cell-wide SOCE. The Ca^{2+} dependent fluorescence of rhod-5N was converted to $[Ca^{2+}]_{t\text{-}system}$ as described in the Methods section of this Chapter. All solutions contained 50 mM EGTA. Data was collected from 23-27 fibers (*n*=23-27) and a summary of the steady-state values is shown in (*B*). All data are shown as mean ± SEM.

5.3.4 $[Ca^{2+}]_{t\text{-}system}$ depends on the activity of the RyR1

The following experiments investigated the effects of increased RyR1 activity on the steady-state levels of $[Ca^{2+}]_{t\text{-}system}$. Figure 5.9*A* shows a continuous recording of $[Ca^{2+}]_{t\text{-}system}$ from a mechanically skinned rat EDL muscle fiber. The fiber was initially subjected to a cycle of maximal t-system Ca^{2+} depletion and uptake at 200 nM $[Ca^{2+}]_{cyto}$ (at 1 mM $[Mg^{2+}]_{cyto}$). Again, this was done to provide a reference to the steady-state value reached at physiological $[Mg^{2+}]_{cyto}$. The fiber was then again challenged with a maximal release solution. After the $[Ca^{2+}]_{t\text{-}system}$ reached a nadir, the fiber was then challenged with a step-wise increase of $[Ca^{2+}]_{cyto}$ in the presence of 0.03 mM $[Mg^{2+}]_{cyto}$. In the presence of low-Mg^{2+}, a decrease in the $[Ca^{2+}]_{t\text{-}system}$ was observed. At 200 nM $[Ca^{2+}]_{cyto}$ at low-Mg^{2+} the $[Ca^{2+}]_{t\text{-}system}$ dropped on average by 60 ± 2.8% (mean ± SEM, n = 20) compared to the steady-state reached at 1 mM $[Mg^{2+}]_{cyto}$. Interestingly, a further decline in $[Ca^{2+}]_{t\text{-}system}$ was observed at 1342 nM $[Ca^{2+}]_{cyto}$ (83 ± 2%, n = 11). These experiments were repeated at 0.13 mM $[Mg^{2+}]_{cyto}$, and the steady-state reached are summarized in Figure 5.9*B*. As demonstrated by the raised steady-state values reached in 0.13 mM $[Mg^{2+}]_{cyto}$ over the range of $[Ca^{2+}]_{cyto}$, increasing the Mg^{2+} inhibition of the RyR1 resulted in a slight recovery of the $[Ca^{2+}]_{t\text{-}system}$.

Here it was demonstrated that under conditions which increase the activity of the RyR1 (*i.e.,* decrease in $[Mg^{2+}]_{cyto}$ and increase free $[Ca^{2+}]_{SR}$ (Figure 5.5, 5.7)) resulted in a decline in $[Ca^{2+}]_{t\text{-}system}$. Collectively these results suggest that the $[Ca^{2+}]_{t\text{-}system}$ is influenced by the activity of the RyR1. To further investigate this hypothesis, as shown in Figure 5.9*A* the fiber was again challenged with a step-wise increase in $[Ca^{2+}]_{cyto}$ (28, 67, 200, 1342 nM) at 0.03 mM $[Mg^{2+}]_{cyto}$ in the presence of 1 mM halothane (blue dashed lines). As demonstrated in previous Chapters (3, 4) and extensively demonstrated by Duke *et al.* (2003), it was expected that the RyR1 activity would increase in the presence of halothane. Consistent with the results obtained at low-Mg^{2+}, increasing the RyR1 activity with halothane resulted in a further decline in the $[Ca^{2+}]_{t\text{-}system}$.

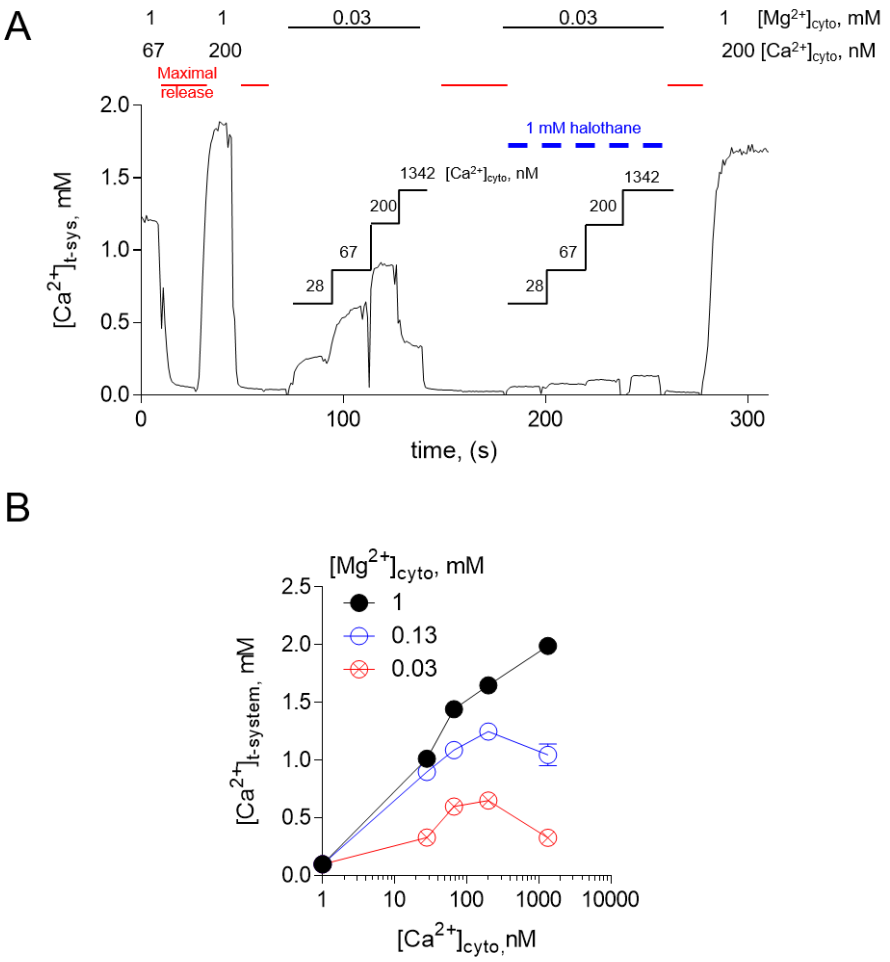

Figure 5.9. Effect of low-cytosolic Mg^{2+} on $[Ca^{2+}]_{t\text{-}system}$.

(*A*) Selected traces of the tracking the $[Ca^{2+}]_{t\text{-}system}$ under low-$[Mg^{2+}]_{cyto}$. The red horizontal lines indicate that the skinned fiber was bathed in a maximal release solution. After depleting the SR of Ca^{2+}, the fiber was challenged with a solution of varying ionic conditions as shown. After obtaining the steady-state values under 0.03 mM $[Mg^{2+}]_{cyto}$, the experiment was repeated but in the continuous presence of 1 mM halothane. The depletion of the $[Ca^{2+}]_{t\text{-}system}$ under these conditions (1 mM halothane) indicates that the reduced steady-state under low-$[Mg^{2+}]_{cyto}$ was due to an open RyR1. These experiments were repeated at 0.13 mM $[Mg^{2+}]_{cyto,}$ and the summarized stead-state values are shown in (*B*). Data were derived from 11-32 fibers (*n*=11-32). All data are shown as mean ± SEM.

The apparent $[Ca^{2+}]_{t\text{-}system}$ dependence RyR1 activity on was further investigated by applying varying concentrations of halothane and Mg^{2+}. Note that in these experiments the $[Ca^{2+}]_{cyto}$ was maintained at 200 nM. As shown in Figure 5.10*A*, the steady-state reached at 10 mM halothane, and 0.13 mM $[Mg^{2+}]_{cyto}$ was comparable to that of the maximal release solution. This suggests that under these conditions the apparent RyR1 P_0 is near a maximum. Gradually decreasing the [halothane] resulted in a step-wise increase in the $[Ca^{2+}]_{t\text{-}system}$, and removal of halothane from the bathing solution restored the $[Ca^{2+}]_{t\text{-}system}$ reached at 0.13 mM $[Mg^{2+}]_{cyto}$. As shown, a drop in $[Ca^{2+}]_{t\text{-}system}$ was observed at relatively low [halothane] (~1 nM), suggesting that the $[Ca^{2+}]_{t\text{-}system}$ is a sensitive measure of RyR1 activity. These experiments were repeated in the presence of endogenous $[Mg^{2+}]_{cyto}$ (Figure 5.10*B*). As shown, a drop in $[Ca^{2+}]_{t\text{-}system}$ was observed at 10 and 1 mM halothane, however, the $[Ca^{2+}]_{t\text{-}system}$ was restored to the control levels at 100 µM halothane.

Taken together it was determined that factors that increase RyR1 activity decreased the steady-state levels of the $[Ca^{2+}]_{t\text{-}system}$. This was demonstrated by increasing the RyR1 activity by decreasing Mg^{2+} inhibition of the RyR1 and furthermore, using pharmacological tools to activate the RyR1 (halothane and caffeine). It is expected under these experimental conditions that an increase RyR1 activity will affect the ability of the SR to load Ca^{2+} (as demonstrated in Figure 5.6). Thus, indicating that the observed depletion in $[Ca^{2+}]_{t\text{-}system}$ is SR store-dependent. These findings are consistent with the RyR1 activating SOCE as a direct consequence of SR 'store-depletion' (Launikonis *et al.*, 2003; Launikonis & Ríos, 2007; Duke *et al.*, 2010; Cully *et al.*, 2016).

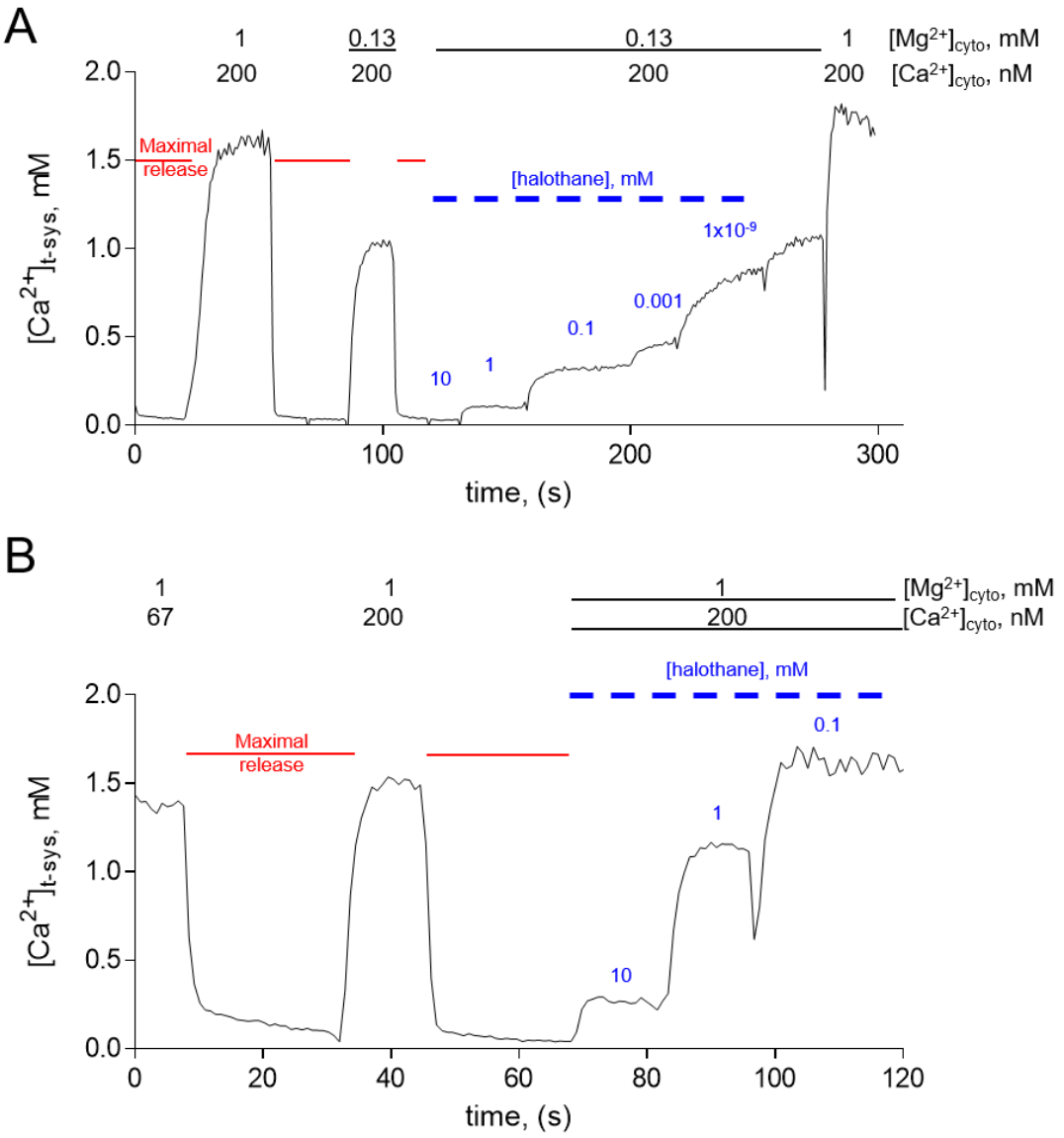

Figure 5.10. Steady-state $[Ca^{2+}]_{t\text{-system}}$ reached under varying concentrations of both Mg^{2+} and halothane.

The preparation was initially bathed with solutions mimicking the cytosol before maximally depleting the SR of Ca^{2+} (Red underscore). From nadir, the fiber was then bathed in solutions that contained 200 nM $[Ca^{2+}]_{cyto}$ with either 0.13 (*A*) or 1 mM $[Mg^{2+}]_{cyto}$ (*B*). The solution was also supplemented with varying [halothane] as indicated by the dashed blue line. The [halothane] was reduced in a step-wise manner (10, 1, 0.1, 0.001, and $1*10^{-9}$ mM).

The results obtained at various $[Mg^{2+}]_{cyto}$, and [halothane] (at 200 nM $[Ca^{2+}]_{cyto}$) are summarized in Figure 5.11. Values were normalized relative to the steady-state reached at 1 mM $[Mg^{2+}]_{cyto}$ in the absence of halothane. Under these conditions, the RyR1 is closed or has only a very low open probability P_0 ~2.5×10^{-8} (Laver *et al.*, 1997b; Baylor & Hollingworth, 2003). The $[Ca^{2+}]_{t\text{-}system}$ reaches its maximal levels when the RyR1s are closed, but declines as the RyR1s are activated, e.g., by lowering $[Mg^{2+}]_{cyto}$ or by application of halothane. In order to obtain a measure of the activity (or openness) of the RyR1, values at the y-axis are displayed as 1 - normalized t-sys values. This dataset was then plotted against the range of [halothane] tested and was fitted with a Hill equation. If we assume the RyR1s to be fully open (P_0~1) under conditions of maximally depleted $[Ca^{2+}]_{t\text{-}system}$ then the apparent activation status of the RyR1s P_0 can be derived from Figure 5.11. Thus, a maximally active RyR1 will have a value of 1 on the y-axis while a closed RyR1 will have a value close to 0. From Fig 5.11 we can see that the RyR1 is open for very low concentrations of Mg^{2+} (black line). Raising $[Mg^{2+}]_{cyto}$ causes a gradual inhibition of the RyR1, with full inhibition (y-axis value of 0) occurring for Mg^{2+} concentrations exceeding 1mM (left side of the graph, low halothane concentrations). The RyR1 agonist halothane can compete with the inhibition of Mg^{2+} allowing for the opening of the RyR1 even under high concentrations of Mg^{2+}. However, as Mg^{2+} concentrations increase, higher and higher halothane concentrations are necessary to open the RyR1 to the same extent. In consequence, apparent affinities for halothane (half activation of the sigmoidal curves) are shifted rightward in Fig 5.11.

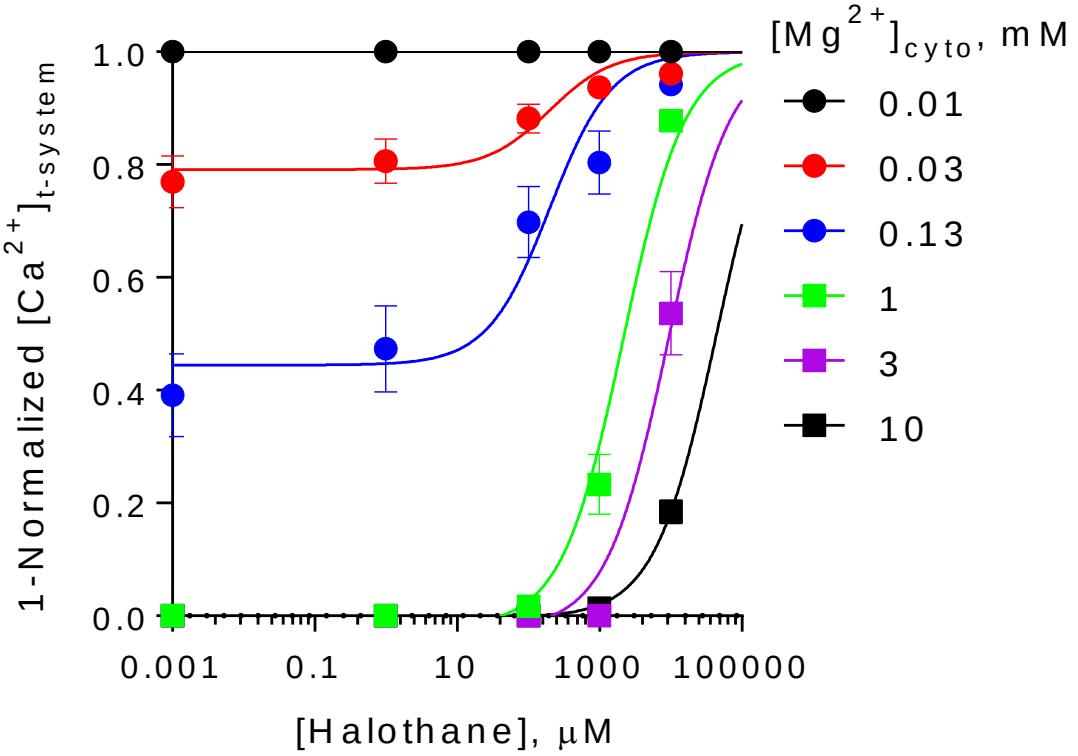

Figure 5.11. Concentration dependence of halothane and cytosolic Mg^{2+} on the apparent activity of the RyR1.

The experiment as described in Figure 5.11 was repeated on 5-11 (*n*=5-11) fibers for each $[Mg^{2+}]_{cyto}$ (as shown on the right). In all experiments, the $[Ca^{2+}]_{cyto}$ was maintained at 200 nM. To obtain a measure for the apparent activity of the RyR1, the accumulated data obtained at each [halothane] and $[Mg^{2+}]_{cyto}$ were normalized to the steady-state value reached at 200 nM $[Ca^{2+}]_{cyto}$ and 1 mM $[Mg^{2+}]_{cyto}$ ($[Ca^{2+}]_{cyto}$= 1.649 ± 0.047 mM) and are displayed as 1-normalized $[Ca^{2+}]_{t\text{-}system}$. All data were fitted with a Hill equation with the maximal value, and hill slope constrained to 1 and 1, respectively. The EC_{50} values are as follows; ($[Mg^{2+}]_{cyto}$, EC_{50}) 0.03 mM, 0.19±1.58; 0.13 mM, 0.19±1.58; 1 mM, 1.1±1.15; 3 mM, 9.6±1.14; 10 mM, 44.6±1.07. Each data point represents the mean ± S.E.M.

5.3.5 Pharmacological inhibition of the RyR1 with tetracaine in the presence of low $[Mg^{2+}]_{cyto}$

In the results presented above, it was demonstrated that an open RyR1 under low $[Mg^{2+}]_{cyto}$ caused a depletion of the $[Ca^{2+}]_{t\text{-}system}$. Increasing the Mg^{2+} inhibition of the RyR1 restored the $[Ca^{2+}]_{t\text{-}system}$ back to control levels. Next, pharmacological inhibition of the RyR1 by tetracaine was used as a secondary measure to demonstrate that the restitution of the t-system Ca^{2+} levels was dependent on blocking the activity of the RyR1. As shown in Figure 5.12*A* the $[Ca^{2+}]_{t\text{-}system}$ reached at 1342 nM $[Ca^{2+}]_{cyto}$ was depressed in the presence of 0.03 mM $[Mg^{2+}]_{cyto}$ (relative to that reached at 1 mM $[Mg^{2+}]_{cyto}$). The fiber was then challenged with increasing concentrations of the RyR1 inhibitor tetracaine while maintaining the same ionic conditions in the bathing solution. Similar to the results obtained by increasing the Mg^{2+} inhibition of the RyR1, the $[Ca^{2+}]_{t\text{-}system}$ increased with increasing [tetracaine]. These experiments were repeated on 4 additional fibers and the apparent activity of the RyR1 (1 - normalized $[Ca^{2+}]_{t\text{-}system}$) at 1342 nM $[Ca^{2+}]_{cyto}$ and 0.03 mM $[Mg^{2+}]_{cyto}$ is displayed in Figure 5.12*B*. In the presence of 10 µM [tetracaine], the RyR1 was almost fully open (~0.8± 0.02, mean ± SEM, n = 5). With increasing [tetracaine] up to 1 mM, the activity of the RyR1 was gradually reduced, with an apparent activity dropping to 0.25 ± 0.04 (n = 5) at 1 mM tetracaine.

These experiments were repeated with varying $[Ca^{2+}]_{cyto}$ (28, 67, 200, 1342 nM) at 0.03 mM $[Mg^{2+}]_{cyto}$ in the presence of 1 mM tetracaine, and these results are summarized in Figure 5.12*C.* As shown, the steady-values increased in the presence of a RyR1 inhibitor, suggesting that the inhibitory effects of tetracaine 'counteracted' the opening of the RyR1 due to reduced inhibition by Mg^{2+}.

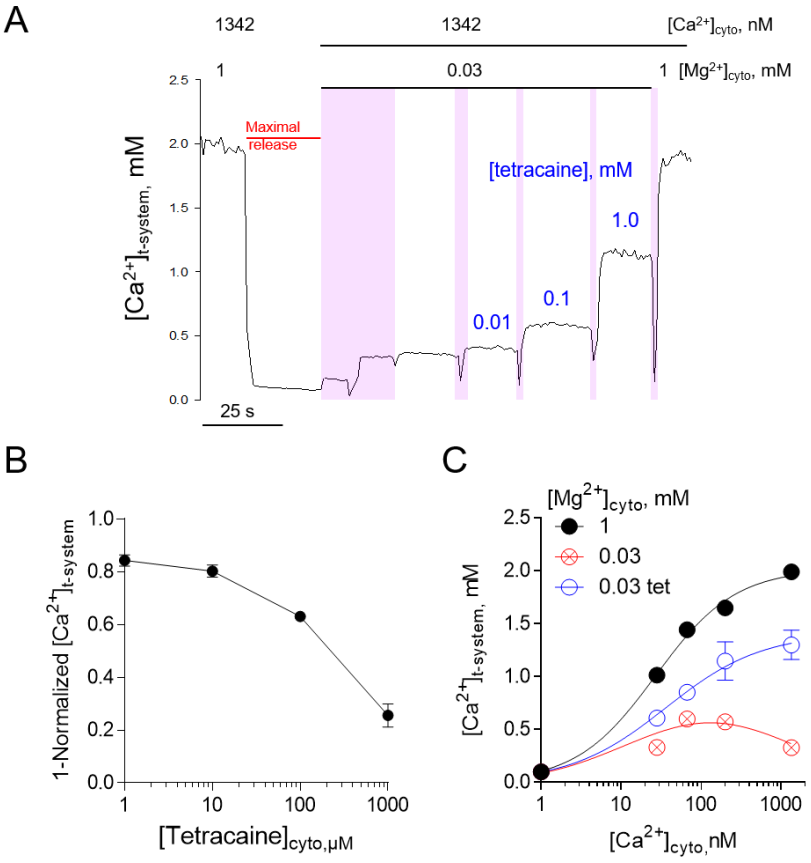

Figure 5.12. The reduced $[Ca^{2+}]_{t\text{-}system}$ observed in low-$[Mg^{2+}]_{cyto}$ is blocked by pharmacological inhibition of the RyR1.

(*A*) A selected trace of tracking the $[Ca^{2+}]_{t\text{-}system}$ in the presence of low-$[Mg^{2+}]_{cyto}$ and varying [tetracaine]. Rat skinned fibers were initially depleted of Ca^{2+} (red underscore) before bathing the fiber in a solution containing 1 mM $[Mg^{2+}]_{cyto}$, and 1342 nM $[Ca^{2+}]_{cyto}$. After another cycle of SR Ca^{2+} depletion, the fiber was then bathed in a solution containing 0.03 mM $[Mg^{2+}]_{cyto}$ and 1342 nM $[Ca^{2+}]_{cyto}$. While maintaining the same ionic conditions, the fiber was subsequently treated with increasing concentrations of tetracaine (0.01, 0.1, 1 mM). These experiments were repeated on 4 additional fibers, and the steady-state values for each [tetracaine] are shown in (*B*). Values were normalized to the steady-state obtained at 1 mM $[Mg^{2+}]_{cyto}$, and 1342 nM ($[Ca^{2+}]_{t\text{-}system}$= 1.9 ± 0.05 mM). The data is presented as 1-normalized $[Ca^{2+}]_{t\text{-}system}$ and the values are shown as mean ± S.E.M. (*C*) Summary of steady-state values for varying $[Ca^{2+}]_{cyto}$ (28, 67, 200, 1342 nM) obtained in the presence of 1 (black closed circles) and 0.03 mM (red crossed open circle) $[Mg^{2+}]_{cyto}$, and in the presence of 0.03 $[Mg^{2+}]_{cyto}$ and 1 mM tetracaine (blue open circles, *n*=3-20).

In Chapter 3 of this thesis, it was demonstrated that the inhibitory effect of dantrolene on the RyR1 was Mg^{2+} dependent. Therefore, it was expected that dantrolene would be ineffective at restoring the $[Ca^{2+}]_{t\text{-}system}$ steady-state levels under low-Mg^{2+}. An example of these experiments is shown in Figure 5.13*A*. Similar to the protocols described previously the $[Ca^{2+}]_{t\text{-}system}$ steady-state obtained at 1342 nM $[Ca^{2+}]_{cyto}$ and 1 mM $[Mg^{2+}]_{cyto}$ served as a reference value. The fiber was then challenged with either 0.03 or 0.13 mM $[Mg^{2+}]_{cyto}$ while maintaining the same $[Ca^{2+}]_{cyto}$. After reaching the steady-state, the low-Mg^{2+} solutions were supplemented with 50 µM dantrolene. As expected, dantrolene did not increase the steady-state levels under low-Mg^{2+} conditions, which indicates that dantrolene did not inhibit the RyR1. Varying the $[Ca^{2+}]_{cyto}$ at either 0.03 or 0.13 mM $[Mg^{2+}]_{cyto}$ did not change this result (summarized in Figure 5.13*B, & C*, respectively). These results further corroborate the hypothesis that the inhibitory effect of dantrolene is Mg^{2+} dependent.

In another series of experiments, the RyR1 was pharmacologically activated with varying [halothane] under physiologically relevant $[Mg^{2+}]_{cyto}$ (1 mM) and 200 nM $[Ca^{2+}]_{cyto}$. In the continued presence of halothane, the fiber was then challenged with varying concentrations of dantrolene. Contrasted to the experiment described above, activating the RyR1 with a pharmacological agent allowed for a direct assessment of the inhibitory effect of dantrolene under more physiologically relevant ionic conditions. These results are summarized in Figure 5.14. Values were normalized as previously described (Figure 5.11). However the values were not presented as 1-normalized $[Ca^{2+}]_{t\text{-}system}$. Therefore, values close to 1 or 0 represents either a near to closed RyR1 or an open RyR1, respectively.

From Figure 5.14 in the absence of dantrolene (purple dashed line), lower concentrations of halothane were required to activate the RyR1. However, in the presence of dantrolene, greater concentrations of halothane were required to open the RyR1 to the same degree (as demonstrated by a rightward shift of the sigmoidal curves). These results suggest that dantrolene acts as a competitive antagonist to the agonistic action of halothane at the RyR1.

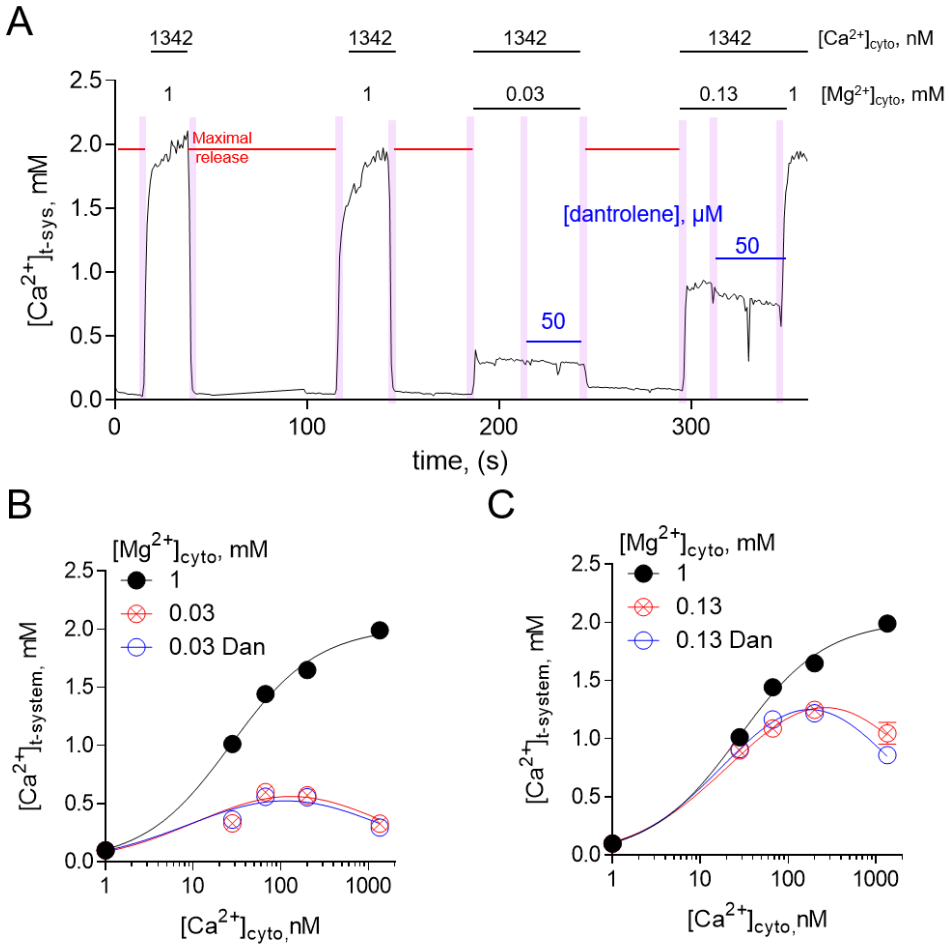

Figure 5.13. The inhibtory effects of dantrolene are not observed in low-$[Mg^{2+}]_{cyto}$. (*A*) A selected trace of tracking the $[Ca^{2+}]_{t\text{-system}}$ in the presence of low-$[Mg^{2+}]_{cyto}$ and 50 µM dantrolene. The skinned rat fiber was subjected to cycles of maximal SR Ca^{2+} depletion (red underscore) and uptake at 1 mM $[Mg^{2+}]_{cyto}$ and 1342 nM $[Ca^{2+}]_{cyto}$. From $[Ca^{2+}]_{t\text{-system}}$ nadir the fiber was then bathed in either 0.03 or 0.13 $[Mg^{2+}]_{cyto}$ and 1342 nM $[Ca^{2+}]_{cyto}$. After reaching a steady-state, the bathing solution was then suplemented with 50 µM dantrolene. These experiments were repeated over varying $[Ca^{2+}]_{cyto}$ and the steady-state reached is summarized in *B* (0.03 mM $[Mg^{2+}]_{cyto}$, *n*=4) and *C* (0.13 mM $[Mg^{2+}]_{cyto}$, *n*=4-7), both with and without dantrolene.

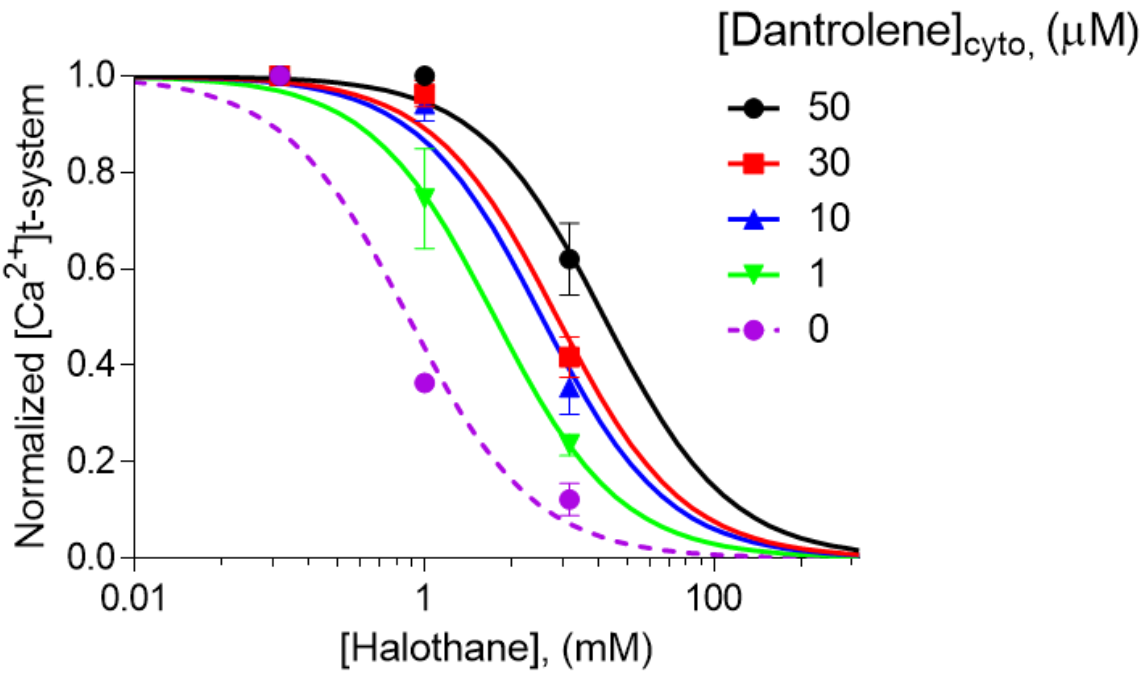

Figure 5.14. Increase in the apparent RyR1 activity by halothane is inhibited by dantrolene in the presence of physiologically relevant $[Mg^{2+}]_{cyto}$.

Similar to the protocol shown in Figure 5.10*B*, mechanically skinned fibers were subjected to varying [halothane] (0.1, 1, 20 mM) in the constant presence of 200 nM $[Ca^{2+}]_{cyto}$ and 1 mM $[Mg^{2+}]_{cyto}$. While maintaining the same ionic conditions in the continued presence of halothane the fiber was then exposed to varying [dantrolene] (0, 1, 10, 30, 50 µM). The steady-state values were normalized to the steady-state obtained at 200 nM $[Ca^{2+}]_{cyto}$ and 1 mM $[Mg^{2+}]_{cyto}$. Data were obtained from 5 fibers (*n*=5; presented as mean ± S.E.M) for each halothane and dantrolene concentration. All data were fitted with a Hill equation with the maximal value, minimal value and hill slope constrained to 1, 1 and 1, respectively. The EC_{50} values are as follows; ([Dantrolene], EC_{50}) 0 µM, 0.77±1.1; 1 µM, 3.01±1.14; 10 µM, 6.45±1.09; 30 µM, 8.25±1.08; 50 µM, 17.41±1.12.

5.4 Discussion

This work aimed to develop a methodology to detect changes in RyR1 activity utilizing Ca^{2+}-dependent fluorescent indicators trapped in the t-system of skinned fibres. Dysfunction of the RyR1 has been implicated in multiple congenital muscle myopathies (Bharucha-Goebel *et al.*, 2013; Dowling *et al.*, 2014; Ríos *et al.*, 2015; Rosenberg *et al.*, 2015), therefore there is a growing demand for additional pharmacological agents that inhibit the activity of the RyR1. However, current methods used to assay the RyR1 are done largely under ionic conditions that do not resemble the skeletal muscle cytosol (Szentesi *et al.*, 2001; Diaz-Sylvester *et al.*, 2008; Wagner Ii *et al.*, 2014). Therefore, potential drug candidate targeting RyR1 that act in a similar manner as dantrolene (Mg^{2+} dependent) may be easily overlooked.

Here it was examined whether the free $[Ca^{2+}]_{SR}$ or $[Ca^{2+}]_{t\text{-}system}$ could serve as a measure of RyR1 activity. It was found that the free $[Ca^{2+}]_{SR}$ remained comparable over the broad range of $[Mg^{2+}]_{cyto}$ tested (Figure 5.5 and 5.7). The reduced capacity of the SR to load Ca^{2+} under low-Mg^{2+} conditions indicates that the RyR1 activity increased under the imposed experimental conditions (Figure 5.6). Similarly, an increase in RyR1 activity (induced by low-Mg^{2+} or pharmacological agonist) resulted in the depletion of the $[Ca^{2+}]_{t\text{-}system}$ (Figure 5.9). Importantly, the degree of $[Ca^{2+}]_{t\text{-}system}$ depletion was shown to be dependent on the activity of the RyR1. Furthermore, pharmacological inhibitors of the RyR1 was shown to attenuate the degree of $[Ca^{2+}]_{t\text{-}system}$ depletion (Figure 5.12 and Figure 5.14). Thus, indicating that the $[Ca^{2+}]_{t\text{-}system}$ is able to report changes in RyR1 activity. An advantage of this technique is that the mechanically skinned fiber allows for direct access to the cytosol for experimental manipulation while maintaining the RyR1 and the associated accessory proteins in their native environment. Therefore, any influence that these accessory proteins may have on the activity of the RyR1 are preserved in the presented experimental approach.

5.4.1 Ca^{2+} uptake into the SR

This study characterized the change in free $[Ca^{2+}]_{SR}$ over varying concentrations of cytosolic Ca^{2+} and Mg^{2+} in rat fast-twitch EDL fibers. The free $[Ca^{2+}]_{SR}$ was calculated based on the determined apparent dissociation constant of fluo-5N (Kd ~ 400 µM). This value is similar to previously calibrated values determined in cardiac myocytes and is in good agreement with values derived from *in vitro* calibrations under similar ionic conditions

(Shannon *et al.*, 2003). Under endogenous ionic conditions in the cytosol (~50 nM $[Ca^{2+}]_{cyto}$, 1 mM $[Mg^{2+}]_{cyto}$), the free $[Ca^{2+}]_{SR}$ was found to be approximately 0.5 mM (expressed relative to the SR volume). Although the determined Kd_{Ca} of fluo-5N was lower in a study done by Ziman *et al.,* (2010) (~133 µM) the resting free $[Ca^{2+}]_{SR}$ was in close agreement (~0.4 mM at rest found in mouse flexor digitorum brevis muscle (Ziman *et al.*, 2010)).

It was also found that the steady-state values of free $[Ca^{2+}]_{SR}$ can remain high despite substantial loss of the total $[Ca^{2+}]_{SR}$ (Figure 5.5, 5.6). This was demonstrated by showing that the free $[Ca^{2+}]_{SR}$ remained saturated at varying open states of the RyR1 ($[Ca^{2+}]_{cyto}$~28, 1342 nM; Figure 5.7). This is likely due to the activity of the SERCA pump, which would be working near maximal capacity at 1342 nM $[Ca^{2+}]_{cyto}$ (Koivumäki *et al.*, 2009; Bakker *et al.*, 2017). Furthermore, it was found that the free $[Ca^{2+}]_{SR}$ saturated at a faster time course relative to the total $[Ca^{2+}]_{SR}$ (Murphy *et al.*, 2009). The time course to reach a maximal total $[Ca^{2+}]_{SR}$ is also consistent with increasing CSQ buffering power (Murphy *et al*., 2009). These observations are in agreement with previous studies which suggests that the free $[Ca^{2+}]_{SR}$ is determined by the net uptake and release of SR Ca^{2+} and is not determined by CSQ nor the total $[Ca^{2+}]_{SR}$ (Fryer & Stephenson, 1996; Murphy *et al.*, 2009; Canato *et al.*, 2010). Collectively these observations suggest that the activity of the RyR cannot be determined from the free $[Ca^{2+}]_{SR}$.

5.4.2 Store dependent depletion of $[Ca^{2+}]_{t\text{-}system}$

The depletion of t-system Ca^{2+} has been demonstrated to be facilitated by SOCE upon SR Ca^{2+} depletion in previous works (Launikonis & Ríos, 2007; Duke *et al.*, 2010; Cully *et al.*, 2016). The short distance between the junctional SR and t-system membrane makes it possible for direct interactions of membrane bound proteins; such as those involved in SOCE (STIM1 and Orai1) and EC-coupling (DHPR and RyR1).

This study observed a graded depletion of t-system Ca^{2+} that was dependent on the activity of the RyR1. It is expected that SR Ca^{2+} will be depleted to varying degrees depending on the activity RyR1 (Figure 5.5, 5.6); therefore, this may suggest that the graded depletion of t-system Ca^{2+} was due to varying activity of SOCE. Interestingly, in this study, the activation of SOCE as detected by the $[Ca^{2+}]_{t\text{-}system}$ was not dependent on the measured free $[Ca^{2+}]_{SR}$. As demonstrated in Figure 5.5, the free $[Ca^{2+}]_{SR}$ remained comparable across the tested $[Mg^{2+}]_{cyto}$ (0.03-1 mM) at 1342 nM $[Ca^{2+}]_{cyto}$; however, under

the same ionic condition imposed in the cytosol a graded depletion of $[Ca^{2+}]_{t\text{-}system}$ was observed (Figure 5.9*B*). These observations may argue against the involvement of SOCE, which requires that Ca^{2+} unbinds from a Ca^{2+} sensing EF-domain of STIM1 (Liou *et al.*, 2005; Stathopulos *et al.*, 2005; Zhang *et al.*, 2005). However, it is important to note that fluo-5N as measured in this study reports the bulk-free $[Ca^{2+}]_{SR}$ and may not reflect the Ca^{2+} environment near the junctional SR where the RyR1, STIM1, and majority of CSQ come in close contact (Franzini-Armstrong *et al.*, 1987; Launikonis & Ríos, 2007; Darbellay *et al.*, 2011; Manno *et al.*, 2017). Thus, it is possible that the vast network of CSQ molecules at the junctional SR lumen become a diffusion barrier between the bulk SR and near membrane at the RyRs. Increases in RyR1 activity would allow a local Ca^{2+} depletion to activate SOCE (dissociated Ca^{2+} from STIM1) without a major change in bulk $[Ca^{2+}]_{SR}$ (Cully *et al.*, 2016). The development of a targeted Ca^{2+} sensor localized to the junctional SR would aid greatly in understanding the dynamic Ca^{2+} environment within this nano-domain and directly test this hypothesis.

5.4.3 Determination of the steady-state $[Ca^{2+}]_{t\text{-}system}$ during increased activity of the RyR1

The two major t-system Ca^{2+} fluxes involved in this system includes Ca^{2+} efflux mediated by SOCE, and Ca^{2+} uptake facilitated by membrane bound Ca^{2+} transporters (PMCA and NCX). Therefore, since both of these pathways are active under conditions where SOCE is occurring (low-Mg^{2+}, and in the presence of a RyR1 agonist; Figure 5.9), the steady-state $[Ca^{2+}]_{t\text{-}system}$ must reflect the point in which all of the major Ca^{2+} flux is at equilibrium. It is important to note that Ca^{2+} influx through the DHPR was also considered. However, as shown in Figure 5.13 dantrolene did not affect the steady-state $[Ca^{2+}]_{t\text{-}system}$ under low-Mg^{2+} concentrations in the cytosol. From previous works (Bannister, 2013), it was demonstrated that dantrolene inhibits L-type Ca^{2+} currents. Therefore, since no changes in $[Ca^{2+}]_{t\text{-}system}$, was observed it could be concluded that L-type Ca^{2+} currents play little role in the Ca^{2+} efflux pathway observed in this study.

Under low-Mg^{2+}, a depletion of $[Ca^{2+}]_{t\text{-}system}$ was observed in the transition from 200 to 1342 nM $[Ca^{2+}]_{cyto}$ (Figure 5.9). To explain this observation, we must consider the two Ca^{2+} fluxes at play. Raised levels of free $[Ca^{2+}]_{SR}$ (as demonstrated in Figure 5.5) and raised $[Ca^{2+}]_{cyto}$ would likely increase the activity of the RyR1 (Laver *et al.*, 2004). It is expected that the activity of SOCE would also increase in parallel with increased RyR1 activity. In addition, due to a raised level of Ca^{2+} in the triadic junction, we would also

expect to observe an increased capacity to extrude Ca^{2+}. Therefore, to observe a net depletion of $[Ca^{2+}]_{t\text{-}system}$ the net Ca^{2+} influx due to SOCE must have been greater than the Ca^{2+} efflux (Ca^{2+} extrusion). These observations suggest that under conditions where the RyR1 is sufficiently open, the steady-state values are largely determined by SOCE. This is further supported by showing the restitution of $[Ca^{2+}]_{t\text{-}system}$ in the presence of tetracaine in low-Mg^{2+}.

In summary, this study provides evidence suggesting that the degree of RyR1 activity can be estimated from the $[Ca^{2+}]_{t\text{-}system}$. The major advantage this technique provides is the ability to measure activity of the RyR1 under physiological ionic conditions with the RyR1 in its endogenous state.

Chapter 6: Concluding remarks

The results presented in this thesis focused on furthering our understanding of the underlying mechanisms involved in Ca^{2+} handling during a malignant hyperthermia event, and the pharmacological agent used to treat it. Utilizing fluorescent Ca^{2+} imaging in mechanically skinned fibers isolated from rat and human malignant hyperthermia susceptible muscle, Chapter 3 considered the role of Mg^{2+} in the inhibitory effect of dantrolene. The two prevailing hypothesis of the mechanism of overactive Ca^{2+} release during a malignant hyperthermia event was addressed in Chapter 4. Chapter 5 in this thesis revisited the results presented in Chapter 3 and purposed a novel assay to detect changes in RyR1 activity under physiologically relevant ionic conditions.

Dantrolene has been used to great success in reducing mortality associated with malignant hyperthermia. A unique characteristic of dantrolene was its ability to inhibit skeletal muscle contractions without producing significant adverse effects on cardiac muscle. Other known RyR inhibitors such as tetracaine have been shown to effect both isoforms of the RyRs (Shannon *et al.*, 2002; Laver & van Helden, 2011), and therefore is unusable candidates to treat malignant hyperthermia. The selective inhibition of skeletal muscle RyR1 might be explained by the drugs dependence on cytosolic Mg^{2+} (Chapter 3, 5 and (Choi *et al.*, 2017)). That is, the reduced affinity for Mg^{2+} on the inhibitory site of cardiac RyR2 (K_i of 1mM and 0.1 mM in RyR2 and RyR1, respectively) (Meissner *et al.*, 1988; Xu *et al.*, 1996; Laver *et al.*, 1997a) may also reduce the efficacy of dantrolene. Therefore, this information may be useful in the developing new candidate drugs, which selectively target the skeletal muscle isoform of the RyR.

As demonstrated in Chapter 5, utilizing $[Ca^{2+}]_{t\text{-}system}$ to detect RyR1 activity is an ideal assay to screen for such a drug. It was shown in this assay that dantrolene was unable to inhibit the RyR1 under low-Mg^{2+} conditions in the cytosol. Tetracaine and raised $[Mg^{2+}]_{cyto}$ both were able to inhibit the RyR1 and therefore were used as a positive control in these experiments. Furthermore, based on the observations made in Chapter 3, dantrolene under low-Mg^{2+} can be used as a negative control. Importantly, in the presence of physiological relevant $[Mg^{2+}]_{cyto}$, dantrolene was able to inhibit halothane induced opening of the RyR1 in a concentration dependent manner. These observations further supported the hypothesis that the inhibitory effect of dantrolene is Mg^{2+} dependent. In addition, collectively these results demonstrate the sensitivity of the purposed assay.

This thesis also demonstrated that raised $[Mg^{2+}]_{cyto}$ (≥1.5 mM) was necessary for dantrolene to inhibit halothane induced Ca^{2+} waves in human muscle susceptible to malignant hyperthermia. However, as previously demonstrated, pre-administration of dantrolene has been shown to inhibit a malignant hyperthermia event in susceptible pigs (Harrison, 1975). To reconcile these observations, it is important to note that the concentration of halothane used in this study (1 mM) is greater than what is commonly used during an IVCT test (~ 2% halothane corresponds to approximately 0.44 mM (Hopkins *et al.*, 2015)). Furthermore, it is also important to consider that RyR1 variants may also show varying sensitivity to halothane (Figure 3.10, *B* and *D*). Therefore, in the study conducted by Harrison *et al.* (1975), it is possible that either the halothane concentration in the muscle never rose above 0.44 mM or the particular RyR1 variant in these pigs have a lower relative sensitivity to halothane.

The role of Ca^{2+} as the triggering molecule of a Ca^{2+}wave was also investigated. This study provided evidence that CICR is not an active mechanism during a malignant hyperthermia event in human skeletal muscle. The role of cytosolic Ca^{2+} is still open to interpretation. As demonstrated in Chapter 4, it is possible that cytosolic Ca^{2+} contributes to the 'pool' of Ca^{2+} necessary for SOICR to occur (Chen *et al.*, 2014; Chen *et al.*, 2017). This mechanism has been demonstrated previously in myocytes (Maxwell & Blatter, 2012); thus, future parallel studies in skeletal muscle will be important to further characterize overactive Ca^{2+} release during a malignant hyperthermia event.

Reference

Allen DG, Lamb GD & Westerblad H. (2008). Impaired calcium release during fatigue. *Journal of applied physiology* **104,** 296-305.

Andersson DC & Marks AR. (2010). Fixing ryanodine receptor Ca^{2+}-leak - a novel therapeutic strategy for contractile failure in heart and skeletal muscle. *Drug discovery today Disease mechanisms* **7,** e151-e157.

Armstrong CM, Bezanilla FM & Horowicz P. (1972). Twitches in the presence of ethylene glycol bis(β-aminoethyl ether)-N,N′-tetraacetic acid. *Biochimica et Biophysica Acta (BBA) - Bioenergetics* **267,** 605-608.

Augusto V, Padovani CR & Campos GER. (2004). Skeletal muscle fiber types in C57BL6J mice. *Braz J Morphol Sci* **21,** 89-94.

Bakker AJ, Cully TR, Wingate CD, Barclay CJ & Launikonis BS. (2017). Doublet stimulation increases Ca^{2+} binding to troponin C to ensure rapid force development in skeletal muscle. *The Journal of General Physiology* **149,** 323-334.

Bannister RA. (2013). Dantrolene-induced inhibition of skeletal L-type Ca^{2+} current requires RyR1 expression. *BioMed Res Int* **2013**.

Barclay CJ. (1996). Mechanical efficiency and fatigue of fast and slow muscles of the mouse. *The Journal of Physiology* **497,** 781-794.

Baylor SM & Hollingworth S. (2003). Sarcoplasmic reticulum calcium release compared in slow-twitch and fast-twitch fibres of mouse muscle. *The Journal of Physiology* **551,** 125-138.

Baylor SM & Hollingworth S. (2012). Intracellular calcium movements during excitation–contraction coupling in mammalian slow-twitch and fast-twitch muscle fibers. *The Journal of General Physiology* **139,** 261-272.

Bellinger AM, Reiken S, Carlson C, Mongillo M, Liu X & Rothman L. (2009). Hypernitrosylated ryanodine receptor calcium release channels are leaky in dystrophic muscle. *Nat Med* **15**.

Bers DM. (2002). Cardiac excitation-contraction coupling. *Nature* **415,** 198-205.

Bers DM & Stiffel VM. (1993). Ratio of ryanodine to dihydropyridine receptors in cardiac and skeletal muscle and implications for E-C coupling. *American Journal of Physiology - Cell Physiology* **264,** C1587-C1593.

Bharucha-Goebel DX, Santi M, Medne L, Zukosky K, Dastgir J, Shieh PB, Winder T, Tennekoon G, Finkel RS, Dowling JJ, Monnier N & Bönnemann CG. (2013). Severe congenital RYR1-associated myopathy: The expanding clinicopathologic and genetic spectrum. *Neurology* **80,** 1584-1589.

Block BA, Imagawa T, Campbell KP & Franzini-Armstrong C. (1988). Structural evidence for direct interaction between the molecular components of the transverse tubule/sarcoplasmic reticulum junction in skeletal muscle. *The Journal of Cell Biology* **107,** 2587-2600.

Boitier E, Rea R & Duchen MR. (1999). Mitochondria Exert a Negative Feedback on the Propagation of Intracellular Ca^{2+} Waves in Rat Cortical Astrocytes. *The Journal of Cell Biology* **145,** 795-808.

Canato M, Scorzeto M, Giacomello M, Protasi F, Reggiani C & Stienen GJM. (2010). Massive alterations of sarcoplasmic reticulum free calcium in skeletal muscle fibers lacking calsequestrin revealed by a genetically encoded probe. *Proceedings of the National Academy of Sciences* **107,** 22326-22331.

Cannell M, Cheng H & Lederer W. (1995). The control of calcium release in heart muscle. *Science* **268,** 1045-1049.

Cannon SC. (2017). Mind the magnesium, in dantrolene suppression of malignant hyperthermia. *Proceedings of the National Academy of Sciences* **114,** 4576-4578.

Chen W, Koop A, Liu Y, Guo W, Wei J, Wang R, MacLennan DH, Dirksen RT & Chen SRW. (2017). Reduced threshold for store overload-induced Ca^{2+}release is a common defect of RyR1 mutations associated with malignant hyperthermia and central core disease. *Biochemical Journal* **474,** 2749-2761.

Chen W, Wang R, Chen B, Zhong X, Kong H, Bai Y, Zhou Q, Xie C, Zhang J, Guo A, Tian X, Jones PP, O'Mara ML, Liu Y, Mi T, Zhang L, Bolstad J, Semeniuk L, Cheng H, Zhang J, Chen J, Tieleman DP, Gillis AM, Duff HJ, Fill M, Song L-S & Chen SRW. (2014a). The ryanodine receptor store-sensing gate controls Ca2+ waves and Ca2+-triggered arrhythmias. *Nat Med* **20,** 184-192.

Cheng H, Lederer MR, Lederer WJ & Cannell MB. (1996). Calcium sparks and $[Ca^{2+}]_i$ waves in cardiac myocytes. *Am J Physiol* **270,** C148-159.

Cheng H, Lederer W & Cannell M. (1993). Calcium sparks: elementary events underlying excitation-contraction coupling in heart muscle. *Science* **262,** 740-744.

Choi RH, Koenig X & Launikonis BS. (2017). Dantrolene requires Mg^{2+} to arrest malignant hyperthermia. *Proceedings of the National Academy of Sciences* **114,** 4811-4815.

Coombes S, Hinch R & Timofeeva Y. (2004). Receptors, sparks and waves in a fire-diffuse-fire framework for calcium release. *Progress in biophysics and molecular biology* **85,** 197-216.

Cully TR, Edwards JN & Launikonis BS. (2014). Activation and propagation of Ca^{2+} release from inside the sarcoplasmic reticulum network of mammalian skeletal muscle. *The Journal of Physiology* **592,** 3727-3746.

Cully TR, Edwards JN, Murphy RM & Launikonis BS. (2016). A quantitative description of tubular system Ca^{2+} handling in fast- and slow-twitch muscle fibres. *The Journal of Physiology* **594,** 2795-2810.

Cully TR, Murphy RM, Roberts L, Raastad T, Fassett RG, Coombes JS, Jayasinghe ID & Launikonis BS. (2017). Human skeletal muscle plasmalemma alters its structure to change its Ca^{2+}-handling following heavy-load resistance exercise. *Nat Commun* **8,** 14266.

Darbellay B, Arnaudeau S, Bader CR, Konig S & Bernheim L. (2011). STIM1L is a new actin-binding splice variant involved in fast repetitive Ca($^{2+}$) release. *The Journal of Cell Biology* **194,** 335-346.

Dawson SP, Keizer J & Pearson JE. (1999). Fire-diffuse-fire model of dynamics of intracellular calcium waves. *Proc Natl Acad Sci U S A* **96,** 6060-6063.

Despa S, Shui B, Bossuyt J, Lang D, Kotlikoff MI & Bers DM. (2014). Junctional Cleft $[Ca^{2+}]_i$ Measurements Using Novel Cleft-Targeted Ca2+ Sensors. *Circulation Research* **115,** 339-347.

Diaz-Sylvester PL, Porta M & Copello JA. (2008). Halothane modulation of skeletal muscle ryanodine receptors: dependence on Ca^{2+}, Mg^{2+} and ATP. *American journal of physiology Cell physiology* **294,** C1103-C1112.

Donoso P & Hidalgo C. (1989). Sodium-calcium exchange in transverse tubules isolated from frog skeletal muscle. *Biochimica et Biophysica Acta (BBA) - Biomembranes* **978,** 8-16.

Dowling JJ, Lawlor MW & Dirksen RT. (2014). Triadopathies: An Emerging Class of Skeletal Muscle Diseases. *Neurotherapeutics* **11,** 773-785.

Duke AM, Hopkins PM, Calaghan SC, Halsall JP & Steele DS. (2010). Store-operated Ca^{2+} Entry in Malignant Hyperthermia-susceptible Human Skeletal Muscle. *The Journal of Biological Chemistry* **285,** 25645-25653.

Duke AM, Hopkins PM, Halsall PJ & Steele DS. (2006). Mg^{2+} dependence of Ca^{2+} release from the sarcoplasmic reticulum induced by sevoflurane or halothane in skeletal

muscle from humans susceptible to malignant hyperthermia. *British Journal of Anaesthesia* **97,** 320-328.

Duke AM, Hopkins PM & Steele DS. (2002). Effects of Mg^{2+} and SR luminal Ca^{2+} on caffeine-induced Ca^{2+} release in skeletal muscle from humans susceptible to malignant hyperthermia. *The Journal of Physiology* **544,** 85-95.

Duke AM, Hopkins PM & Steele DS. (2003). Mg^{2+} dependence of halothane-induced Ca^{2+} release from the sarcoplasmic reticulum in rat skeletal muscle. *The Journal of Physiology* **551,** 447-454.

Duke Adrian M, Hopkins Philip M, Halsal Jane & Steele Derek S. (2004). Mg^{2+} Dependence of Halothane-induced Ca^{2+}Release from the Sarcoplasmic Reticulum in Skeletal Muscle from Humans Susceptible to Malignant Hyperthermia. *Anesthesiology* **101,** 1339-1346.

Dulhunty AF, Casarotto MG & Beard NA. (2011). The ryanodine receptor: a pivotal Ca^{2+} regulatory protein and potential therapeutic drug target. *Curr Drug Targets* **12,** 709-723.

Dulhunty A, Wei L & Beard N. (2009). Junctin – the quiet achiever. *The Journal of Physiology* **587,** 3135-3137.

Dumonteil E, Barre H & Meissner G. (1993). *Sarcoplasmic reticulum Ca^{2+}-ATPase and ryanodine receptor in cold-acclimated ducklings and thermogenesis*, vol. 265.

Dutka TL & Lamb GD. (2004). Effect of low cytoplasmic [ATP] on excitation–contraction coupling in fast-twitch muscle fibres of the rat. *The Journal of Physiology* **560,** 451-468.

Edwards JN, Blackmore DG, Gilbert DF, Murphy RM & Launikonis BS. (2011). Store-operated calcium entry remains fully functional in aged mouse skeletal muscle despite a decline in STIM1 protein expression. *Aging Cell* **10,** 675-685.

Edwards JN & Launikonis BS. (2008). The accessibility and interconnectivity of the tubular system network in toad skeletal muscle. *J Physiol* **586,** 5077-5089.

Edwards JN, Murphy RM, Cully TR, von Wegner F, Friedrich O & Launikonis BS. (2010). Ultra-rapid activation and deactivation of store-operated Ca^{2+} entry in skeletal muscle. *Cell Calcium* **47,** 458-467.

Eisenberg BR. (2010). Quantitative Ultrastructure of Mammalian Skeletal Muscle. In *Comprehensive Physiology*. John Wiley & Sons, Inc.

Endo M. (1977). *Calcium release from the sarcoplasmic reticulum*, vol. 57.

Endo M. (2009). Calcium-induced calcium release in skeletal muscle. *Physiol Rev* **89,** 1153-1176.

Endo M, Tanaka M & Ogawa Y. (1970). Calcium Induced Release of Calcium from the Sarcoplasmic Reticulum of Skinned Skeletal Muscle Fibres. *Nature* **228,** 34-36.

Fabiato A. (1985). Time and calcium dependence of activation and inactivation of calcium-induced release of calcium from the sarcoplasmic reticulum of a skinned canine cardiac Purkinje cell. *The Journal of General Physiology* **85,** 247-289.

Felder E & Franzini-Armstrong C. (2002). Type 3 ryanodine receptors of skeletal muscle are segregated in a parajunctional position. *Proceedings of the National Academy of Sciences* **99,** 1695-1700.

Figueroa L, Shkryl VM, Zhou J, Manno C, Momotake A, Brum G, Blatter LA, Ellis-Davies GCR & Ríos E. (2012). Synthetic localized calcium transients directly probe signalling mechanisms in skeletal muscle. *The Journal of Physiology* **590,** 1389-1411.

Franzini-Armstrong C. (2004). Functional implications of RyR-DHPR relationships in skeletal and cardiac muscles. *Biol Res* **37,** 507-512.

Franzini-Armstrong C & Jorgensen AO. (1994). Structure and Development of E-C Coupling Units in Skeletal Muscle. *Annual Review of Physiology* **56,** 509-534.

Franzini-Armstrong C, Kenney LJ & Varriano-Marston E. (1987). The structure of calsequestrin in triads of vertebrate skeletal muscle: a deep-etch study. *The Journal of Cell Biology* **105,** 49-56.

Franzini-Armstrong C & Peachey LD. (1981). Striated muscle-contractile and control mechanisms. *The Journal of Cell Biology* **91,** 166s-186s.

Fruen BR, Mickelson JR & Louis CF. (1997). Dantrolene Inhibition of Sarcoplasmic Reticulum Ca^{2+}Release by Direct and Specific Action at Skeletal Muscle Ryanodine Receptors. *Journal of Biological Chemistry* **272,** 26965-26971.

Fryer MW & Stephenson DG. (1996). Total and sarcoplasmic reticulum calcium contents of skinned fibres from rat skeletal muscle. *The Journal of Physiology* **493,** 357-370.

Gillies RL, Bjorksten AR, Du Sart D & Hockey BM. (2015). Analysis of the entire ryanodine receptor type 1 and alpha 1 subunit of the dihydropyridine receptor (CACNA1S) coding regions for variants associated with malignant hyperthermia in Australian families. *Anaesth Intensive Care* **43,** 157-166.

Grabner M, Dirksen RT, Suda N & Beam KG. (1999). The II-III Loop of the Skeletal Muscle Dihydropyridine Receptor Is Responsible for the Bi-directional Coupling with the Ryanodine Receptor. *Journal of Biological Chemistry* **274,** 21913-21919.

Györke I, Hester N, Jones LR & Györke S. (2004). The Role of Calsequestrin, Triadin, and Junctin in Conferring Cardiac Ryanodine Receptor Responsiveness to Luminal Calcium. *Biophysical journal* **86,** 2121-2128.

Hainaut K & Desmedt JE. (1974). Effect of dantrolene sodium on calcium movements in single muscle fibres. *Nature* **252,** 728-730.

Harrison GG. (1975). Control of the malignant hyperpyrexic syndrome in MHS swine by dantrolene sodium. *Br J Anaesth* **47,** 62-65.

Hidalgo C, González ME & García AM. (1986). Calcium transport in transverse tubules isolated from rabbit skeletal muscle. *Biochimica et Biophysica Acta (BBA) - Biomembranes* **854,** 279-286.

Hidalgo C, Gonzalez ME & Lagos R. (1983). Characterization of the Ca^{2+}- or Mg^{2+}-ATPase of transverse tubule membranes isolated from rabbit skeletal muscle. *Journal of Biological Chemistry* **258,** 13937-13945.

Hidalgo J, Luxoro M & Rojas E. (1979). On the role of extracellular calcium in triggering contraction in muscle fibres from barnacle under membrane potential control. *The Journal of Physiology* **288,** 313-330.

Hogan PG & Rao A. (2015). Store-operated calcium entry: mechanisms and modulation. *Biochemical and biophysical research communications* **460,** 40-49.

Hopkins PM. (2006). Skeletal muscle physiology. *Continuing Education in Anaesthesia, Critical Care & Pain* **6,** 1-6.

Hopkins PM. (2011). Malignant hyperthermia: pharmacology of triggering. *Br J Anaesth* **107**.

Hopkins PM, Rüffert H, Snoeck MM, Girard T, Glahn KPE, Ellis FR, Müller CR, Urwyler A, Bandschapp O, Gillies R, Glauber V, Heytens L, Islander G, Klingler W, Kraft B, Krivosic-Horber R, Pollock N, Schuster F, Silva H, Sorrentino V, Street N, Tegazzin V & Tzanova I. (2015). European Malignant Hyperthermia Group guidelines for investigation of malignant hyperthermia susceptibility. *BJA: British Journal of Anaesthesia* **115,** 531-539.

Huxley HE. (1973). Structural Changes in the Actin- and Myosin-eontaining Filaments during Contraction. *Cold Spring Harbor Symposia on Quantitative Biology* **37,** 361-376.

Ikemoto N, Antoniu B, Kang JJ, Meszaros LG & Ronjat M. (1991). Intravesicular calcium transient during calcium release from sarcoplasmic reticulum. *Biochemistry* **30,** 5230-5237.

Izu LT, Wier WG & Balke CW. (2001). Evolution of cardiac calcium waves from stochastic calcium sparks. *Biophysical journal* **80,** 103-120.

Jayasinghe ID & Launikonis BS. (2013). Three-dimensional reconstruction and analysis of the tubular system of vertebrate skeletal muscle. *Journal of Cell Science* **126,** 4048-4058.

Jayasinghe ID, Lo HP, Morgan GP, Baddeley D, Parton RG, Soeller C & Launikonis BS. (2013). Examination of the subsarcolemmal tubular system of mammalian skeletal muscle fibers. *Biophysical journal* **104,** L19-21.

Jiang D, Chen W, Xiao J, Wang R, Kong H & Jones PP. (2008). Reduced threshold for luminal Ca^{2+} activation of RyR1 underlies a causal mechanism of porcine malignant hyperthermia. *J Biol Chem* **283**.

Jungbluth H. (2007). Central core disease. *Orphanet J Rare Dis* **2**.

Kaneko T, Tanaka H, Oyamada M, Kawata S & Takamatsu T. (2000). Three distinct types of Ca^{2+} waves in Langendorff-perfused rat heart revealed by real-time confocal microscopy. *Circ Res* **86,** 1093-1099.

Karatzaferi C, de Haan A, Ferguson RA, van Mechelen W & Sargeant AJ. (2001). Phosphocreatine and ATP content in human single muscle fibres before and after maximum dynamic exercise. *Pflugers Archiv : European journal of physiology* **442,** 467-474.

Kashiyama T, Murayama T, Suzuki E, Allen PD & Ogawa Y. (2010). Frog alpha- and beta-ryanodine receptors provide distinct intracellular Ca^{2+} signals in a myogenic cell line. *PLoS One* **5,** e11526.

Keizer J, Smith GD, Ponce-Dawson S & Pearson JE. (1998). Saltatory propagation of Ca^{2+} waves by Ca^{2+} sparks. *Biophysical journal* **75,** 595-600.

Keller M, Kao JP, Egger M & Niggli E. (2007). Calcium waves driven by "sensitization" wave-fronts. *Cardiovasc Res* **74,** 39-45.

Klein MG, Simon BJ & Schneider MF. (1990). Effects of caffeine on calcium release from the sarcoplasmic reticulum in frog skeletal muscle fibres. The Journal of Physiology 425, 599-626.

Kobayashi S, Bannister ML, Gangopadhyay JP, Hamada T, Parness J & Ikemoto N. (2005). Dantrolene Stabilizes Domain Interactions within the Ryanodine Receptor. *Journal of Biological Chemistry* **280,** 6580-6587.

Koivumäki JT, Takalo J, Korhonen T, Tavi P & Weckström M. (2009). Modelling sarcoplasmic reticulum calcium ATPase and its regulation in cardiac myocytes. *Philosophical Transactions of the Royal Society A: Mathematical, Physical and Engineering Sciences* **367,** 2181-2202.

Kort AA, Capogrossi MC & Lakatta EG. (1985). Frequency, amplitude, and propagation velocity of spontaneous Ca^{2+}-dependent contractile waves in intact adult rat cardiac muscle and isolated myocytes. *Circ Res* **57,** 844-855.

Kurebayashi N & Ogawa Y. (2001). Depletion of Ca^{2+} in the sarcoplasmic reticulum stimulates Ca^{2+} entry into mouse skeletal muscle fibres. *The Journal of Physiology* **533,** 185-199.

Lai FA, Liu QY, Xu L, el-Hashem A, Kramarcy NR, Sealock R & Meissner G. (1992). Amphibian ryanodine receptor isoforms are related to those of mammalian skeletal or cardiac muscle. *American Journal of Physiology - Cell Physiology* **263,** C365-C372.

Lamb G. (2000). Excitation–Contraction Coupling In Skeletal Muscle: Comparisons With Cardiac Muscle. *Clinical and Experimental Pharmacology and Physiology* **27,** 216-224.

Lamb GD. (1993). Ca^{2+} inactivation, Mg^{2+} inhibition and malignant hyperthermia. *Journal of Muscle Research & Cell Motility* **14,** 554-556.

Lamb GD, Cellini MA & Stephenson DG. (2001). Different Ca^{2+} releasing action of caffeine and depolarisation in skeletal muscle fibres of the rat. *The Journal of Physiology* **531,** 715-728.

Lamb GD, Junankar PR & Stephenson DG. (1995). Raised intracellular [Ca^{2+}] abolishes excitation-contraction coupling in skeletal muscle fibres of rat and toad. *The Journal of Physiology* **489,** 349-362.

Lamb GD & Stephenson DG. (1991). Effect of Mg^{2+} on the control of Ca^{2+} release in skeletal muscle fibres of the toad. *The Journal of Physiology* **434,** 507-528.

Lamb GD & Stephenson DG. (1994). Effects of intracellular pH and [Mg^{2+}] on excitation-contraction coupling in skeletal muscle fibres of the rat. *The Journal of Physiology* **478,** 331-339.

Lamb GD & Walsh T. (1987). Calcium currents, charge movement and dihydropyridine binding in fast- and slow-twitch muscles of rat and rabbit. *The Journal of Physiology* **393,** 595-617.

Lamboley CR, Murphy RM, McKenna MJ & Lamb GD. (2013). Endogenous and maximal sarcoplasmic reticulum calcium content and calsequestrin expression in type I and type II human skeletal muscle fibres. *The Journal of Physiology* **591,** 6053-6068.

Lamboley CR, Murphy RM, McKenna MJ & Lamb GD. (2014). Sarcoplasmic reticulum Ca^{2+} uptake and leak properties, and SERCA isoform expression, in type I and type II fibres of human skeletal muscle. *J Physiol* **592,** 1381-1395.

Larach Marilyn G, Brandom Barbara W, Allen Gregory C, Gronert Gerald A & Lehman Erik B. (2008). Cardiac Arrests and Deaths Associated with Malignant Hyperthermia in North America from 1987 to 2006A Report from The North American Malignant Hyperthermia Registry of the Malignant Hyperthermia Association of the United States. *Anesthesiology* **108,** 603-611.

Launikonis BS, Barnes M & Stephenson DG. (2003). Identification of the coupling between skeletal muscle store-operated Ca2+ entry and the inositol trisphosphate receptor. *Proceedings of the National Academy of Sciences* **100,** 2941-2944.

Launikonis BS, Murphy RM & Edwards JN. (2010). Toward the roles of store-operated Ca2+ entry in skeletal muscle. *Pflügers Archiv - European Journal of Physiology* **460,** 813-823.

Launikonis BS & Ríos E. (2007). Store-operated Ca^{2+} entry during intracellular Ca^{2+} release in mammalian skeletal muscle. *The Journal of Physiology* **583,** 81-97.

Launikonis BS & Stephenson DG. (1997). Effect of saponin treatment on the sarcoplasmic reticulum of rat, cane toad and crustacean (yabby) skeletal muscle. *J Physiol* **504 (Pt 2),** 425-437.

Launikonis BS & Stephenson DG. (2002a). Properties of the vertebrate skeletal muscle tublular system as a sealed compartment. *Cell Biology International* **26,** 921-929.

Launikonis BS & Stephenson DG. (2002b). Tubular system volume changes in twitch fibres from toad and rat skeletal muscle assessed by confocal microscopy. *J Physiol* **538,** 607-618.

Launikonis BS, Zhou J, Royer L, Shannon TR, Brum G & Ríos E. (2006). Depletion “skraps” and dynamic buffering inside the cellular calcium store. *Proceedings of the National Academy of Sciences of the United States of America* **103,** 2982-2987.

Laver DR. (2001). Proceedings of the Australian Physiological and Pharmacological Society Symposium: New Frontiers in Muscle Research The power of single

channel recording and analysis: its application to ryanodine receptors in lipid bilayers. *Clinical and Experimental Pharmacology and Physiology* **28,** 675-686.

Laver DR, Baynes TM & Dulhunty AF. (1997a). Magnesium Inhibition of Ryanodine-Receptor Calcium Channels: Evidence for Two Independent Mechanisms. *J Membrain Biol* **156,** 213-229.

Laver DR, O'Neill ER & Lamb GD. (2004). Luminal Ca^{2+}–regulated Mg^{2+} Inhibition of Skeletal RyRs Reconstituted as Isolated Channels or Coupled Clusters. *The Journal of General Physiology* **124,** 741-758.

Laver DR, Owen VJ, Junankar PR, Taske NL, Dulhunty AF & Lamb GD. (1997b). Reduced inhibitory effect of Mg^{2+} on ryanodine receptor-Ca^{2+} release channels in malignant hyperthermia. *Biophysical journal* **73,** 1913-1924.

Laver DR & van Helden DF. (2011). Three independent mechanisms contribute to tetracaine inhibition of cardiac calcium release channels. *Journal of Molecular and Cellular Cardiology* **51,** 357-369.

Lehman W, Craig R & Vibert P. (1994). Ca^{2+}-induced tropomyosin movement in Limulus thin filaments revealed by three-dimensional reconstruction. *Nature* **368,** 65.

Leslie GC & Part NJ. (1981). The action of dantrolene sodium on rat fast and slow muscle in vivo. *British Journal of Pharmacology* **72,** 665-672.

Liou J, Kim ML, Do Heo W, Jones JT, Myers JW, Ferrell JE, Jr. & Meyer T. (2005). STIM is a Ca^{2+} Sensor Essential for Ca^{2+}-Store-Depletion-Triggered Ca^{2+} Influx. *Current Biology* **15,** 1235-1241.

López Jose R, Contreras J, Linares N & Allen Paul D. (2000). Hypersensitivity of Malignant Hyperthermia–susceptible Swine Skeletal Muscle to Caffeine Is Mediated by High Resting Myoplasmic [Ca^{2+}]. *Anesthesiology* **92,** 1799-1806.

Luik R, Wang B, Prakriya M, Wu M & Lewis R. (2008). Oligomerization of STIM1 couples ER calcium depletion to CRAC channel activation. *Nature* **454,** 538 - 542.

Luik RM, Wu MM, Buchanan J & Lewis RS. (2006). The elementary unit of store-operated Ca^{2+} entry: local activation of CRAC channels by STIM1 at ER–plasma membrane junctions. *The Journal of Cell Biology* **174,** 815-825.

Lukyanenko V, Subramanian S, Gyorke I, Wiesner TF & Gyorke S. (1999). The role of luminal Ca^{2+} in the generation of Ca^{2+} waves in rat ventricular myocytes. *J Physiol* **518,** 173-186.

Manno C, Figueroa L, Royer L, Pouvreau S, Lee CS, Volpe P, Nori A, Zhou J, Meissner G, Hamilton SL & Ríos E. (2013a). Altered Ca^{2+} concentration, permeability and buffering in the myofibre Ca^{2+} store of a mouse model of malignant hyperthermia. *The Journal of Physiology* **591,** 4439-4457.

Manno C, Figueroa LC, Gillespie D, Fitts R, Kang C, Franzini-Armstrong C & Rios E. (2017). Calsequestrin depolymerizes when calcium is depleted in the sarcoplasmic reticulum of working muscle. *Proceedings of the National Academy of Sciences* **114,** E638-E647.

Manno C, Sztretye M, Figueroa L, Allen PD & Ríos E. (2013b). Dynamic measurement of the calcium buffering properties of the sarcoplasmic reticulum in mouse skeletal muscle. *The Journal of Physiology* **591,** 423-442.

Marie V & Silva JE. (1998). Calcium pool size modulates the sensitivity of the ryanodine receptor channel and calcium-dependent ATPase of heavy sarcoplasmic reticulum to extravesicular free calcium concentration. *Journal of Cellular Physiology* **175,** 283-294.

Marieb EN. (2001). *Human anatomy & physiology*. Benjamin Cummings, San Francisco.

Martonosi AN & Pikula S. (2003). The network of calcium regulation in muscle. *Acta biochimica Polonica* **50,** 1-30.

Maxwell JT & Blatter LA. (2012). Facilitation of cytosolic calcium wave propagation by local calcium uptake into the sarcoplasmic reticulum in cardiac myocytes. *J Physiol* **590,** 6037-6045.

Meissner G, Rousseau E, Lai FA, Liu Q-Y & Anderson KA. (1988). Biochemical characterization of the Ca^{2+} release channel of skeletal and cardiac sarcoplasmic reticulum. *Molecular and Cellular Biochemistry* **82,** 59-65.

Melzer W, Herrmann-Frank A & Lüttgau HC. (1995). The role of Ca^{2+} ions in excitation-contraction coupling of skeletal muscle fibres. *Biochimica et Biophysica Acta (BBA) - Reviews on Biomembranes* **1241,** 59-116.

Miura M, Boyden PA & ter Keurs HE. (1999). Ca^{2+} waves during triggered propagated contractions in intact trabeculae. Determinants of the velocity of propagation. *Circ Res* **84,** 1459-1468.

Miura M, Ishide N, Oda H, Sakurai M, Shinozaki T & Takishima T. (1993). Spatial features of calcium transients during early and delayed afterdepolarizations. *Am J Physiol* **265,** H439-444.

Moisescu DG & Thieleczek R. (1978). Calcium and strontium concentration changes within skinned muscle preparations following a change in the external bathing solution. *The Journal of Physiology* **275,** 241-262.

Monnier N, Krivosic-Horber R, Payen J F, Kozak-Ribbens G, Nivoche Y, Adnet P, Reyford H & Lunardi J. (2002). Presence of Two Different Genetic Traits in Malignant Hyperthermia FamiliesImplication for Genetic Analysis, Diagnosis, and Incidence of Malignant Hyperthermia Susceptibility. *Anesthesiology* **97,** 1067-1074.

Murayama T & Kurebayashi N. (2011). Two ryanodine receptor isoforms in nonmammalian vertebrate skeletal muscle: Possible roles in excitation–contraction coupling and other processes. *Progress in biophysics and molecular biology* **105,** 134-144.

Murayama T, Oba T, Hara H, Wakebe K, Ikemoto N & Ogawa Y. (2007). Postulated role of interdomain interaction between regions 1 and 2 within type 1 ryanodine receptor in the pathogenesis of porcine malignant hyperthermia. *Biochemical Journal* **402,** 349-357.

Murayama T & Ogawa Y. (2002) Roles of Two Ryanodine Receptor Isoforms Coexisting in Skeletal Muscle. *Trends in Cardiovascular Medicine* **12,** 305-311.

Murayama T & Ogawa Y. (2001). Selectively Suppressed Ca^{2+}-induced Ca^{2+}Release Activity of α-Ryanodine Receptor (α-RyR) in Frog Skeletal Muscle Sarcoplasmic Reticulum: Potential distnct modes in Ca^{2+} release between α- and β-RyR. *Journal of Biological Chemistry* **276,** 2953-2960.

Murphy RM, Larkins NT, Mollica JP, Beard NA & Lamb GD. (2009). Calsequestrin content and SERCA determine normal and maximal Ca^{2+} storage levels in sarcoplasmic reticulum of fast- and slow-twitch fibres of rat. *The Journal of Physiology* **587,** 443-460.

Nakai J, Dirksen RT, Nguyen HT, Pessah IN, Beam KG & Allen PD. (1996). Enhanced dihydropyridine receptor channel activity in the presence of ryanodine receptor. *Nature* **380,** 72.

Nakai J, Sekiguchi N, Rando TA, Allen PD & Beam KG. (1998). Two Regions of the Ryanodine Receptor Involved in Coupling withl-Type Ca^{2+} Channels. *Journal of Biological Chemistry* **273,** 13403-13406.

Natori R. (1954). The role of myofibrils, sarcoplasm and sarcolemma *Jikeikai Med J* **1,** 177-192.

Nelson PD, Thomas E. (1992). Halothane Effects on Human Malignant Hyperthermia Skeletal Muscle Single Calcium-release Channels in Planar Lipid Bilayers. *Anesthesiology* **76,** 588-595.

O'Brien J, Valdivia HH & Block BA. (1995). Physiological differences between the alpha and beta ryanodine receptors of fish skeletal muscle. *Biophysical journal* **68,** 471-482.

O'Neill SC, Miller L, Hinch R & Eisner DA. (2004). Interplay between SERCA and sarcolemmal Ca^{2+} efflux pathways controls spontaneous release of Ca^{2+} from the sarcoplasmic reticulum in rat ventricular myocytes. *The Journal of Physiology* **559,** 121-128.

Okada J-i, Sugiura S, Nishimura S & Hisada T. (2005). Three-dimensional simulation of calcium waves and contraction in cardiomyocytes using the finite element method. *American Journal of Physiology - Cell Physiology* **288,** C510-C522.

Oo YW, Gomez-Hurtado N, Walweel K, van Helden DF, Imtiaz MS, Knollmann BC & Laver DR. (2015). Essential Role of Calmodulin in RyR Inhibition by Dantrolene. *Molecular pharmacology* **88,** 57-63.

Owen VJ, Lamb GD, Stephenson DG & Fryer MW. (1997a). Relationship between depolarization-induced force responses and Ca^{2+} content in skeletal muscle fibres of rat and toad. *The Journal of Physiology* **498,** 571-586.

Owen VJ, Taske NL & Lamb GD. (1997b). Reduced Mg^{2+} inhibition of Ca^{2+} release in muscle fibers of pigs susceptible to malignant hyperthermia. *Am J Physiol* **272,** C203-211.

Pape PC, Fénelon K, Lamboley CRH & Stachura D. (2007). Role of calsequestrin evaluated from changes in free and total calcium concentrations in the sarcoplasmic reticulum of frog cut skeletal muscle fibres. *The Journal of Physiology* **581,** 319-367.

Parekh AB & Putney JW. (2005). Store-Operated Calcium Channels. *Physiological Reviews* **85,** 757-810.

Park H, Park IY, Kim E, Youn B, Fields K, Dunker AK & Kang C. (2004). Comparing skeletal and cardiac calsequestrin structures and their calcium binding: a proposed mechanism for coupled calcium binding and protein polymerization. *J Biol Chem* **279,** 18026-18033.

Park H, Wu S, Dunker AK & Kang C. (2003). Polymerization of Calsequestrin: Implications for Ca^{2+} regulation. *Journal of Biological Chemistry* **278,** 16176-16182.

Parkash J & Asotra K. (2012). Calcium Oscillations and Waves in Cells. In *Calcium Signaling*, ed. Islam MS, pp. 521-529. Springer Netherlands, Dordrecht.

Parod RJ & Putney JW. (1978). The role of calcium in the receptor mediated control of potassium permeability in the rat lacrimal gland. *The Journal of Physiology* **281,** 371-381.

Parry DAD & Squire JM. (1973). Structural role of tropomyosin in muscle regulation: Analysis of the X-ray diffraction patterns from relaxed and contracting muscles. *Journal of Molecular Biology* **75,** 33-55.

Paul-Pletzer K, Palnitkar SS, Jimenez LS, Morimoto H & Parness J. (2001). The Skeletal Muscle Ryanodine Receptor Identified as a Molecular Target of [^{3}H]Azidodantrolene by Photoaffinity Labeling. *Biochemistry* **40,** 531-542.

Paul-Pletzer K, Yamamoto T, Bhat MB, Ma J, Ikemoto N, Jimenez LS, Morimoto H, Williams PG & Parness J. (2002). Identification of a Dantrolene-binding Sequence on the Skeletal Muscle Ryanodine Receptor. *Journal of Biological Chemistry* **277,** 34918-34923.

Petrovič P, Valent I, Cocherová E, Pavelková J & Zahradníková A. (2015). Ryanodine receptor gating controls generation of diastolic calcium waves in cardiac myocytes. *The Journal of General Physiology* **145,** 489-511.

Pinali C, Bennett H, Davenport JB, Trafford AW & Kitmitto A. (2013). Three-Dimensional Reconstruction of Cardiac Sarcoplasmic Reticulum Reveals a Continuous Network Linking Transverse-Tubules. *Circulation research* **113,** 1219-1230.

Podranski T, Bouillon T, Schumacher PM, Taguchi A, Sessler DI & Kurz A. (2005). Compartmental Pharmacokinetics of Dantrolene in Adults: Do Malignant Hyperthermia Association Dosing Guidelines Work? *Anesthesia & Analgesia* **101,** 1695-1699.

Putney JW. (1977). Muscarinic, alpha-adrenergic and peptide receptors regulate the same calcium influx sites in the parotid gland. *The Journal of Physiology* **268,** 139-149.

Rahimov F & Kunkel LM. (2013). Cellular and molecular mechanisms underlying muscular dystrophy. *The Journal of Cell Biology* **201,** 499-510.

Rebbeck RT, Essawy MM, Nitu FR, Grant BD, Gillispie GD, Thomas DD, Bers DM & Cornea RL. (2017). High-Throughput Screens to Discover Small-Molecule Modulators of Ryanodine Receptor Calcium Release Channels. *SLAS DISCOVERY: Advancing Life Sciences R&D* **22,** 176-186.

Rich TL, Langer GA & Klassen MG. (1988). Two components of coupling calcium in single ventricular cell of rabbits and rats. *American Journal of Physiology - Heart and Circulatory Physiology* **254,** H937-H946.

Rios E & Brum G. (2002). Initiation and termination of calcium sparks in skeletal muscle. *Front Biosci* **7,** d1212-1222.

Ríos E, Figueroa L, Manno C, Kraeva N & Riazi S. (2015). The couplonopathies: A comparative approach to a class of diseases of skeletal and cardiac muscle. *The Journal of General Physiology* **145,** 459-474.

Rodney GG & Schneider MF. (2003). Calmodulin Modulates Initiation but Not Termination of Spontaneous Ca^{2+} Sparks in Frog Skeletal Muscle. *Biophysical journal* **85,** 921-932.

Roos J, DiGregorio P, Yeromin A, Ohlsen K, Lioudyno M, Zhang S, Safrina O, Kozak J, Wagner S, Cahalan M, Velicelebi G & Stauderman K. (2005). STIM1, an essential and conserved component of store-operated Ca^{2+} channel function. *J Cell Biol* **169,** 435 - 445.

Rosemblatt M, Hidalgo C, Vergara C & Ikemoto N. (1981). Immunological and biochemical properties of transverse tubule membranes isolated from rabbit skeletal muscle. *Journal of Biological Chemistry* **256,** 8140-8148.

Rosenberg H, Pollock N, Schiemann A, Bulger T & Stowell K. (2015). Malignant hyperthermia: a review. *Orphanet Journal of Rare Diseases* **10,** 93.

Rossi D, Murayama T, Manini I, Franci D, Ogawa Y & Sorrentino V. (2007). Expression and functional activity of ryanodine receptors (RyRs) during skeletal muscle development. *Cell Calcium* **41,** 573-580.

Rousseau E & Meissner G. (1989). Single cardiac sarcoplasmic reticulum Ca^{2+}-release channel: activation by caffeine. *American Journal of Physiology - Heart and Circulatory Physiology* **256,** H328-H333.

Royer L & Ríos E. (2009). Deconstructing calsequestrin. Complex buffering in the calcium store of skeletal muscle. *The Journal of Physiology* **587,** 3101-3111.

Sacchetto R, Volpe P, Damiani E & Margreth A. (1993). Postnatal development of rabbit fast-twitch skeletal muscle: accumulation, isoform transition and fibre distribution of calsequestrin. *Journal of Muscle Research & Cell Motility* **14,** 646-653.

Sambuughin N, Sei Y, Gallagher S, Kathleen L, Wyre Hadley W, Madsen D, Nelson D, Thomas E, Fletcher D, Jeffrey E, Rosenberg H, Muldoon D, Sheila M. (2001). North American Malignant Hyperthermia PopulationScreening of the Ryanodine Receptor Gene and Identification of Novel Mutations. *Anesthesiology* **95,** 594-599.

Schiaffino S & Reggiani C. (2011). *Fiber Types in Mammalian Skeletal Muscles*, vol. 91.

Schneider MF & Chandler WK. (1973). Voltage Dependent Charge Movement in Skeletal Muscle: a Possible Step in Excitation–Contraction Coupling. *Nature* **242,** 244.

Shannon TR, Ginsburg KS & Bers DM. (2002). Quantitative assessment of the SR Ca^{2+} leak-load relationship. *Circ Res* **91,** 594-600.

Shannon TR, Guo T & Bers DM. (2003). Ca^{2+} scraps: local depletions of free [Ca^{2+}] in cardiac sarcoplasmic reticulum during contractions leave substantial Ca^{2+} reserve. *Circ Res* **93,** 40-45.

Shirokova N, García J, Pizarro G & Ríos E. (1996). Ca^{2+} release from the sarcoplasmic reticulum compared in amphibian and mammalian skeletal muscle. *The Journal of General Physiology* **107,** 1-18.

Shirokova N, Garcia J & Rios E. (1998). Local calcium release in mammalian skeletal muscle. *J Physiol* **512 (Pt 2),** 377-384.

Shirokova N & Rios E. (1997). Small event Ca^{2+} release: a probable precursor of Ca^{2+} sparks in frog skeletal muscle. *J Physiol* **502 (Pt 1),** 3-11.

Song Z, Qu Z & Karma A. (2017). Stochastic initiation and termination of calcium-mediated triggered activity in cardiac myocytes. *Proceedings of the National Academy of Sciences* **114,** E270-E279.

Spencer MJ & Mellgren RL. (2002). Overexpression of a calpastatin transgene in mdx muscle reduces dystrophic pathology. *Human Molecular Genetics* **11,** 2645-2655.

Stathopulos PB, Zheng L, Li G-Y, Plevin MJ & Ikura M. (2005). Structural and Mechanistic Insights into STIM1-Mediated Initiation of Store-Operated Calcium Entry. *Cell* **135,** 110-122.

Steele DS & Duke AM. (2007). Defective Mg^{2+} regulation of RyR1 as a causal factor in malignant hyperthermia. *Archives of Biochemistry and Biophysics* **458,** 57-64.

Sutko JL & Airey JA. (1996). Ryanodine receptor Ca^{2+} release channels: does diversity in form equal diversity in function? *Physiological Reviews* **76,** 1027-1071.

Szentesi P, Collet C, Sárközi S, Szegedi C, Jona I, Jacquemond V, Kovács L & Csernoch L. (2001). Effects of Dantrolene on Steps of Excitation-Contraction Coupling in Mammalian Skeletal Muscle Fibers. *The Journal of General Physiology* **118,** 355-376.

Murayama T, Seagar MJ, Jones JF, Reber BF & Catterall WA. (1987). Subunit structure of dihydropyridine-sensitive calcium channels from skeletal muscle. *Proceedings of the National Academy of Sciences* **84,** 5478-5482.

Tanabe T, Beam KG, Adams BA, Niidome T & Numa S. (1990). Regions of the skeletal muscle dihydropyridine receptor critical for excitation–contraction coupling. *Nature* **346,** 567.

Tripathy A, Xu L, Mann G & Meissner G. (1995). Calmodulin activation and inhibition of skeletal muscle Ca2+ release channel (ryanodine receptor). Biophysical journal 69, 106-119.

Turner PR, Fong PY, Denetclaw WF & Steinhardt RA. (1991). Increased calcium influx in dystrophic muscle. *The Journal of Cell Biology* **115,** 1701-1712.

Wagner Ii LE, Groom LA, Dirksen RT & Yule DI. (2014). Characterization of ryanodine receptor type 1 single channel activity using “on-nucleus” patch clamp. *Cell Calcium* **56,** 96-107.

Weiss RG, O’Connell KMS, Flucher BE, Allen PD, Grabner M & Dirksen RT. (2004). Functional analysis of the R1086H malignant hyperthermia mutation in the DHPR reveals an unexpected influence of the III-IV loop on skeletal muscle EC coupling. *American Journal of Physiology - Cell Physiology* **287,** C1094-C1102.

Westerblad H & Allen DG. (1992). Myoplasmic free Mg^{2+} concentration during repetitive stimulation of single fibres from mouse skeletal muscle. *The Journal of Physiology* **453,** 413-434.

Wu KD. (1993). Molecular cloning and quantification of sarcoplasmic reticulum Ca^{2+}-ATPase isoforms in rat muscles. *The American journal of physiology* **264,** C333-341.

Xu L, Mann G & Meissner G. (1996). Regulation of Cardiac Ca^{2+} Release Channel (Ryanodine Receptor) by Ca^{2+}, H^{+}, Mg^{2+}, and Adenine Nucleotides Under Normal and Simulated Ischemic Conditions. *Circulation Research* **79,** 1100-1109.

Yu X, Carroll S, Rigaud JL & Inesi G. (1993). H^{+} countertransport and electrogenicity of the sarcoplasmic reticulum Ca^{2+} pump in reconstituted proteoliposomes. *Biophysical journal* **64,** 1232-1242.

Zhang SL, Yu Y, Roos J, Kozak JA, Deerinck TJ, Ellisman MH, Stauderman KA & Cahalan MD. (2005). STIM1 is a Ca^{2+} sensor that activates CRAC channels and migrates from the Ca^{2+} store to the plasma membrane. *Nature* **437,** 902-905.

Zhou Y, Meraner P, Kwon HT, Machnes D, Oh-hora M, Zimmer J, Huang Y, Stura A, Rao A & Hogan PG. (2009). STIM1 gates the store-operated calcium channel ORAI1 in vitro. *Nature Structural &Amp; Molecular Biology* **17,** 112.

Ziman AP, Ward CW, Rodney GG, Lederer WJ & Bloch RJ. (2010). Quantitative Measurement of Ca^{2+} in the Sarcoplasmic Reticulum Lumen of Mammalian Skeletal Muscle. *Biophysical journal* **99,** 2705-2714.

UQ Research and Innovation
Director, Research Management Office
Nicole Thompson

Animal Ethics Approval Certificate

27-Apr-2016

Please check all details below and inform the Animal Welfare Unit within 10 working days if anything is incorrect.

Activity Details

Chief Investigator: Dr Bradley Launikonis

Title: Calcium regulation in healthy and dystrophic skeletal muscle

AEC Approval Number: SCMB/032/14/ARC

Previous AEC Number: SBMS/419/10/ARC (NF)

Approval Duration: 17-Mar-2014 to 17-Mar-2017

Funding Body: ARC

Group: Anatomical Biosciences

Other Staff/Students: Wally Thomas, Xaver Konig, Tanya Cully

Location(s): St Lucia Bldg 76 - Chemistry (SCMB)
St Lucia Bldg 64 - Sir William MacGregor

Summary

Subspecies	Strain	Class	Gender	Source	Approved	Remaining
Amphibians	Cane Toad (Bufo Marinus)	Adults	Mix	Commercial breeding colony	150	111
Mice - non genetically modified	C57BJ/6	Adults	Male	Commercial breeding colony	150	138
Mice - non genetically modified	C57BL10 ScSn mdx	Adults	Male	Commercial breeding colony	162	149
Mice - non genetically modified	C57Bl/10	Adults	Mix	Commercial breeding colony	50	50
Rats - non genetically modified	Wistar	Adults	Male	Commercial breeding colony	300	146
Rats - non genetically modified	Sprague-Dawley	Adults	Male	Commercial breeding colony	14	14

Permits

Provisos

Approval Details

Description	Amount	Balance
Amphibians (Cane Toad (Bufo Marinus), Mix, Adults, Commercial breeding colony)		
12 Mar 2014 Initial approval	150	150
31 Dec 2014 Use in 2014 (from 2015 MAR)	-31	119

31 Dec 2015	Use in 2015 (from 2016 MAR)	-8	111
Mice - non genetically modified (C57BJ/6, Male, Adults, Commercial breeding colony)			
12 Mar 2014	Initial approval	150	150
31 Dec 2014	Use in 2014 (from 2015 MAR)	-9	141
31 Dec 2015	Use in 2015 (from 2016 MAR)	-3	138
Mice - non genetically modified (C57Bl/10, Mix, Adults, Commercial breeding colony)			
11 Nov 2015	Mod #1	50	50
31 Dec 2015	Use in 2015 (from 2016 MAR)	0	50
Mice - non genetically modified (C57BL10 ScSn mdx, Male, Adults, Commercial breeding colony)			
12 Mar 2014	Initial approval	150	150
31 Dec 2014	Use in 2014 (from 2015 MAR)	-6	144
31 Dec 2015	Use in 2015 (from 2016 MAR)	-7	137
13 Apr 2016	Mod #2	12	149
Rats - non genetically modified (Sprague-Dawley, Male, Adults, Commercial breeding colony)			
20 Apr 2016	Mod #2	14	14
Rats - non genetically modified (Wistar, Male, Adults, Commercial breeding colony)			
12 Mar 2014	Initial approval	150	150
31 Dec 2014	Use in 2014 (from 2015 MAR)	-50	100
11 Nov 2015	Mod #1	150	250
31 Dec 2015	Use in 2015 (from 2016 MAR)	-90	160
13 Apr 2016	Modification #2	-14	146

Please note the animal numbers supplied on this certificate are the total allocated for the approval duration

Please use this Approval Number:

1. When ordering animals from Animal Breeding Houses
2. For labelling of all animal cages or holding areas. In addition please include on the label, Chief Investigator's name and contact phone number.
3. When you need to communicate with this office about the project.

It is a condition of this approval that all project animal details be made available to Animal House OIC.
(UAEC Ruling 14/12/2001)

The Chief Investigator takes responsibility for ensuring all legislative, regulatory and compliance objectives are satisfied for this project.

This certificate supercedes all preceeding certificates for this project (i.e. those certificates dated before 27-Apr-2016)

THE UNIVERSITY OF QUEENSLAND

Institutional Human Research Ethics Approval

Project Title:	Examining Functional And Structural Changes Of Skeletal Muscle In Inherited Muscle Myopathies - 28/07/2016 - AMENDMENT
Chief Investigator:	Dr Bradley Launikonis
Supervisor:	None
Co-Investigator(s):	Prof Jeff Coombes
School(s):	Human Movement Studies; Biomedical Sciences
Approval Number:	2014000826
Granting Agency/Degree:	None
Duration:	31st July 2019

Comments/Conditions:

Extension of project duration to 31st July 2019

Note: if this approval is for amendments to an already approved protocol for which a UQ Clinical Trials Protection/Insurance Form was originally submitted, then the researchers must directly notify the UQ Insurance Office of any changes to that Form and Participant Information Sheets & Consent Forms as a result of the amendments, before action.

Name of responsible Committee:
Medical Research Ethics Committee
This project complies with the provisions contained in the *National Statement on Ethical Conduct in Human Research* and complies with the regulations governing experimentation on humans.

Name of Ethics Committee representative:
Dr Jennifer Paratz
Chairperson
Medical Research Ethics Committee

Signature _____ Date 28/7/16